



Max Planck **Graduate Center**
mit der Johannes Gutenberg-Universität



Hydroclimate and Extreme Rainfall Variability over the Past 7500 years in Southeastern and Southern Brazil

Dissertation

for attaining the academic degree of
„Doctor rerum naturalium“ (Dr. rer. nat.)

of the Departments

08 – Physics, Mathematics, and Computer Science,

09 – Chemistry, Pharmaceutics and Geosciences,

10 – Biology, and University Medicine

of the Johannes Gutenberg University Mainz

by

Julio Cauhy Rodrigues

born 07.11.1992

in São Paulo

Johannes Gutenberg University Mainz with the Max Planck Graduate Center
prepared at the Institute of Geosciences

Mainz, October 2025

Faculty director: Prof. Dr. Eva Rentschler

1st supervisor: Prof. Dr. Denis Scholz

2nd supervisor: Dr. Hubert Vonhof

Date of oral examination: 19.12.2026

Scientific Board:

Prof. Dr. Monika Markowska

Prof. Dr. Igor Obreht

Prof. Dr. Anne Jantschke

Reuse License:

Copyright protection (in C-1.0)

Sworn declaration

I hereby declare that I wrote the dissertation submitted without any unauthorized external assistance and used only sources acknowledged in the work. All textual passages which are appropriated verbatim or paraphrased from published and unpublished texts as well as all information obtained from oral sources are duly indicated and listed in accordance with bibliographical rules. In carrying out this research, I complied with the rules of standard scientific practice as formulated in the statutes of Johannes Gutenberg University Mainz to insure standard scientific practice.

.....

Julio Cauhy Rodrigues

Mainz, October 2025

Zusammenfassung

Der Süden und Südosten Brasiliens sind stark von extremen Niederschlagsereignissen (ERE) betroffen, die häufig Erdbeben und Sturzfluten auslösen und schwerwiegende sozioökonomische Auswirkungen haben, von denen gefährdete Bevölkerungsgruppen unverhältnismäßig stark betroffen sind. Aktuelle Klimaprognosen deuten darauf hin, dass die Häufigkeit und das Ausmaß von ERE aufgrund der erhöhten Luftfeuchtigkeit und Verdunstungsrate im Zuge der globalen Erwärmung wahrscheinlich zunehmen werden. Darüber hinaus wird prognostiziert, dass sich El-Niño-Southern-Oscillation-Ereignisse (ENSO) verstärken und häufiger auftreten werden, was die Extreme durch Fernverbindungen zwischen dem Pazifik und Südamerika weiter verstärken wird.

Trotz dieser Prognosen schränkt der Mangel an zuverlässigen ERE-Aufzeichnungen, die über den Zeitraum des anthropogenen Klimawandels hinausgehen, unser Verständnis der natürlichen Variabilität und der Antriebsmechanismen hinter solchen Ereignissen ein, insbesondere über lange Zeiträume hinweg. In diesem Zusammenhang bieten Speläotheme, die aus Höhlen gesammelt wurden, die als Reaktion auf EREs überflutet werden, ein wertvolles Archiv für die Rekonstruktion vergangener ERE-Ereignisse. Die Integration der hydrologischen Überwachung von Höhlen mit paläoklimatischen Rekonstruktionen bietet einen robusten Rahmen für die Untersuchung der natürlichen Variabilität von EREs. Präzise ^{230}Th -U-Datierungen in Kombination mit detaillierten mikrostratigraphischen Analysen ermöglichen die Rekonstruktion von ERE-Zeitreihen und lassen uns beurteilen, wie sich ihre Häufigkeit und Intensität im Laufe der Zeit verändert haben. Darüber hinaus bieten Speläotheme das Potenzial für Multi-Proxy-Analysen, die die Rekonstruktion von Hydroklima- und Umweltbedingungen über mehrere Zeitskalen hinweg ermöglichen. Durch die Kombination von ERE-Rekonstruktionen mit einem Multi-Proxy-Ansatz können wir eine umfassende Aufzeichnung der vergangenen ERE-Variabilität und hydroklimatischen Veränderungen erstellen und so die Treiber und Rückkopplungen bewerten, die das Auftreten von EREs modulieren.

In dieser Studie analysieren wir mehrere Speläotheme aus der Malfazido-Höhle, um die extremen Niederschlagsschwankungen der letzten 7.500 Jahre zu rekonstruieren. Ein mehrjähriges Höhlenüberwachungsprogramm hat gezeigt, dass die Malfazido-Höhle empfindlich auf extreme Niederschlagsereignisse reagiert. Aufzeichnungen von stabilen Isotopen und Spurenelementen zeigen anhaltende interannuelle Periodizitäten, die mit der ENSO-Variabilität übereinstimmen, sowie mehrhundertjährige Zyklen, die wechselnde Nass- und Trockenphasen über Südostbrasilien widerspiegeln. Die Niederschlagsanomalien stimmen weitgehend mit Episoden der Abkühlung des Nordatlantiks überein, wie beispielsweise der Kleinen Eiszeit und den Bond-Ereignissen, und stehen im Zusammenhang mit einer Abschwächung der Atlantischen Meridionalen Umwälzströmung (AMOC) und einer großräumigen Umstrukturierung der Atmosphäre. Unsere Ergebnisse zeigen auch ein Niederschlagsdipolmuster zwischen Süd- und Südostbrasilien auf multizentennialer Skala, das dem südamerikanischen Dipol ähnelt – einem markanten intrasaisonalen Merkmal des südamerikanischen Sommermonsuns (SASM). Schließlich zeigen Vergleiche mit Aufzeichnungen aus der Antarktis, dem Pazifik und dem Nordatlantik eine starke Modulation sowohl tropischer als auch extratropischer Antriebe auf das Hydroklima im Südosten und Süden Brasiliens.

Abstract

Southern and Southeastern Brazil are strongly affected by extreme rainfall events (ERE), which frequently trigger landslides and flash floods, causing severe socioeconomic impacts that disproportionately affect vulnerable populations. Current climate projections indicate that the frequency and magnitude of ERE are likely to increase due to enhanced atmospheric moisture and evaporative demand under global warming. In addition, El Niño–Southern Oscillation (ENSO) events are projected to intensify and occur more frequently, further amplifying ENSO-related extremes through Pacific–South American teleconnections.

Despite these projections, the lack of reliable ERE records extending beyond the period of anthropogenic climate change constrains our understanding of the natural variability and forcing mechanisms behind such events, particularly over longer time-scales. In this context, speleothems collected from caves subjected to flood in response to ERE offer a valuable archive for reconstructing past ERE occurrences. The integration of cave hydrological monitoring with paleoclimate reconstructions provides a robust framework for investigating the natural variability of ERE. Precise ^{230}Th –U dating combined with detailed microstratigraphic analyses provide a robust framework for the reconstruction of ERE time series and allows us to assess how their frequency have changed through time. Furthermore, speleothems offer the potential for multi-proxy analyses, allowing the reconstruction of hydroclimate and environmental conditions across multiple temporal scales along with the ERE. By combining ERE reconstructions with a multi-proxy approach, we can generate a comprehensive record of past ERE variability and hydroclimatic changes, allowing us to evaluate the how forcings and changes in the hydroclimate impact the ERE occurrence.

In this study, we use multiple speleothems from Malfazido Cave to reconstruct extreme rainfall variability over the past 7,500 years. A multi-year cave monitoring program has evidenced Malfazido Cave response to extreme rainfall events. Stable isotope ($\delta^{18}\text{O}$ and $\delta^{13}\text{C}$) and trace element records reveal persistent interannual periodicities consistent with ENSO variability, as well as multi-centennial cycles evidencing a pattern of shifting wet/dry phases over Southeastern Brazil. The wet anomalies are synchronous with events of North Atlantic cooling, such as the Little Ice Age and Bond events, and are associated with a weakening of the Atlantic Meridional Overturning Circulation (AMOC) and large-scale atmospheric reorganization related to shifts in the Intertropical Convergence Zone (ITCZ). Our results also evidenced a multi-centennial rainfall dipole pattern between Southern (SB) and Southeastern Brazil (SEBRA), resembling the intraseasonal South American Dipole. Finally, comparisons with Antarctic, Pacific, and North Atlantic records highlight the influence of both tropical and extratropical teleconnections on the modulation of the hydroclimate and ERE of SEBRA and SB.

Table of Contents

Sworn declaration	ii
Zusammenfassung	iv
Abstract	vi
Table of Contents	viii
List of Figures	xi
List of Tables	xiv
1. Chapter 1 - Introduction	16
1.1. References.....	19
2. Basics	22
2.1. Speleothems archives: A window to past environmental and climate conditions	22
2.2. Stalagmite formation	23
2.2.1. CALCIUM CARBONATE PRECIPITATION – FROM RAINFALL TO STALAGMITE FORMATION	23
2.2.2. FLOOD-DERIVED DETRITAL LAYERS WITHIN STALAGMITES	24
2.3. Stalagmite dating - U-Series disequilibrium dating method	27
2.3.1. STUDY CASE OF ²³⁰ Th/U-DATING OF SAMPLES UNDER FLOODING CONDITIONS.....	30
2.4. Microstratigraphy of flood-derived detrital layers and past flood reconstruction	34
2.4.1. VISUAL IDENTIFICATION METHODS.....	35
2.4.2. GEOCHEMICAL ANALYSIS.....	36
2.4.3. MAGNETIC MEASUREMENTS	37
2.4.4. FLOOD-DERIVED LAYERS CHARACTERIZATION – MALFAZIDO CAVE STUDY CASE	37
2.4.5. CAVE FLOOD FREQUENCY RECONSTRUCTION.....	42
2.5. Oxygen stable isotopes ($\delta^{18}\text{O}$) in speleothems	42
2.6. Carbon isotopes ($\delta^{13}\text{C}$) in speleothems.....	45
2.7. Geochemical controls on speleothem trace elementary ratios with calcium	47
2.8. References.....	49
3. Chapter 3 – Manuscript I	55
3.1. Abstract	56
3.2. Introduction.....	57
3.3. Results and Disucssion	58
3.3.1. CAVE SETTING AND EXPERIMENTAL APPROACH.....	58
3.3.2. TRACKING PAST EXTREME RAINFALL EVENTS IN SOUTHERN BRAZIL VIA THE MALFAZIDO RECORD.....	60
3.3.3. EXTREME RAINFALL VARIABILITY OVER THE HOLOCENE	61
3.3.4. ERE MODULATION AND TELECONNECTIONS OVER THE HOLOCENE	63
3.4. Summary and Conclusion	66
3.5. Methods	67
3.5.1. FLOOD LAYER STRATIGRAPHY (²³⁰ Th/U-DATING, AGE MODELLING, CORRECTIONS, THIN SECTIONS).....	67

3.5.2. CAVE MONITORING AND INSTRUMENTAL DATA	68
3.6. References.....	69
3.7. Supplementary Material – Manuscript I.....	72
3.7.1. SUPPLEMENTARY FIGURES.....	72
3.7.2. SUPPLEMENTARY TABLES	76
3.7.3. SUPPLEMENTARY TEXT 1.....	79
4. Chapter 4 – Manuscript II.....	82
4.1. Abstract.....	84
4.2. Introduction.....	85
4.3. Materials and methods.....	87
4.3.1. CAVE SITE AND STALAGMITE SAMPLES.....	87
4.3.2. TRACE-ELEMENTS RATIOS AND PRINCIPAL COMPONENT ANALYSIS.....	88
4.3.3. $\Delta^{18}\text{O}$ COMPOSITE (MFZ-N-1 + CR-1)	88
4.3.4. REDFIT ANALYSIS, WAVELET COHERENCE TRANSFORMS (WCT) AND CROSS WAVELET ANALYSES	89
4.4. Results.....	89
4.4.1. STALAGMITE $\Delta^{18}\text{O}$ AND COMPOSITE (MFZ-N-1 + CR-1).....	89
4.4.2. STALAGMITE TRACE ELEMENT RATIOS AND PRINCIPAL COMPONENTS	90
4.4.3. SPECTRAL ANALYSIS - REDFIT AND CONTINUOUS WAVELET TRANSFORM (CWT)	92
4.5. Discussion.....	93
4.5.1. PRIOR-CALCITE PRECIPITATION INDICES AS INDICATORS OF PAST RAINFALL VARIABILITY.....	93
4.5.2. SOUTHEASTERN BRAZIL HYDROCLIMATE VARIABILITY OVER THE LATE HOLOCENE	93
4.5.3. MULTI-CENTENNIAL SCALE RAINFALL SEESAW (SEBRA-SESA)	97
4.5.4. RAINFALL SEESAW MECHANISM AND FORCINGS	98
4.5.5. SEBRA-SESA DIPOLE AND EXTREME EVENTS	101
4.6. References.....	103
4.7. Supplementary material – Manuscript II.....	107
5. Chapter 5 – Manuscript III.....	115
5.1. Abstract.....	116
5.2. Introduction.....	118
5.3. Cave settings and samples.....	120
5.4. Materials and Methods.....	121
5.4.1. ^{230}Th -U DATING	121
5.4.2. STABLE ISOTOPE ANALYSES.....	122
5.4.3. TRACE ELEMENT ANALYSIS AND PRINCIPAL COMPONENT ANALYSIS	122
5.4.4. $\Delta^{18}\text{O}$ COMPOSITE	122
5.5. Results.....	123
5.5.1. ^{230}Th -U DATING	123
5.5.2. STALAGMITE STABLE ISOTOPES AND $\Delta^{18}\text{O}$ COMPOSITE RECORD	123

5.6. Discussion.....	127
5.6.1. PROXY INTERPRETATIONS	127
5.6.2. HYDROCLIMATE VARIABILITY OVER THE PAST 7500 YEARS.....	128
5.6.3. BOND EVENT EXPRESSION OVER SEBRA REGION.....	131
5.6.4. INTERNAL STRUCTURES OF BOND EVENTS IN SOUTH AMERICA.....	133
5.7. Summary and implications	135
5.8. References.....	137
5.9. Supplementary material – Manuscript III.....	141
5.9.1. SUPPLEMENTARY FIGURES.....	141
5.9.2. SUPPLEMENTARY TABLES	144
6. Conclusions.....	145
Acknowledgements	147

List of Figures

Chapter 2 – Basics

Figure 2.1	Schematic figure of Malfazido cave profile under flood conditions.	27
Figure 2.2	Schematic illustration of part of the ^{238}U decay chain	29
Figure 2.3	Temporal evolution of the activity ratios from u-decay-series	30
Figure 2.4	Boxplot of activity ratios ($^{230}\text{Th}/^{232}\text{Th}$) within the same cave and within samples.	33
Figure 2.5	^{230}Th -U ages with conventional (1.244), detrital correction factors (0.998) and uncorrected ages.	35
Figure 2.6	Comparison between PIXE analyses (Proton Induced X-Ray Emission) and LA-ICP-MS analyses of trace elements	40
Figure 2.7	Fe PIXE analysis on MFZ-N-1	41
Figure 2.8	Raman map of sample MFZ10_top1 from 59072 individual measurements	42
Figure 2.9	Schematic figure of microstratigraphy analysis using thin section analysis.	43

Chapter 3 – Manuscript I

Figure 3.1	Study area and cave setting	60
Figure 3.2	Accumulated rainfall (mm/30-days) for the October 2023 event.	61
Figure 3.3	Malfazido cave flood frequency and periodicity.	64
Figure 3.4	Global map centered in South America with discussed sites indicated. LLJ (low-level jets) and CF (cold fronts).	67

Chapter 3.7 – Supplementary Figures – Manuscript I

Figure S3.1	Cave flood events recorded in upper and lower gallery between June of 2019 and April of 2024	73
Figure S3.2	Stalagmite samples from Malfazido Cave.	74
Figure S3.3	Cave flood events recorded in the upper and lower gallery between June 2019 and April 2024.	75
Figure S3.4	Historical extreme discharge events related to ERE's on Turvo river with similar or higher magnitude than the event of October 2023.	76
Figure S3.5	REDFIT analysis of Malfazido ERE record.	77
Figure S3.6	Stalagmite thin sections	81

Chapter 4 – Manuscript II

Figure 4.1	Cave site locations and climatic settings.	86
Figure 4.2	Trace element ratios of CR-1 and PC-1.	91
Figure 4.3	$\delta^{18}\text{O}$ and $\delta^{13}\text{C}$ records and $\delta^{18}\text{O}$ composite.	92
Figure 4.4	SEBRA past hydroclimate conditions during Late Holocene.	95

Figure 4.5	PCP-indices from BTV and CR-1.	98
Figure 4.6	PCPCR-1-Index compared with ITCZ displacement.	102
Figure 4.7	Dipole-index and ERE occurrence.	103
Chapter 4.8 – Supplementary Figures – Manuscript II		
Figure S4.1	Stalagmite samples (CR-1 and MFZ-N-1) with $^{230}\text{Th}/\text{U}$ -ages and analyses profile indicated.	108
Figure S4.2	Distribution of maximum correlation coefficients for 2000 pairs of AR1 time series.	108
Figure S4.3	Trace element ratios and PCs and comparison with $\delta^{13}\text{C}$ record.	109
Figure S4.4	REDFIT and Continuous Wavelet Transform (CWT) of CR-1 $\delta^{18}\text{O}$ for periods from -55 to 4175 B.P.	110
Figure S4.5	REDFIT and Continuous Wavelet Transform (CWT) of MFZ-N-1 $\delta^{18}\text{O}$ for periods from -68 to 868 B.P.	111
Figure S4.6	REDFIT and Continuous Wavelet Transform (CWT) of $\delta^{18}\text{O}$ composite (MFZ-N-1 + CR-1) for periods from -68 to 4146 B.P.	112
Figure S4.7	Continuous Wavelet Transform (CWT) of CR-1 trace element ratios (Mg/Ca, Sr/Ca and Ba/Ca) and PC-1.	113
Figure S4.8	Continuous Wavelet Transform (CWT) of BTV trace element ratios (Mg/Ca, Sr/Ca and Ba/Ca) and PC-1	113
Figure S4.9	Stalagmites and marine sediment cores from South America.	114
Figure S4.10	Cross wavelet analyses between Antarctic Summer δD and BTV-PC-1.	115
Chapter 5 – Manuscript III		
Figure 5.1	Cave site locations and climatic settings.	122
Figure 5.2	Distribution of maximum correlation coefficients for 2000 pairs of AR1 time series with the same characteristics as the measured $\delta^{18}\text{O}$ stalagmite time series.	125
Figure 5.3	Petar and Paraná sites stalagmites $\delta^{18}\text{O}$ records and SEBRA $\delta^{18}\text{O}$ composite.	126
Figure 5.4	Trace element ratios cross plot (Sinclair test) and PC-1.	127
Figure 5.5	PCP-indices and composite record.	128
Figure 5.6	SEBRA composite $\delta^{18}\text{O}$ and PCP index.	131
Figure 5.7	Regional and interhemispheric comparisons.	133
Figure 5.8	Period related to Bond event 2 and Bond event 3.	135
Chapter 5.8 – Supplementary Figures – Manuscript III		
Figure S5.1	Stalagmite samples and analyses profile (trace elements and stable isotopes) indicated and $^{230}\text{Th}/\text{U}$ -ages and age models.	142
Figure S5.2	Hypsometric map of the study area showing elevation (a.s.l.), carbonate units, and cave sites.	143

Figure S5.3	Laje Branca cave topography map provided by Meandros espeleo group.	143
Figure S5.4	$\delta^{13}\text{C}$ records from SEBRA; Cross plot between stable isotopes ($\delta^{13}\text{C}$ vs $\delta^{18}\text{O}$) from SEBRA and Laje Branca host rock stable isotopes values	144

List of Tables

Chapter 3 – Manuscript I

Table S3.1	Cave flood events recorded in the lower gallery between 2019 and 2024.	77
Table S3.2	MFZ-10 $^{230}\text{Th}/\text{U}$ ages and activity ratios.	78
Table S3.3	MFZ-N-11 $^{230}\text{Th}/\text{U}$ ages and activity ratios.	79
Table S3.4	MFZ-11 $^{230}\text{Th}/\text{U}$ ages and activity ratios.	79

Chapter 5 – Manuscript III

Table S5.1	LB-1 and LB-3 $^{230}\text{Th}-\text{U}$ ages.	145
-------------------	--	-----

Chapter 1 - Introduction

The 6th Intergovernmental Panel on Climate Change (IPCC) report has shown that rainfall-induced floods are projected to become more common and severe in the future (IPCC, 2023). Extreme rainfall events (ERE) are expected to intensify in both frequency and magnitude due to increased atmospheric moisture and evaporative demand (Zhang et al., 2025). Additionally, more frequent and intense ENSO events (El Niño and La Niña) are expected, further amplifying extreme weather events (droughts and floods) related to ENSO teleconnections across South America (Cai et al., 2021). However, ERE are limited to instrumental period and historical records, not going beyond the pre-industrial era, which constrain predictions of future ERE variability (Wilhelm et al., 2019, 2018). Developing longer, ERE-sensitive hydroclimate records would therefore be critical for improving our understanding of the natural variability of ERE (Wilhelm et al., 2019; Cai et al., 2021) and the influence of large-scale climate teleconnections across South America (Cai et al., 2021, 2020).

The frequency and magnitude of ERE and floods can be reconstructed using historical records, sedimentary deposits (e.g. slack-water deposits), tree rings, and speleothems (Denniston and Luetscher, 2017; Wilhelm et al., 2018, 2019). Historical records and tree rings archives provide high-resolution, socio-economically relevant information over short timescales but are often temporally limited and discontinuous (Wilhelm et al., 2019). In contrast, geological and speleothem records provide long-term, quantitative information into low-frequency, high-magnitude events (Denniston and Luetscher, 2017; Wilhelm et al., 2019). Speleothems as past flood archives, in particular, have gained attention over the past two decades because they can be precisely dated, often provide continuous records, and, with potential for high-resolution reconstructions of both short- and long-term extremes (Dasgupta et al., 2010; Denniston et al., 2015; Denniston and Luetscher, 2017; Feinberg et al., 2020, 2020; Frappier et al., 2014; Gázquez et al., 2014; González-Lemos et al., 2015; Jaillet et al., 2006; Ray et al., 2005; Zhu et al., 2017).

From a wide range of speleothems, stalagmites stand out as particularly reliable archives of past climate and environmental conditions (Fairchild, 2012). The combination of a simple stratigraphic structure with precise dating methods (e.g. ^{230}Th -U dating) (Cheng et al., 2013; Richards and Dorale, 2003) allow the reconstruction of multi-scale variability from seasonal to millennial timescales. Stalagmites also preserve a wide range of geochemical (e.g. isotopic, trace element, biomarkers) and physical (e.g. mineralogy, detrital content) proxies that record climatic and environmental signal (Fairchild et al., 2006). Their global distribution, from equatorial to high latitudes and from alpine to below sea level, provides the potential for near-

global coverage, while caves act as natural shields against erosion and post-depositional disturbance (Feinberg and Johnson, 2021).

Detrital layers within the stalagmites are used as hydrologically sensitive proxies that allows the identification of past flood and ERE, providing high-resolution, long-term reconstructions of flood frequency and in some cases of magnitude (Dasgupta et al., 2010; Denniston et al., 2015; Denniston and Luetscher, 2017; Dorale et al., 2005; Gázquez et al., 2014; González-Lemos et al., 2015; Zhu et al., 2017). The incorporation of flood-derived detritus can provide an exceptional record of episodic flood and extreme hydrological activity, recording high-resolution processes from seasonal to intraseasonal timescales (Dasgupta et al., 2010). However, speleothems affected by flooding are often excluded from traditional paleoclimate studies because floodwaters can cause corrosion or abrasion, and detrital sediments are a source of detrital ^{230}Th complicating or even precluding precise ^{230}Th -U dating (Denniston and Luetscher, 2017). Moreover, cave floods are highly dependent on cave hydrology (e.g hydraulic properties of the cave conduct network) and hydrological catchment (Denniston and Luetscher, 2017; Jeannin, 2001). Therefore, integrated analyses from site-specific assessments combining with monitoring of cave hydrology and detailed microstratigraphic analyses represents a critical component for accurately distinguish flood-derived layers and in the transfer of speleothem flood data to a reconstruction of ERE (Denniston and Luetscher, 2017). Alongside the ERE records, multiple geochemical proxies, such as stable isotopes ($\delta^{18}\text{O}$ and $\delta^{13}\text{C}$) and trace elements, allows a more comprehensive reconstruction of past climate and environmental conditions. This multi-proxy approach provides a robust framework for reconstruct changes in atmospheric circulation and hydroclimate variability (Bernal et al., 2016), with the opportunity to access how long-term climatic forcings and hydroclimate changes affected the occurrence of ERE. Consequently, speleothems represent a valuable archive for placing ERE within a long-term paleoclimate context, improving our understanding on how atmospheric circulation, hydroclimate changes, and teleconnections can impact the occurrence of those events.

In this context, the goal of this thesis is to reconstruct, for the first time, a reliable record of ERE in Brazil by combining detailed microstratigraphic analyses of multiple stalagmites with multi-year cave monitoring in caves subjected to flood activity. Moreover, a multiproxy approach, combining stable isotope and trace element analyses, allow the reconstruction of high-resolution (sub-annual to decadal) records of past atmospheric circulation and hydroclimate variability over southern (SB) and southeastern Brazil (SEBRA). This region is severely impacted by ERE, often triggering devastating landslides and floods, with high socioeconomic damage, and disproportional impacts on vulnerable populations (Debortoli et

al., 2017; Marengo et al., 2021; Simoes-Sousa et al., 2025). The occurrence of ERE in this area is primarily linked to circulation anomalies associated with cold-front activity and its interaction with low-level jets transporting warm, moist air from the Amazon Basin (Boers et al., 2014; Cai et al., 2020; Reboita et al., 2024, 2021). These events are not random but are influenced by major ocean–atmosphere teleconnections between the Pacific and Atlantic basins, with Rossby wave trains playing a key role in modulating low-level jets and cyclogenesis (Boers et al., 2014; Cai et al., 2020; Zhang et al., 2025). Therefore, the novel high-resolution, multi-proxy stalagmite records, combined with the ERE reconstructions, provide a unique opportunity to assess how ERE variability has changed through time and how dominant regional rainfall systems, such as the South Atlantic Convergence Zone (SACZ) and the South American Low-Level Jet (SALLJ), have modulated their occurrence. Furthermore, these records allow investigation of long-term changes in the teleconnections and climatic forcings driving extreme rainfall variability across the region.

1.1. References

- Bernal, J.P., Cruz, F.W., Stríkis, N.M., Wang, X., Deininger, M., Catunda, M.C.A., Ortega-Obregón, C., Cheng, H., Edwards, R.L., Auler, A.S., 2016. High-resolution Holocene South American monsoon history recorded by a speleothem from Botuverá Cave, Brazil. *Earth and Planetary Science Letters* 450, 186–196. <https://doi.org/10.1016/j.epsl.2016.06.008>
- Boers, N., Rheinwalt, A., Bookhagen, B., Barbosa, H.M.J., Marwan, N., Marengo, J., Kurths, J., 2014. The South American rainfall dipole: A complex network analysis of extreme events. *Geophysical Research Letters* 41, 7397–7405. <https://doi.org/10.1002/2014GL061829>
- Cai, W., McPhaden, M.J., Grimm, A.M., Rodrigues, R.R., Taschetto, A.S., Garreaud, R.D., Dewitte, B., Poveda, G., Ham, Y.G., Santoso, A., Ng, B., Anderson, W., Wang, G., Geng, T., Jo, H.S., Marengo, J.A., Alves, L.M., Osman, M., Li, S., Wu, L., Karamperidou, C., Takahashi, K., Vera, C., 2020. Climate impacts of the El Niño–Southern Oscillation on South America. *Nature Reviews Earth and Environment*. <https://doi.org/10.1038/s43017-020-0040-3>
- Cai, W., Santoso, A., Collins, M., Dewitte, B., Karamperidou, C., Kug, J.S., Lengaigne, M., McPhaden, M.J., Stuecker, M.F., Taschetto, A.S., Timmermann, A., Wu, L., Yeh, S.W., Wang, G., Ng, B., Jia, F., Yang, Y., Ying, J., Zheng, X.T., Bayr, T., Brown, J.R., Capotondi, A., Cobb, K.M., Gan, B., Geng, T., Ham, Y.G., Jin, F.F., Jo, H.S., Li, X., Lin, X., McGregor, S., Park, J.H., Stein, K., Yang, K., Zhang, L., Zhong, W., 2021. Changing El Niño–Southern Oscillation in a warming climate. *Nature Reviews Earth and Environment*. <https://doi.org/10.1038/s43017-021-00199-z>
- Bernal, J.P., Cruz, F.W., Stríkis, N.M., Wang, X., Deininger, M., Catunda, M.C.A., Ortega-Obregón, C., Cheng, H., Edwards, R.L., Auler, A.S., 2016. High-resolution Holocene South American monsoon history recorded by a speleothem from Botuverá Cave, Brazil. *Earth and Planetary Science Letters* 450, 186–196. <https://doi.org/10.1016/j.epsl.2016.06.008>
- Boers, N., Rheinwalt, A., Bookhagen, B., Barbosa, H.M.J., Marwan, N., Marengo, J., Kurths, J., 2014. The South American rainfall dipole: A complex network analysis of extreme events. *Geophysical Research Letters* 41, 7397–7405. <https://doi.org/10.1002/2014GL061829>
- Cai, W., McPhaden, M.J., Grimm, A.M., Rodrigues, R.R., Taschetto, A.S., Garreaud, R.D., Dewitte, B., Poveda, G., Ham, Y.G., Santoso, A., Ng, B., Anderson, W., Wang, G., Geng, T., Jo, H.S., Marengo, J.A., Alves, L.M., Osman, M., Li, S., Wu, L., Karamperidou, C., Takahashi, K., Vera, C., 2020. Climate impacts of the El Niño–Southern Oscillation on South America. *Nature Reviews Earth and Environment*. <https://doi.org/10.1038/s43017-020-0040-3>
- Cai, W., Santoso, A., Collins, M., Dewitte, B., Karamperidou, C., Kug, J.S., Lengaigne, M., McPhaden, M.J., Stuecker, M.F., Taschetto, A.S., Timmermann, A., Wu, L., Yeh, S.W., Wang, G., Ng, B., Jia, F., Yang, Y., Ying, J., Zheng, X.T., Bayr, T., Brown, J.R., Capotondi, A., Cobb, K.M., Gan, B., Geng, T., Ham, Y.G., Jin, F.F., Jo, H.S., Li, X., Lin, X., McGregor, S., Park, J.H., Stein, K., Yang, K., Zhang, L., Zhong, W., 2021. Changing El Niño–Southern Oscillation in a warming climate. *Nature Reviews Earth and Environment*. <https://doi.org/10.1038/s43017-021-00199-z>
- Cheng, H., Edwards, R.L., Shen, C.C., Polyak, V.J., Asmerom, Y., Woodhead, J., Hellstrom, J., Wang, Y., Kong, X., Spötl, C., Wang, X., Alexander, E.C., 2013. Improvements in 230Th dating, 230Th and 234U half-life values, and U-Th isotopic measurements by multi-collector inductively coupled plasma mass spectrometry. *Earth and Planetary Science Letters* 371–372, 82–91. <https://doi.org/10.1016/j.epsl.2013.04.006>
- Dasgupta, S., Saar, M.O., Edwards, R.L., Shen, C.C., Cheng, H., Alexander, E.C., 2010. Three thousand years of extreme rainfall events recorded in stalagmites from Spring Valley

- Caverns, Minnesota. *Earth and Planetary Science Letters* 300, 46–54. <https://doi.org/10.1016/j.epsl.2010.09.032>
- Debortoli, N.S., Camarinha, P.I.M., Marengo, J.A., Rodrigues, R.R., 2017. An index of Brazil's vulnerability to expected increases in natural flash flooding and landslide disasters in the context of climate change. *Natural Hazards* 86, 557–582. <https://doi.org/10.1007/s11069-016-2705-2>
- Denniston, R.F., Luetscher, M., 2017. Speleothems as high-resolution paleoflood archives. *Quaternary Science Reviews* 170, 1–13. <https://doi.org/10.1016/j.quascirev.2017.05.006>
- Denniston, R.F., Villarini, G., Gonzales, A.N., Wyrwoll, K.H., Polyak, V.J., Ummenhofer, C.C., Lachniet, M.S., Wanamaker, A.D., Humphreys, W.F., Woods, D., Cugley, J., 2015. Extreme rainfall activity in the Australian tropics reflects changes in the El Niño/Southern Oscillation over the last two millennia. *Proceedings of the National Academy of Sciences of the United States of America* 112, 4576–4581. <https://doi.org/10.1073/pnas.1422270112>
- Dorale, J.A., Lepley, S., Edward, R.L., 2005. The ultimate flood recorder: flood-deposited sediments preserved in stalagmites. *EGU General Assembly 2005* 7, 5–6.
- Fairchild, I.J., 2012. *Blackwell Quaternary Geoscience Series: Speleothem Science: From Process to Past Environments (1)*. Wiley-Blackwell.
- Fairchild, I.J., Smith, C.L., Baker, A., Fuller, L., Spötl, C., Matthey, D., McDermott, F., E.I.M.F., 2006. Modification and preservation of environmental signals in speleothems. *Earth-Science Reviews* 75, 105–153. <https://doi.org/10.1016/j.earscirev.2005.08.003>
- Feinberg, J.M., Johnson, K.R., 2021. Cave and speleothem science: From local to planetary scales. *Elements* 17, 81–86. <https://doi.org/10.2138/GSELEMENTS.17.2.81>
- Feinberg, J.M., Lascu, I., Lima, E.A., Weiss, B.P., Dorale, J.A., Alexander, E.C., Edwards, R.L., 2020. Magnetic detection of paleoflood layers in stalagmites and implications for historical land use changes. *Earth and Planetary Science Letters* 530. <https://doi.org/10.1016/j.epsl.2019.115946>
- Frappier, A.B., Pyburn, J., Pinkey-Drobnis, A.D., Wang, X., Corbett, D.R., Dahlin, B.H., 2014. Two millennia of tropical cyclone-induced mud layers in a northern Yucatán stalagmite: Multiple overlapping climatic hazards during the Maya Terminal Classic “megadroughts.” *Geophysical Research Letters* 41, 5148–5157. <https://doi.org/10.1002/2014GL059882>
- Gázquez, F., Calaforra, J.M., Forti, P., Stoll, H., Ghaleb, B., Delgado-Huertas, A., 2014. Paleoflood events recorded by speleothems in caves. *Earth Surface Processes and Landforms* 39, 1345–1353. <https://doi.org/10.1002/esp.3543>
- González-Lemos, S., Müller, W., Pisonero, J., Cheng, H., Edwards, R.L., Stoll, H.M., 2015. Holocene flood frequency reconstruction from speleothems in northern Spain. *Quaternary Science Reviews* 127, 129–140. <https://doi.org/10.1016/j.quascirev.2015.06.002>
- IPCC, 2023: Summary for Policymakers. In: *Climate Change 2023: Synthesis Report. Contribution of Working Groups I, II and III to the Sixth Assessment Report of the Intergovernmental Panel on Climate Change* [Core Writing Team, H. Lee and J. Romero (eds.)]. IPCC, Geneva, Switzerland, pp. 1-34, doi: 10.59327/IPCC/AR6-9789291691647.001
- Jaillet, S.; Pons-Branchu, E.; Maire, R.; Hamelin, B.; Brulhet, J., 2006. Record of Holocene palaeo-groundwater floods in two stalagmites of the Rupt-du-Puits system (Barrois, France). Morphological analysis of laminae and U/Th TIMS datings. *Geologica Belgica*, 9 (3-4), p. 297-307. ISSN 1374-8505.
- Jeannin, P., 2001. Modeling flow in phreatic and epiphreatic Karst conduits in the Hölloch Cave (Muotatal, Switzerland). *Water Resources Research* 37, 191–200. <https://doi.org/10.1029/2000WR900257>
- Marengo, J.A., Camarinha, P.I., Alves, L.M., Diniz, F., Betts, R.A., 2021. Extreme Rainfall and Hydro-Geo-Meteorological Disaster Risk in 1.5, 2.0, and 4.0°C Global Warming

- Scenarios: An Analysis for Brazil. *Frontiers in Climate* 3. <https://doi.org/10.3389/fclim.2021.610433>
- Ray, S., Edwards, R.L., Alexander, E.C., Dorale, J.A., 2005. A 1400-year history of extreme rainfall events from stalagmites from Spring Valley Caverns, southeastern Minnesota. *Geological Society of America*, Vol.37(5), p.13. Geological Society of America, North-Central Section, 39th annual meeting.
- Reboita, M.S., Ambrizzi, T., Crespo, N.M., Dutra, L.M.M., Ferreira, G.W. de S., Rehbein, A., Drumond, A., Rocha, R.P. da, Souza, C.A. de, 2021. Impacts of teleconnection patterns on South America climate. *Annals of the New York Academy of Sciences* 1504, 116–153. <https://doi.org/10.1111/nyas.14592>
- Reboita, M.S., Mattos, E.V., Capucin, B.C., Souza, D.O. de, Ferreira, G.W. de S., 2024. A Multi-Scale Analysis of the Extreme Precipitation in Southern Brazil in April/May 2024. *Atmosphere* 15. <https://doi.org/10.3390/atmos15091123>
- Richards, D.A., Dorale, J.A., 2003. Uranium-series Chronology and Environmental Applications of Speleothems. *Reviews in Mineralogy and Geochemistry* 52, 407–460. <https://doi.org/10.2113/0520407>
- Simoës-Sousa, I.T., Camargo, C.M.L., Tavora, J., Piffer-Braga, A., Farrar, J.T., Pavelsky, T.M., 2025. The May 2024 Flood Disaster in Southern Brazil: Causes, Impacts, and SWOT-Based Volume Estimation. *Geophysical Research Letters* 52. <https://doi.org/10.1029/2024GL112442>
- Wilhelm, B., Cánovas, J.A.B., Aznar, J.P.C., Kämpf, L., Swierczynski, T., Stoffel, M., Støren, E., Toonen, W., 2018. Recent advances in paleoflood hydrology: From new archives to data compilation and analysis. *Water Security*. <https://doi.org/10.1016/j.wasec.2018.07.001>
- Wilhelm, B., Cánovas, J.A.B., Macdonald, N., Toonen, W.H.J., Baker, V., Barriendos, M., Benito, G., Brauer, A., Corella, J.P., Denniston, R., Glaser, R., Ionita, M., Kahle, M., Liu, T., Luetscher, M., Macklin, M., Mudelsee, M., Munoz, S., Schulte, L., George, S.S., Stoffel, M., Wetter, O., 2019. Interpreting historical, botanical, and geological evidence to aid preparations for future floods. *Wiley Interdisciplinary Reviews: Water* 6, e1318. <https://doi.org/10.1002/wat2.1318>
- Zhang, W., Zhou, T., Ye, W., Zhang, T., Zhang, L., Wolski, P., Risbey, J., Wang, Z., Min, S.K., Ramsay, H., Brody, M., Grimm, A., Clark, R., Ren, K., Jiang, J., Chen, X., Fu, S., Li, L., Tang, S., Hu, S., 2025. A Year Marked by Extreme Precipitation and Floods: Weather and Climate Extremes in 2024. *Advances in Atmospheric Sciences*. <https://doi.org/10.1007/s00376-025-4540-4>
- Zhu, Z., Feinberg, J.M., Xie, S., Bourne, M.D., Huang, C., Hu, C., Cheng, H., 2017. Holocene ENSO-related cyclic storms recorded by magnetic minerals in speleothems of central China. *Proceedings of the National Academy of Sciences of the United States of America* 114, 852–857. <https://doi.org/10.1073/pnas.1610930114>

Basics

2.1. Speleothems archives: A window to past environmental and climate conditions

Speleothems are secondary cave deposits, with a wide variety of forms and mineralogical composition (Hill and Forti, 1995). From these, calcium carbonate (CaCO_3) dripstones and flowstones stand out as valuable records of past climate and environmental conditions (Fairchild et al., 2006; Fairchild and Baker, 2012). In this thesis, we use exclusively stalagmites, a dripstone that grows from the cave floor (or any surface) towards the ceiling (our dripping source).

In the last decades, stalagmites have been widely used to as robust past climate and environmental archives due to the combination of a simple internal structure, mainly consisting of continuous superposition of carbonate layers, together with a series of dating techniques available for these records, especially U-series disequilibrium dating method (section 2.3), and the presence of multiple physical and chemical paleoenvironmental proxies within their growth layers (Fairchild et al., 2006).

Stalagmites used as archives are mainly composed by calcite (thermodynamically stable form of CaCO_3 , at surface pressure and temperature) and/or aragonite (high-pressure polymorph of CaCO_3) (Frisia and Borsato, 2010), and occur mainly within carbonate rocks such as limestones and/or dolomites and its metamorphic correspondents (metallimestones, metadolomites and marbles) (Fairchild and Baker, 2012). They are formed as a result of complex interactions within the meteoric water cycle (from the atmosphere to in-cave processes), where rainwater infiltrates through the soil and flows into the cave systems, responding to environmental processes above the cave and within the cave atmosphere (Fairchild and Baker, 2012; Lauritzen and Lundberg, 1999). Therefore, stalagmites present the opportunity to track changes within these systems (atmosphere, soil, vegetation etc) and processes through their geochemistry (e.g. isotopic composition and trace element concentrations) and physical properties (e.g. fabric, fluid inclusions etc). These proxies can record a wide range of environmental signals, including variations in temperature (Meckler et al., 2021; Wassenburg et al., 2021), precipitation (Bernal et al., 2016; Patterson et al., 2024), vegetation cover (Novello et al., 2021), past fire activity (Homann et al., 2022), extreme rainfall and tropical storms (Denniston et al., 2015) and others.

Finally, speleothems stands out as natural archives, combining a variety of proxies with precise dating methods up to ~600ky (e.g. $^{230}\text{Th}/\text{U}$ -dating) (Richards and Dorale, 2003) or older

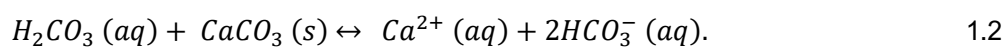
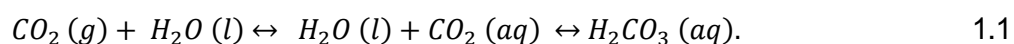
(e.g. U–Pb dating) (Bajo et al., 2012), with natural preservation provided by cave environment, and widespread global distribution, from tropical to high-latitude regions, from below sea level to alpine altitudes, and across diverse climatic zones and biomes (Feinberg and Johnson, 2021). This broad temporal and spatial coverage give the opportunity for comprehensive reconstructions of past environmental and climatic conditions on a global scale, with potential for reconstructions from sub-seasonal to millennial time-scales.

2.2. Stalagmite formation

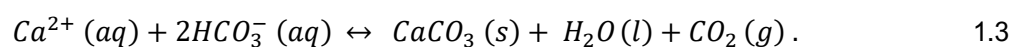
Understanding the mechanisms behind stalagmite formation is fundamental for interpreting the climatic and environmental information recorded in their physical and geochemical proxies. This section examines the principal chemical and physical processes involved in the formation of stalagmites, from the percolation of meteoric water through the soil and bedrock to the precipitation of calcium carbonate and growing of stalagmites.

2.2.1. Calcium carbonate precipitation – from rainfall to stalagmite formation

The first process of stalagmite formation take place in the interaction between the rainfall water with the soil above the cave. The percolating solution encounters a higher partial pressure (p_{CO_2}) environment derived from organic matter decomposition, root respiration and microbial activity, presenting several orders of magnitude higher than the atmosphere (Fairchild and Baker, 2012). The solution (unsaturated in CO_2) dissolves the CO_2 resulting in the formation of carbonic acid (H_2CO_3) (Eq1.1). This process acidifies the solution during the percolation through the soil, until it reaches the cave epikarst. The interaction between the acidified solution (unsaturated in calcium carbonate) results in the dissolution of the cave host-rock (carbonate rocks) (Eq 1.2).



Dissolution takes place until the solution gets saturated in Ca^{2+} , and further reaches the cave atmosphere, which usually presents lower p_{CO_2} than the solution. The lower solution p_{CO_2} leads to the most common reaction in speleothem formation: the CO_2 degassing from the solution to the cave atmosphere (Eq. 1.3) through molecular diffusion (Dreybrodt, 2012), resulting in the precipitation of CaCO_3 , as given in the reaction:



Therefore, differences of p_{CO_2} between the solution and its percolating environment (soil, karst aquifer above the cave, and cave atmosphere) are the main driver of carbonate

precipitation processes that result in speleothem formation. The formation of carbonate therefore, is not restricted to the stalagmite in the end route of the percolating solution, but it is susceptible to carbonate precipitation prior to the stalagmite formation, as for example in the stalactite (during the first contact between percolating solution and cave atmosphere) or even before in the epikarst. This process is known as prior-carbonate precipitation (PCP) and refers to the precipitation of calcium carbonate (calcite or aragonite) prior to the formation of the speleothem (Fairchild et al., 2000). This process has important application on the interpretation of stalagmite records specially on trace element ratios and on stable isotopes which is further in more detail in section 2.6 and 2.7.

The carbonate precipitation over the stalagmite is therefore driven by CO₂ degassing from a thin, saturated film of water (typically ~0.1 mm thick) that flows slowly from the stalagmite tip down to its flanks (Frisia, 2019). The continuous precipitation of calcium carbonate from oversaturated dripping solution results in the formation of stalagmites, which grows as successive overlapping layers with structure resembling a stack of cups, and growth axis aligned beneath the dripping point.

Although most studies focus on the carbonate phase, stalagmites also incorporate non-carbonate components such as organic compounds and detrital particles, which offer complementary information into surface processes and environmental conditions during deposition (Blyth et al., 2016; Denniston and Luetscher, 2017). Organic compounds, including humic and fulvic acids derived from soil and vegetation above the cave, can be transported by percolating water and incorporated within the carbonate matrix. Their concentration and composition may reflect variations in soil productivity, vegetation cover, and microbial activity, serving as valuable proxies for paleoenvironmental reconstructions (Blyth et al., 2016). Also, detrital material, comprising fine mineral grains, clays, and other insoluble particles, can be introduced into the cave system during episodes of intense rainfall or flooding, being deposited within the growing carbonate layers (Denniston and Luetscher, 2017). The detrital content of stalagmites has been increased attention, with important application for reconstructing short-term variations in Earth magnetic field (Borlina et al., 2024) and past flood activity (Denniston and Luetscher, 2017). In the following section, we explore in detail the detrital content of stalagmites, with particular focus on its relationship to cave flooding and the reconstruction of extreme hydrological events.

2.2.2. Flood-derived detrital layers within stalagmites

Detrital material in stalagmites can be originated by a variety of sources such as soil particles transmitted into the cave via fractures, airborne silts and clays entering through cave entrances or ventilation, iron oxyhydroxide minerals precipitated in situ on stalagmite surfaces (Lascau and

Feinberg, 2011), biogenic remains such as bat or bird guano, dust from fires, as well as fine-grained sediments suspended by floodwaters and deposited during flood events (Denniston and Luetscher, 2017; Lascu and Feinberg, 2011; Wilhelm et al., 2019, 2018). Detrital content within stalagmites can provide valuable information for palaeomagnetism studies and past flood activity (Denniston and Luetscher, 2017; Lascu and Feinberg, 2011).

When floodwaters recede, fine clay and silt can settle onto stalagmite surfaces, and if the speleothem growth resumes after the flood recession, these detrital layers become incorporated as distinct dark bands (often rust-coloured) within the calcium carbonate matrix, along single growth horizons (Fig. 2.1) (Wilhelm et al., 2018; Denniston and Luetscher, 2017). The depositional and post-depositional process controls the textural and structural characteristics of the detrital layers, which may appear as discrete laminae, thin or thick discontinuous (or continuous) bands, or diffuse particle distributions within the carbonate matrix. Preservation of detrital material depends on subsequent calcite precipitation, which encapsulates the particles and isolates them from diagenetic alteration or erosion during a successive flood event (Gázquez et al., 2014; González-Lemos, 2014; González-Lemos et al., 2015). As a result, detrital layers can remain remarkably well preserved over thousands of years, persevering a detailed flood record (Dorale et al., 2005; Denniston and Luetscher, 2017).

The detrital material deposited on top of the stalagmite is preferentially preserved along the flanks of the growth surface, while the central axis, directly beneath the drip point, often exhibits lower detrital concentrations due to the remobilization of detritus along the stalagmite axis by drip-water impact (central-washing). The mineral composition of the detritus phase within stalagmites can consist in clay, silt, sand, and agglomerates with associated minerals (e.g. quartz, clay minerals, Fe/Mn oxides, magnetite), sourced both from the external catchment (allochthones) and from the remobilization of cave sediment.

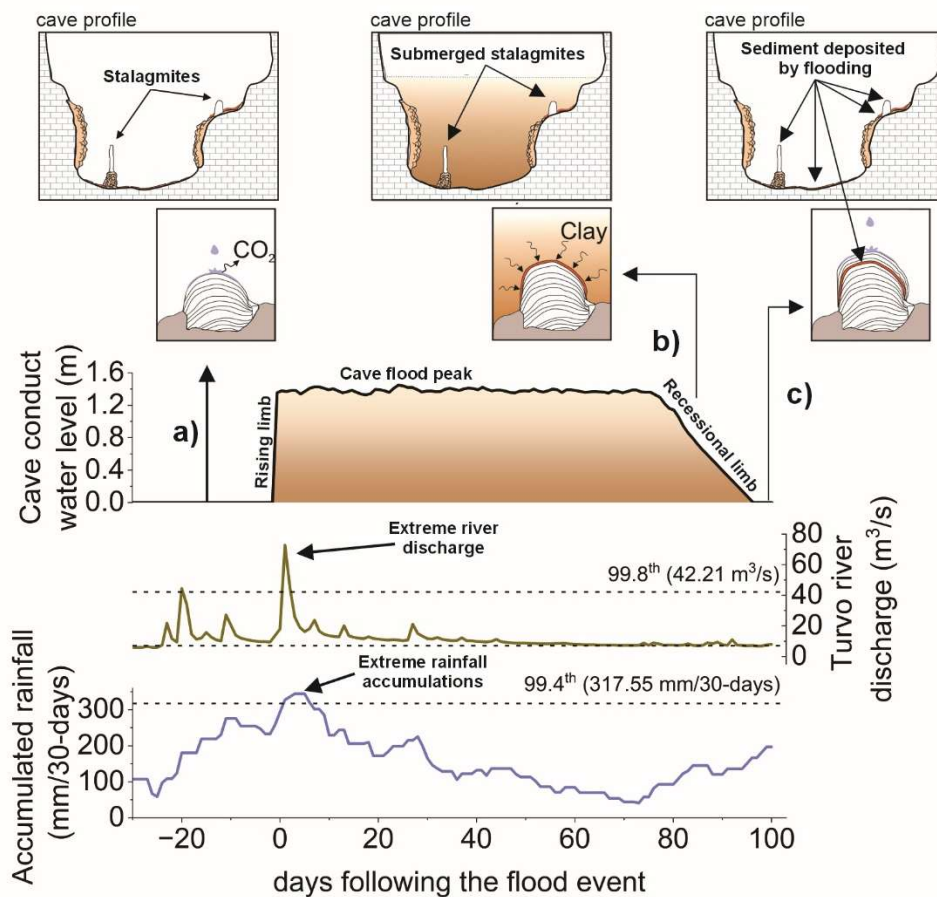


Figure 1.1 - Schematic figure of Malfazido cave profile under flood conditions. A) normal conditions with speleothem growth prior to flood event. B) recession phase, with sediment load deposited over the stalagmites. C) encapsulation of detrital layers following the resumption of carbonate precipitation from drip water. The plots shows, from bottom to top monthly accumulations, river discharge and cave water level.

These flood layers can vary from a few microns to several millimetres thick (Denniston et al., 2015). The thickness of detrital layers can sometimes be correlated with the magnitude of the flood event, with thin layers (microns to <0.1 mm) often represent minor or short-duration floods, while thicker, laterally continuous layers (>0.1 mm, sometimes >1 mm) reflecting more intense, long-lasting, or highly energetic flood events capable of transporting abundant sediment (González-Lemos et al., 2014; Denniston and Luetscher, 2017). However, this relationship between flood magnitude and layer thickness can be complex since detritus deposition can be strongly influenced by cave morphology, hydrology, and preservation biases, as well as by stalagmite geometry, all of which affect the type of flood that are recorded and how layer thickness is expressed (Denniston and Luetscher, 2017). Therefore, a detailed site-specific assessment of cave conditions, hydrological response, and stalagmite morphology and microstratigraphy is essential for interpreting flood-derived detrital layers.

In summary, the detrital phase within stalagmites represents a valuable yet complex archive of surface and hydrological processes (Denniston and Luetscher, 2017). The incorporation of flood-derived detritus material provides an exceptional record of episodic flood and extreme hydrological activity, providing a record of very high temporal resolution processes (seasonal to intraseasonal) such as extreme rainfall events. Therefore, the detailed characterization of detrital layers, together with an understanding of local depositional conditions, enables the reconstruction of flood frequency and offers the opportunity to reconstruct the variability of extreme rainfall events over longer timescales (Dasgupta et al., 2010; Denniston and Luetscher, 2017). However, speleothems affected by flooding are often excluded from traditional paleoclimate studies because floodwaters can cause corrosion or abrasion of the calcite surface, and the incorporation of detrital sediments introduces excess ^{230}Th , which can complicate or even preclude precise U–Th dating (Frappier et al., 2014) (discussed in section 2.3). These challenges highlight the need for detailed characterization of cave settings with site-specific assessments (e.g. cave morphology and hydrological monitoring), and microstratigraphic analyses to accurately distinguish flood-derived layers and to reconstruct past flood events with confidence (discussed in section 2.4).

2.3. Stalagmite dating - U-Series disequilibrium dating method

The rapid increase in speleothem-based paleoclimate records over the past few decades and its use as high-resolution archives with the possibility of study of multi-proxies can be attributed to advances in U-series disequilibrium methods, also known as U/Th or $^{230}\text{Th}/\text{U}$ -dating method. This method allows for precise dating from modern speleothems to <600 ka (thousands of years), or even further in the range of million years with U-Pb-method (Richards and Dorale, 2003; Scholz and Hoffmann 2008; Cheng et al., 2013; Feinberg and Johnson., 2021). We discuss here only U/Th-dating method that was used for dating Holocene samples from this study.

The U/Th method is a robust and widely applied technique for determining the absolute ages of carbonate materials such as speleothems and corals (Scholz and Hoffmann, 2008). It is based on measuring the radioactive disequilibrium within the ^{238}U decay series, specifically the decay of ^{238}U to ^{234}U to ^{230}Th (Fig. 2.2). There are three natural occurring radioactive decay chains, each beginning with a long live ($t_{1/2}$) actinide parent isotope (^{238}U , ^{235}U , or ^{232}Th ; $t_{1/2} > 0.7$ billion year) and ending in a stable isotope of lead. In between is a sequence of intermediate daughter nuclides with half-lives ranging from microseconds to hundreds of thousands of years.

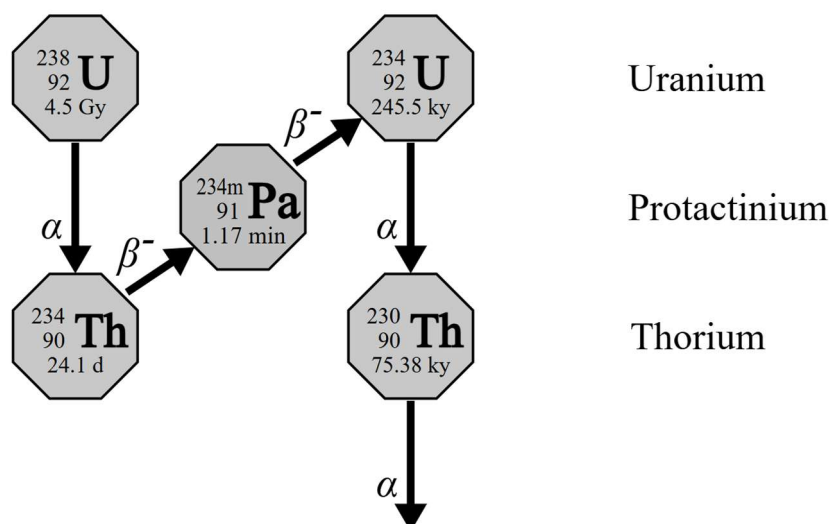


Figure 2.2 – Schematic illustration of part of the ^{238}U decay chain, with the half-lives given for each isotope. Arrows indicate the decay pathway.

When uranium decays, it produces a sequence of daughter isotopes (e.g., ^{238}U - ^{234}Th - ^{230}Th). When the activity (rate of decay) of each isotope in the chain is equal like a series of water tanks connected by pipes, where the inflow and outflow are balanced, a steady-state condition is established known as secular equilibrium (Bourdon et al., 2003). Therefore, when fractionation occurs between the isotopes (e.g., chemical fractionation) within the decay chain, it creates a departure from the secular equilibrium known as the U-series disequilibrium.

The fact that Uranium (soluble in water) and Thorium (insoluble, and highly particle reactive) have very distinct geochemical behaviour, the formation of speleothems through carbonate precipitation (as described in section 2.2.1) result in U-series disequilibrium, with their activity ratios (e.g., $^{230}\text{Th}/^{238}\text{U}$) deviating from 1. Uranium is commonly incorporated into the carbonate with a large range of concentrations varying from close to zero in calcite up to 100 $\mu\text{g/g}$ in aragonite (Ford and Williams, 2010).

Over time, the system reaches the equilibrium through radioactive decay, reaching secular equilibrium, with the rate of this return controlled by the half-life of the daughter nuclide (Fig. 2.3) (Bourdon et al., 2003). This defines the upper age limit of the method, typically around ~ 600 ka, corresponding to approximately five to six half-lives of ^{230}Th (Fig. 2.3) (Scholz and Hoffmann, 2008; Bourdon et al., 2003).

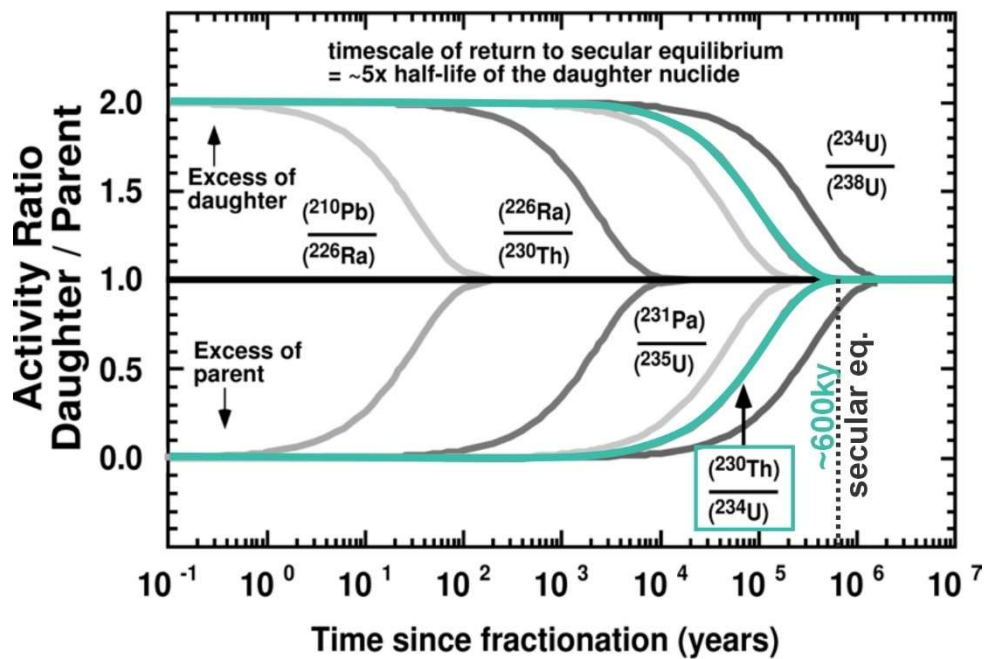


Figure 2.3 – Modified from Bourdon et al. (2003). Temporal evolution of the activity ratios from u-decay-series, with $(^{230}\text{Th}/^{234}\text{U})$ curve in green. The curve shows the return to equilibrium over a known time scale related to the half-life of the daughter nuclide.

Therefore, to calculate ages using ^{230}Th method, the activity ratios $(^{234}\text{U}/^{238}\text{U})$ and $(^{230}\text{U}/^{238}\text{U})$ are measured. These ratios can be used to quantify the degree of disequilibrium within the different isotopes, and the rate at which they evolve back toward secular equilibrium provides a direct measure of the time passed since carbonate formation (Bourdon et al., 2003). The age (t) of a sample can be calculated iteratively by the following equations using the activity ratios of $(^{234}\text{U}/^{238}\text{U})$ and $(^{230}\text{U}/^{238}\text{U})$ and considering the decay constants of the nuclides (λ) (Ivanovich and Harmon (1992)):

$$\left(\frac{^{234}\text{U}}{^{238}\text{U}}\right)(t) = \left(\left(\frac{^{234}\text{U}}{^{238}\text{U}}\right)_{init} - 1\right) * e^{-\lambda_{234}t} + 1$$

$$\left(\frac{^{230}\text{Th}}{^{238}\text{U}}\right)(t) = (1 - e^{-\lambda_{230}t}) + \left(\left(\frac{^{234}\text{U}}{^{238}\text{U}}\right)(t) - 1\right) * \frac{\lambda_{230}}{\lambda_{230} - \lambda_{234}} * (1 - e^{-(\lambda_{230} - \lambda_{234})t})$$

In order to obtain reliable ages using this method, some fundamental assumptions should be fulfilled (Ivanovich and Harmon, 1992; Scholz and Hoffmann, 2008): Firstly, only Uranium is transported by karst waters into the cave system and initially incorporated into CaCO_3 , in contrast to the Thorium (low solubility) (Scholz and Hoffmann, 2008). Secondly, the calcium carbonate behaves as a closed system, meaning that neither U nor Th is added or removed after precipitation. The key assumption, that thorium is absent from the groundwater due to its low solubility, effectively resets the radioactive decay “clock” of uranium to zero during precipitation (Scholz and Hoffmann, 2008). Consequently, the accumulation of daughter

isotopes provides a direct measure of the time passed since incorporation into the speleothem (Scholz and Hoffmann, 2008).

To test if the first assumption is true, ^{232}Th is measured, once this isotope does not occur in the ^{238}U decay chain, and shares similar geochemical characteristics with ^{230}Th (highly particle reactive) (Richards and Dorale, 2003; Huang et al., 2024). Therefore, the activity ratio ($^{230}\text{Th}/^{232}\text{Th}$) can be used to check for contamination of detrital Th, which make it a suitable tracer for initial ^{230}Th input (Richards and Dorale, 2003; Huang et al., 2024). The effect of detrital contamination on $^{230}\text{Th}/\text{U}$ -ages is considered to be significant if ($^{230}\text{Th}/^{232}\text{Th}$) < 200 (Richards and Dorale, 2003).

The first assumption of no initial ^{230}Th in most cases is not archived, with ^{232}Th consistently detected in speleothems samples, indicating potential contamination of initial ^{230}Th (Huang et al., 2024). Therefore, detrital Th is one of the main uncertainty sources of $^{230}\text{Th}/\text{U}$ dating method, with accurate accounting for initial ^{230}Th an essential issue in the speleothem studies, especially for speleothem samples with low U concentrations and high detrital content, such as speleothems subjected to flooding (Huang et al., 2024).

Thus, for samples with high detrital content, such as stalagmites affected by flood events like those examined in this thesis, this can pose a significant challenge for obtaining precise ages, and in some cases may even preclude the dating of certain stalagmites. In the next section (2.3.1) we discuss the dating of samples used in this thesis and the detrital correction methods used to account for contamination of initial ^{230}Th on the stalagmite ages.

2.3.1. Study case of $^{230}\text{Th}/\text{U}$ -dating of samples under flooding conditions

Most of the stalagmite samples analysed in this thesis were collected from cave galleries or conduits periodically affected by flooding. The Figure 2.4 presents boxplots of the activity ratios ($^{230}\text{Th}/^{232}\text{Th}$) compiled for each stalagmite sample and cave. Samples from Cristais (CR) and Santana (ST) caves, which are not subjected to flooding, exhibit similar activity ratio ranges, with mean ($^{230}\text{Th}/^{232}\text{Th}$) values of approximately 2800 and 3900, respectively. In contrast, samples from Laje Branca (LB), Malfazido (MFZ), and Varzeão (VZA) caves, subjected to flooding, show markedly different values. LB displays the highest mean ($^{230}\text{Th}/^{232}\text{Th}$) ratio (~15,700), whereas MFZ and VZA present substantially lower mean values of ~700 and ~137 (significant contamination, <200) (Richard and Dorale., 2003), respectively.

The remarkably low ($^{230}\text{Th}/^{232}\text{Th}$) ratios in MFZ and VZA are attributed to the high concentration of flood-derived detrital material incorporated into the stalagmites. For instance, 656 detrital layers were identified within 524 mm of MFZ-N-10, corresponding to an average spacing of ~0.8 mm between layers. This makes sampling for $^{230}\text{Th}/\text{U}$ -dating particularly

challenging, once detrital layers should be avoided. Furthermore, most samples from these two caves are relatively young, generally covering only the past two millennia, which limits the accumulation of radiogenic ^{230}Th (daughter nuclide). VZA represents the most challenging case for ^{230}Th dating between the studied caves, combining young ages, high concentration of detrital layers, and low ^{238}U concentrations (average ~ 0.6 ppm).

In contrast, despite the frequent flooding at MFZ, its higher ^{238}U concentrations (average ~ 3 ppm) partially mitigate the detrital contamination effect. Similarly, LB, although subjected to flood events, shows a lower density of detrital layers that can be easily avoided during sampling and relatively high ^{238}U concentrations (average ~ 5.6 ppm, reaching up to 10 ppm). The impact of flood contamination is also clearly illustrated by candle-shaped stalagmites such as MFZ1 and MFZ2, where the upper portions that grew above the flooding zone exhibit higher ($^{230}\text{Th}/^{232}\text{Th}$) ratios, whereas the basal sections formed under flood conditions display significantly lower values.

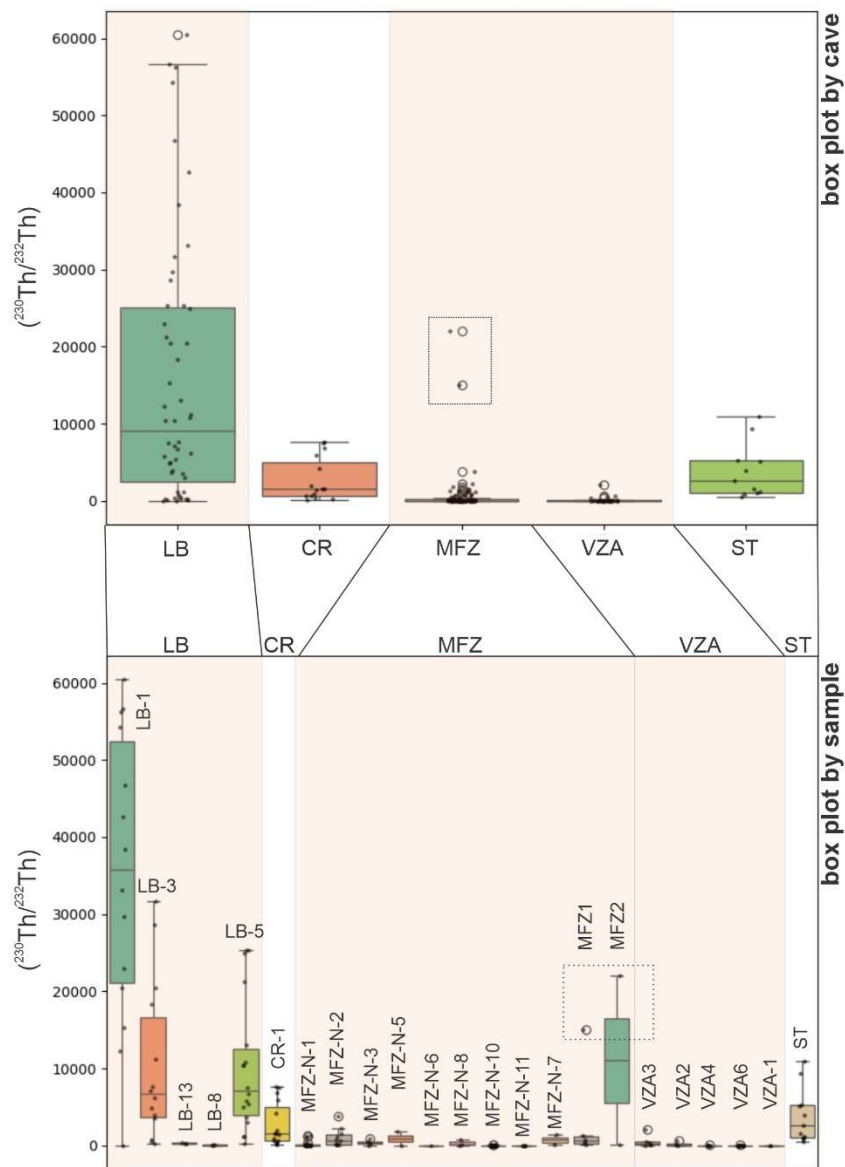


Figure 2.4 - Boxplot of activity ratios ($^{230}\text{Th}/^{232}\text{Th}$) within the same cave and within samples. Laje Branca (LB), Cristais (CR), Malfazido (MFZ), Varzeão (VZA) and Santana (ST) cave. The light-yellow shading indicates caves and samples subjected to flooding and the area marked by dotted line shows the upper part of candle-shape stalagmites that grew above the flood zone.

Without correcting for this initial thorium input, the resulting ages can be substantially overestimated (Huang et al., 2024). The correction for initial radiogenic ^{230}Th is typically calculated based on the content of the stable ^{232}Th isotope, under the assumption that the ratio of ^{230}Th to ^{232}Th in the detrital material is constant and that all isotopes in the uranium-series decay chains are in secular equilibrium. A commonly used reference is the bulk-Earth activity ratio of $(^{230}\text{Th}/^{232}\text{Th}) = 0.8 \pm 0.8$, corresponding to an average mass ratio of $(^{232}\text{Th}/^{238}\text{U}) = 1.25$ (Taylor and McLennan, 1995).

Detrital correction for initial ^{230}Th in $^{230}\text{Th}/\text{U}$ -dating is performed by measuring ^{232}Th and applying an assumed detrital ratio (correction factor). However, these values can vary considerably depending on factors such as host rock and soil characteristics, with reported

ratios varying on a wide range (Huang et al., 2024). Because detrital contamination can differ between samples, we applied the methodology proposed by Budsky et al. (2019a) for stalagmites exhibiting significant age inversions. This approach tests a range of detrital correction factors beyond the conventional value to identify the factor that minimizes both the number and cumulative magnitude of age inversions.

This methodology was applied to two stalagmite samples presented in Chapter 3. A series of $(^{232}\text{Th}/^{238}\text{U})_d$ activity ratios (correction factors) from 0.08 to 4, in increments of 0.01, was used to calculate corrected activity ratios $(^{234}\text{U}/^{238}\text{U})_{\text{corr}}$ and $(^{230}\text{Th}/^{238}\text{U})_{\text{corr}}$, assuming secular equilibrium between detrital ^{230}Th , ^{234}U , and ^{238}U . Corrected $^{230}\text{Th}/\text{U}$ ages were then computed for each factor, and age inversions were quantified by comparing each age with all others in stratigraphic order. For instance, for MFZ-10, the lowest cumulative inversions were obtained with $(^{232}\text{Th}/^{238}\text{U})_d = 0.998$ (Fig. 2.5d), and a conservative uncertainty of $\pm 50\%$ was applied to this ratio, which was propagated to the corrected ages. This procedure is particularly important for samples with high detrital content, such as MFZ stalagmites, where conventional corrections fail to fully account for contamination.

Several advanced age-depth modelling approaches are available in the literature. For example, the StalAge algorithm (Scholz and Hoffmann, 2011) generates age models based on Monte Carlo simulations that fit straight lines through at least three data points, improving upon the limitations of point-to-point linear interpolation. By rejecting major outliers and increasing the uncertainty of minor outliers, StalAge minimizes age inversions and produces more robust age-depth models. Such models are essential for integrating high-resolution proxy data, allowing the construction of reliable and robust paleoclimate records.

In conclusion, the ^{230}Th dating method is crucial for obtaining reliable ages to reconstruct high-resolution proxies in stalagmites. Detrital contamination can be further mitigated using the approach of Budsky et al. (2013a), based on sedimentary law and assumed stratigraphical constrain of stalagmite layers, applying a range of detrital correction factors. This method is particularly effective for samples exhibiting age inversions or high detrital content.

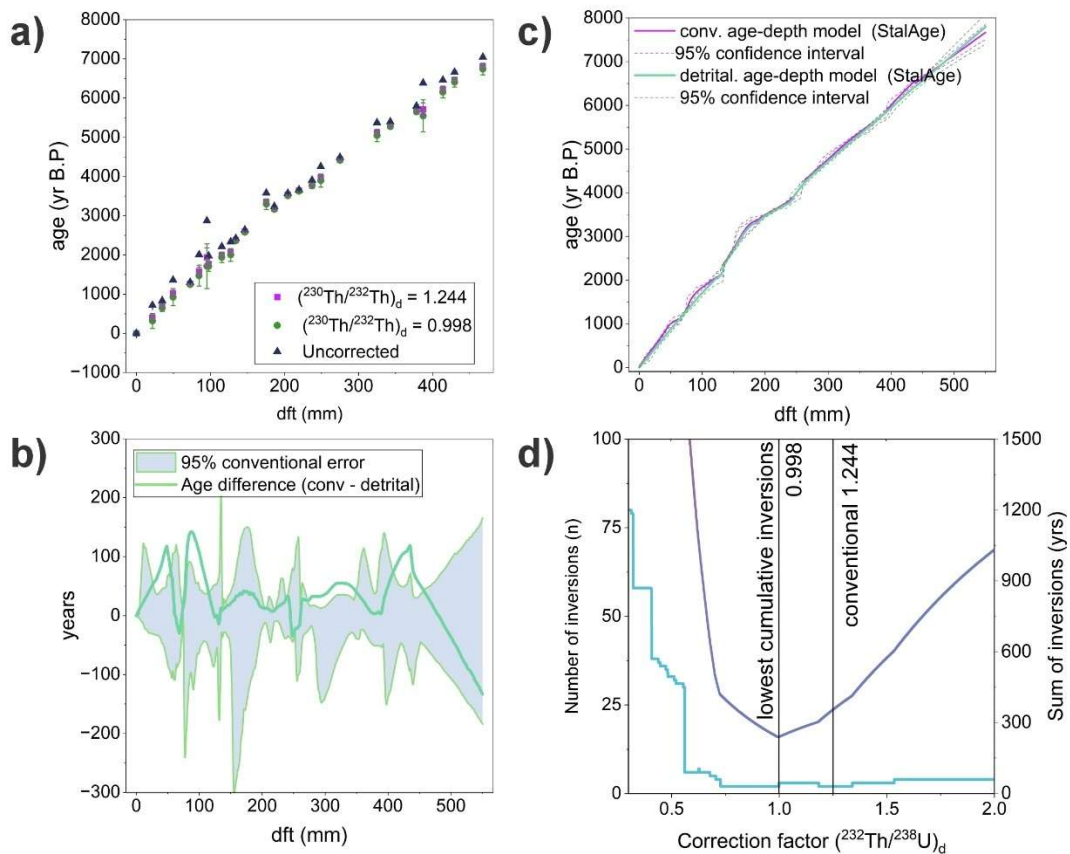


Figure 2.5 – a) ^{230}Th -U ages with conventional (1.244) (pink), detrital correction factors (0.998) (green) and uncorrected ages (purple); b) green line showing the difference between age model calculated with conventional correction factor and age model calculated with detrital correction factor, with blue shaded area showing 95% confidence interval of conventional age model. C) age models and confidence intervals. D) simulated number of inversions and sum of inversions for each possible correction factor.

2.4. Microstratigraphy of flood-derived detrital layers and past flood reconstruction

Paleoflood reconstructions from speleothems are a relatively new and underutilized tool (Denniston and Luetscher., 2017; Feinberg et al., 2020). Flood records preserved within speleothems offer a number of advantages over existing paleo flood indicators (Wilhelm et al., 2019). Stalagmites can present a continuous record reliably dated radio isotopically with very high precision using ^{230}Th dating techniques covering the past ~600,000 years (Richards and Dorale., 2003; Cheng et al., 2013). Moreover, caves are shielded from surface erosion and reworking that commonly disturb fluvial or lake sediments, resulting in better preservation of discrete flood events (Wilhelm et al., 2019).

Besides that, most of the studies using stalagmites as paleoflood records are concentrated at North America (Lepley et al., 2004; Dorale et al., 2005; Knight et al., 2006; Dasgupta et al., 2010; Pyburn and Frappier, 2008; Frappier et al., 2014; Feinberg et al 2020), Europe (Gazquez et al., 2014; Gonzalez-Lemos et al., 2015a, 2015b; Meyer et al., 2012), with some

studies at China (Zhu et al 2017) and Australia (Denniston et al 2015). To put in perspective, this is the first study reconstructing past flood frequency using stalagmites in South America.

As described in section 2.2.2, the flood-derived detritus layers within the stalagmites requires detailed microstratigraphic analyses and site-specific assessments (e.g., hydrological and sediment deposition monitoring) to accurately distinguish flood-derived layers from other clastic sources (Denniston et al., 2017). In this section we discuss the different methods of identification of flood-derived layers and the reconstruction of past flood frequency.

2.4.1. Visual Identification Methods

Flood-derived detritus layers often appear as dark, brownish to rust-coloured laminae interbedded with lighter carbonate layers. Preliminary analysis for potential flood-derived layers can be supported by visual inspection using high-resolution scans from polished slabs (Denniston et al., 2017). Also, grey scale analyses can further help identifying intervals of contrast between the carbonate fabric and the flood layers. The visual identification should be used as a preliminary step, and requires further complementary analysis (e.g., thin section petrography analysis).

Thin-section analysis under a petrographic microscope is a powerful technique for identifying and characterizing flood-derived layers in stalagmites. This method allows direct observation of siliciclastic components such as quartz, phyllosilicates, iron oxyhydroxides, opaques minerals and aggregates of minerals (e.g., mud chunk) within the detrital phase. Also, it allows the detailed assessment of detritus granulometry and its distribution across the speleothem growth surface, evidencing the distinct types of detritus material and layers within the stalagmite. Additionally, petrographic analysis supports the identification fabrics associated with the detritus layers, providing textural evidence for growth hiatuses, such as abrupt changes in crystal morphology, or signs of recrystallization and/or diagenesis linked to periods of flooding or subsequent alteration (Frisia, 2015; Denniston and Luetscher., et al 2017). Therefore, they provide critical context for interpreting the environmental significance and conditions of deposition of the detrital layers. This step has also important application for the stalagmite dating and proxy interpretation, allowing to track potential area subjected to post-deposition alterations (diagenesis).

For thin section analysis, the samples slabs should be oriented to capture primary growth surfaces (perpendicular to growth direction) including the flanks of the stalagmite samples in the analysis to avoid bias from central washing. In case of discontinuous flood-derived detritus layers with potential biases in its preservation, the sample should be analysed in multiple areas across the growth surface and multiple planes oriented parallel to the growth axis either using

parallel cuts to produce a slab or by making cuts at right angles to one other (Denniston and Luetscher et al., 2017).

In addition to thin section analysis, high-resolution scans of thin sections can be coupled with imaging software (such as ImageJ or Inkscape) for precise measurement of the depth and thickness of detrital layers. Creating a detailed log including mineralogy, grain characteristics (size, shape), layer thickness, and type of layer (e.g., continuous, discontinuous, or localized). This can offer valuable insights into the deposition and post-deposition characteristics and, in some cases, the potential magnitude of past flood events (Denniston and Luetscher., 2017). However, the deposition and preservation of detrital layers is strongly influenced by local depositional and hydrological conditions, making interpretations of flood magnitude based on these properties complex. Comparisons between speleothems from different sampling sites (different gallery or topography height) or caves may introduce significant biases due to differences in topography and site-specific hydrology. Therefore, layer properties should be interpreted cautiously and contextually, prioritizing intra-sample rather than inter-sample comparisons.

2.4.2. Geochemical Analysis

Geochemical methods such as X-ray fluorescence (XRF) (Finne et al., 2015), laser ablation inductively coupled plasma mass spectrometry (LA-ICP-MS) or Proton induced X-ray emission (PIXE) analyses enable the quantification of flood-associated detrital elements (e.g., Al, Si, Fe, Ti), distinguishing them from the carbonate matrix. Trace elemental ratios such as Al/Ca, Fe/Ca, and Ti/Ca are particularly diagnostic detrital material, once these elements are relatively geochemical immobile, being suitable tracers of sediment source or transport processes (e.g., soil transport through seepage or flood transport). These approaches allow for the characterization of the geochemical signatures of detrital layers and associated mineral phases (e.g., via XRF). However, flood-derived detrital layers often exhibit complex and heterogeneous morphologies, which may require multiple analysis transects or even spatial mapping to minimize depositional bias, procedures that can be time, and very resource expensive compared to other analytical methods.

Characterization via thin section analysis can be further supported by integrating Raman spectroscopy (White, 2006; Denniston and Luetscher et al., 2017). Raman spectroscopy offers non-destructive, high-resolution mineral identification by providing distinct spectral fingerprints for minerals directly on individual grains (White, 2006). Its application allows for precise discrimination between minerals, such as differentiating calcite from aragonite. This technique is particularly valuable in analysing fine-scale detrital material, distinguishing original and

diagenetic mineral phases, and supporting interpretations of flood-derived or hiatus layers observed in thin section. Moreover, Raman spectroscopy also allows mapping of organic distributions associated with detrital material, offering an additional geochemical dimension to speleothem characterization. We briefly discuss the application of this method in section 2.4.4 on a stalagmite from Malfazido cave.

2.4.3. Magnetic Measurements

Magnetic methods provide a powerful means for identifying paleoflood layers in speleothems by detecting and characterizing ferromagnetic particles incorporated during detrital deposition events (Lascu and Feinberg., 2011; Feinberg et al., 2020). Scanning SQUID (Superconducting Quantum Interference Device) microscopy (Feinberg et al., 2020) and Quantum Diamond Microscopy (QDM) (Piascik et al., 2025), have significantly improved the precision and interpretive potential of magnetic analyses. SQUID microscopy enables the visualization of magnetic mineral distributions at a spatial resolution of ~200 μm , revealing localized magnetic anomalies that correspond to detrital horizons deposited by flood events. QDM advances this further, achieving micrometer-scale resolution and directly imaging the remanent magnetic fields of individual grains. This technique allows for detailed mapping of grain-size distributions, discrimination between flood-derived and background particles, and comparison with cave mud deposits, providing a process-based understanding of sediment incorporation during floods (Feinberg et al 2020; Piascik et al., 2025). Collectively, these magnetic methods enhance the detection, characterization, and interpretation of flood-derived detrital layers in speleothems, enabling high-resolution paleoflood and hydrological reconstructions. The application of QDM analysis on Malfazido stalagmites was part of a collaboration with Prof. Dr. Roger Fu and the PhD. Student Samuel L. Piasick from Harvard University and was published in Piascik et al. (2025).

2.4.4. Flood-derived layers characterization – Malfazido cave study case

We discuss here several different optical and geochemical techniques including visual identification (thin section analysis), geochemical (LA-ICP-MS, PIXE and RAMAN spectroscopy) and magnetic measurements (Quantum Diamond Microscopy) applied to stalagmites from Malfazido cave within the scope of this research and collaborations (Piascik et al., 2025). For Malfazido cave, we use mainly thin section analysis of three stalagmites detailed described in Chapter 3. In total, 921 micro-detrital layers were identified within 3 different samples. This method is highly time-consuming but allow the precise determination of individual detritus layers and the features associated. The detailed description of thin section analysis of Malfazido cave are presented in section 3.7.3.

LA-ICP-MS and PIXE analyses along the growth axis of stalagmite MFZ-N-1c shows that trace element ratios associated with detrital phases (Fe/Ca, Al/Ca, Ti/Ca) generally peak in intervals corresponding to high detrital concentrations (Fig. 2.6, 2.7). In the 60–36 mm interval, Fe/Ca remains elevated, while Ti/Ca peaks mainly between 60 and 50 mm, and Al/Ca shows strong anomalies around 60 mm (Fig. 2.6). Another detritus rich interval (5–18 mm) exhibits elevated Fe/Ca and Al/Ca but no corresponding Ti/Ca anomalies (Fig. 2.6). PIXE data show limited coherence for Al and Ti, while Fe counts correlate with detrital-rich intervals (Fig. 2.7). Overall, LA-ICP-MS captures fine-scale detrital variability, whereas PIXE provides a coarser and lower-resolution overview of elemental distributions. However, single LA-ICP-MS transects can be biased due to the irregular distribution of detrital material along flood horizons, requiring multiple transects or mapping to account for this variability. Depending on stalagmite size and number of samples, such high-resolution analyses can be time and resource expensive when compared with other geochemical or optical methods.

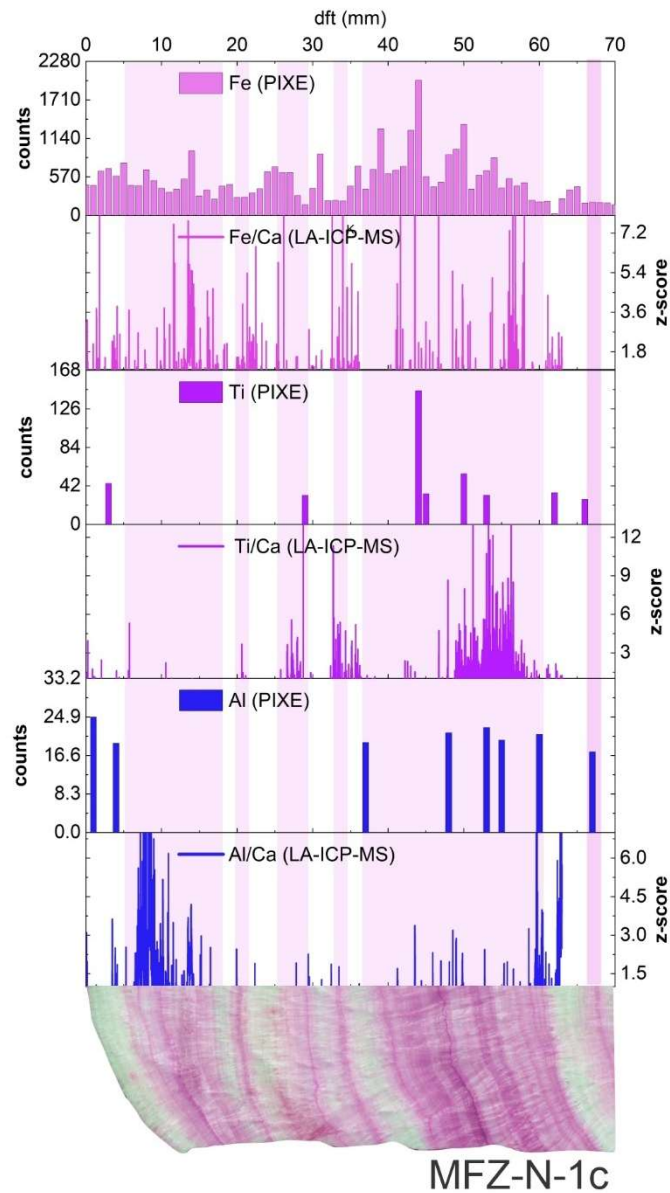


figure 2.6 – Comparison between PIXE analyses (Proton Induced X-Ray Emission) and LA-ICP-MS analyses of trace elements. the detrital layers within the stalagmite are coloured to increase visibility. pink coloured bar represents intervals with high concentration of detrital layers within the stalagmite. the PIXE analyse was performed using a 1mm diameter proton beam with 1mm step size at LAMFI-USP (Laboratório de Análises de Materiais por Feixes Iônicos).

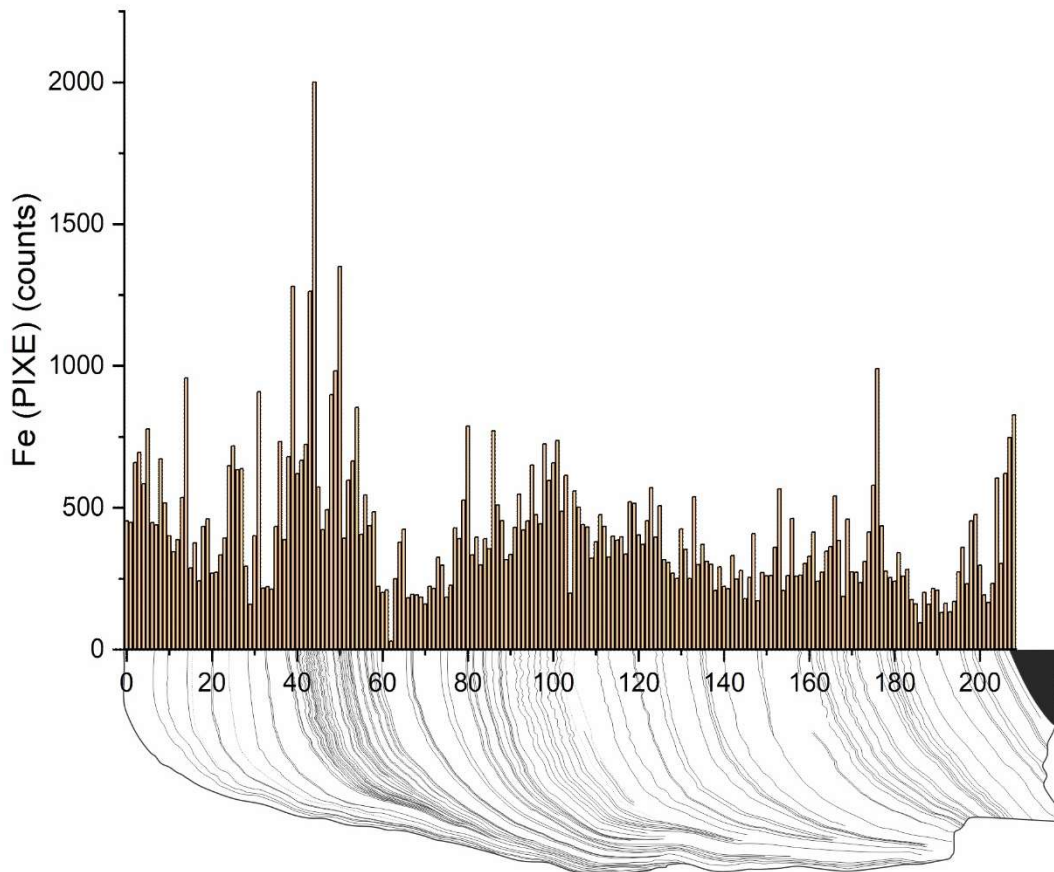


Figure 2.7 – Fe PIXE analysis on MFZ-N-1 with each individual detrital layer marked by continuous black line. The interval between 60 and 40mm shows a higher concentration of detrital layers (corresponding to the little ice age period) with correspondence of peaks in the Fe counts. The analyse was performed using a 1mm diameter proton beam with 1mm step size at LAMFI-USP (Laboratório de Análises de Materiais por Feixes Iônicos).

A Raman map was acquired from the thin section MFZ10_Top1 of Malfazido Cave in collaboration with Prof. Dr. Anne Jantschke and Julian Schwarz. The map comprises 59,072 individual spectra, allowing a fine-scale spatial analysis. The mapping is based on the band intensity ratio between the calcite ν_1 band ($\sim 1086 \text{ cm}^{-1}$) and the C–H stretching region ($2800\text{--}2950 \text{ cm}^{-1}$), serving as a semi-quantitative proxy for relative organic content. In the resulting false-color map (Fig. 2.8), blue areas indicate carbonate-rich zones (strong calcite signal), red areas correspond to organic-enriched layers, and green to yellow tones represent intermediate compositions. The map evidences a correlation between the detrital layers and organic content. Moreover, the dispersion of organics seems to follow the post-detritus deposition growth of thin aragonite needles. This once more evidences the complex morphology that flood-derived detritus layers can acquire.

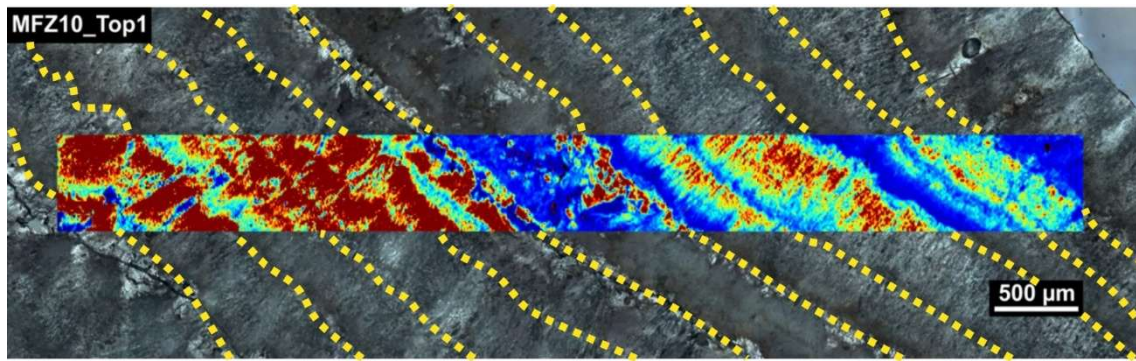


Figure 2.8 - Raman map of sample MFZ10_top1 from 59072 individual measurements (acq. time 0.25 s, 1 acc., 300 g/mm grating), showing organic signal intensity related to flood-derived detritus layers (red = high organic content, blue = carbonate-rich).

This approach demonstrates the significant advantage of Raman mapping for speleothem studies. By providing non-destructive, high-resolution spatial data, Raman mapping enables simultaneous characterization of both mineralogical and organic components directly within thin sections (White, 2006). Furthermore, the method allows for the identification of subtle compositional variations that are often undetectable through optical or geochemical analyses alone. Consequently, Raman mapping serves as a powerful complementary tool for interpreting flood-derived detrital layers and the features associated.

Piascik et al. (2025) in collaboration with this research used a QDM micrometer-resolution magnetic maps of a portion of stalagmite MFZ-N-1. The magnetic field imaging reveals distinct highly magnetic bands corresponding to detrital layers deposited during flood events. Within these bands, the ferromagnetic grain population shows a pronounced bimodal distribution biased toward coarser sizes, closely resembling the grain-size characteristics of flood-deposited mud from Malfazido cave (Piascik et al., 2025). QDM imaging provides a non-destructive, high-resolution method to distinguish between flood-related and background magnetic mineral inputs, allowing for reliable identification of flood-deposited layers.

Overall, thin section analysis supported by Raman spectroscopy remains the most effective method for precisely identifying micro-detrital layers and their associated textures, although it is highly time-consuming. The complementary Raman spectroscopy and mapping provide a powerful, non-destructive tool for characterizing flood-derived detrital layers, enabling the identification of subtle mineralogical and compositional changes often associated with flood horizons. LA-ICP-MS mapping can also serve as a valuable approach for detecting and quantifying flood-related layers with high spatial resolution. However, its application is time- and resource expensive, particularly when dealing with large sample sets or long stalagmites, making mapping analysis logistically demanding.

2.4.5. Cave flood frequency reconstruction

The cave flood reconstruction performed in this research was primarily based on microstratigraphy of the stalagmite samples and is exemplified in Fig 2.9. Firstly, we perform thin sections under polarized light microscopy to characterize mineralogy, fabrics, and distribution of detrital material. Each detrital layer identified was tracked using high-resolution scans of the thin sections and the relative depth from the top (dft) was measured using imaging software Inkscape. For calculate the age modelling, each individual detrital layer was projected over the same dft profile used for the ^{230}Th -U ages. We then calculate the age of each individual detrital layer using StalAge (Scholz and Hoffmann, 2011) and if necessary, applying the corrections for detrital thorium based on (Budsky et al. 2019a). The resulting age model provides a bimodal data set, which is further used to calculate the frequency of events using running frequency analysis with specified time bins (e.g., 100-yr bin) and step (e.g., 5-yr), resulting in a past flood frequency time series. This method improves comparisons across flood records and enables analysis of multidecadal to millennial variability. This methodology is used in Chapter 3 for reconstructing the past flood frequency of Malfazido cave for the past 7,500 years. The monitoring of Malfazido cave is also detailed describe in Chapter 3.

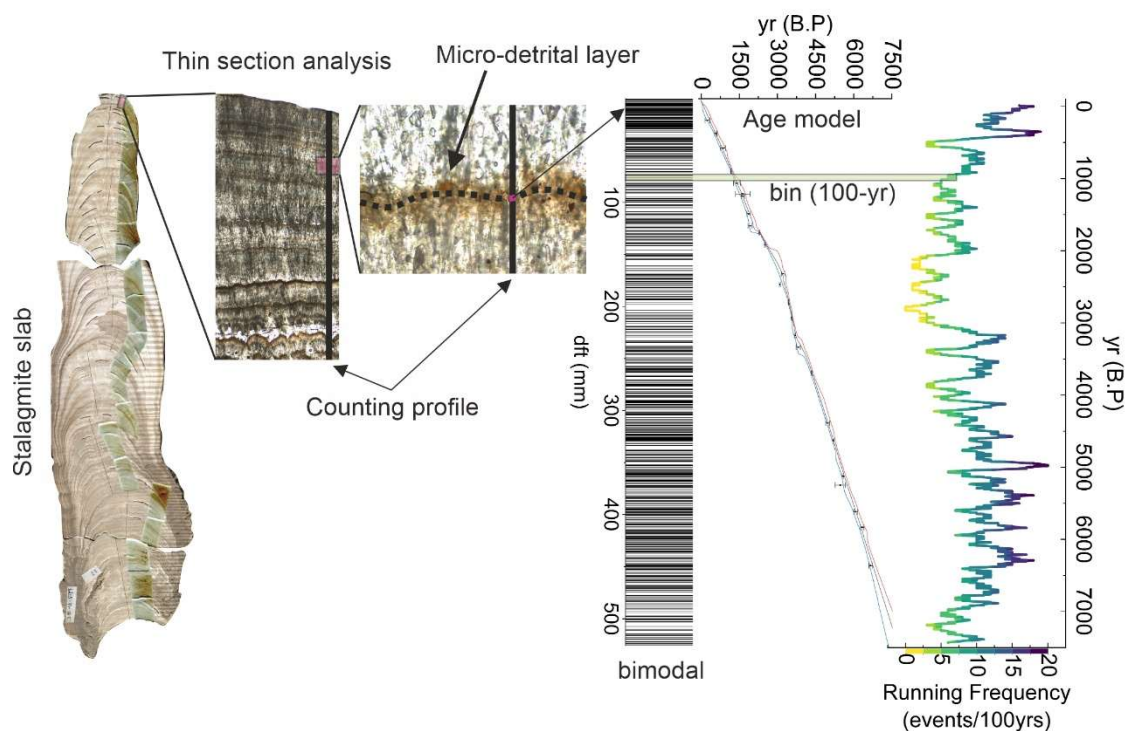


Figure 2.9 – Schematic figure of microstratigraphy analysis using thin section analysis. From left to right: stalagmite samples and corresponding thin-section areas; scanned thin section under the microscope; detailed thin-section image showing a micro-detrital layer with a black line marking the layer-counting profile; bimodal data showing each identified detrital layer represented by a black line; and the resulting age model and running frequency analysis using 100-year time bins with 5-yr step.

2.5. Oxygen stable isotopes ($\delta^{18}\text{O}$) in speleothems

The oxygen isotopic composition ($\delta^{18}\text{O}$) is one of the most widely used proxy in speleothem science. It has been used for past variations in temperature, precipitation amount, and atmospheric circulation patterns (Lachniet, 2009; Fairchild and Baker, 2012). Because oxygen

isotopes in speleothems are affected by processes occurring in the atmosphere, soil, epikarst, and cave environment, $\delta^{18}\text{O}$ values reflect both climatic forcing and hydrological dynamics related to the karst (Lachniet, 2009; Treble et al., 2022). Therefore, its interpretation requires a detailed understanding of isotopic fractionation mechanisms, site-specific cave processes, and regional climatology supported by modern monitoring data (Lachniet, 2009; Treble et al., 2022).

The $\delta^{18}\text{O}$ of speleothem primarily reflects to the isotopic composition of the drip water, which correspond to the isotopic signature of meteoric precipitation (Hendy, 1971). The relationship between water and carbonate isotopic compositions is governed by temperature-dependent fractionation during CaCO_3 precipitation. Under equilibrium conditions, this fractionation follows well-established thermodynamic relationships (Kim and O'Neil, 1997). Therefore, speleothem $\delta^{18}\text{O}$ records can, in some cases, provide direct evidence of past changes in temperature or rainfall isotopic composition, depending on the dominant climatic control in a given region (Fairchild and Treble, 2009).

The isotopic composition of precipitation reflects atmospheric and surface conditions, combining temperature, precipitation intensity, and moisture source effects (Lachniet, 2009). In mid and high latitude regions, $\delta^{18}\text{O}$ in rainfall present a positive correlation with temperature with stronger isotopic fractionation due to temperature effects during condensation, leading to isotopically depleted precipitation (Lachniet, 2009). In contrast, in tropical and monsoonal regions, $\delta^{18}\text{O}$ values in rainfall decrease with increasing rainfall amount, a process known as amount effect (Lachniet 2009). This process occurs as deep convective systems progressively deplete heavy isotopes (^{18}O and ^2H) during rainout (Rozanski et al., 2013). Under such conditions, lower $\delta^{18}\text{O}$ values in speleothems typically indicate wetter intervals or intensified monsoonal activity, whereas higher values reflect drier conditions or weakened convection (Lachniet, 2009; Stríkis et al., 2011).

The source and transport pathways of air masses also exert a strong influence on precipitation $\delta^{18}\text{O}$ (Cruz et al., 2005; Lachniet 2009; Ampuero et al., 2020). Air masses that have undergone extensive rainout or originate from isotopically depleted regions produce lower $\delta^{18}\text{O}$ values, while shifts between oceanic and continental moisture sources, or between tropical and extratropical influences, can drive substantial isotopic variability in speleothem records (Cruz et al., 2005). In South America, for instance, the interplay between Amazonian (tropical) and extratropical South Atlantic (extratropical) moisture sources strongly modulates precipitation $\delta^{18}\text{O}$ across both seasonal and interannual timescales (Cruz et al., 2005). In regions with high seasonality (e.g., dominated by monsoonal influence), with distinct wet and

dry seasons, the isotopic composition of annual precipitation might reflect primarily the dominant recharge period (Stríkis et al., 2011).

As precipitation infiltrates through the soil and epikarst, several processes can affect its isotopic composition before the percolating solution reaches the cave atmosphere as dripping water (Lachniet., 2009; Treble et al., 2022). Evaporation from soil moisture or near-surface karst layers can enrich the infiltrating water in ^{18}O , particularly under dry or warm conditions (McDermott, 2004). Mixing of waters with different residence times and recharge histories in the epikarst tends to homogenize the isotopic signal, attenuating short-term variability, with the degree of this homogenization depends on the porosity and hydraulic structure of the karst system (Baldini et al., 2006). Thin or fractured epikarsts transmit isotopic variability more rapidly, while thick or well-buffered systems produce stable drip water $\delta^{18}\text{O}$ values that reflects multi-annual to decadal changes. Therefore, the hydrological context of the cave exerts a strong filtering effect, determining the temporal resolution and climatic sensitivity of the speleothem $\delta^{18}\text{O}$ record (Treble et al., 2022). Consequently, cave drip water and speleothem $\delta^{18}\text{O}$ represent a hydrologically weighted average of infiltration over time rather than the instantaneous isotopic composition of individual rainfall events (Baker et al., 2019).

In-cave processes can also play a crucial role on the isotopic composition of speleothems, and can impact how records reflect external climatic signals (Lachniet, 2009; Treble et al., 2022). For example, isotopic fractionation occurs between dissolved carbonate species and water molecules during carbonate precipitation, and the nature of this fractionation depends on cave conditions. Under stable cave environments, where CO_2 degassing and evaporation progress slowly, carbonate precipitation happens in thermodynamic equilibrium with the drip water. In such cases, the carbonate $\delta^{18}\text{O}$ accurately reflects either the isotopic composition of the drip water or the cave temperature, depending on which factor exerts the dominant control (Mickler et al., 2006). However, when calcite precipitation is rapid, CO_2 degassing is intense, or cave ventilation and humidity are not constant, kinetic fractionation can have a strong influence on the isotopic value of carbonate $\delta^{18}\text{O}$ (Mickler et al., 2006). These non-equilibrium conditions increase heavy isotopes in the carbonate relative to the equilibrium value, potentially affecting or amplifying the climatic signal recorded in the speleothem (Hendy, 1971; Dreybrodt and Scholz, 2011). Indicators of kinetic fractionation include strong covariation between $\delta^{18}\text{O}$ and $\delta^{13}\text{C}$, abrupt isotopic shifts not supported by regional climate evidence, or petrographic textures evidencing rapid carbonate precipitation (Mickler et al., 2006). Distinguishing whether a stalagmite formed under equilibrium or kinetic conditions is therefore essential for reliable paleoclimate interpretation, and modern cave monitoring can help identifying these processes.

Modern monitoring programs are crucial for interpret speleothem $\delta^{18}\text{O}$ values. These programs typically measure rainfall and drip water isotopes, modern carbonate isotopes, cave air temperature, humidity, CO_2 concentration, and drip rate (Treble et al., 2022). This approach allows to identify whether calcite forms under equilibrium conditions and can reveal the time lag between surface climate variations and their expression in drip water (Treble et al., 2022). Therefore, monitoring also helps quantify how much of the $\delta^{18}\text{O}$ variability in stalagmites reflects local meteorological conditions and/or larger-scale climatic oscillations.

Therefore, although $\delta^{18}\text{O}$ is a robust and widely applied proxy, several sources of uncertainty must be considered. Kinetic fractionation can introduce isotopic enrichments unrelated to climate, while variability in cave ventilation, humidity, and drip rate also affects isotopic composition during calcite growth (Fairchild et al., 2006). Hydrological processes such as water mixing and delayed infiltration can smooth or distort climatic signals, and growth rate variations affect temporal resolution. To mitigate these uncertainties, $\delta^{18}\text{O}$ data should be interpreted alongside complementary proxies such as $\delta^{13}\text{C}$, trace element ratios (e.g., Mg/Ca, Sr/Ca) and constrained by independent chronological and environmental information (Fairchild and Baker, 2012; Treble et al., 2022). Coeval speleothems from different part of the same cave or different caves can also shows common variability, and therefore be used as an indicative that regional processes (e.g., rainfall amount, source effect) play a major role on the modulation of $\delta^{18}\text{O}$ variability rather than local cave conditions.

We reconstruct novel $\delta^{18}\text{O}$ records from multiple stalagmites and caves from Southeastern Brazil, detailed described in Chapter. 4 and 5.

2.6. Carbon isotopes ($\delta^{13}\text{C}$) in speleothems

Stable carbon isotopes ($\delta^{13}\text{C}$) variations within stalagmites are mainly influenced by changes in soil productivity, vegetation cover, and carbonate dissolution, making $\delta^{13}\text{C}$ a suitable proxy for reconstructing past environmental conditions at cave sites (McDermott, 2004; Fairchild and Baker, 2012; Novello et al., 2021).

The main source of carbon for cave dripwater is soil CO_2 , produced by root respiration and microbial activity of organic matter decomposition. The isotopic composition of soil CO_2 reflects the photosynthetic pathway and productivity of the overlying vegetation. For example, C_3 plants, typical dominating temperate and humid environments, have $\delta^{13}\text{C}$ values averaging around -26‰ , whereas C_4 plants, common in tropical grasslands and savannas, average around -13‰ (Cerling, 1984; Ehleringer et al., 1997; Pessenda et al., 2010). Consequently, the $\delta^{13}\text{C}$ of speleothems can reflect changes in vegetation composition and density through time (Novello et al., 2021).

Soil CO₂ and bedrock carbonate are the main sources for dissolved inorganic carbon (DIC) δ¹³C composition in the drip water. The relative contribution of each depends on the mode of dissolution, classically described by the open and closed system models (Hendy, 1971; McDermott, 2004). In an open system, continuous exchange with the soil CO₂ reservoir maintains isotopic equilibrium with biogenic CO₂, producing more negative δ¹³C values in the resulting calcite. In contrast, in a closed system, where percolating water becomes isolated from the soil atmosphere, limited CO₂ availability and progressive dissolution of bedrock result in isotopic enrichment and higher δ¹³C values. Most karst systems function under partially open conditions, where hydrology, infiltration rates, and CO₂ availability modulate δ¹³C through time (Fairchild et al., 2006; Fohlmeister et al., 2020).

Within the cave atmosphere, additional processes can influence δ¹³C before carbonate precipitation. For example, the CO₂ degassing from drip water into the cave atmosphere preferentially removes the lighter isotope (¹²C) increasing the δ¹³C of CO₂, enriching the residual DIC in ¹³C, with degassing being intensified with low drip rates or under strong ventilation (Mickler et al., 2006; Dreybrodt & Scholz, 2011). Prior-carbonate precipitation (PCP) within the epikarst or along stalactite formation also enriches drip water in ¹³C by preferentially removing ¹²C during PCP (Fairchild and Treble, 2009; Patterson et al., 2024). PCP tends to be more pronounced during dry periods, when reduced water availability promotes degassing in air filled voids, while wetter conditions suppress PCP, leading to lower δ¹³C values in speleothems (Patterson et al., 2024). Seasonal variations in cave air pCO₂ can also increase the impact of these effects, especially in shallow caves or well-ventilated such as caves with large entrances (Stríkis et al., 2024). The Hendy test (Hendy, 1971), can help identifying kinetic fractionation along the stalagmite. This test checks for stable δ¹⁸O along a single layer and for the lack of covariation between isotopic ratios (δ¹³C vs δ¹⁸O). This can be a useful diagnostic tool, although it can pose biases such as in tropical climates where vegetation and water rock processes (e.g., PCP) covary with rainfall amount, also resulting in covariation between the isotopic ratios (Novello et al., 2021). Therefore, reproducibility across multiple contemporaneous stalagmites from the same site provides the most robust confirmation of equilibrium deposition.

Interpreting δ¹³C variations in speleothems thus requires accounting for different influences such as climatic, biological, and kinetic. In tropical South America, δ¹³C primarily reflects soil productivity and vegetation density, both closely tied to hydroclimate (Novello et al., 2021). During humid phases, enhanced rainfall promotes dense vegetation, high soil respiration, and greater CO₂ availability, can lead to more negative δ¹³C values. In contrast, drier periods reduce soil respiration and increase PCP, resulting in more positive δ¹³C values (McDermott, 2004; Fairchild and Baker, 2012; Novello et al., 2021).

Overall, the $\delta^{13}\text{C}$ signal in speleothems reflects the balance between vegetation type and productivity, soil CO_2 and water-rock interaction processes (e.g., dissolution and PCP). Therefore, the interpretation of $\delta^{13}\text{C}$ is more robust when combining with other proxies (e.g., $\delta^{18}\text{O}$ and trace element ratios), providing complementary data for the interpretation of hydroclimate and environmental changes. We present in Chapter 4 and 5 $\delta^{13}\text{C}$ analysis as complementary analysis to support the interpretation of trace element ratios related to water-rock interaction processes such as PCP.

2.7. Geochemical controls on speleothem trace elementary ratios with calcium

Speleothems contain a range of trace elements that can be used as proxies for rainfall, temperature, soil conditions, fire occurrence, and other environmental conditions (Fairchild and Treble., 2009). Their incorporation into speleothem carbonate (calcite and aragonite) is controlled by a complex interplay of geochemical, hydrological, and environmental factors operating from the soil through the epikarst to the cave environment (Fairchild and Treble, 2009; Fairchild and Baker, 2012). Advances in analytical techniques, particularly laser ablation inductively coupled plasma mass spectrometry (LA-ICP-MS), have enabled the analysis of trace element distributions at micrometre scales (including mapping), allowing sub-annual to even seasonal resolution in stalagmite records (Fairchild et al., 2006; Weber et al., 2018a).

The main trace elements of interest in this study are related to water-rock interaction processes such as prior-carbonate precipitation (PCP) and incongruent calcite dissolution (ICD), including the trace element ratios of Mg/Ca, Sr/Ca and Ba/Ca (Fairchild and Treble, 2009). Divalent cations such as Mg^{2+} , Sr^{2+} , and Ba^{2+} can substitute for Ca^{2+} in the calcite crystal structure during precipitation, with their incorporation controlled by partition coefficients that vary with temperature, drip rate, and solution chemistry (Fairchild and Treble, 2009; Sinclair et al., 2012). In contrast, elements such as Al, Fe, and Ti are typically associated with detrital input or colloidal material derived from the soil or weathered bedrock (Fairchild et al., 2000; Wassenburg et al., 2012). The trace element composition of dripwater reflects a mixture of sources, including dissolution of the carbonate host rock, soil-derived inputs influenced by organic acids and vegetation activity, and contributions from atmospheric or marine aerosols (Fairchild et al., 2006). The relative importance of these sources depends on infiltration pathways, residence time, and the process related to water–rock interaction within the epikarst zone (Sinclair, 2011; Weber et al., 2018a).

The trace element ratios of Mg/Ca and Sr/Ca are the most widely used as hydroclimatic proxies (Bernal et al., 2016). Their variations are primarily controlled by water-rock interaction,

such as PCP and ICD, with tied relation with effective moisture over in the epikarst, or associated with stalactite formation before the water reaches the stalagmite surface (Fairchild et al., 2000; McMillan et al., 2005; Karmann et al., 2007). During PCP, Ca^{2+} is preferentially removed from solution relative to Mg^{2+} and Sr^{2+} , enriching the residual dripwater in these trace elements. As a result, enhanced PCP during drier conditions leads to elevated Mg/Ca and Sr/Ca ratios, typically coinciding with $\delta^{13}\text{C}$ enrichment caused by reduced soil CO_2 production and increased degassing (Baldini et al., 2006; Karmann et al., 2007; Fairchild and Treble, 2009). ICD provides another mechanism capable of altering trace element ratios (Sinclair, 2011). This process is related to saturated dripwater with respect to calcite under closed-system conditions, with dissolution preferentially removing Ca^{2+} , resulting in a solution enriched in Mg and Sr (Sinclair, 2011; Sinclair et al., 2012). Both PCP and ICD thus produce positive, near-linear covariation between Mg/Ca and Sr/Ca ratios, typically with slope of between 0.71–1.45, in logarithmic space (ln), as described by the “Sinclair test” (Sinclair et al., 2012; Wassenburg et al., 2020). When these ratios vary independently, however, alternative processes such as variable water-rock interaction times, mixing of different water sources, or differences in host-rock mineralogy may influence the ratios variations, making interpretation more complex (Fairchild et al., 2006; Weber et al., 2018a).

Trace element variations in speleothems have been used as effective proxies for reconstructing hydroclimatic variability across timescales ranging from seasonal to millennial (Fairchild et al., 2006; Bernal et al. 2016; Weber et al., 2018a). Also, modern cave monitoring, have shown that ratios are closely correlate with effective moisture, drip rate, and $\delta^{13}\text{C}$ signals, reinforcing their interpretation as proxies sensitive to PCP and hydrological dynamics (Karmann et al., 2007; Wassenburg et al., 2016; Treble et al., 2022). When combined with stable isotope records, they present a potential for robust reconstructions of cave hydrology and external climate forcing (Bernal et al., 2016). In Brazilian cave systems, for instance, elevated Mg/Ca and Sr/Ca ratios often accompany $\delta^{13}\text{C}$ enrichment during drier intervals associated with weakened South American Monsoon phases, consistent with enhanced PCP due to reduced infiltration (Karmann et al., 2007; Cruz et al., 2006; Bernal et al., 2016; Novello et al., 2019). The opposite is observed during wet phases with lower trace element ratios correspond to lower $\delta^{13}\text{C}$ and $\delta^{18}\text{O}$ values, reflecting intensified soil productivity and recharge. Such multi-proxy approaches evidence the value of combining trace element and isotopic analyses for robust assessments over past hydroclimate. We discuss in detail trace element ratios related to water-rock interactions (Mg/Ca, Sr/Ca and Ba/Ca) in chapter 4 and 5.

2.8. References

- Ampuero, A., Stríkis, N.M., Apaéstegui, J., Vuille, M., Novello, V.F., Espinoza, J.C., Cruz, F.W., Vonhof, H., Mayta, V.C., Martins, V.T.S., Cordeiro, R.C., Azevedo, V., Sifeddine, A., 2020. The Forest Effects on the Isotopic Composition of Rainfall in the Northwestern Amazon Basin. *JGR Atmospheres* 125, e2019JD031445. <https://doi.org/10.1029/2019JD031445>
- Bajo, P., Drysdale, R., Woodhead, J., Hellstrom, J., Zanchetta, G., 2012. High-resolution U–Pb dating of an Early Pleistocene stalagmite from Corchia Cave (central Italy). *Quaternary Geochronology* 14, 5–17. <https://doi.org/10.1016/j.quageo.2012.10.005>
- Baker, A., Shanafield, M., Timms, W., Andersen, M.S., Priestley, S., Melo Zurita, M., 2024. An underground drip water monitoring network to characterize rainfall recharge of groundwater at different geologies, environments, and climates across Australia. *Geosci. Instrum. Method. Data Syst.* 13, 117–129. <https://doi.org/10.5194/gi-13-117-2024>
- Baldini, J.U.L., McDermott, F., Fairchild, I.J., 2006. Spatial variability in cave drip water hydrochemistry: Implications for stalagmite paleoclimate records. *Chemical Geology* 235, 390–404. <https://doi.org/10.1016/j.chemgeo.2006.08.005>
- Bernal, J.P., Cruz, F.W., Stríkis, N.M., Wang, X., Deininger, M., Catunda, M.C.A., Ortega-Obregón, C., Cheng, H., Edwards, R.L., Auler, A.S., 2016. High-resolution Holocene South American monsoon history recorded by a speleothem from Botuverá Cave, Brazil. *Earth and Planetary Science Letters* 450, 186–196. <https://doi.org/10.1016/j.epsl.2016.06.008>
- Blyth, A.J., Hartland, A., Baker, A., 2016. Organic proxies in speleothems – New developments, advantages and limitations. *Quaternary Science Reviews* 149, 1–17. <https://doi.org/10.1016/j.quascirev.2016.07.001>
- Borlina, C.S., Lima, E.A., Feinberg, J.M., Jaqueto, P., Lascu, I., Trindade, R.I.F., Font, E., Sánchez-Moreno, E.M., Dimuccio, L.A., Yokoyama, Y., Parés, J.M., Weiss, B.P., Dorale, J.A., 2024. Obtaining High-Resolution Magnetic Records From Speleothems Using Magnetic Microscopy. *Geochem Geophys Geosyst* 25, e2024GC011594. <https://doi.org/10.1029/2024GC011594>
- Bourdon, B., Turner, S., Henderson, M., Lundstrom, C. C., 2003. Introduction to U-series Geochemistry. *Reviews in Mineralogy and Geochemistry*; 52 (1): 1–21. doi: <https://doi.org/10.2113/0520001>
- Budsky, A., Scholz, D., Wassenburg, J.A., Mertz-Kraus, R., Spötl, C., Riechelmann, D.F.C., Gibert, L., Jochum, K.P., Andreae, M.O., 2019. Speleothem $\delta^{13}\text{C}$ record suggests enhanced spring/summer drought in south-eastern Spain between 9.7 and 7.8 ka – A circum-Western Mediterranean anomaly? *Holocene* 29, 1113–1133. <https://doi.org/10.1177/0959683619838021>
- Cheng, H., Edwards, R.L., Shen, C.C., Polyak, V.J., Asmerom, Y., Woodhead, J., Hellstrom, J., Wang, Y., Kong, X., Spötl, C., Wang, X., Alexander, E.C., 2013. Improvements in ^{230}Th dating, ^{230}Th and ^{234}U half-life values, and U–Th isotopic measurements by multi-collector inductively coupled plasma mass spectrometry. *Earth and Planetary Science Letters* 371–372, 82–91. <https://doi.org/10.1016/j.epsl.2013.04.006>
- Cruz, F.W., Burns, S.J., Karmann, I., Sharp, W.D., Vuille, M., Ferrari, J.A., 2006. A stalagmite record of changes in atmospheric circulation and soil processes in the Brazilian subtropics during the Late Pleistocene. *Quaternary Science Reviews* 25, 2749–2761. <https://doi.org/10.1016/j.quascirev.2006.02.019>
- Cruz, F.W., Karmann, I., Viana, O., Burns, S.J., Ferrari, J.A., Vuille, M., Sial, A.N., Moreira, M.Z., 2005. Stable isotope study of cave percolation waters in subtropical Brazil: Implications

- for paleoclimate inferences from speleothems. *Chemical Geology* 220, 245–262. <https://doi.org/10.1016/j.chemgeo.2005.04.001>
- Dasgupta, S., Saar, M.O., Edwards, R.L., Shen, C.C., Cheng, H., Alexander, E.C., 2010. Three thousand years of extreme rainfall events recorded in stalagmites from Spring Valley Caverns, Minnesota. *Earth and Planetary Science Letters* 300, 46–54. <https://doi.org/10.1016/j.epsl.2010.09.032>
- Denniston, R.F., Luetscher, M., 2017. Speleothems as high-resolution paleoflood archives. *Quaternary Science Reviews* 170, 1–13. <https://doi.org/10.1016/j.quascirev.2017.05.006>
- Denniston, R.F., Villarini, G., Gonzales, A.N., Wyrwoll, K.H., Polyak, V.J., Ummenhofer, C.C., Lachniet, M.S., Wanamaker, A.D., Humphreys, W.F., Woods, D., Cugley, J., 2015. Extreme rainfall activity in the Australian tropics reflects changes in the El Niño/Southern Oscillation over the last two millennia. *Proceedings of the National Academy of Sciences of the United States of America* 112, 4576–4581. <https://doi.org/10.1073/pnas.1422270112>
- Dorale, J.A., Lepley, S., Edward, R.L., 2005. The ultimate flood recorder: flood-deposited sediments preserved in stalagmites. *EGU General Assembly 2005* 7, 5–6.
- Dreybrodt, W., 2012. Speleothem Deposition, in: *Encyclopedia of Caves*. Elsevier, pp. 769–777. <https://doi.org/10.1016/B978-0-12-383832-2.00112-2>
- Dreybrodt, W., Scholz, D., 2011. Climatic dependence of stable carbon and oxygen isotope signals recorded in speleothems: From soil water to speleothem calcite. *Geochimica et Cosmochimica Acta* 75, 734–752. <https://doi.org/10.1016/j.gca.2010.11.002>
- Fairchild, I.J., 2012. *Blackwell Quaternary Geoscience Series: Speleothem Science: From Process to Past Environments* (1). Wiley-Blackwell.
- Fairchild, I.J., Baker, A., 2012. *Speleothem science: from process to past environments*, *Blackwell Quaternary Geoscience Series*. Wiley, Oxford, U.K Hoboken, N.J. <https://doi.org/10.1002/9781444361094>
- Fairchild, I.J., Borsato, A., Tooth, A.F., Frisia, S., Hawkesworth, C.J., Huang, Y., McDermott, F., Spiro, B., 2000. Controls on trace element Sr-Mg compositions of carbonate cave waters: implications for speleothem climatic records, *Chemical Geology*.
- Fairchild, I.J., Smith, C.L., Baker, A., Fuller, L., Spötl, C., Matthey, D., McDermott, F., 2006. Modification and preservation of environmental signals in speleothems. *Earth-Science Reviews* 75, 105–153. <https://doi.org/10.1016/j.earscirev.2005.08.003>
- Fairchild, I.J., Treble, P.C., 2009. Trace elements in speleothems as recorders of environmental change. *Quaternary Science Reviews* 28, 449–468. <https://doi.org/10.1016/j.quascirev.2008.11.007>
- Feinberg, J.M., Johnson, K.R., 2021. Cave and speleothem science: From local to planetary scales. *Elements* 17, 81–86. <https://doi.org/10.2138/GSELEMENTS.17.2.81>
- Feinberg, J.M., Lascu, I., Lima, E.A., Weiss, B.P., Dorale, J.A., Alexander, E.C., Edwards, R.L., 2020. Magnetic detection of paleoflood layers in stalagmites and implications for historical land use changes. *Earth and Planetary Science Letters* 530. <https://doi.org/10.1016/j.epsl.2019.115946>
- Finné, M., Kylander, M., Boyd, M., Sundqvist, H.S., Löwemark, L., 2015. Can XRF scanning of speleothems be used as a non-destructive method to identify paleoflood events in caves? *International Journal of Speleology* 44, 17–23. <https://doi.org/10.5038/1827-806X.44.1.2>
- Ford, D., n.d. *Karst Hydrogeology and Geomorphology*.
- Frappier, A.B., Pyburn, J., Pinkey-Drobnis, A.D., Wang, X., Corbett, D.R., Dahlin, B.H., 2014. Two millennia of tropical cyclone-induced mud layers in a northern Yucatán stalagmite:

- Multiple overlapping climatic hazards during the Maya Terminal Classic “megadroughts.” *Geophysical Research Letters* 41, 5148–5157. <https://doi.org/10.1002/2014GL059882>
- Frisia, S., 2019. Stalactites and stalagmites, in: *Encyclopedia of Caves*, Third Edition. Elsevier, pp. 1041–1048. <https://doi.org/10.1016/B978-0-12-814124-3.00120-5>
- Frisia, S., Borsato, A., 2010. Chapter 6 Karst, in: *Developments in Sedimentology*. Elsevier, pp. 269–318. [https://doi.org/10.1016/S0070-4571\(09\)06106-8](https://doi.org/10.1016/S0070-4571(09)06106-8)
- Gázquez, F., Calaforra, J.M., Forti, P., Stoll, H., Ghaleb, B., Delgado-Huertas, A., 2014. Paleoflood events recorded by speleothems in caves. *Earth Surface Processes and Landforms* 39, 1345–1353. <https://doi.org/10.1002/esp.3543>
- González-Lemos, S., Jiménez-Sánchez, M., Stoll, H.M., 2014. Sediment transport during recent cave flooding events and characterization of speleothem archives of past flooding. *Geomorphology* 228, 87–100. <https://doi.org/10.1016/j.geomorph.2014.08.029>
- González-Lemos, S., Müller, W., Pisonero, J., Cheng, H., Edwards, R.L., Stoll, H.M., 2015. Holocene flood frequency reconstruction from speleothems in northern Spain. *Quaternary Science Reviews* 127, 129–140. <https://doi.org/10.1016/j.quascirev.2015.06.002>
- Hendy, C.H., 1971. The isotopic geochemistry of speleothems-I. The calculation of the effects of different modes of formation on the isotopic composition of speleothems and their applicability as palaeoclimatic indicators. *Geochimica et Cosmochimica Acta* 35, 801–824. [https://doi.org/10.1016/0016-7037\(71\)90127-X](https://doi.org/10.1016/0016-7037(71)90127-X)
- Hill, C., Forti, P., 1995. The classification of cave minerals and speleothems. *IJS* 24, 77–82. <https://doi.org/10.5038/1827-806X.24.1.5>
- Homann, J., Oster, J.L., De Wet, C.B., Breitenbach, S.F.M., Hoffmann, T., 2022. Linked fire activity and climate whiplash in California during the early Holocene. *Nat Commun* 13, 7175. <https://doi.org/10.1038/s41467-022-34950-x>
- Huang, S., Cai, Y., Cheng, H., Xue, G., Cheng, X., He, M., Li, R., Ma, L., Wei, Y., Lu, Y., Yang, L., Edwards, R.L., 2024. An integrated study of constraining the initial ^{230}Th of a stalagmite and its implications. *Quaternary Geochronology* 80, 101497. <https://doi.org/10.1016/j.quageo.2024.101497>
- Ivanovich, M., & Harmon, R. S., 1992. *Uranium-Series Disequilibrium: Applications to Earth, Marine, and Environmental Sciences* (2nd ed.). Clarendon Press.
- Karmann, I., Cruz, F.W., Viana, O., Burns, S.J., 2007. Climate influence on geochemistry parameters of waters from Santana–Pérolas cave system, Brazil. *Chemical Geology* 244, 232–247. <https://doi.org/10.1016/j.chemgeo.2007.06.029>
- Kim, S.-T., O’neil, J.R., 1997. Equilibrium and nonequilibrium oxygen isotope effects in synthetic carbonates, *Geochimica et Cosmochimica Acta*.
- Knight, •, Dorale, C.W., Edwards, J.A., 2006. Stalagmite Records of Interglacial and Glacial Flooding at Crevice Cave, Missouri, USA Show affiliations.
- Lachniet, M.S., 2009. Climatic and environmental controls on speleothem oxygen-isotope values. *Quaternary Science Reviews* 28, 412–432. <https://doi.org/10.1016/j.quascirev.2008.10.021>
- Lascu, I., Feinberg, J.M., 2011. Speleothem magnetism. *Quaternary Science Reviews* 30, 3306–3320. <https://doi.org/10.1016/j.quascirev.2011.08.004>
- Lauritzen, S.-E., Lundberg, J., 1999. Speleothems and climate: a special issue of *The Holocene*. *The Holocene* 9, 643–647. <https://doi.org/10.1191/095968399666229065>
- Lepley, S.W., Dorale, J.A., Edwards, R.L., n.d. A high-resolution Holocene El Niño record from flood deposited sediments preserved in speleothems.

- McDermott, F., 2004. Palaeo-climate reconstruction from stable isotope variations in speleothems: a review. *Quaternary Science Reviews* 23, 901–918. <https://doi.org/10.1016/j.quascirev.2003.06.021>
- McMillan, E.A., Fairchild, I.J., Frisia, S., Borsato, A., McDermott, F., 2005. Annual trace element cycles in calcite-aragonite speleothems: Evidence of drought in the western Mediterranean 1200-1100 yr BP. *Journal of Quaternary Science* 20, 423–433. <https://doi.org/10.1002/jqs.943>
- Meckler, A.N., Vonhof, H., Martínez-García, A., 2021. Temperature Reconstructions Using Speleothems. *Elements* 17, 101–106. <https://doi.org/10.2138/gselements.17.2.101>
- Meyer, M.C., Spötl, C., Mangini, A., Tessedri, R., 2012. Speleothem deposition at the glaciation threshold - An attempt to constrain the age and paleoenvironmental significance of a detrital-rich flowstone sequence from Entrische Kirche Cave (Austria). *Palaeogeography, Palaeoclimatology, Palaeoecology* 319–320, 93–106. <https://doi.org/10.1016/j.palaeo.2012.01.010>
- Mickler, P.J., Stern, L.A., Banner, J.L., 2006. Large kinetic isotope effects in modern speleothems. *Bulletin of the Geological Society of America*. <https://doi.org/10.1130/B25698.1>
- Novello, V.F., Cruz, F.W. da, Vuille, M., Campos, J.L.P.S., Stríkis, N.M., Apaéstegui, J., Moquet, J.S., Azevedo, V., Ampuero, A., Utida, G., Wang, X., Paula-Santos, G.M., Jaqueto, P., Pessenda, L.C.R., Breecker, D.O., Karmann, I., 2021. Investigating $\delta^{13}\text{C}$ values in stalagmites from tropical South America for the last two millennia. *Quaternary Science Reviews* 255. <https://doi.org/10.1016/j.quascirev.2021.106822>
- Novello, V.F., Cruz, F.W., McGlue, M.M., Wong, C.I., Ward, B.M., Vuille, M., Santos, R.A., Jaqueto, P., Pessenda, L.C.R., Atorre, T., Ribeiro, L.M.A.L., Karmann, I., Barreto, E.S., Cheng, H., Edwards, R.L., Paula, M.S., Scholz, D., 2019. Vegetation and environmental changes in tropical South America from the last glacial to the Holocene documented by multiple cave sediment proxies. *Earth and Planetary Science Letters* 524. <https://doi.org/10.1016/j.epsl.2019.115717>
- Patterson, E.W., Skiba, V., Wolf, A., Griffiths, M.L., McGee, D., Búi, T.N., Trần, M.X., Đinh, T.H., Đỗ-Trọng, Q., Goldsmith, G.R., Ersek, V., Johnson, K.R., 2024. Local hydroclimate alters interpretation of speleothem $\delta^{18}\text{O}$ records. *Nat Commun* 15, 9064. <https://doi.org/10.1038/s41467-024-53422-y>
- Pyburn, J., n.d. A 2,205-year record of tropical cyclone strikes near Yucatán, Mexico, from mud layers in a stalagmite.
- Richards, D.A., Dorale, J.A., n.d. Uranium-series Chronology and Environmental Applications of Speleothems.
- Rozanski, K., Araguás-Araguás, L., Gonfiantini, R., 2013. Isotopic Patterns in Modern Global Precipitation. pp. 1–36. <https://doi.org/10.1029/gm078p0001>
- Scholz, D., Hoffmann, D., 2008. $^{230}\text{Th}/\text{U}$ -dating of fossil corals and speleothems. *Earth and Planetary Science Letters* 271, 52–76. <https://doi.org/10.1016/j.epsl.2008.08.011>
- Scholz, D., Hoffmann, D.L., 2011. StalAge - An algorithm designed for construction of speleothem age models. *Quaternary Geochronology* 6, 369–382. <https://doi.org/10.1016/j.quageo.2011.02.002>
- Sinclair, D.J., 2011. Two mathematical models of Mg and Sr partitioning into solution during incongruent calcite dissolution. *Chemical Geology* 283, 119–133. <https://doi.org/10.1016/j.chemgeo.2010.05.022>

- Sinclair, D.J., Banner, J.L., Taylor, F.W., Partin, J., Jenson, J., Mylroie, J., Goddard, E., Quinn, T., Jocson, J., Miklavič, B., 2012. Magnesium and strontium systematics in tropical speleothems from the Western Pacific. *Chemical Geology* 294–295, 1–17. <https://doi.org/10.1016/j.chemgeo.2011.10.008>
- Strikis, N.M., Cruz, F.W., Cheng, H., Karmann, I., Edwards, R.L., Vuille, M., Wang, X., De Paula, M.S., Novello, V.F., Auler, A.S., 2011. Abrupt variations in South American monsoon rainfall during the Holocene based on a speleothem record from central-eastern Brazil. *Geology* 39, 1075–1078. <https://doi.org/10.1130/G32098.1>
- Taylor, S.R., McLennan, S.M., 1995. The geochemical evolution of the continental crust. *Reviews of Geophysics* 33, 241–265. <https://doi.org/10.1029/95RG00262>
- Treble, P.C., Baker, A., Abram, N.J., Hellstrom, J.C., Crawford, J., Gagan, M.K., Borsato, A., Griffiths, A.D., Bajo, P., Markowska, M., Priestley, S.C., Hankin, S., Paterson, D., 2022. Ubiquitous karst hydrological control on speleothem oxygen isotope variability in a global study. *Communications Earth and Environment* 3. <https://doi.org/10.1038/s43247-022-00347-3>
- Wassenburg, J.A., Immenhauser, A., Richter, D.K., Jochum, K.P., Fietzke, J., Deininger, M., Goos, M., Scholz, D., Sabaoui, A., 2012. Climate and cave control on Pleistocene/Holocene calcite-to-aragonite transitions in speleothems from Morocco: Elemental and isotopic evidence. *Geochimica et Cosmochimica Acta* 92, 23–47. <https://doi.org/10.1016/j.gca.2012.06.002>
- Wassenburg, J.A., Riechelmann, S., Schröder-Ritzrau, A., Riechelmann, D.F.C., Richter, D.K., Immenhauser, A., Terente, M., Constantin, S., Hachenberg, A., Hansen, M., Scholz, D., 2020. Calcite Mg and Sr partition coefficients in cave environments: Implications for interpreting prior calcite precipitation in speleothems. *Geochimica et Cosmochimica Acta* 269, 581–596. <https://doi.org/10.1016/j.gca.2019.11.011>
- Wassenburg, J.A., Scholz, D., Jochum, K.P., Cheng, H., Oster, J., Immenhauser, A., Richter, D.K., Häger, T., Jamieson, R.A., Baldini, J.U.L., Hoffmann, D., Breitenbach, S.F.M., 2016. Determination of aragonite trace element distribution coefficients from speleothem calcite–aragonite transitions. *Geochimica et Cosmochimica Acta* 190, 347–367. <https://doi.org/10.1016/j.gca.2016.06.036>
- Wassenburg, J.A., Vonhof, H.B., Cheng, H., Martínez-García, A., Ebner, P.-R., Li, X., Zhang, H., Sha, L., Tian, Y., Edwards, R.L., Fiebig, J., Haug, G.H., 2021. Penultimate deglaciation Asian monsoon response to North Atlantic circulation collapse. *Nat. Geosci.* 14, 937–941. <https://doi.org/10.1038/s41561-021-00851-9>
- Weber, M., Scholz, D., Schröder-Ritzrau, A., Deininger, M., Spötl, C., Lugli, F., Mertz-Kraus, R., Jochum, K.P., Fohlmeister, J., Stumpf, C.F., Riechelmann, D.F.C., 2018. Evidence of warm and humid interstadials in central Europe during early MIS 3 revealed by a multi-proxy speleothem record. *Quaternary Science Reviews* 200, 276–286. <https://doi.org/10.1016/j.quascirev.2018.09.045>
- White, W., 2006. Identification of cave minerals by Raman spectroscopy: new technology for non-destructive analysis. *IJS* 35, 103–107. <https://doi.org/10.5038/1827-806X.35.2.6>
- Wilhelm, B., Canovas, J.A.B., Aznar, J.P.C., Kämpf, L., Swierczynski, T., Stoffel, M., Støren, E., Toonen, W., 2018. Recent advances in paleoflood hydrology: From new archives to data compilation and analysis. *Water Security*. <https://doi.org/10.1016/j.wasec.2018.07.001>
- Wilhelm, B., Cánovas, J.A.B., Macdonald, N., Toonen, W.H.J., Baker, V., Barriendos, M., Benito, G., Brauer, A., Corella, J.P., Denniston, R., Glaser, R., Ionita, M., Kahle, M., Liu, T., Luetscher, M., Macklin, M., Mudelsee, M., Munoz, S., Schulte, L., George, S.S., Stoffel,

- M., Wetter, O., 2019. Interpreting historical, botanical, and geological evidence to aid preparations for future floods. *Wiley Interdisciplinary Reviews: Water* 6, e1318. <https://doi.org/10.1002/wat2.1318>
- Zhu, Z., Feinberg, J.M., Xie, S., Bourne, M.D., Huang, C., Hu, C., Cheng, H., 2017. Holocene ENSO-related cyclic storms recorded by magnetic minerals in speleothems of central China. *Proceedings of the National Academy of Sciences of the United States of America* 114, 852–857. <https://doi.org/10.1073/pnas.1610930114>

Chapter 3 – Manuscript I

A Holocene History of Extreme Rainfall Events in Southern Brazil

Julio Cauhy^{a,b*}; Marcela Eduarda Della Libera^{a,b}; Nicolás M. Stríkis^{c,d}; Mathias Vuille^e; Isabel Tamara Pedron^f; Victor Azevedo^{c,g}; Francisco W. Cruz Junior^c; Valdir F. Novello^h; Hubert Vonhof^b; Denis Scholz^a

^aInstitut für Geowissenschaften, Johannes Gutenberg-Universität Mainz, Germany

^bMax-Planck-Institut für Chemie, Mainz, Germany

^cInstituto de Geociências, Universidade de São Paulo, São Paulo-SP, Brazil

^dDept. Geoquímica, Universidade Federal Fluminense

^eDepartment of Atmospheric and Environmental Sciences, University at Albany, State University of New York, Albany, New York, USA

^fCentro de Ciências Agrárias, Universidade Estadual do Oeste do Paraná

^gSchool of Natural Sciences, Trinity College Dublin, Ireland

^hInstitute of Geosciences, University of Brasília, Brasília – DF, Brazil

*Corresponding author:

Julio Cauhy

Email: cauhy.r@gmail.com

Paper under review in Earth and Environmental Communications

3.1. Abstract

Extreme rainfall events (ERE) are projected to increase in intensity and frequency worldwide. Southern Brazil, a densely populated region, is strongly affected by these events with severe socioeconomic impacts, such as the catastrophic flooding in Rio Grande do Sul State in April/May of 2024. Understanding its variability is fundamental for predicting plausible outcomes in a global warming scenario. The lack of long-term records hampers our ability to assess ERE variability and the role of large-scale climate drivers over longer timescales. Here we present the first ERE record from southern Brazil spanning the past 7500 years, based on stalagmites from Malfazido cave. Our results suggest a strong influence of Antarctic-tropical teleconnections on the long-term modulation of ERE and important contribution of strong/moderate El Niño events to the frequency of ERE in the last millennium. Unparalleled ERE frequency in the 20th century suggest an increased influence of anthropogenic forcing on their modulation.

3.2. Introduction

The densely populated region of southern Brazil is severely impacted by extreme rainfall events (ERE), often triggering devastating landslides and floods. The socioeconomic damage is costly, with disproportional impacts on vulnerable populations (Debortoli et al., 2017; Simoes-Sousa et al., 2025; Marengo et al., 2021). ERE in southern Brazil are primarily triggered by circulation anomalies that enhance the transport of warm, moist air from the Amazon basin via the South American low-level jet (SALLJ) to southern Brazil, where it interacts with advancing cold fronts from the south and creates favourable conditions for intense convection over the region (Reboita et al., 2024, 2021; Cai et al., 2020). These circulation anomalies are mainly related to teleconnection patterns, particularly to the tropical Pacific during El Niño years and to Antarctic–tropical teleconnections (Cai et al., 2020; Queiroz et al., 2022; Reis et al., 2020).

Historical data analysis reveals that 67% of ERE since 1960 occurred during El Niño years, with the intensity of events increasing with higher ENSO 3.4 index values, evidencing that El Niño increases the likelihood of ERE in southern Brazil 2,6. A disastrous example occurred in April 2024 under strong El Niño conditions, reported as the region’s worst climate tragedy in history (Simoes-Sousa et al., 2025; Reboita et al., 2024; Zhang et al., 2025). The disaster was caused by record accumulations of rainfall, precipitating over 600 mm of rainfall accumulating over a 10-day period, leaving 600,000 people displaced, 2.4 million people affected, and 183 dead (Simões-Souza et al., 2025; Reboita et al., 2024). The ERE was triggered by the interaction of warm, moist air brought by the SALLJ with two cold fronts that reached the region, likely intensified by global warming (Zhang et al., 2025; Reboita et al., 2024).

Projections of the ERE indicate an intensification both in terms of frequency and magnitude (Debortoli et al., 2017; Marengo et al., 2021) due to an increase in atmospheric moisture and evaporative demand 9. A strong likelihood of an increased frequency and magnitude of El Niño events (Cai et al., 2021; McPhaden et al., 2021) is also suggested to lead to a higher probability of occurrence of ERE over southern Brazil in the future (Simões-Souza et al., 2025; Zhang et al., 2025). Yet, a major challenge in predicting plausible scenarios for future changes in ERE frequency lies in the limited availability of historical data extending beyond the pre-industrial era. Developing longer ERE-sensitive hydroclimate time series would thus significantly improve our understanding of the natural variability of ERE frequency and help to clarify the influence of large-scale climate teleconnections in South America (Debortoli et al., 2017; Cai et al., 2020; Denniston et al., 2017).

Detrital layers within speleothems have been used to reconstruct episodic flood or heavy rainfall events associated with ERE, tropical cyclones and storms (Denniston et al., 2015, 2017;

Dasgupta et al., 2010; Wilhelm et al., 2019; Zhu et al., 2017). While speleothems are widely used for paleoclimate reconstructions, short-term extreme events are, in many cases, not captured by geochemical proxies in speleothems, which tend to reflect averaged or smoothed climate signals due to aquifer storage/mixing (Dasgupta et al., 2010). Paleoflood records preserved in detrital layers within speleothems provide a unique opportunity to evaluate multi-annual variability in ERE frequency through extended periods of time (Denniston et al., 2017).

Here we present a record of ERE in Southern Brazil spanning the past 7500 years based on stalagmites from Malfazido cave. The combination of petrographic analysis, our multi-year hydrological monitoring data, instrumental data and $^{230}\text{Th}/\text{U}$ -dating demonstrate the suitability of Malfazido cave stalagmites as high-resolution archives of regional ERE, providing information about ERE frequencies from interannual to millennial time scales. This record provides a valuable opportunity for investigating long-term natural variability in ERE and associated teleconnections throughout the Holocene.

3.3. Results and Discussion

3.3.1. Cave setting and experimental approach

Malfazido cave ($24^{\circ}39'\text{S}$; $49^{\circ}32'\text{W}$; 885 m asl) is located in Paraná State, southern Brazil (Figs. 3.1b, c). It is a typical linear cave, characterized by a main conduit fed by an intermittent underground river that forms a vadose canyon. The main conduit features a knickpoint that divides the cave into two main galleries: the upper and the lower gallery (Fig. 3.1d). The first consists of a narrow passage that showcases well-defined flood zones and is highly ornamented by numerous candle-shaped stalagmites (supp. Figs. 3.1b, c, d). The latter contains a remarkable sequence of large travertine dams that disrupt the flow and create a system of siphons, trapping water and sediment during episodic flood events (supp. Fig. 3.1a). Three aragonitic stalagmites from Malfazido Cave were used for paleoflood reconstructions (supp. Fig. 2). MFZ-N-1 was collected in 2019 from the cave wall at ~40 cm above the thalweg of the upper gallery, with its top surpassing the flood zone limit. MFZ-10 and MFZ-11 were collected in 2021 from the lower gallery (Fig. 3.1e, f). MFZ-11 was located on the thalweg and thus more frequently exposed to small water level variations. MFZ-10 was located near the upper limit of the flood zone with its base partially buried in ~200 mm of mud (Fig. 3.1f). Both MFZ-N-1 and MFZ-10 were actively dripping and precipitating carbonate at the time of collection.

The damming of water in both galleries is crucial to record flood events because it permits the deposition of fine sediment on top of the speleothems during extended periods of flooding (Figs. 3.1h). The flooding starts at the deeper part of the cave and gradually progresses towards

the entrance, successively flooding the sequence of travertine dams. Depending on the magnitude of the rainfall event, the flood can reach dams further downstream, eventually reaching the cave entrance (supp. Figs. 3.1e, f). The water from the cave feeds into the Turvo River, a small but vital waterway in the Atlantic Forest. With a drainage area of roughly 400 km², the Turvo river basin (Fig. 3.1c) is part of the larger Ribeira de Iguape River basin, a crucial water source for local communities, including small farmers, Quilombolas (descendants of Afro-Brazilian maroons), and Indigenous people.

The study area is located in the subtropics, with rainfall well-distributed throughout the year (Ferreira et al., 2022). During austral spring and summer, large amounts of warm and moist air are transported from the Amazon to the subtropics, particularly through the SALLJ (Marengo et al., 2004; Vera et al., 2006). The interaction between this moisture flux and advancing cold fronts that occur year-round (Fig. 3.1b) enhances convective activity and can lead to intense precipitation episodes and ERE (Ferreira et al., 2022; Eichholz et al., 2015). During austral winter, cyclonic systems and the passage of cold fronts are the main sources of rainfall in the region, which explain the considerable rainfall in the cold season (Vera et al., 2009). The cold fronts contribute substantially to rainfall totals and are thus crucial for the occurrence of intense precipitation and ERE (Ferreira et al., 2022).

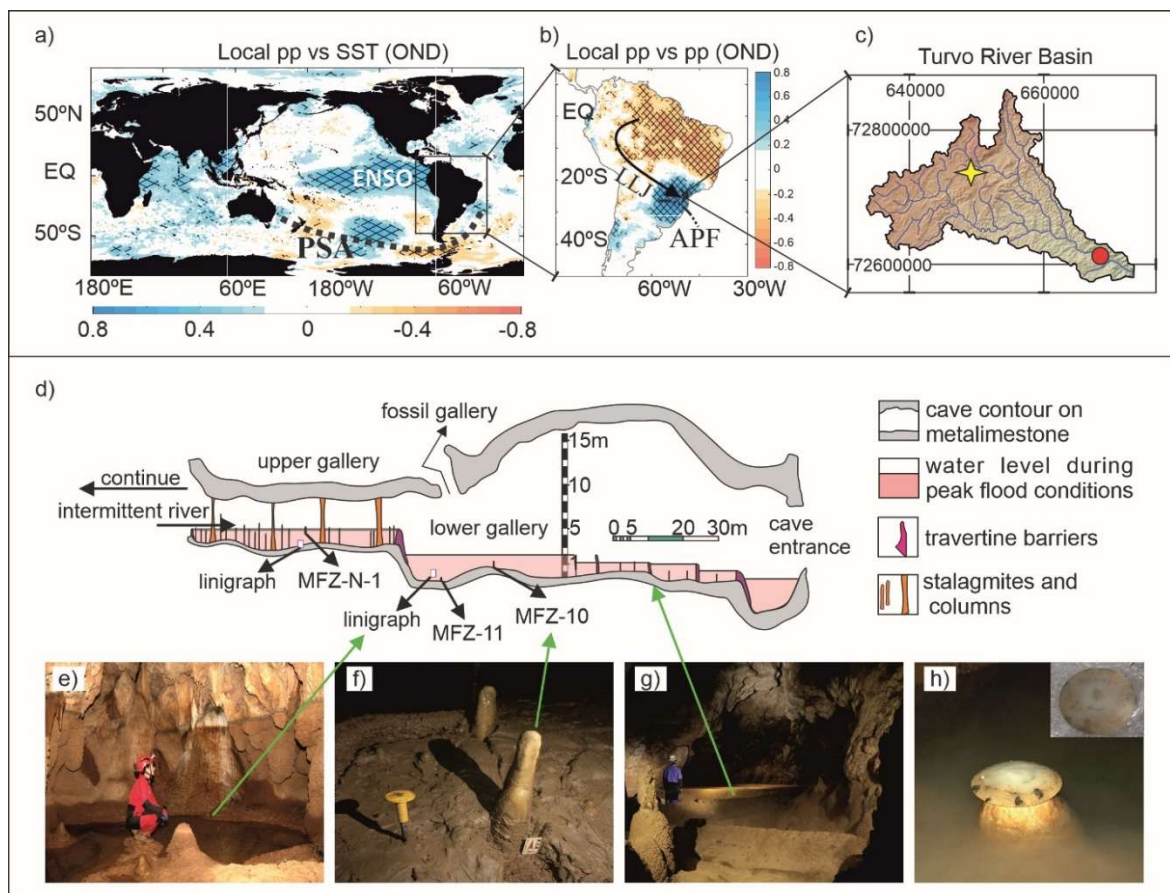


Figure 3.1 - Study area and cave setting. a) and b) correlation maps of local precipitation (CHIRPS) vs SST (OISST) and local precipitation (CHIRPS) vs precipitation (CHIRPS), respectively, for October, November and December

(OND). El Niño - southern oscillation region and pacific-south America (PSA) pattern are indicated. the hatched area represents significant correlations with a p value < 0.05. the paths of the low-level jet (LLJ) and Atlantic polar fronts (APF) are indicated by the black arrow and dashed line, respectively. c) Turvo river basin with the location of Malfazido cave indicated by the yellow star and the fluviometric station of Turvo river (81125000) and basin outlet indicated by the red circle. d) Malfazido cave profile with water level during peak flood conditions indicated by the pinkish area. stalagmite samples and linigraph positions are indicated. e) lower gallery water level monitoring area and mfz-11 collection site. the underwater carbonate crust on the walls marks the maximum water level during ponding conditions. f) mfz-10 in-situ with its base buried by a mud deposit. g) sequence of travertine dams. h) artificial substrate (watch glass) with detrital sediment deposited. the flanks of the artificial surface show a higher concentration of detrital sediment due to the washing effect of the water in the center of the dripping. modern carbonate deposited on the artificial surface is observed a few months after detrital deposition.

3.3.2. Tracking Past Extreme Rainfall Events in Southern Brazil via the Malfazido Record

Multi-year hydrological monitoring recorded four flood events in Malfazido Cave between February 2019 and March 2024 (Jun. 2019, Dec. 2022, Oct. 2023, Feb. 2024., supp. Fig. 3.3), with associated rainfall and river discharge data summarized in supplementary Table 1. The October 2023 flood was the most intense, with prolonged high-water levels (up to 1.44 m) sustaining for 81 days (Fig. 3.2) and sediment deposition observed for the first time as recorded by watch glasses on top of stalagmites (Fig. 3.1h).

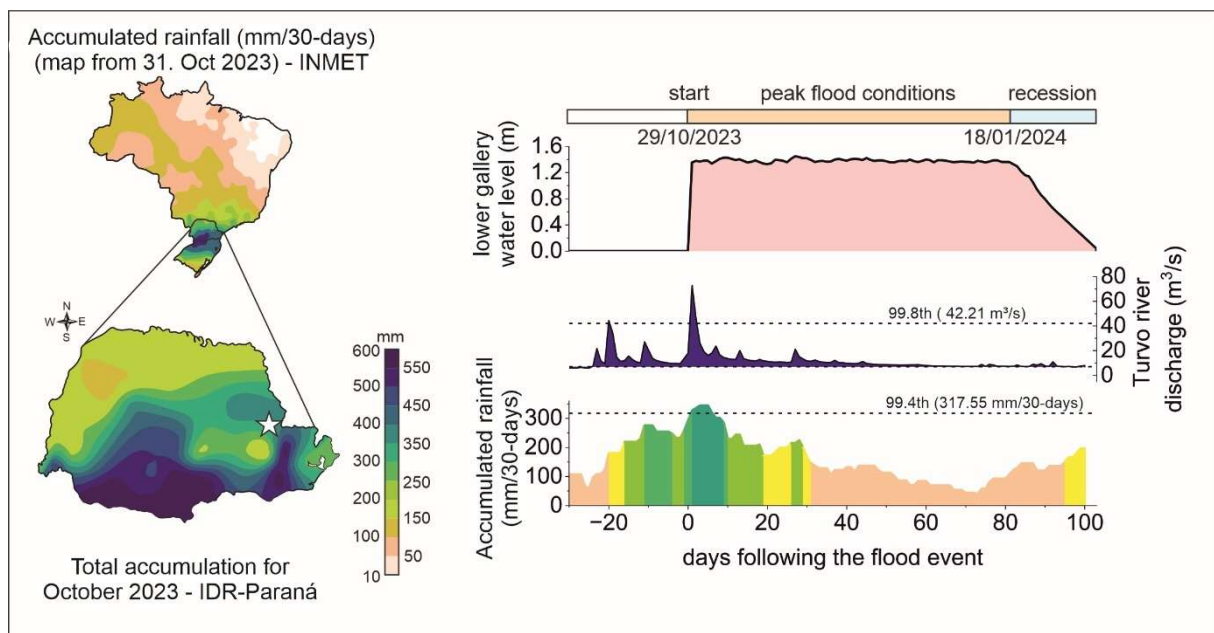


Figure 3.2 - Accumulated rainfall (mm/30-days) for the October 2023 event. The maps showing accumulated rainfall for Brazil and Paraná state were modified from INMET and Instituto de Desenvolvimento Rural do Paraná (IDR). Top plot shows the variation of the water level in the lower conduct during the event. Center plot shows the daily maximum discharge (m^3/s) for Turvo river. Bottom plot shows the accumulated rainfall (mm/30 days) extracted from the CHIRPS database. x-axis in days following the flood event with 0 representing 29/10/2023.

The major flood peaked on 29. October 2023 and receded gradually until early February 2024 (Fig. 3.2). A field visit in December 2023 recorded the cave entrance still flooded (supp.

Fig. 3.1e). October 2023 recorded 343 mm of rain, 280 % above the historical mean for October, with an extreme response on the Turvo River discharge (peak discharge of 72 m³/s exceeding the 99.98th percentile, Fig. 3.2). More than 64,000 people were affected in Paraná State due to widespread flooding and weather-related impacts. These events are driven by cumulative rainfall over periods of days to weeks, sufficient to overcome natural cave siphons and mobilize sediment downstream. Our observations suggest that flood-derived sediment is exclusively deposited on top of stalagmites in Malfazido Cave during major floods triggered by high-magnitude ERE.

All four events recorded in Malfazido cave were related to cold fronts (supp. Table 3.1), with the major event linked to extreme rainfall triggered by low-pressure systems and cold fronts (National Institute of Meteorology -INMET- Brazil - <http://www.inmet.gov.br/portal/>). The circulation mechanism related to flood events in Malfazido cave highlight the role of cold fronts and the interaction between these advancing frontal systems with the low-level jets bearing warm moist air from the Amazon. Furthermore, the circulation anomalies related to October 2023 were triggered during strong El Niño conditions (Niño3.4 = 2.02, supp. Table 3.1). Comparison between hydrological monitoring in Malfazido cave and historical discharge data from Turvo River show comparable events in the past. They mainly occurred during strong El Niño years, such as 1983, 1997-1998 and 2023 (supp. Fig. 3.4), evidencing the impact of warm Pacific SSTs anomalies on the occurrence of floods in the region (Grimm et al., 2003; Cai et al., 2020).

Therefore, the flood events in Malfazido cave are mainly triggered by advancing cold fronts in combination with warm moist air from the Amazon further creating conditions for severe rainfall episodes that lead to major floods in the cave. Deposition of detrital sediment on top of stalagmites highlights the potential of these speleothems to record ERE in Malfazido cave, and the fast growth rates at Malfazido cave even provide the opportunity for preservation of interannual flood activity. The reconstruction of the flood activity beyond the instrumental period using Malfazido stalagmites allows us to access the frequency of short term EREs in the region.

3.3.3. Extreme Rainfall Variability over the Holocene

The Malfazido ERE record presents insights into past southern Brazil ERE variability beyond the industrial period for the first time, covering the past 7500 years. Our record shows notable centennial to multi-centennial variability, with a long-term sinusoidal pattern (Fig. 3.3a, c). The average frequency of ERE for the past 7500 years is ~9 events/100-yrs (i.e., 11.5 years between

events), with maximum values reached in the 20th century (1900 to 2000 C.E) with 18 events/100-yrs (5.5 yrs between events) (Fig. 3.3c).

The Middle Holocene (MH) (4200-7500 B.P.) is characterized by enhanced flood activity (~11 events/100-yrs), with peak activity (17 events/100-yrs) close to 20th century values around 4950-5050 B.P and 6250-6350 B.P. The Late Holocene (LH) shows a more variable pattern with alternating intervals of enhanced and suppressed flood activity, with a general mean value of 7.2 events/100-yrs. It starts with a highly variable flood activity between 4200-3000 B.P, with values ranging from 4 to 13 events/100-yrs. This interval is followed by a dampening in ERE activity at 3000-2000 B.P., with values ranging from 0 to 5 events/100-yrs (average of 2.9 events/100-yrs). From 2000 B.P. to the present, the ERE activity presents a rising trend, yet with lower activity between 2000-1000 yr. B.P. (average of 6.1 events/100-yrs) and subsequently greater activity during the last millennium (average of 10.7 events/100-yrs). With the exception of the period between 450-550 B.P, the last millennium shows above average ERE frequencies, with the period from 450 B.P. to the present showing enhanced activity, peaking in 450-350 B.P. during the Little Ice Age (LIA) and again in the 20th century.

Wavelet (Fig. 3.3d) and REDFIT (supp. Fig. 3.5) analyses reveal an important low-frequency variability on ERE occurrence (periodicities of 170 to 448 years, ERE, Fig. 3.3d). These multi-centennial cycles suggest a persistent pacing mechanism underlying ERE recurrence in southern Brazil. REDFIT analysis also shows multidecadal frequencies (~60 yrs above 99% χ^2), and wavelet analysis shows that these cycles are more dominant during the Middle Holocene (Fig. 3.3d).

In summary, our record shows a long-term sinusoidal pattern with enhanced ERE frequencies observed during the Middle Holocene and the Last Millennium and weak EREs activity in the Late Holocene. Moreover, multi-centennial cycles suggest a persistent pacing mechanism underlying ERE recurrence in southern Brazil. Our record documents an unprecedented increase in ERE frequency in the 20th century, with higher values than any time over the past 7500 years (Fig. 3.3c).

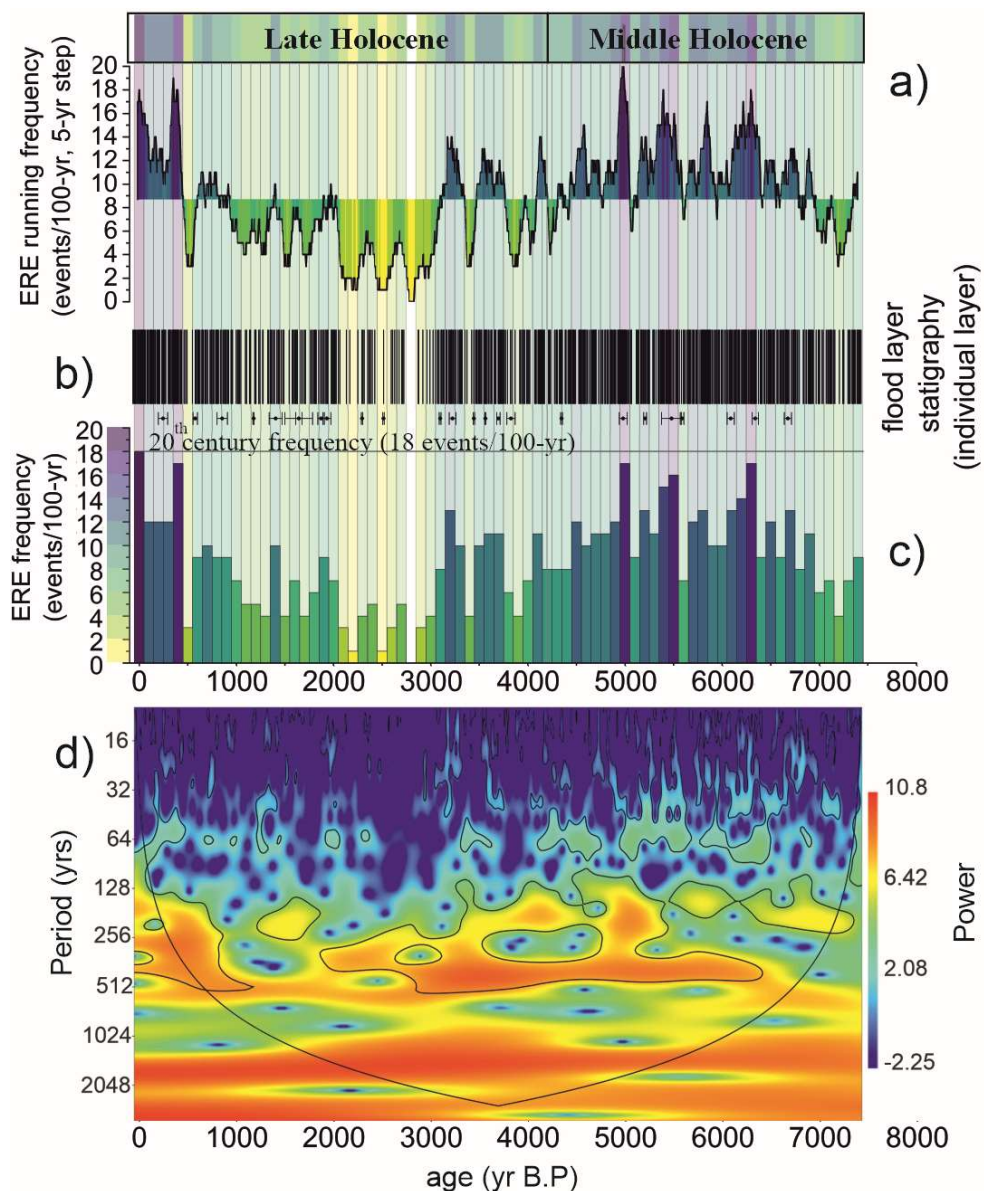


Figure 3.3 - Malfazido cave flood frequency and periodicity. Top panel shows the running frequency of cave floods with a time bin of 100 yrs and a 5-yr step. Bimodal data plot showing each individual micro-detrital layer identified within MFZ-10. Black line marks the enhanced frequency values of the 20th century. ²³⁰Th/U-ages are represented by dots with error bars. Third panel from the top shows ERE frequency with century bins (100-yr) without overlap between each other (100-yr step). Colormap is used to enhance visualization of high/low flood activity periods. Bottom panel shows wavelet analysis performed on running frequency time series; black line contours highlight periods with p -value ≤ 0.05 .

3.3.4. ERE modulation and teleconnections over the Holocene

The long-term variability with a marked sinusoidal pattern (Fig. 3.4a) of the ERE record is also observed in Antarctic summer temperature records from West Antarctic ice cores (Jones et al., 2023) (Fig. 3.4b), which show a striking agreement with the Malfazido ERE record for the past 7000 yrs. The comparison between the records reveals a significant negative correlation (100 – 7000 B.P; $r=-0.45$, $p<0.01$), indicating that colder (warmer) summer temperatures in West Antarctica are associated with enhanced (suppressed) ERE occurrence. These findings are in agreement with modern observations showing that Antarctic–tropical teleconnections

driven by temperature gradients between southern Brazil and western Antarctica can further contribute to the occurrence of ERE.

Carpenido et al. (2023) demonstrated that summer surface air temperature variability trends between the Antarctic Peninsula and South America are closely linked to changes in atmospheric systems operating in the region, such as the SALLJ, mesoscale convective systems, atmospheric blockings, and the South Atlantic Convergence Zone, with all of them potentially contributing to the occurrence of EREs. Their study shows that colder surface air temperatures over Antarctica are typically associated with an El Niño event characterized by a strengthening of the SALLJ, enhanced warm air advection from tropical latitudes towards southern Brazil, a Pacific-South American (PSA) wave train pattern and intensified convection over southeastern South America (Fig. 3.1a) (Cai et al., 2020). The PSA is a pattern of stationary Rossby wave trains induced by an El Niño extratropical teleconnection pathway, triggered by anomalous convection over the tropical Pacific and consists of a series of positive and negative atmospheric pressure anomalies that extend southwards into the mid-latitudes before veering into the Atlantic basin (Cai et al., 2020). The PSA wave train generates a persistent high-pressure centre over the eastern coast of South America (Cai et al., 2020; Aguierre-Correa et al., 2025), resulting in anomalous subsidence over our study region and a weakening of the South Atlantic Convergence Zone (Cai et al., 2020; Aguierre-Correa et al., 2025). Concurrently, the winds associated with the anomalous high-pressure centre enhance the SALLJ ⁶. In total, such changes in atmospheric circulation, combined with favourable synoptic meteorological conditions, are associated with heavy rainfall and flooding across the region (Cai et al., 2020; Aguierre-Correa et al., 2025; Grimm et al., 2009; Montanher et al., 2023).

For instance, during the 2015/2016 El Niño, temperature gradients between southern Brazil and the Antarctic Peninsula presented an anomalous temperature dipole associated with intense cyclogenesis, driven by the interaction between the SALLJ and cold front passages (Reis et al., 2020). Collectively, these circulation anomalies increase the likelihood of ERE, with a direct impact on the frequency of these events in southern Brazil. These findings are in agreement with modern observations that show increasing (decreasing) cold frontal activity associated with Antarctic-tropical teleconnections driven by higher (lower) temperature gradients between Antarctica and southern Brazil (Reis et al., 2020; Carpenedo et al., 2023), suggesting that this high-latitude teleconnection helped modulating ERE activity over much of the Holocene.

In the modern climate, ERE tend to cause the most damage during strong El Niño years, since its conditions and circulation anomalies create favourable conditions for ERE in southern

Brazil, highlighting the role of the Pacific in modulating both the frequency and intensity of these events (Simões-Souza et al., 2025; Cai et al., 2020). For comparison between El Niño conditions and ERE activity, we calculate the frequency of moderate-to-strong El Niño years using the El Niño/Southern Oscillation index ($ENSO_{index}$) reconstruction from Li et al. (2011), using years with $ENSO_{index} > 1$ (for moderate-to-strong El Niño conditions) for the period between -52 to 1050 years B.P (900 to 2002 years C.E) (Fig 3.4d). The comparison between the frequency of ERE and moderate-to-strong El Niño years for the last millennium shows a significant positive correlation ($r=0.61$, $p<0.01$) calculated for frequency bins of 50-yrs without overlap between bins. The strong coherence between ERE frequency and El Niño conditions reveals the persistent influence of El Niño on extreme events in southern Brazil during the last millennium. Moreover, 20th century El Niño and ERE frequencies are unprecedented in the context of at least the last millennium, and this activity is even unrivalled for ERE frequency during the past 7500 years (Fig. 3.3c). This coherent behaviour highlights the importance of El Niño-induced circulation anomalies as a forcing of ERE in the current climate, and it emphasizes its increased relevance over the last millennium. On longer time scales, however, the ERE record shows a discrepancy with other El Niño reconstructions, especially during the Middle Holocene. While El Niño activity is reduced during this period, as supported by several proxy records and modelling experiments (Mark et al., 2022), ERE frequency is predominantly enhanced (Fig. 3.4c). Comparison with the Pallcacocha Lake record (Mark et al., 2022), a unique El Niño frequency record in terms of temporal resolution and continuity further evidences the differences between El Niño frequency and EREs during MH (Fig. 3.4c).

In summary, El Niño seems to significantly modulate ERE activity in southern Brazil during the LH, with a strong impact during the last millennium. The contrasting pattern during the MH, with reduced El Niño frequency and enhanced ERE activity, might reflect a change in the teleconnection patterns, local effects at our cave site or other forcings becoming more relevant. The increased frequency of El Niño in the 20th century might already reflect a contribution from anthropogenic greenhouse forcing (Cai et al., 2021), which could partially explain the highest values of ERE frequency observed in our Malfazido record.

The persistent multi-centennial cycles observed in Malfazido ERE record are also present in a monsoon intensity record from Botuvera cave (Sr/Ca – BTV record), southern Brazil (Bernal et al., 2016). Both records show a 420- and 210-yr signals persistent throughout the Holocene (Bernal et al., 2016). This cycle was shown to modulate South America Monsoon System intensity during the Late Holocene and is attributed to the Vries-Suess solar cycle (208-yr) (Novello et al., 2016). Therefore, these cycles suggest a persistent pacing mechanism underlying ERE recurrence in southern Brazil, potentially linked to low-frequency climate variability throughout solar modulation of SAMS (Novello et al., 2016). The periodicity of ~64

yrs observed in both REDFIT and wavelet analysis might indicate a modulation contribution from the Atlantic Multidecadal Oscillation (AMO), especially during the Middle Holocene. This is in agreement with wavelet analysis of the BTV record with a more pronounced multidecadal signal in the range of the AMO during the Middle Holocene, showing a greater modulation via Atlantic Ocean during this period.

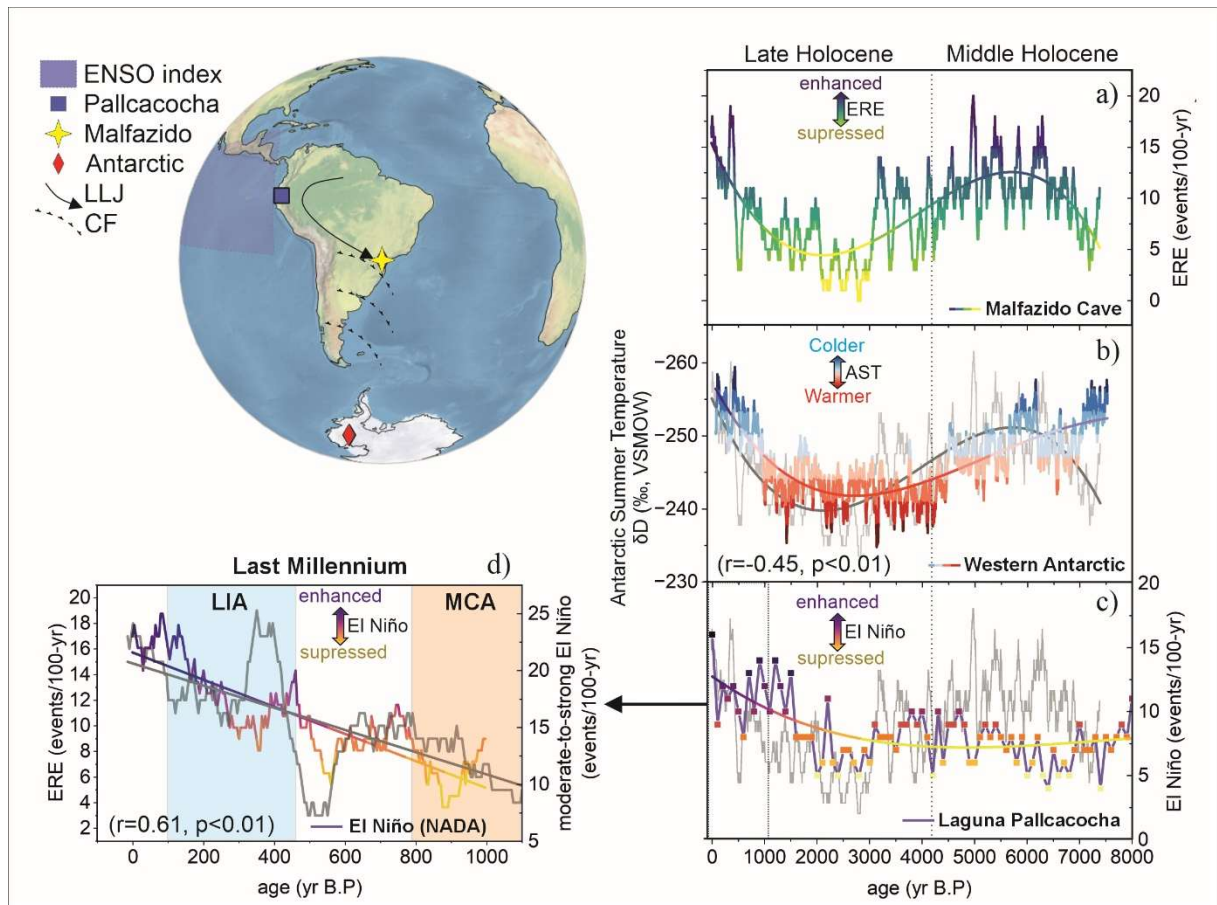


Figure 3.4 - Global map centered in South America with discussed sites indicated. LLJ (low-level jets) and CF (cold fronts). a) Malfazido ERE record (events/100-yrs). The record is plotted in light grey in the other plots for visual comparison; b) Antarctic summer temperature (AST) reconstruction based on δD values from Western Antarctic ice cores (Jones et al., 2023); c) El Niño frequency reconstruction based on Laguna Pallcacocha (Mark et al., 2022); d) Moderate-to-strong (ENSIndex > 1) El Niño years frequency calculated based on ENSO index reconstruction from Li et al., (2011).

3.4. Summary and Conclusion

Our ERE record provides the first reconstruction of high-frequency ERE variability in southern Brazil and South America extending over the past 7,500 years. The results reveal pronounced centennial to multi-centennial-scale variability and a long-term sinusoidal pattern. Notably, the 20th century exhibits the highest frequency of ERE in the entire record, indicating the emergence of an unprecedented, likely anthropogenically forced increase in extreme rainfall and flooding in the region.

Comparison with Antarctic summer temperature reveals a strong relationship: periods of colder summer temperatures in West Antarctica are associated with increased ERE frequency in southern Brazil, likely reflecting enhanced meridional temperature gradients, resulting in intensified cold front activity, and Amazonian moisture transport to the region. Conversely, warmer Antarctic summers are associated with suppressed ERE occurrence.

Over the last millennium, ERE frequency shows a statistically significant correlation with El Niño activity, evidencing the importance of Pacific–South America teleconnections. This relationship is also observed during the LH, but much weaker during the MH.

The unprecedented frequency of ERE observed in the 20th century suggests a possible decoupling from natural variability, with potential additional external forcings on ERE modulation. Additionally, under increased greenhouse gas warming, higher frequencies and magnitudes of El Niño events as well as an increase in atmospheric moisture and evaporative demand are expected. Therefore, future warming scenarios indicates an increase in ERE activity in southern Brazil, emphasizing the immediately need for mitigation and adaptation strategies, particularly in vulnerable regions and for communities most exposed vulnerable to the impacts of ERE.

3.5. Methods

3.5.1. Flood layer stratigraphy ($^{230}\text{Th}/\text{U}$ -dating, age modelling, corrections, thin sections)

Stalagmite chronologies were established by $^{230}\text{Th}/\text{U}$ dating, using multi-collector inductively coupled plasma mass spectrometry (MC-ICP-MS). MFZ-10 and MFZ-11 were dated at the Institute for Geosciences, Johannes-Gutenberg University-Mainz (Germany), following the methodology described in (Klose et al., 2024). MFZ-N-1 was analysed at the Geochronology Laboratory at the University of Minnesota (USA) and the Institute of Global Environmental Change, Xi'an Jiaotong University (China) following (Klose et al., 2024). $^{230}\text{Th}/\text{U}$ ages are provided in the supplementary material (supp. Table 3.2, 3.3 and 3.4). Detrital $^{230}\text{Th}/^{232}\text{Th}$ ratios were determined following (Budsky et al., 2019) (supp. Text 3.1). Age models were constructed using StalAge (Scholz and Hoffmann, 2011), assuming the top of actively dripping MFZ-10 and MFZ-N-1 corresponds to the collection year (2019 and 2021 C.E., respectively). In total, 21 thin sections were analysed under polarized light microscopy to characterize mineralogy, fabrics, and distribution of detrital material (supp. Text 3.2). High-resolution thin section scans and petrographic observation were used to identify flood layers and measure their depth from the top using Inkscape. We identified 921 micro-detrital layers (657 layers in MFZ-10; 205 layers in MFZ-11; and 130 layers in MFZ-N-1). Given the bimodal nature of detrital layer data in speleothems (Denniston et al., 2017), we applied a running frequency analysis with 10 to 100-

year bins at 5-year steps. This method improves comparisons across flood records and enables analysis of multidecadal to millennial variability. For correlation analysis, we calculated the frequency of events using individual time bins without overlapping.

3.5.2. Cave monitoring and instrumental data

Water levels in the flood zones of Malfazido Cave were monitored from February 2019 to March 2024 using HOBO U20 Water Level Loggers (models U20-001-01 and U20-001-04 for the upper and lower conduits, respectively). Barometric compensation was applied using pressure data from the loggers. Artificial substrates made of watch glasses were installed at stalagmite sites to track sediment deposition from flood events and ongoing carbonate precipitation.

Daily rainfall data were obtained from Climate Hazards Group InfraRed Precipitation with Station data (CHIRPS³⁷) at $0.05^\circ \times 0.05^\circ$ resolution for Malfazido Cave covering the period 01/01/1981 to 29/02/2024. River discharge data for the Rio do Turvo were sourced from Brazil's National Water Agency via HIDROWEB³⁶, based on records from the fluviometric station Rio do Turvo (81125000), located at the watershed outlet (Fig. 3.1c) (24.755913° S, 49.338306° W). El Niño conditions were determined using the Niño3.4 monthly index obtained from the NOAA Physical Sciences Laboratory (PSL) at <https://psl.noaa.gov/data/correlation/nina34.anom.data>.

Acknowledgements

We acknowledge financial support from the Max Planck Graduate Center Mainz. This work was also supported by the São Paulo Research Foundation –FAPESP (the PIRE-CREATE project 2017/50085-3) and Rio de Janeiro Research Foundation - FAPERJ (the project HOT: “The role of Human-induced warming in the Hydrology Of Tropics” grants E-26211.352-2021 and E-26-201.421-20210) and the Deutsche Forschungsgemeinschaft through grant INST 247/889-1 FUGG.

Author contributions

Fieldwork: J.C., M.E.D.L., N.S. and V.L., ²³⁰Th-U dating: J.C., M.E.D.L., V.A. and D.S., Microscopy analysis and stratigraphy: J.C. Cave Monitoring: J.C. and N.S., Visualization: J.C.; Supervision: H.V., and D.S., Writing—original draft: J.C., Writing—review & editing: J.C., M.E.D.L., N.S., F.W.C.J., I. T.P., M.V., V.N., H.V., D.S

Corresponding authors

Correspondence to J. Cauhy

Competing interests

The authors declare no competing interests.

3.6. References

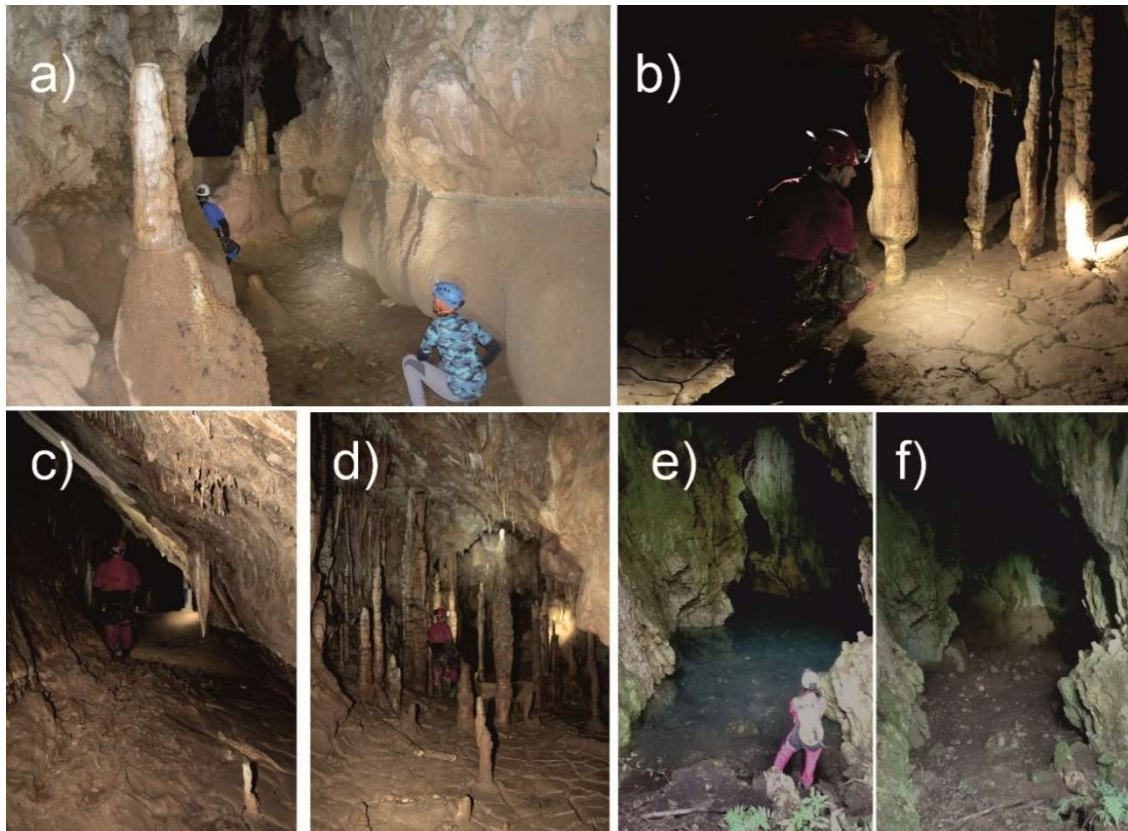
- Bernal, J.P., Cruz, F.W., Stríkis, N.M., Wang, X., Deininger, M., Catunda, M.C.A., Ortega-Obregón, C., Cheng, H., Edwards, R.L., Auler, A.S., 2016. High-resolution Holocene South American monsoon history recorded by a speleothem from Botuverá Cave, Brazil. *Earth and Planetary Science Letters* 450, 186–196. <https://doi.org/10.1016/j.epsl.2016.06.008>
- Budsky, A., Scholz, D., Wassenburg, J.A., Mertz-Kraus, R., Spötl, C., Riechelmann, D.F., Gibert, L., Jochum, K.P., Andreae, M.O., 2019. Speleothem $\delta^{13}\text{C}$ record suggests enhanced spring/summer drought in south-eastern Spain between 9.7 and 7.8 ka – A circum-Western Mediterranean anomaly? *The Holocene* 29, 1113–1133. <https://doi.org/10.1177/0959683619838021>
- Cai, W., McPhaden, M.J., Grimm, A.M., Rodrigues, R.R., Taschetto, A.S., Garreaud, R.D., Dewitte, B., Poveda, G., Ham, Y.-G., Santoso, A., Ng, B., Anderson, W., Wang, G., Geng, T., Jo, H.-S., Marengo, J.A., Alves, L.M., Osman, M., Li, S., Wu, L., Karamperidou, C., Takahashi, K., Vera, C., 2020. Climate impacts of the El Niño–Southern Oscillation on South America. *Nat Rev Earth Environ* 1, 215–231. <https://doi.org/10.1038/s43017-020-0040-3>
- Cheng, H., Lawrence Edwards, R., Shen, C.C., Polyak, V.J., Asmerom, Y., Woodhead, J., Hellstrom, J., Wang, Y., Kong, X., Spötl, C., Wang, X., Calvin Alexander, E., 2013. Improvements in ^{230}Th dating, ^{230}Th and ^{234}U half-life values, and U-Th isotopic measurements by multi-collector inductively coupled plasma mass spectrometry. *Earth and Planetary Science Letters*. <https://doi.org/10.1016/j.epsl.2013.04.006>
- Dasgupta, S., Saar, M.O., Edwards, R.L., Shen, C.C., Cheng, H., Alexander, E.C., 2010. Three thousand years of extreme rainfall events recorded in stalagmites from Spring Valley Caverns, Minnesota. *Earth and Planetary Science Letters* 300, 46–54. <https://doi.org/10.1016/j.epsl.2010.09.032>
- Debortoli, N.S., Camarinha, P.I.M., Marengo, J.A., Rodrigues, R.R., 2017. An index of Brazil's vulnerability to expected increases in natural flash flooding and landslide disasters in the context of climate change. *Natural Hazards* 86, 557–582. <https://doi.org/10.1007/s11069-016-2705-2>
- Denniston, R.F., Luetscher, M., 2017. Speleothems as high-resolution paleoflood archives. *Quaternary Science Reviews* 170, 1–13. <https://doi.org/10.1016/j.quascirev.2017.05.006>
- Denniston, R.F., Villarini, G., Gonzales, A.N., Wyrwoll, K.H., Polyak, V.J., Ummenhofer, C.C., Lachniet, M.S., Wanamaker, A.D., Humphreys, W.F., Woods, D., Cugley, J., 2015. Extreme rainfall activity in the Australian tropics reflects changes in the El Niño/Southern Oscillation over the last two millennia. *Proceedings of the National Academy of Sciences of the United States of America* 112, 4576–4581. <https://doi.org/10.1073/pnas.1422270112>
- Eichholz, C.W., Campos, C.R.J., Maria, D.M., Pinto, L.B., 2015. Extreme Rainfall Event Observed in Northern of Rio Grande do Sul. *Anuário IGEO UFRJ* 38, 86. https://doi.org/10.11137/2015_1_86_94
- Ferreira, G.W.S., Reboita, M.S., 2022. A New Look into the South America Precipitation Regimes: Observation and Forecast. *Atmosphere* 13, 873. <https://doi.org/10.3390/atmos13060873>
- Funk, C., Peterson, P., Landsfeld, M., Pedreros, D., Verdin, J., Shukla, S., Husak, G., Rowland, J., Harrison, L., Hoell, A., Michaelsen, J., 2015. The climate hazards infrared precipitation with stations—a new environmental record for monitoring extremes. *Sci Data* 2, 150066. <https://doi.org/10.1038/sdata.2015.66>

- Grimm, A.M., 2003. The El Niño Impact on the Summer Monsoon in Brazil: Regional Processes versus Remote Influences. *Journal of Climate* 16, 263–280. [https://doi.org/10.1175/1520-0442\(2003\)016%253C0263:TENIOT%253E2.0.CO;2](https://doi.org/10.1175/1520-0442(2003)016%253C0263:TENIOT%253E2.0.CO;2)
- Grimm, A.M., Tedeschi, R.G., 2009. ENSO and extreme rainfall events in South America. *Journal of Climate* 22, 1589–1609. <https://doi.org/10.1175/2008JCLI2429.1>
- Jones, T.R., Cuffey, K.M., Roberts, W.H.G., Markle, B.R., Steig, E.J., Stevens, C.M., Valdes, P.J., Fudge, T.J., Sigl, M., Hughes, A.G., Morris, V., Vaughn, B.H., Garland, J., Vinther, B.M., Rozmiarek, K.S., Brashear, C.A., White, J.W.C., 2023. Seasonal temperatures in West Antarctica during the Holocene. *Nature* 613, 292–297. <https://doi.org/10.1038/s41586-022-05411-8>
- Klose, J., Weber, M., Scholz, D., 2024. Central European warm phases recorded by episodic speleothem growth during MIS 3. *Communications Earth and Environment* 5. <https://doi.org/10.1038/s43247-024-01863-0>
- Li, J., Xie, S.-P., Cook, E.R., Huang, G., D'Arrigo, R., Liu, F., Ma, J., Zheng, X.-T., 2011. Interdecadal modulation of El Niño amplitude during the past millennium. *Nature Clim Change* 1, 114–118. <https://doi.org/10.1038/nclimate1086>
- Marengo, J.A., 2004. Interdecadal variability and trends of rainfall across the Amazon basin. *Theoretical and Applied Climatology* 78, 79–96. <https://doi.org/10.1007/s00704-004-0045-8>
- Marengo, J.A., Camarinha, P.I., Alves, L.M., Diniz, F., Betts, R.A., 2021. Extreme Rainfall and Hydro-Geo-Meteorological Disaster Risk in 1.5, 2.0, and 4.0°C Global Warming Scenarios: An Analysis for Brazil. *Front. Clim.* 3. <https://doi.org/10.3389/fclim.2021.610433>
- Mark, S.Z., Abbott, M.B., Rodbell, D.T., Moy, C.M., 2022. XRF analysis of Laguna Pallcacocha sediments yields new insights into Holocene El Niño development. *Earth and Planetary Science Letters* 593, 117657. <https://doi.org/10.1016/j.epsl.2022.117657>
- Montanher, O.C., Minaki, C., De Moraes, E.S., De Paula Silva, J., Pereira, P., 2023. Geosystemic Impacts of the Extreme Rainfall Linked to the El Niño 2015/2016 Event in Northern Paraná, Brazil. *Applied Sciences* 13, 9678. <https://doi.org/10.3390/app13179678>
- Novello, V.F., Vuille, M., Cruz, F.W., Strikis, N.M., De Paula, M.S., Edwards, R.L., Cheng, H., Karmann, I., Jaqueto, P.F., Trindade, R.I.F., Hartmann, G.A., Moquet, J.S., 2016. Centennial-scale solar forcing of the South American Monsoon System recorded in stalagmites. *Scientific Reports* 6, 1–8. <https://doi.org/10.1038/srep24762>
- Queiroz, M.G.S., Parise, C.K., Pezzi, L.P., Carpenedo, C.B., Vasconcellos, F.C., Torres, A.L.R., Barbosa, W.L., Lima, L.G., 2022. Response of southern troposphere meridional circulation to historical maxima of Antarctic sea ice. *An. Acad. Bras. Ciênc.* 94, e20210795. <https://doi.org/10.1590/0001-3765202220210795>
- Reboita, M.S., Ambrizzi, T., Crespo, N.M., Dutra, L.M.M., Ferreira, G.W. de S., Rehbein, A., Drumond, A., da Rocha, R.P., Souza, C.A. de, 2021. Impacts of teleconnection patterns on South America climate. *Annals of the New York Academy of Sciences* 1504, 116–153. <https://doi.org/10.1111/nyas.14592>
- Reboita, M.S., Mattos, E.V., Capucin, B.C., Souza, D.O. de, Ferreira, G.W. de S., 2024. A Multi-Scale Analysis of the Extreme Precipitation in Southern Brazil in April/May 2024. *Atmosphere* 15, 1123. <https://doi.org/10.3390/atmos15091123>
- Reis, P.A., Aquino, F.E., Schosler, V., Bernardo, R.T., Simões, J.C., n.d. Tropical–Antarctic connections of an explosive cyclone in southern Brazil: rainfall stable isotope ratios and atmospheric analysis.
- Scholz, D., Hoffmann, D.L., 2011. StalAge - An algorithm designed for construction of speleothem age models. *Quaternary Geochronology* 6, 369–382. <https://doi.org/10.1016/j.quageo.2011.02.002>
- Simoës-Sousa, I.T., Camargo, C.M.L., Tavora, J., Piffer-Braga, A., Farrar, J.T., Pavelsky, T.M., 2025. The May 2024 Flood Disaster in Southern Brazil: Causes, Impacts, and SWOT-Based Volume Estimation. *Geophysical Research Letters* 52, e2024GL112442. <https://doi.org/10.1029/2024GL112442>

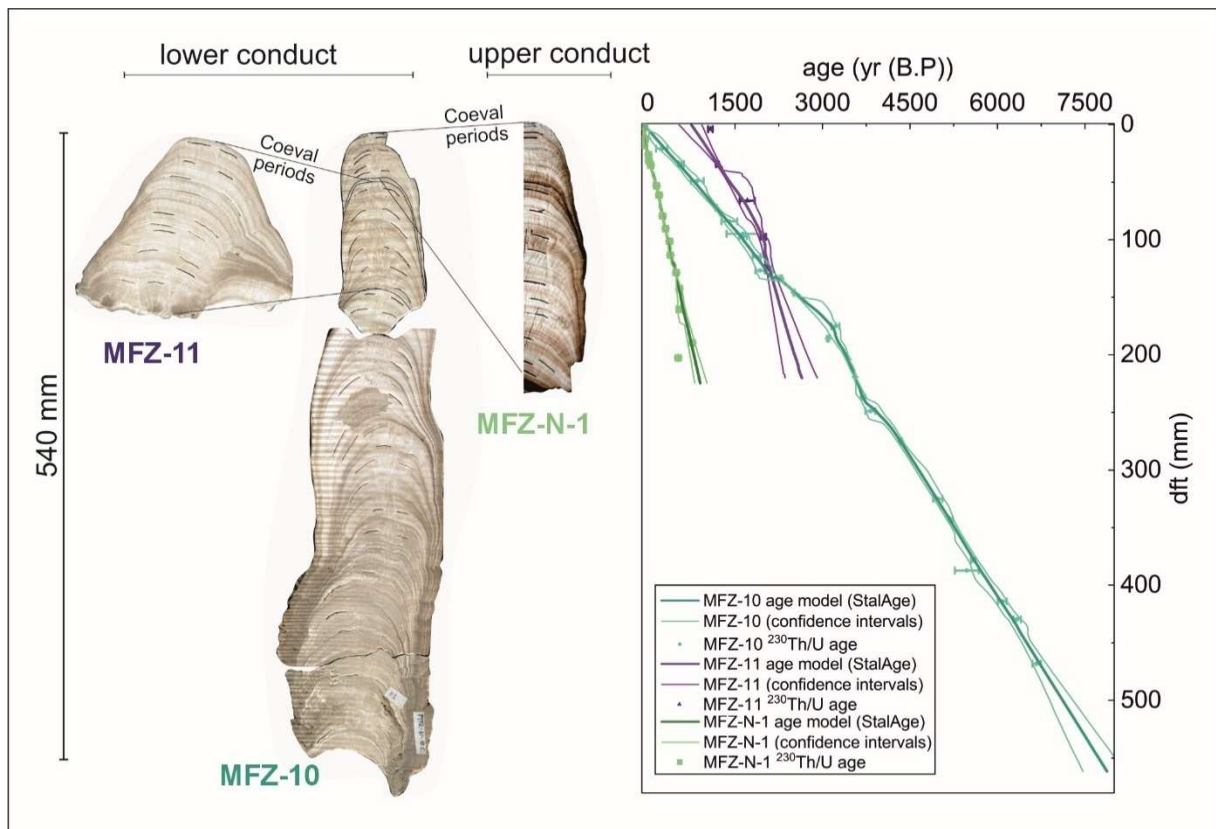
- Vera, C., Baez, J., Douglas, M., Emmanuel, C.B., Marengo, J., Meitin, J., Nicolini, M., Noguez-Paegle, J., Paegle, J., Penalba, O., Salio, P., Saulo, C., Dias, M.A.S., Dias, P.S., Zipser, E., 2006. The South American Low-Level Jet Experiment. *Bulletin of the American Meteorological Society* 87, 63–78. <https://doi.org/10.1175/BAMS-87-1-63>
- Vera, C.S., Vigliarolo, P.K., Berbery, E.H., 2002. Cold season synoptic-scale waves over subtropical South America. *Monthly Weather Review* 130, 684–699. [https://doi.org/10.1175/1520-0493\(2002\)130%253C0684:CSSSWO%253E2.0.CO;2](https://doi.org/10.1175/1520-0493(2002)130%253C0684:CSSSWO%253E2.0.CO;2)
- Wilhelm, B., Ballesteros Cánovas, J.A., Macdonald, N., Toonen, W.H.J., Baker, V., Barriendos, M., Benito, G., Brauer, A., Corella, J.P., Denniston, R., Glaser, R., Ionita, M., Kahle, M., Liu, T., Luetscher, M., Macklin, M., Mudelsee, M., Munoz, S., Schulte, L., St. George, S., Stoffel, M., Wetter, O., 2019. Interpreting historical, botanical, and geological evidence to aid preparations for future floods. *Wiley Interdisciplinary Reviews: Water* 6, e1318–e1318. <https://doi.org/10.1002/wat2.1318>
- Zhang, W., Zhou, T., Ye, W., Zhang, T., Zhang, L., Wolski, P., Risbey, J., Wang, Z., Min, S.-K., Ramsay, H., Brody, M., Grimm, A., Clark, R., Ren, K., Jiang, J., Chen, X., Fu, S., Li, L., Tang, S., Hu, S., 2025. A Year Marked by Extreme Precipitation and Floods: Weather and Climate Extremes in 2024. *Adv. Atmos. Sci.* 42, 1045–1063. <https://doi.org/10.1007/s00376-025-4540-4>
- Zhao, B., Russell, J.M., Blaus, A., Nascimento, M.D.N., Freeman, A., Bush, M.B., 2024. Tropical Andean climate variations since the last deglaciation. *Proc. Natl. Acad. Sci. U.S.A.* 121, e2320143121. <https://doi.org/10.1073/pnas.2320143121>
- Zhu, Z., Feinberg, J.M., Xie, S., Bourne, M.D., Huang, C., Hu, C., Cheng, H., 2017. Holocene ENSO-related cyclic storms recorded by magnetic minerals in speleothems of central China. *Proceedings of the National Academy of Sciences of the United States of America* 114, 852–857. <https://doi.org/10.1073/pnas.1610930114>

3.7. Supplementary Material – Manuscript I

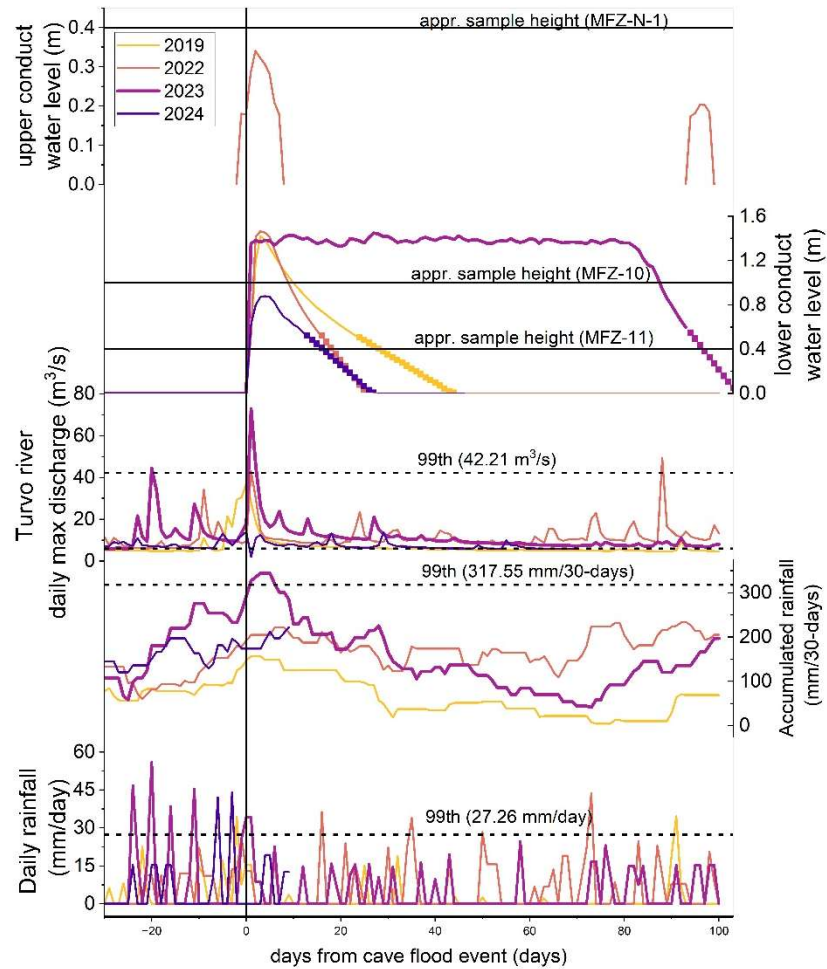
3.7.1. Supplementary Figures



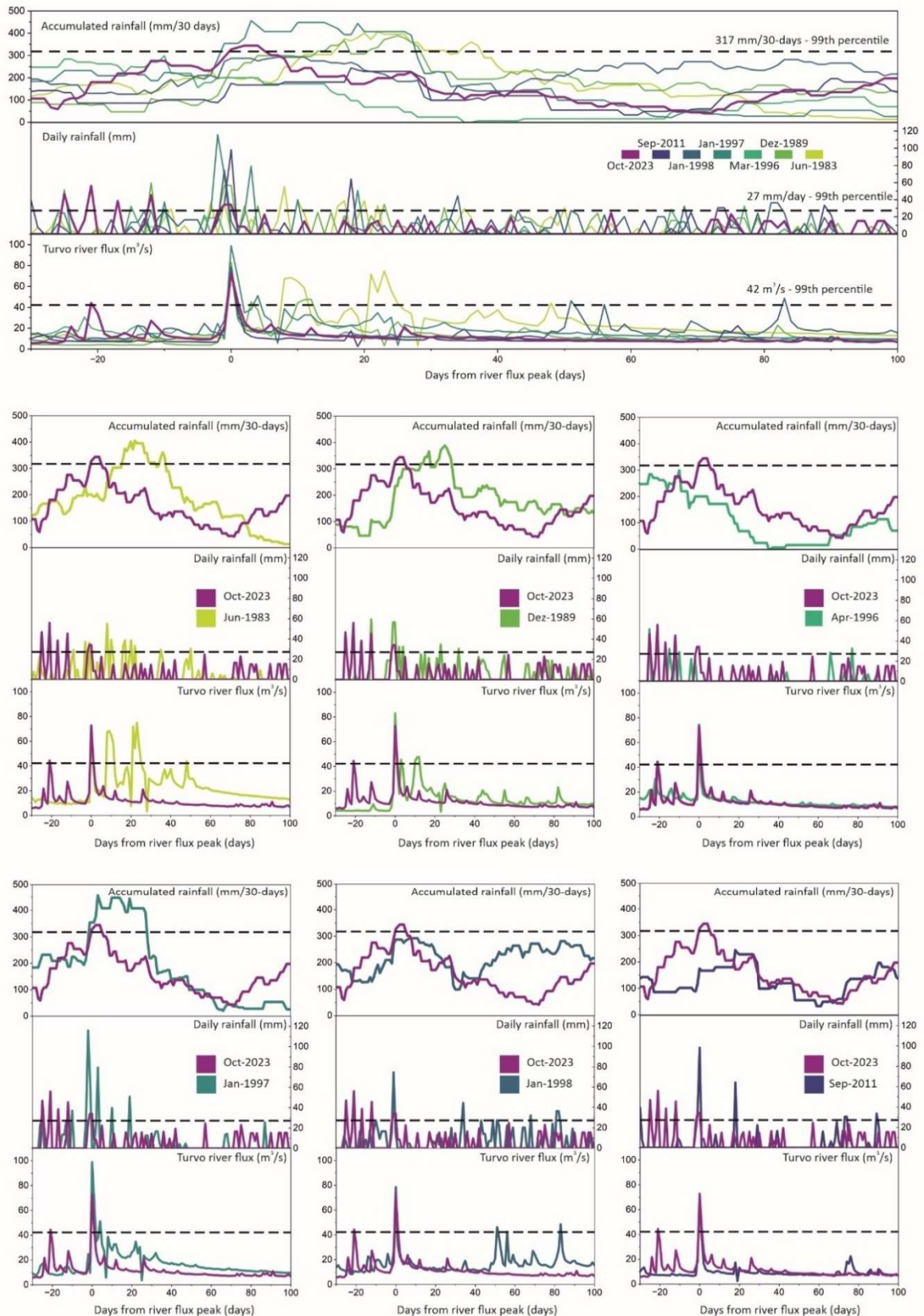
Supplementary Figure 3.1 - Cave flood events recorded in upper and lower gallery between June of 2019 and April of 2024. From top to bottom: Upper gallery water level; lower gallery water level (height of stalagmites collected indicated by continuous black line); daily maximum discharge from Turvo river fluviometric station; accumulated rainfall (mm/30-days) extracted from CHIRPS; daily rainfall extracted from CHIRPS.



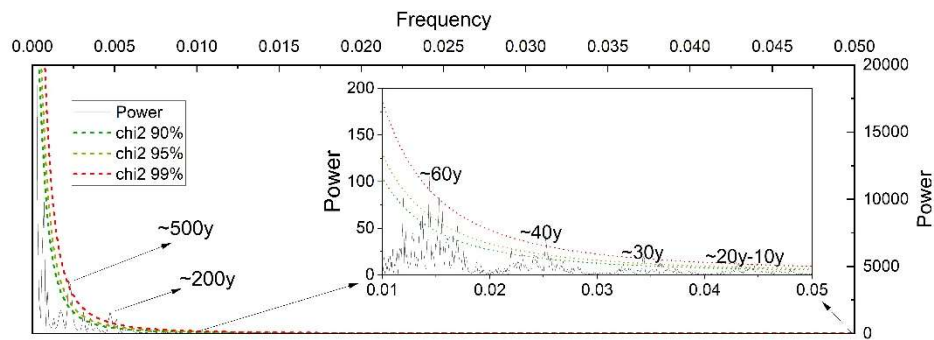
Supplementary Figure 3.2 - Stalagmite samples from Malfazido Cave. MFZ-10 and MFZ-11 were collected in the lower conduct. MFZ-N-1 was collected in the upper conduct. The overlapping growth period between the samples and MFZ-10 is shown by the black lines. Samples are plotted on identical spatial scales. Plot showing $^{230}\text{Th}/\text{U}$ ages and age-depth model obtained using StalAge.



Supplementary Figure 3.3 - Cave flood events recorded in the upper and lower gallery between June 2019 and April 2024. From top to bottom: Upper gallery water level; lower gallery water level (height of stalagmites collected indicated by continuous black line); daily maximum discharge from Turvo river fluviometric station; accumulated rainfall (mm/30-days) extracted from CHIRPS; daily rainfall extracted from CHIRPS. 99th percentiles (1980-2024) calculated for each time series indicated by dotted line.



Supplementary Figure 3.4 - Historical extreme discharge events related to ERE's on Turvo river with similar or higher magnitude than the event of October 2023. Each individual event is compared with October 2023. maximum daily discharge (Turvo river flux) from fluviometric station rio do Turvo (81125000). daily rainfall from chirps using parameter described in the section cave monitoring and instrumental data. Accumulated rainfall calculated using a 30-day bin prior to the date.



Supplementary Figure 3.5 – REDFIT analysis of Malfazido ERE record.

3.7.2. Supplementary Tables

Supplementary Table 3.1 - Cave flood events recorded in the lower gallery between 2019 and 2024. Rainfall accumulations (daily, 7-days and 30-days) from CHIRPs and percentile exceeded for the period between 1980 and 2024. Synoptic conditions with circulation mechanism indicated as cold fronts and interaction between low level jet and cold fronts (cold fronts +LLJ). The synoptic conditions were compiled from online reports from the Instituto de Desenvolvimento Rural do Paraná (IDR). Niño3.4 index obtained from <https://psl.noaa.gov/data/correlation/nina34.anom.data>.

Cave flood event						Rainfall and river discharge		99th percentile exceeded				Circulation mechanism	Niño 3.4 monthly index
Event	Start	Reach peak phase	End	Peak phase duration	Recession rate (m/day)	Rainfall acc. Prior to event (mm/30-days)	Peak river discharge (m3/s)	Max daily discharge	Daily rainfall	7-days acc.	30-days acc.		
Jun-19	03.Jun. 2019	05. Jun. 2019	16. Jul. 2019	1 day	41 days	0.04	37		>99th	>99th		Cold fronts	0.45
Dec-22	12. Dec. 2022	15. Dec. 2022	03. Jan. 2023	1 day	19 days	0.07	42			>99th		Cold fronts + LLJ	-0.85
Oct-23	28. Oct. 2023	29. Oct. 2023	07. Feb. 204	81 days	20 days	0.064	72	>99th	>99th	>99th	>99th	Cold fronts + LLJ	2.02
Mar-24	21. Feb. 2024	24. Feb. 2024	04. Mar. 2024	1 day	9 days	0.04	36		>99th	>99th		Cold fronts + LLJ	1.13

Supplementary Table 3.2– MFZ-10 $^{230}\text{Th}/\text{U}$ ages and activity ratios. The activity ratios were used to calculate the correction factor following the method of Budsky et al. (2019b). Corrected ages are reported in kyr B.P., with 0 corresponding to the year of analysis (2023).

Sample	^{238}U [μg/g]	±	$(^{230}\text{Th}/^{232}\text{Th})$	±	$(^{234}\text{U}/^{238}\text{U})$	±	$(^{230}\text{Th}/^{238}\text{U})$	±	age corr.[a]	error [a]	age uncorr. [a]	error [a]	dft [cm]
MFZ-10-D2	1.494	0.0092	1.7851	0.0085	1.15207	0.00031	0.007531	0.000037	0.39	0.16	0.715	0.0035	21.78
MFZ-10-D3	0.955	0.0071	4.4664	0.0284	1.29669	0.00549	0.009846	0.000076	0.68	0.08	0.8309	0.0073	34.98
MFZ-10 C7	1.134	0.0072	3.115	0.0146	1.15083	0.00035	0.014256	0.000069	1.01	0.17	1.3589	0.0066	49.685
MFZ-10 B9	1.251	0.0078	24.0556	0.1041	1.15344	0.00037	0.013672	0.00006	1.26	0.02	1.2999	0.0057	72.835
MFZ-10 D31	0.884	0.0053	3.7498	0.0177	1.14618	0.00028	0.020891	0.000099	1.58	0.22	2.0052	0.0096	84.76
MFZ-10 D32	1.148	0.007	2.4577	0.0071	1.14441	0.00026	0.029768	0.000086	1.94	0.48	2.8725	0.0083	95.48
MFZ-10 C6	0.675	0.0043	7.4078	0.0327	1.42853	0.00121	0.025684	0.000118	1.76	0.11	1.9767	0.0092	97.695
MFZ-10 C4	1.63	0.0106	8.1192	0.0221	1.15048	0.00035	0.023091	0.000067	1.99	0.11	2.21	0.0065	115.475
MFZ-10 D33	1.846	0.0115	6.8946	0.0178	1.16179	0.00064	0.024651	0.000064	2.07	0.13	2.3376	0.0063	127.42
MFZ-10-D4	1.709	0.0105	40.0983	0.1088	1.15048	0.00023	0.025288	0.000071	2.37	0.02	2.4225	0.007	134.21
MFZ-10 B8	1.913	0.0118	44.8755	0.104	1.15427	0.00031	0.027632	0.000069	2.59	0.02	2.6408	0.0068	146.45
MFZ-10 D34	1.949	0.0122	12.3751	0.0211	1.15564	0.00036	0.037337	0.000064	3.35	0.11	3.5788	0.0063	175.47
MFZ-10 B7	2.796	0.0176	45.0091	0.1122	1.15132	0.0005	0.033692	0.000089	3.18	0.03	3.2367	0.0088	186.26
MFZ-10 C1	1.618	0.0106	58.54	0.0998	1.15257	0.00036	0.037183	0.000073	3.53	0.03	3.5735	0.0072	204.56
MFZ-10 B6	1.996	0.0125	124.7271	0.2817	1.15933	0.00032	0.038292	0.000093	3.64	0.01	3.6599	0.0088	219.535
MFZ-10 D35	1.075	0.0069	27.856	0.0766	1.15477	0.00027	0.040642	0.000112	3.79	0.06	3.9041	0.0111	237.34
MFZ-10 C3	1.199	0.0084	11.7302	0.026	1.14556	0.00031	0.043844	0.000106	3.97	0.14	4.2521	0.0105	249.18
MFZ-10 C2	1.476	0.0098	59.5505	0.0959	1.15362	0.00032	0.04657	0.000088	4.43	0.03	4.4895	0.0088	274.975
MFZ-10 B4	1.489	0.0095	16.2423	0.06	1.15387	0.0006	0.055531	0.00021	5.11	0.13	5.3729	0.0205	325.075
MFZ-10-D5	1.019	0.5135	43.67	0.1035	1.14716	0.00032	0.055439	0.00014	5.3	0.05	5.3961	0.0139	342.82
MFZ-10 B3	1.434	0.0088	40.6157	0.1965	1.15068	0.00085	0.059623	0.000292	5.68	0.06	5.7955	0.0293	378.295
MFZ-10 D37	0.823	0.0051	7.4217	0.016	1.14706	0.00029	0.065318	0.00014	5.71	0.34	6.3857	0.0143	387.32
MFZ-10-D6	1.247	0.0076	20.504	0.0408	1.15026	0.00029	0.066261	0.000145	6.22	0.12	6.4619	0.0146	413.905
MFZ-10 B2	1.223	0.0075	25.6934	0.1481	1.14949	0.00074	0.068196	0.000396	6.46	0.11	6.6608	0.0399	429.59
MFZ-10 B1	1.207	0.0076	22.7273	0.0645	1.15429	0.00041	0.07231	0.000216	6.8	0.12	7.0448	0.0217	468.005

Supplementary Table 3.3 – MFZ-11 ²³⁰Th/U ages and activity ratios. Corrected ages are reported in kyr B.P., with 0 corresponding to the year of analysis (2023).

Sample	²³⁸ U [μg/g]	±	(²³⁰ Th/ ²³² Th)	±	(²³⁴ U/ ²³⁸ U)	±	(²³⁰ Th/ ²³⁸ U)	±	age corr.[ka]	error [ka]	age uncorr. [ka]	error [ka]	dft [mm]
MFZ-N-11 T	0.6774	0.0044	6.411	0.028	1.28517	0.0003	0.01537	0.00007	1.148	0.082	1.3117	0.0056	4.8
MFZ-N-11 B	0.2615	0.0014	15.137	0.091	1.21217	0.0005	0.02465	0.00015	2.121	0.060	2.2386	0.0133	124.59
MFZ-N-11 40mm	0.2671	0.0016	11.541	0.078	1.31789	0.0005	0.01639	0.00011	1.27	0.048	1.364	0.0092	35.25
MFZ-N-11 65mm	0.3099	0.0019	3.724	0.146	1.14984	0.0005	0.02367	0.00092	1.782	0.259	2.267	0.0884	66.74
MFZ-N-11 100mm	0.5395	0.0033	9.658	0.049	1.16429	0.0005	0.02371	0.00012	2.057	0.092	2.2422	0.0116	98.19

Supplementary Table 3.4 – MFZ-N-1 ²³⁰Th/U ages and activity ratios. The activity ratios were used to calculate the correction factor following the method of Budsky et al. (2019b). Corrected ages are reported in kyr B.P., with 0 corresponding to the year of analysis (2019).

Sample	²³⁸ U [μg/g]	±	(²³⁰ Th/ ²³² Th)	±	(²³⁴ U/ ²³⁸ U)	±	(²³⁰ Th/ ²³⁸ U)	±	age corr.[ka]	error [ka]	age uncorr. [ka]	error [ka]	dft [mm]
MFZ-N1-1	1.8176	0.032	0.00012	0.000072	1.0251	0.0219	0.0002	0.0001	0.012	0.011	0.023	0.008	1
MFZ-N-1-3	1.4378	0.007	0.000083	0.000043	1.104	0.0029	0.0002	0.0001	0.015	0.006	0.023	0.003	3
MFZ-N1-13	1.5976	0.003	0.000236	0.000045	1.1057	0.002	0.0007	0.0001	0.047	0.015	0.065	0.008	13
MFZ-N1-27	1.873	0.006	0.00011	0.000014	1.1018	0.0032	0.001	0.0001	0.087	0.01	0.096	0.008	27
MFZ-N1-32	2.9572	0.008	0.000166	0.000016	1.1069	0.0022	0.0012	0.0001	0.103	0.012	0.116	0.007	32
MFZ-N1-36	1.9251	0.003	0.000048	0.000005	1.1051	0.0014	0.0013	0.0001	0.126	0.007	0.13	0.007	36
MFZ-N1-54	4.4434	0.007	0.000104	0.000007	1.1051	0.0015	0.0024	0.0001	0.228	0.012	0.236	0.01	54
MFZ-N1-62	4.045	0.006	0.000013	0.000001	1.1031	0.0015	0.0027	0.0001	0.267	0.003	0.268	0.003	62
MFZ-N1-80	5.0117	0.007	0.000014	0.000001	1.1062	0.0013	0.0033	0.0001	0.326	0.003	0.327	0.003	80
MFZ-N1-91	6.0713	0.01	0.000054	0.000002	1.1065	0.0014	0.0039	0.0001	0.383	0.007	0.387	0.006	91
MFZ-N1-102	2.5121	0.003	0.000185	0.00001	1.109	0.0015	0.0048	0.0002	0.459	0.019	0.474	0.016	102
MFZ-N1-114	1.3373	0.003	0.000211	0.000008	1.1066	0.0024	0.005	0.0001	0.473	0.016	0.489	0.011	114
MFZ-N1-129	2.9642	0.003	0.000025	0.000001	1.1044	0.0013	0.00566	0.0001	0.558	0.007	0.56	0.007	129
MFZ-N1-143	1.488	0.005	0.000433	0.00002	1.1028	0.0037	0.0069	0.0002	0.649	0.029	0.684	0.016	143
MFZ-N1-161	1.4871	0.005	0.001406	0.000054	1.1036	0.0031	0.0086	0.0002	0.738	0.084	0.852	0.023	161
MFZ-N1-190	3.0629	0.019	0.00077	0.000028	1.1029	0.0053	0.0097	0.0002	0.9	0.05	0.963	0.023	190

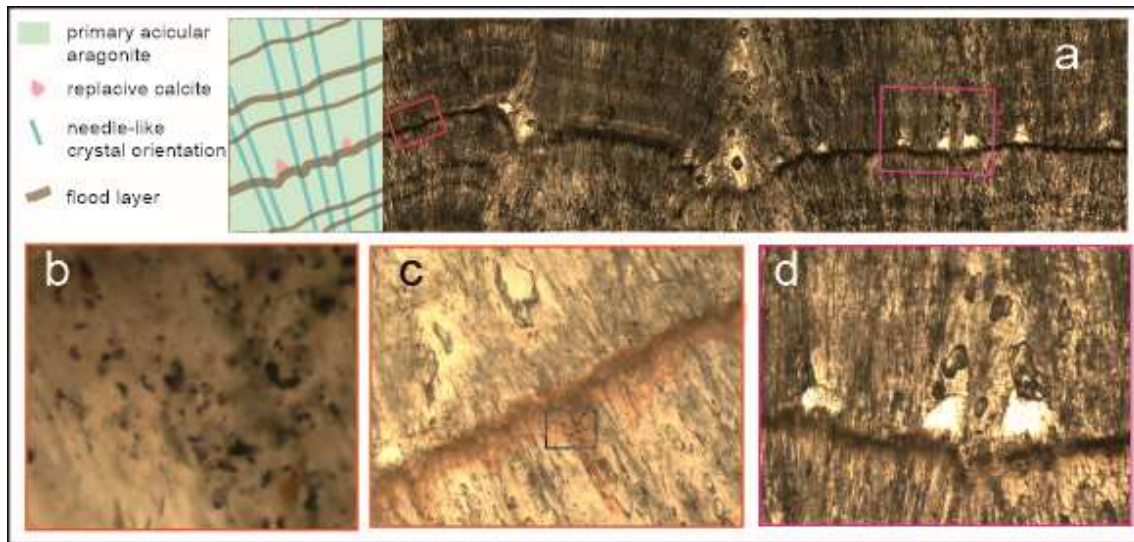
3.7.3. Supplementary Text 1

Thin section analysis of micro-detrital layers (flood layers) within the stalagmites

All stalagmites are composed of primary acicular aragonite fans, and needle-like crystals with restricted botryoidal aragonite fans observed close to the growth axis. Despite the frequent occurrence of micro-detrital layers within the stalagmites, the thin section analysis (Fig. 3) and the $^{230}\text{Th}/\text{U}$ -ages support continuous growth without any evidence for hiatuses.

The micro-detrital layers (flood layers) appear as stained zones (brown to grey), with detrital material deposited between aragonite needles (Fig. 3a, b). Detrital concentration varies significantly from the flanks to the center of the growth axis due to washing-off of detrital sediment by the drip water. In addition, higher accumulation of detrital material is observed in rugosity, depressions, or voids within the growth surface. The detritus includes opaque minerals (iron oxides) with a large range of size from 0.5 to 50 microns, a translucent rust-coloured amorphous phase, also varying within a large range, and aggregates of translucent amorphous phases with inclusions of opaques, ranging from several microns to millimetres at the flanks. Thin section analysis of flood sediment (mud samples cemented next to the base of the stalagmites) reveals similar detrital material, constituted by mud aggregates with high concentration of opaque minerals alongside residual of vegetal matter.

The aragonite needles cross the micro-detrital layers without signs of discontinuity or evidence of hiatus related to the flood events. New nucleation spots of micro aragonite fans are observed restricted to high detrital content spots. Replacive neomorphic rhombohedral calcite crystals are observed associated with micro-detrital layers, suggesting that the same event that transported the fine detrital grains triggered minor recrystallisation. MFZ-10 presents minor recrystallization zones that are visually distinct (e.g., translucent grey zones contrasting with milky aragonite fabric), bounded by detrital layers.



Chapter 4 – Manuscript II

Persistent Rainfall Seesaw Across Multi-Centennial Timescales over Southeastern and Southern Brazil

Julio Cauhy^{1,2*}; Marcela Eduarda Della Libera^{1,2}; Nicolás M. Stríkis^{3,4}; Mathias Vuille⁵; Francisco W. Cruz Junior³; Valdir F. Novello⁶; J.P Bernal⁷; Hubert Vonhof²; Denis Scholz¹

¹Institut für Geowissenschaften, Johannes Gutenberg-Universität Mainz, Germany

²Max-Planck-Institut für Chemie, Mainz, Germany

³Instituto de Geociências, Universidade de São Paulo, São Paulo-SP, Brazil

⁴Dept. Geoquímica, Universidade Federal Fluminense

⁵Department of Atmospheric and Environmental Sciences, University at Albany, State University of New York, Albany, New York, USA

⁶Institute of Geosciences, University of Brasília, Brasília – DF, Brazil

⁷Centro de Geociencias, Universidad Nacional Autónoma de México, Campus UNAM, Juriquilla, Querétaro 76230, México

Corresponding author: Julio Cauhy (cauhy.r@gmail.com)

Paper in preparation - a

4.1. Abstract

A leading mode of rainfall variability within the South American Summer Monsoon is the intraseasonal seesaw pattern of precipitation between Southeastern South America and Southeastern Brazil (SEBRA). This rainfall dipole has significant climatic and societal impacts, as its alternating wet–dry phases modulate rainfall distribution and influence flood and drought risks across two densely populated and agriculturally critical regions. The dipole mainly reflects variations in low-level moisture transport via the South American Low-Level Jet (SALLJ) and the South Atlantic Convergence Zone (SACZ), both modulated by Rossby wave propagation associated with the Pacific–South American (PSA) pattern. While this mechanism is well understood at intraseasonal scales, its expression over longer time scales and associated forcings remain poorly constrained. Here, we present new stalagmites high-resolution records (trace elements and stable isotopes) from Cristais and Malfazido Cave to reconstruct past hydroclimate conditions over SEBRA. Trace element ratios at Cristais Cave primarily reflect prior-calcite precipitation, providing robust indicators of local hydrological recharge, while $\delta^{18}\text{O}$ variations mainly track changes in atmospheric circulation between extratropical and monsoonal moisture sources. Our records reveal multi-centennial variability characterized by shifts between wet and dry conditions at the Cristais site, mainly associated with SACZ and Intertropical Convergence Zone (ITCZ) displacement. Comparisons the Botuverá Cave record (Southern Brazil; Bernal et al., 2016), reveals similar multi-centennial variability, but in opposite phase, evidencing a persistent dipole between SEBRA and Southern Brazil (SB) over the past 4,000 years. Principal component analysis of trace element ratios of each record allows us to reconstruct PCP-indices, and a dipole-index between SEBRA and SB is obtained by the difference between the PCP-indices. Therefore, positive phases of the dipole reflect wet conditions at SEBRA associated with enhanced SACZ while dry conditions are observed in BTV, associated to reduced SALLJ activity, while negative phases show the opposite. Comparison between the dipole and Antarctic summer temperature reconstructions (T. R. Jones et al., 2023) and a newly developed extreme rainfall event (ERE) record from Malfazido Cave (Cauhy et al., under review) indicates alternating dominance between tropical and extratropical forcings on the dipole and occurrence of ERE. During the beginning of Late Holocene, Antarctic–tropical teleconnections modulated both the dipole and ERE variability, whereas the last millennium was dominated by stronger tropical control linked to ENSO and SACZ dynamics.

4.2. Introduction

A leading mode of spatial rainfall variability within the South American Summer Monsoon (SASM) is the seesawing pattern of precipitation between Southeastern South America (SESA) and Southeastern Brazil (SEBRA) (Fig. 4.1b) (Aguirre-Correa et al., 2025; Boers et al., 2014; Gelbrecht et al., 2018). This rainfall dipole has profound climatic and societal significance: its opposing wet–dry phases modulate drought and flood risks across two densely populated and agriculturally productive regions (Boers et al., 2014). The dipole reflects a seesaw-like distribution of rainfall anomalies, in which enhanced convection and rainfall in SEBRA coincide with suppressed rainfall in SESA, and vice versa (Aguirre-Correa et al., 2025; Boers et al., 2014; Gelbrecht et al., 2018).

The dipole is fundamentally linked to changes in the strength and orientation of the northerly low-level jets (LLJ) that work as important moisture pathway from the Amazon Basin towards SEBRA/SESA (Fig. 4.1a) (Boers et al., 2014; C. Jones et al., 2023), supplying moisture to two key atmospheric features of the SASM: the South Atlantic Convergence Zone (SACZ) and the South American Low-Level Jet (SALLJ) (Fig. 4.1a). SACZ is a convective band extending southeastward from the Amazon toward Southeastern Brazil and protruding into the subtropical Atlantic Ocean (Carvalho et al., 2004). The moisture supplied to SACZ is in part related to the SALLJ, which is a northerly low-level flow on the eastern slopes of central Andes near Bolivia, transporting moisture toward SESA (C. Jones et al., 2023). The convective activity between SEBRA and SESA is governed by the trajectory of moisture after it crosses the Amazon Basin. After being deflected southward by the Andes moisture is carried toward SESA by a strong SALLJ, while eastward veering jet strength the SACZ activity and rainfall over SEBRA (Fig. 4.1) (Boers et al., 2014; C. Jones et al., 2023).

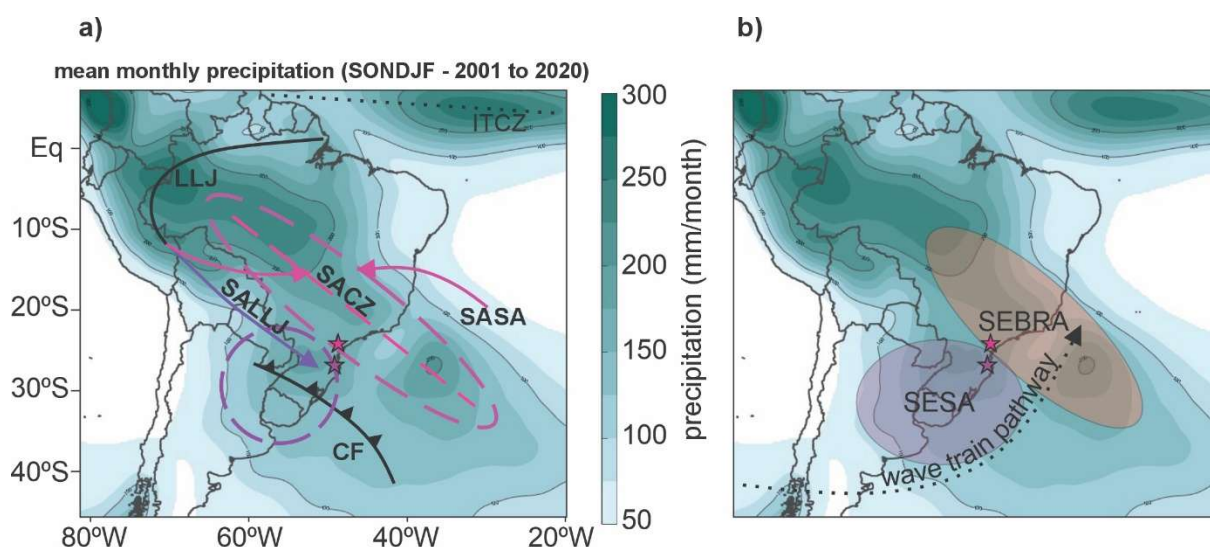


Figure 4.1 – Cave site locations and climatic settings. Pink (purple) star shows Cristais (Botuverá) cave location. Mean monthly precipitation during austral spring–summer (SONDJF), based on Global Precipitation Measurement Mission data (2001–2020; Huffman et al., 2023). A) Main atmospheric moisture pathways: black line indicates Low-

Level Jets (LLJ); pink line shows moisture source for the South Atlantic Convergence Zone (SACZ) and from the South Atlantic Subtropical Anticyclone (SASA) (Ferreira and Reboita, 2022) and purple line for South American Low-Level Jets (SALLJ) (Ferreira and Reboita, 2022). Pink and purple dashed ellipses indicate regions mainly influenced by SACZ (pink) and SALLJ (purple). The dashed pink line marks the SACZ axis. Black solid line with triangles indicates the advance of Antarctic cold fronts (CF). b) Colored Ellipses based on Boers et al. (2014) shows the South American Rainfall dipole, with pink area showing the dipole regions of Southeastern Brazil (SEBRA) and Southeastern South America (SESA). The dotted line shows the Rossby wave train pathway across South America.

The main mechanism driving the rainfall dipole is associated with the eastward propagation of Rossby wave trains along the Southern hemisphere mid-latitude jet as part of the Pacific South American (PSA) pattern (Aguirre-Correa et al., 2025; Boers et al., 2014; Gelbrecht et al., 2018). The Rossby wave trains propagate from the southern Pacific Ocean along the southern tip of the South American continent, veering northward to sub-tropical Atlantic Ocean (Fig. 4.1b). This results in alternating pressure waves (ridges and troughs) that modulates the large-scale circulation, affecting the direction of low-level moisture flow (Boers et al., 2014; Gelbrecht et al., 2018). Their passage modulates the SALLJ, increasing moisture transport toward SESA (wet phase) while suppressing moisture over SEBRA (dry phase) (Aguirre-Correa et al., 2025; Boers et al., 2014). In the subtropics, wave induced troughs trigger cold fronts that move northward. The influence of this frontal system reinforces atmospheric patterns responsible for dry conditions in SEBRA (Boers et al., 2014).

This mechanism is well understood at intraseasonal timescales, where Rossby wave trains and their modulation of the SALLJ and SACZ clearly drive the South American rainfall dipole (Aguirre-Correa et al., 2025; Boers et al., 2014; Gelbrecht et al., 2018). However, at longer timescales its persistence and variability remain poorly investigated. For example, Bahr et al. (2021) explored a rainfall dipole-pattern between SACZ and SALLJ using a marine sediment core reflecting SACZ variability over eastern Brazil and a stalagmite trace-element record from Botuverá Cave in southern Brazil (SB) (Bernal et al., 2016). The author mainly attributes the rainfall variability in Eastern Brazil and the dipole to high northern-latitude origin transmitted via changes in Atlantic Meridional Overturning Circulation (AMOC) strength (Bahr et al., 2021). According to (Bahr et al., 2021), shifts in Atlantic heat distribution altered the South Atlantic Dipole (SAD) and Atlantic Multidecadal Oscillation (AMO), reinforcing the SACZ–SALLJ dipole, and weakened AMOC and North Atlantic cooling reduced SACZ activity, enhancing rainfall over SESA while driving drought in eastern Brazil (Bahr et al., 2021). These findings evidence that the rainfall dipole is not only a feature of sub-seasonal variability but can also emerge on longer timescales (Bahr et al., 2021). However, this interpretation is limited by its strong focus on Northern Hemisphere drivers, completely neglecting Southern Hemisphere forcings. Moreover, North Atlantic cooling and waken of AMOC in multi-centennial time scales was previously associated with increased SACZ rainfall (Strikis et al., 2011). Meier et al. (2022), further evidences the need to account for synoptic climatic features across the Southern Hemisphere on longer time scales, such as the Rossby wave trains. This wave trains impact

the position of cyclonic and anticyclonic circulation across South America and the South Atlantic, which dominates the moisture flux towards the realm of the SACZ and subtropical South America (Meier et al., 2022). Processes related to the modulation of Rossby wave train propagation, the balance between SACZ and SALLJ (Aguirre-Correa et al., 2025) and their potential role in sustaining or modulating the rainfall dipole at longer timescales remains poorly explored.

We present new high-resolution trace element ratio record from Cristais Cave located under SEBRA climatological domain, paired with a previously published trace element record from Southern Brazil (SB), Botuverá cave (Bernal et al., 2016), located under SESA climatological domain. At both sites, prior calcite precipitation (PCP) is the dominant process controlling trace element variability, making these records robust indicators of local hydrological recharge. They cover the past 4,000 years and provide a unique framework to investigate the Late Holocene evolution of the SESA–SEBRA rainfall dipole. Moreover, new annually solved seasonal Antarctic temperature record (T. R. Jones et al., 2023) allow us to access how Southern Hemisphere forcings impact the long-term variability over the SESA-SEBRA rainfall dipole.

4.3. Materials and methods

4.3.1. Cave site and stalagmite samples

The study area is situated within the transitional zone between Southern Brazil (SB) and Southeastern Brazil (SEBRA), in the region between the major capitals São Paulo and Curitiba, approximately 300 km north of Botuverá Cave (Supp. Fig. 4.1) (BTV; Bernal et al. (2016)). This area lies in the exit region of the SACZ and close to the boundary region affected by SALLJ, within the limit of the SEBRA dipole region (Fig. 1b) (Boers et al., 2014). In contrast, Botuverá Cave is located further south, within the region more directly influenced by the SALLJ and within the dipole area under influence of SESA climate (Boers et al., 2014; Ferreira and Reboita, 2022).

The stalagmite CR-1 (Supp. Fig. 4.2) was collected from Cristais Cave (24°26'32.55"S, 48°36'9.57"W; 600 m a.s.l.) (Supp. Fig. 4.1), which is developed within the metalimestones of the Bairro da Serra Formation (Lajeado Group) (Paula-Santos et al., 2021). The cave is located between the municipalities of Iporanga and Apiaí, near the Alto Ribeira State Park (PETAR) in southern São Paulo State. The stalagmite MFZ-N-1 was collected while still actively growing in 2019 from Malfazido Cave (24°39'34.6"S, 49°32'27.5"W; 885 m a.s.l.), formed within metadolomites of the Itaiacoca Formation (Supp. Fig. 4.1). This cave is located near the municipality of Dr. Ulysses, approximately 60 km west of Cristais Cave, in Paraná State, southern Brazil. The sample was previously dated by Cauhy et al. (under review). Stalagmite

CR-1 is a 282 mm long calcite speleothem (Supp. Fig. 4.2) that was collected while active in 2007. MFZ-N-1 is a 210 mm-long aragonite stalagmite (Supp. Fig. 4.2) collected while active in 2019. CR-1 was previously dated and analysed for stable isotopes and the $\delta^{18}\text{O}$ record was partially shown in Vuille et al. (2012) and Novello et al. (2018), although the complete results were never described and published. CR-1 records continuous growth throughout the Late Holocene (4,200 B.P. to present), covering the interval between its collection date (–57 B.P., 2007 C.E.) and 4170 B.P. (Supp. Fig. 4.2), with a median growth rate of 0.07 mm yr^{-1} . The sample was previously dated by Cauhy et al. (under review) and now is analysed for stable isotopes here, and records continuous growth throughout the last millennium, covering the period from its collection date (–69 B.P., 2019 C.E.) to 831 B.P. (Supp. Fig. 4.2), with a relatively fast average growth rate of 0.2 mm yr^{-1} .

4.3.2. Trace-elements ratios and Principal Component Analysis

CR-1 was analysed for trace element ratios with calcium (TE/Ca) with sub-annual resolution at Centro de Geociencias, Universidad Nacional Autónoma de México (UNAM) using Laser-ablation Inductively Coupled Plasma Mass Spectrometer (LA- ICP-MS) with a Resonetics L-50 excimer laser-ablation workstation (ArF, $\lambda = 193\text{ns}$, 23ns FWHM, fluence of $\sim 6\text{J/cm}^2$). Details on the analytical protocols used here are described in (Bernal et al., 2016). The stalagmite chronology was established by $^{230}\text{Th}/\text{U}$ dating at the Geochronology Laboratory at the University of Minnesota (USA) following (Cheng et al., 2013). The age model was constructed using StalAge (Scholz and Hoffmann, 2011) assuming stalagmite top as actively growing during collection.

Principal Component Analyses (PCA) was applied to the speleothem trace-element ratios (Mg/Ca, Sr/Ca and Ba/Ca) dataset to reduce dimensionality and identify dominant modes of variability, which is particularly useful given that multivariate data can reflect multiple processes acting at different timescales (Jamieson et al., 2016). Prior to PCA, trace-element ratios were normalized to z-scores to remove sensitivity to variable scaling. Analyses were conducted in PAST v4.13 (Hammer, 2001), which provided principal component coefficients, scores, and explained variance. Statistical significance was assessed using a bootstrapping procedure (20,000 resamples, 95% confidence interval) and the broken stick model (Hammer, 2001). The same procedure was used for PCs of trace-element data from Botuverá Cave (Bernal et al., 2016).

4.3.3. $\delta^{18}\text{O}$ composite (MFZ-N-1 + CR-1)

The intra-site correlation model (iscam; (Fohlmeister, 2012) was used to construct a $\delta^{18}\text{O}$ composite record for CR-1 and MFZ-N-1. The method correlates dated proxy records from

contemporaneous stalagmites to derive a unified age–depth model and a single composite proxy series (Fohlmeister, 2012). The software assumes a common climatic signal among the input records and minimizes age uncertainties within overlapping intervals (Fohlmeister, 2012). For the composite, the age–depth modeling routine was set to point-wise linear interpolation, performing 10,000 Monte Carlo simulations on the absolute age determinations. To estimate the uncertainty of the composite age–depth model, 2,000 first-order autoregressive (AR1) processes were generated, with 1,000 Monte Carlo simulations for each AR1 process. Age data were treated as Gaussian distributed and calculated pointwise. The individual stalagmite records were arranged from the youngest to the oldest before compositing to maximize the correlation between overlapping intervals (Fohlmeister, 2012).

4.3.4. REDFIT analysis, wavelet coherence transforms (WCT) and Cross wavelet analyses

Spectral analyses were carried out using REDFIT and Wavelet module of Past v4.13 (Hammer 2001). The time-series are interpolated to evenly sampled in time considering the lower temporal resolution of each record using the function interpolate/extrapolate from software Origin v.2025. For trace element ratios, annually interpolated time series were used since all series present sub-annual resolution. These cross-wavelet analyses were made using the software MATLAB with routines based on the studies of Grinsted et al. (2004) and Torrence and Compo (1998), available at <http://www.glaciology.net/wavelet-coherence>.

4.4. Results

4.4.1. Stalagmite $\delta^{18}\text{O}$ and composite (MFZ-N-1 + CR-1)

The CR-1 trace element records have sub-annual resolution (average 0.07 years), Mg/Ca values range between 100–400 mmol/mol (mean = 260 mmol/mol), Sr/Ca between 35–200 mmol/mol (mean = 113 mmol/mol), and Ba/Ca between 0.1–1.3 mmol/mol (mean = 0.42 mmol/mol) (Fig. 4.2). Cross-plots in ln-space indicates prior-calcite precipitation (PCP) control: $\ln(\text{Mg}/\text{Ca})$ vs $\ln(\text{Sr}/\text{Ca})$ shows a strong positive correlation ($r = 0.75$, $p < 0.01$) with a slope of 0.72 ± 0.024 (Fig. 4.2b, c), while $\ln(\text{Sr}/\text{Ca})$ vs $\ln(\text{Ba}/\text{Ca})$ shows $r = 0.74$ ($p < 0.01$) with a slope of 1.148 ± 0.007 . Both slopes fall within the slope range expected for PCP control (Bernal et al., 2016; Sinclair, 2011; Wassenburg et al., 2020). Similar relationship between trace element ratios is observed in Botuverá Cave trace element ratios (BTV – (Bernal et al., 2016), with the TE/Ca covarying within expected PCP slopes as detailed described in Bernal et al. (2016).

We calculate principal component analysis for CR-1 using TE/Ca (Mg/Ca, Sr/Ca and Ba/Ca) aiming to deconvolute the signal of PCP from other potential processes affecting individuals et/Ca variability (Jamieson et al., 2016). We calculate a statistically significant PC1 for CR-1

with eigenvalues of 2.24457, accounting for 74.819% of the variance. CR-1 PC1 shows strong positive correlation with all the TE/Ca series (Mg/Ca $r=0.83$; Sr/Ca $r=0.94$; Ba/Ca $r=0.81$) (Fig. 4.2c) and weak positive correlation with $\delta^{18}\text{O}$ ($r=0.15$, $p<0.01$) and $\delta^{13}\text{C}$ ($r=0.20$, $p<0.01$). Despite the weak correlation, $\delta^{13}\text{C}$ shares a similar multi-centennial variability throughout the record (Supp. Fig. 4.4b). For BTV (Bernal et al., 2016), PC1 has an eigenvalue of 2.00 (66.8% variance explained) and also correlates strongly with Mg/Ca ($r = 0.74$), Sr/Ca ($r = 0.90$), and Ba/Ca ($r = 0.80$) (Supp. Fig. 4.4a). BTV PC1 shows a moderate positive correlation with $\delta^{13}\text{C}$ for the Late Holocene ($r = 0.49$, $p<0.01$) (Supp. 4.4a) and weak correlation with $\delta^{18}\text{O}$ ($r=0.29$, $p<0.29$).

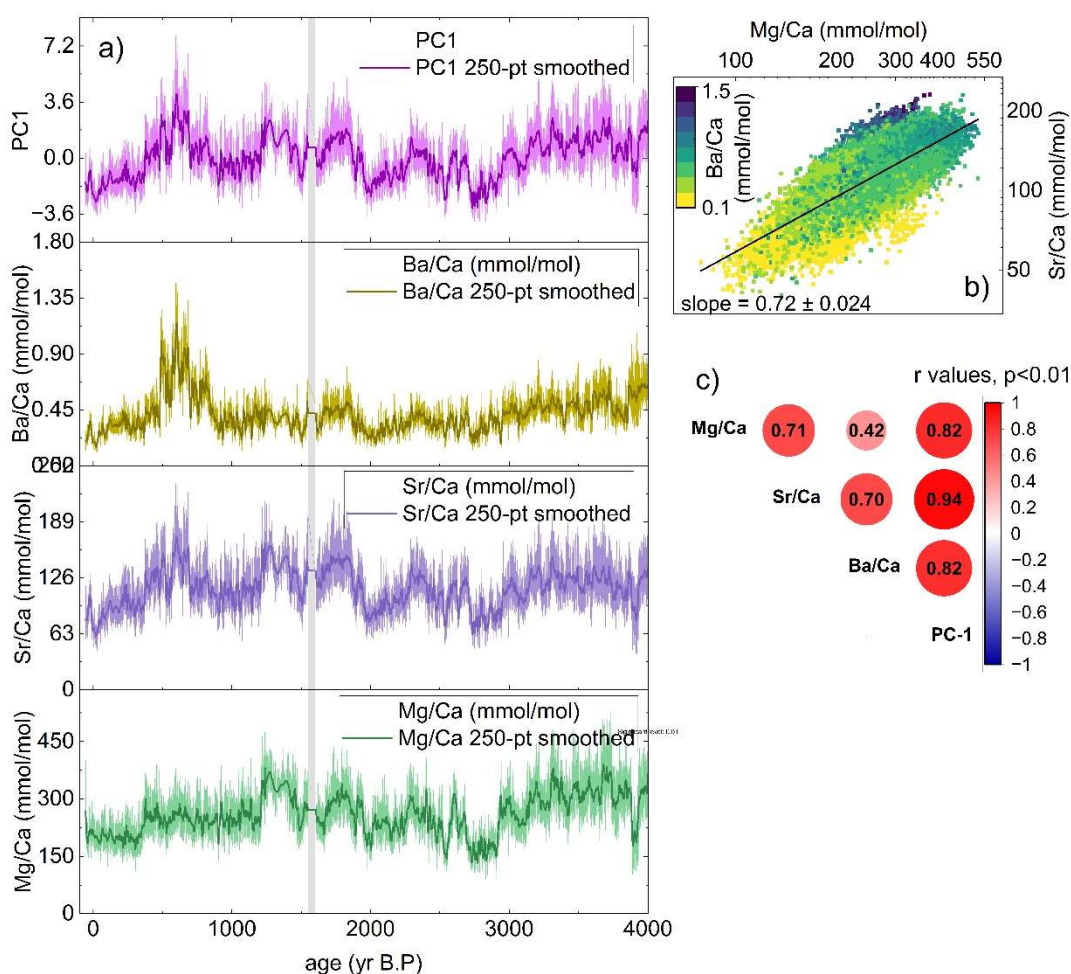


Figure 4.2 – Trace element ratios of CR-1 and PC-1. The panel a) shows the trace element ratios and PC-1 of CR-1. Grey bar shows the data gap interval between sample pieces broken during sample preparation. b) shows the cross plot between Mg/Ca and Sr/Ca in ln-space with linear fit represented by black line and color map showing Ba/Ca concentration. c) shows correlation matrix between trace element ratios and PC-1.

4.4.2. Stalagmite trace element ratios and Principal Components

The CR-1 and MFZ-N-1 stable isotope records ($\delta^{18}\text{O}$ and $\delta^{13}\text{C}$) consists of 1528 and 1138 points of analysis covering the entire Late Holocene (LH), with the CR-1 record ranging from -57 to 4175 B.P, with a mean resolution of 2.9 years, and MFZ-N-1 record from -68 to 868 B.P,

with mean resolution of 0.9 yrs. The $\delta^{13}\text{C}$ record of CR-1 ranges from -4.0 to -10.3‰, with mean values of -7.32‰, and $\delta^{18}\text{O}$ ranges from -2.2 to -7.7‰ with mean values of -5‰, with a moderate positive correlation between $\delta^{13}\text{C}$ and $\delta^{18}\text{O}$ of 0.5 ($p < 0.001$) (Fig. 4.3). MFZ-N-1 $\delta^{18}\text{O}$ and $\delta^{13}\text{C}$ are mostly around the same interval of CR-1, with $\delta^{13}\text{C}$ showing values around -1.4 to -8.7‰ with some few values reaching extremes (1 to -12‰), while $\delta^{18}\text{O}$ ranges from -2.6 to -7 ‰, and showing a weak positive correlation between $\delta^{18}\text{O}$ and $\delta^{13}\text{C}$ of 0.35 ($p < 0.001$) (Fig. 4.3e).

The composite record of MFZ-N-1 and CR-1 stalagmites $\delta^{18}\text{O}$, results in a continuous record covering the past ~4100 years (Fig. 4.3b, Supp. Fig. 4.3b). The correlation between each measure $\delta^{18}\text{O}$ stalagmite time series is 0.9, significant at the 95% level (Supp. Fig. 4.3). The composite is composed by 2665 $\delta^{18}\text{O}$ measurements, with an average temporal resolution of ~1.5 years. The composite $\delta^{18}\text{O}$ record ranges from -3 to -9 ‰ with average value of -5‰.

Overall, the composite record shows a decrease in $\delta^{18}\text{O}$ values from the start of the Late Holocene towards 2700 B.P (Fig. 4.3b), where $\delta^{18}\text{O}$ present a slight increase in variability (Fig. 4.3d) with some abrupt excursions on $\delta^{18}\text{O}$ values around 2800 and 2700 B.P, coinciding with Bond event 2 (Fig. 4.3b) (Bond et al., 2001; Strikis et al., 2011). This trend is followed by a period of stability towards the last millennium (Fig. 4.3b). The last millennium presents a significant increase in $\delta^{18}\text{O}$ variability with peak increase during the Little Ice Age (400-100 B.P) with extreme $\delta^{18}\text{O}$ values around 327 B.P reaching -14‰ (Fig. 4.3b, d).

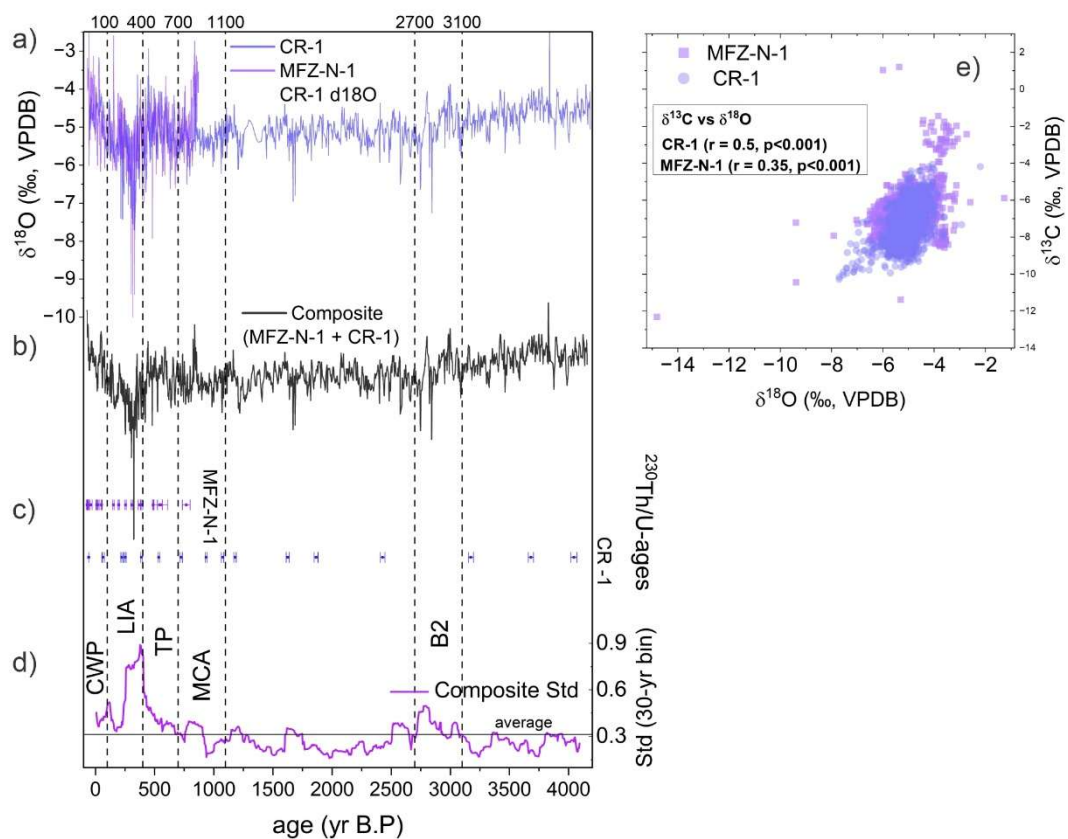


Figure 4.3 - $\delta^{18}\text{O}$ and $\delta^{13}\text{C}$ records and $\delta^{18}\text{O}$ composite. a) MFZ-N-1 and CR-1 $\delta^{18}\text{O}$ records; b) $\delta^{18}\text{O}$ composite record (MFZ-N-1 + CR-1); c) $^{230}\text{Th}/\text{U}$ -ages; d) running standard deviation (std) of $\delta^{18}\text{O}$ composite record with 30-yr bin; e) cross plot between $\delta^{18}\text{O}$ and $\delta^{13}\text{C}$ records of MFZ-N-1 and CR-1. The dashed lines represent climate anomalies of Bond 2 (B2 – Bond et al 2001), Medieval Climate Anomaly (MCA), Little Ice age (LIA), transition period between MCA and LIA (TP) and the current warm period (CWP).

4.4.3. Spectral analysis - REDFIT and continuous wavelet transform (CWT)

The REDFIT spectral analysis of the CR-1 $\delta^{18}\text{O}$ record (3-yr interpolated) reveals significant multi-centennial (594–519 yr), multidecadal (~30 yr), decadal (13–11 yr), and interannual (~6 yr) periodicities throughout the Late Holocene (Supp. Fig. 4.4). However, the Continuous Wavelet Transform (CWT) analysis does not confirm significant power in the multi-centennial band, except during the last millennium, where it lies outside the cone of influence and thus may be affected by edge effects (Hammer 2001) (Supp. Fig. 4.4). The CWT shows multidecadal to centennial variability (16-64 and ~128 yr) during the last millennium and between ~2700 B.P. and at the beginning of the Late Holocene. Persistent 23–11 yr periodicities, corresponding to known solar activity cycles are evident throughout the Late Holocene, showing stronger expression during the last millennium. Additionally, the wavelet analysis identifies an interannual band (8–6 yr), consistent with variability associated with ENSO-like forcing.

Similarly, the REDFIT analysis of the MFZ-N-1 $\delta^{18}\text{O}$ record, covering the last millennium, indicates significant multi-centennial variability (~468 yr), multidecadal (20 yr) to decadal (14–10 yr), and interannual variability (5–2 yr) (Supp. Fig 4.5). The CWT shows persistent multidecadal variability (~32–11 yr) and a consistent interannual signal (8–2 yr) (Supp. Fig. 5) supporting the presence of both solar and ENSO-related forcing mechanisms in the high-frequency component of the $\delta^{18}\text{O}$ variability.

The REDFIT analysis of the $\delta^{18}\text{O}$ composite record shows multi-centennial variability (596-521, 463 yrs) to centennial (149 yrs), and multi-decadal (24-20 yrs) to decadal (15-11 yrs), in agreement with the individual records (Supp. Fig. 4.6) The $\delta^{18}\text{O}$ composite CWT shows multi-decadal (~64 – 128 yrs) variability over the last millennium and over 2700 B.P. Persistent multi-decadal variability in the band of AMO (~64 yrs) is observed with lower expression between 2400-900 B.P., and multi-decadal to decadal periodicity is observed (64-12 yrs) is persistent through most of the Late Holocene.

CWT analysis of CR-1 trace-element ratios present persistent periodicities at interannual (3–8 years) and multi-centennial (128-500 years) timescales, which are also expressed in the PC-1_{CR-1} (Supp. Fig. 4.7). Similarly, the BTV record exhibits significant interannual to multidecadal variability (3-8 and 16-64 yrs), with Sr/Ca and Ba/Ca ratios showing strong periodicities in the 4–16 year, and Mg/Ca and Sr/Ca ratios with well-marked periodicities

at 16–64 years (Supp. Fig. 4.8). In addition, centennial to multi-centennial variability is evident in both Mg/Ca and Sr/Ca, with Mg/Ca in particular showing a more persistent signal in the 128–500-year range (Supp. Fig. 4.8).

4.5. Discussion

4.5.1. Prior-calcite precipitation indices as indicators of past rainfall variability

The strong covariation between Mg/Ca, Sr/Ca, and Ba/Ca ratios in Cristais and Botuverá caves indicates prior calcite precipitation (PCP) as the dominant process controlling trace-element variability (Bernal et al., 2016; Sinclair, 2011; Wassenburg et al., 2020). The first principal component (PC-1) of these ratios is therefore interpreted as a proxy for recharge conditions over the cave sites, reflecting degree of PCP. Accordingly, the PCP-indices (PCPCR-1-index and PCPBTV-Index) reflect effective rainfall above the cave sites, with positive values representing reduced recharge (drier conditions) and negative values indicating wetter conditions.

In SEBRA and SB region, the speleothem $\delta^{18}\text{O}$ variations primarily reflect shifts in moisture sources between tropical (monsoonal) versus extratropical (Bernal et al., 2016; Cruz et al., 2005; Vasconcelos et al., 2025; Vuille and Werner, 2005), with the tropical source being modulated by the degree of upstream rainout along tropical (Ampuero et al., 2020; Vuille and Werner, 2005). The PCPCR-1-Index covaries with $\delta^{18}\text{O}$ records from the SASM and SACZ domains (Supp. Fig. 4.9) (e.g., (Kanner et al., 2013; Libera et al., 2022; Novello et al., 2018), indicating persistent SACZ influence over Cristais Cave. In contrast, the PCPBTV-index present an antiphase relationship with these records, consistent with the modern rainfall dipole, in which enhanced SACZ activity suppresses SALLJ-related precipitation over southern Brazil (Boers et al., 2014).

Together, these PCP indices reveal a persistent hydroclimatic seesaw between Cristais and Botuverá cave regions, driven by shifts in the relative dominance of SACZ and SALLJ systems through the Late Holocene.

4.5.2. Southeastern Brazil Hydroclimate Variability over the Late Holocene

Overall, the $\delta^{18}\text{O}$ composite record presents a gradual decrease in $\delta^{18}\text{O}$ values from the beginning of Late Holocene (LH) to 2700 B.P (Fig. 4.4a, c), followed by a period of stability until the Last Millennium (Fig. 4.4a). During the Last Millennium the in $\delta^{18}\text{O}$ composite shows increased variability and pronounced shifts from the mean state such as observed during the Little Ice Age period (LIA – 100 – 400 B.P) and the Current Warm Period (CWP – 100 B.P to present) (Fig. 4.4d). The PCPCR-1-Index also present a negative trend from the onset of Late

Holocene until 2700 B.P, which is followed by multi-centennial shifts from wet to dry conditions. Wetter condition is predominant at the period between 3000 to 2000 B.P, while drier conditions are predominant between 2000 to 400 B.P, with the exception to the Medieval Climate Anomaly period (MCA – 700- 1100 B.P) that shows neutral to wet conditions (Fig. 4.4a). The LIA is also marked by a strong dry negative anomaly in PCPCR-1-Index but differently from the $\delta^{18}\text{O}$ composite, the negative trend persists through the CWP towards the present (Fig. 4.4b, d).

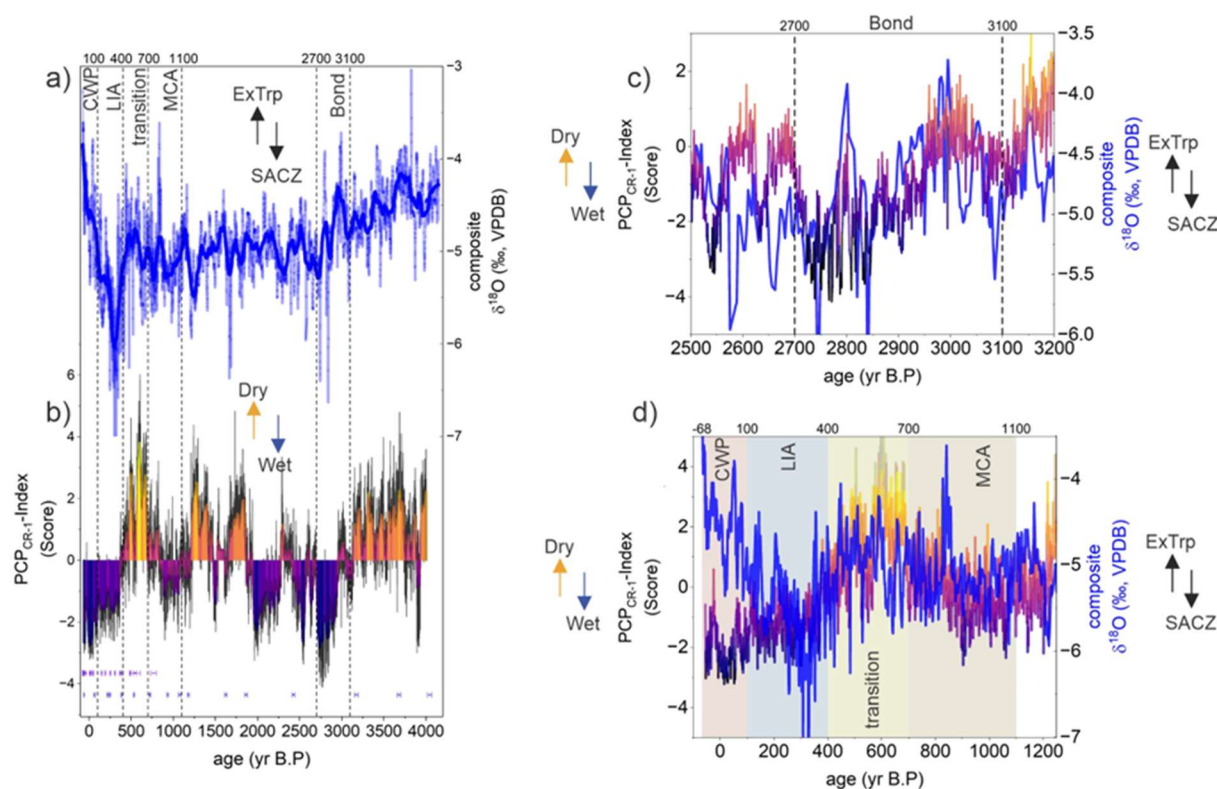


Figure 4.4 – SEBRA past hydroclimate conditions during Late Holocene. (a) Composite $\delta^{18}\text{O}$ record (MFZ-N-1 + CR-1), with major climate events indicated by dashed line; (b) PCPCR-1-index. (c) Close-up view of the Bond event; (d) Detail of the Last Millennium, with periods highlighted by colored intervals.

The beginning of Late Holocene presents an intensification of the SACZ activity over SEBRA indicated by coupled decrease in composite values from $\delta^{18}\text{O}$ and PCPCR-1-index from 4100 to 2700 B.P. The increasing SACZ activity during this period can be associated as result of the intensification of SASM over West to Southeast South America from the Mid-to-Late Holocene in response to the increased austral summer insolation (DJF), in accordance with the trend observed in Botuverá cave $\delta^{18}\text{O}$ record (Bernal et al., 2016). Around 2950 B.P., the PCPCR1-index presents an abrupt negative shift, marking the onset of the wettest period (lowest PCPCR1-index) of the Late Holocene. Moreover, the interval between 3100 and 2700 B.P. exhibits increased $\delta^{18}\text{O}$ variability with pronounced negative excursions that coincide with Bond Event 2 (Bond et al., 2001). This reflects the intensification of SACZ which is also recorded at other sites under its domain, as for example, in Lapa Grande $\delta^{18}\text{O}$ record (LG - (Strikis et al., 2011) and over SASM core region, as in Cuíca cave record (Supp. Fig. 4.9c) (PIM - Della Libera et al., 2022). These synchronous negative isotopic excursions, concurrent with

North Atlantic SST cooling events (Bond et al., 2001), indicate a strong teleconnection between the North Atlantic and tropical South American rainfall (Strikis et al., 2011). The influence of Bond events on the SACZ was previously discussed by Strikis et al. (2011) for Central Brazil, who proposed that centennial- to millennial-scale North Atlantic cooling intensified the northeasterly trade winds, promoting a southward displacement of the ITCZ and enhancing convection over the SACZ region. Although such events have been documented in $\delta^{18}\text{O}$ records from Central Brazil, the pronounced wet anomaly recorded in the PCPCR-1-Index further South is unprecedented, emphasizing the need to reconstruct complementary hydroclimate proxies to better resolve the expression of these events in South American rainfall regimes.

Following this event, predominantly wet conditions persisted in SEBRA until ~2000 B.P., interrupted by minor dry excursions at 2600 and 2420–2270 B.P (Fig. 4.4b). Around 2000 B.P., a sharp shift from wet to dry conditions marks the onset of a prolonged dry phase lasting until the beginning of the LIA (Fig. 4.4b). Within this interval, three main dry periods—1840–1700, 1400–1230, and 700–500 B.P.—are identified, with the latter corresponding to the transition between the MCA and the LIA, named here as Transition period (TP – 700 – 400 B.P) (Fig. 4.4b, d).

The MCA present as wet to neutral conditions over SEBRA, as indicate by slightly negative values in PCPCr-1-Index, with $\delta^{18}\text{O}$ values below the record average (Fig. 4.4a, d), in contrast with other $\delta^{18}\text{O}$ records from SACZ/SASM region such as from Jaragua $\delta^{18}\text{O}$ record (JAR – Novello et al., 2018) (Supp. Fig. 4.9h, j), Pau d’Alho $\delta^{18}\text{O}$ record (PDA – Novello et al., 2018) (Supp. Fig. 4.9f, j) and Cúica cave (Supp. Fig. 4.9c). All of these record shows weak SACZ/SASM activity in the onset of MCA and increase activity in the end of MCA (~700 B.P). Another $\delta^{18}\text{O}$ record located in the eastern Bolivian Andes that reflects SALLJ activity (BOTO – Apaéstegui et al., 2018) (Supp. Fig. 4.9g, j) aligns with the PCPCR-1-Index over the Last Millennium with a positive correlation with the PCPCR-1-Index of 0.54 ($p < 0.001$) (Supp. Fig. 4.9k) and with similar structure during MCA. PCPBTv-index also presents similar variability with PCPCR-1-Index during MCA, with SEBRA and Southern Brazil showing brief in phase behavior (Supp. Fig. 4.9i).

The transition period (850-450 B.P - Apaéstegui et al., 2018) marks a significant shift toward drier conditions, peaking around 600 B.P., characterized by weakened SACZ activity evidenced by increased composite $\delta^{18}\text{O}$ values (Fig. 4.4d). This period represents the driest conditions observed in CR-1 for the past 4100 yrs. This dry anomaly is not well documented in the $\delta^{18}\text{O}$ records being expressed as slightly increased $\delta^{18}\text{O}$ values in BOTO, Sao Matheus cave record (SMT; Della Libera et al., accepted) (Supp. Fig. 4.9e) and in our composite $\delta^{18}\text{O}$

(Fig. 4.4a). In contrast, BTV records a strong wet anomaly during the transitional period, evidencing one more time a strong antiphase pattern between SEBRA and Southern Brazil (Supp. Fig 4.9i). This arid phase is followed by a rapid shift towards wetter conditions at the onset of the LIA, when both $\delta^{18}\text{O}$ and PCPCR1-index exhibit pronounced negative excursions (Fig. 4.4d).

Orrison et al. (2022) attribute the LIA anomaly over Southeastern Brazil to a southwestward displacement of the SACZ during the LIA, associated with enhanced SASM convection triggered by volcanic and solar forcing. This resulted in increased rainfall and more depleted $\delta^{18}\text{O}$ values in southeastern Brazil, concurrent with a reduction in precipitation along the northeastern SACZ margin (Orrison et al., 2022). After the strongest composite $\delta^{18}\text{O}$ anomaly during LIA, the values present a positive trend towards the present showing the most positive values of the entire record during the CWP (Fig. 4.4a, d), while PCPCR1-Index continues to present wet conditions (Fig. 4.4b, d)—indicating a possible decoupling between isotopic and hydrological proxies, potentially driven by increased extratropical moisture incursions rather than weakened monsoon intensity.

Overall, the SEBRA region aligns closely with SACZ and SASM records throughout most of the Late Holocene, demonstrating that regional hydroclimate variability has been largely governed by large-scale atmospheric reorganizations within the SASM/SACZ regime. Periods of intensified SACZ activity correspond to enhanced SASM convection, often linked to increased austral summer insolation (such as the onset of LH) and teleconnections with North Atlantic climate variability (e.g 2700 B.P Bond event). Conversely, multi-centennial dry intervals, such as the prolonged drought after ~2000 B.P. and the Transition Period (~700–500 B.P.), reflect weakened SACZ influence associated with northward ITCZ displacements and possible reductions in AMOC strength (Bahr et al., 2021). Evidence of proxy decoupling during the Current Warm Period, suggesting a growing role of extratropical moisture incursions in shaping modern rainfall regimes. These results highlight the complex interplay between tropical and extratropical forcings in modulating SEBRA hydroclimate over the LH and underscore the value of multi-proxy reconstructions for disentangling the mechanisms behind past and ongoing hydroclimate variability in South America. Moreover, the SEBRA record reveals an antiphase relationship with southern Brazil, with intensification of SACZ and rainfall over SEBRA associated with reduced monsoon rainfall in Southern Brazil. This seesaw pattern is further discussed in detail in the next section.

4.5.3. Multi-centennial scale rainfall seesaw (SEBRA-SESA)

The new high-resolution PCP indices calculated for CR-1 and BTV evidence a persistent dipole pattern between SEBRA (CR-1) and Southern Brazil (SB) characterized by multi-centennial antiphase between recharge over Cristais and Botuvera Caves, which ultimately should reflect a seesaw pattern between effective rainfall over SB and SEBRA (Bernal et al., 2016) (Fig. 4.5 b, c). Because Cristais Cave lies within the exit region of the SACZ and Botuvera Cave is located at the transition between the SACZ and the SALLJ (Fig. 4.1), both sites are ideally positioned to capture the contrasting variability and interactions between these two key components of the SASM. At longer timescales, wetter conditions at Cristais cave (enhanced SACZ) coincide with drier phases at Botuvera (weakened SALLJ), and vice versa.

To better visualize the dipole pattern between the records, we define a dipole index as $PCP_{BTV}\text{-index} - PCP_{CR-1}\text{-index}$ (Fig. 4.5). The dipole index positive phases indicate predominantly wet conditions at SEBRA reflecting increased recharge in Cristal cave, with enhanced SACZ and weakened SALLJ (following the intraseasonal mechanism interpretation), while negative phases indicate opposite. That is, enhanced recharge at SB with enhanced SALLJ and weakened SACZ. This reflects shifts in the balance of low-level jet contributions (SACZ vs SALLJ).

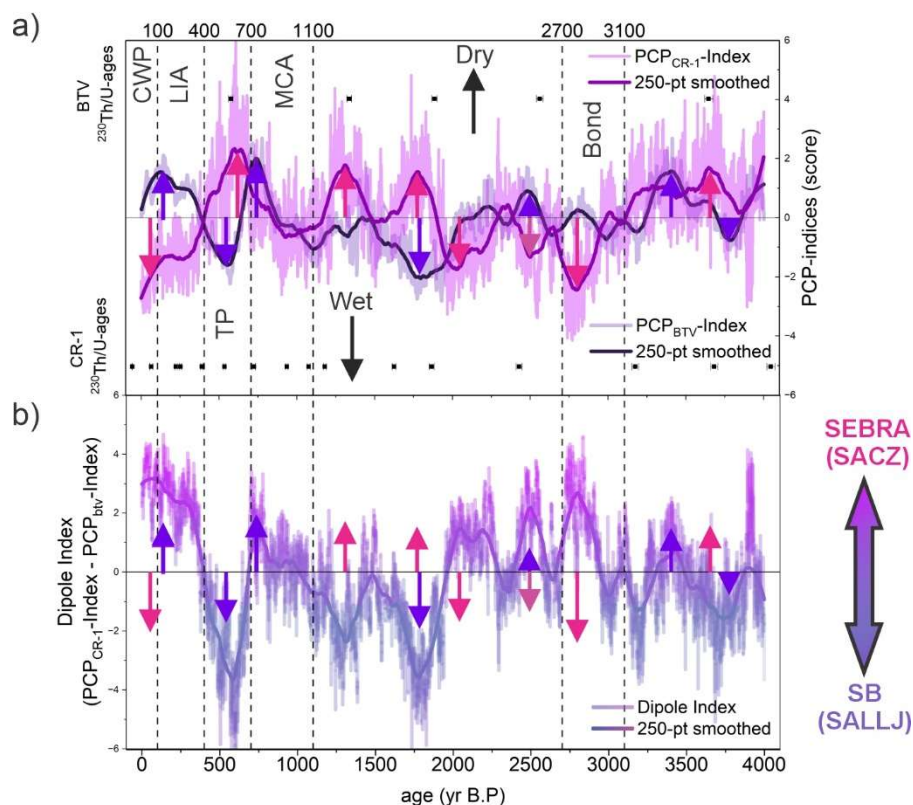


Figure 4.5 – a) PCP-indices from BTV and CR-1. Colored signs show the deviations from the mean of each index (pink for CR-1 and purple for BTV). These signs are then projected in b). b) Dipole-index between SEBRA-SB.

The dipole index shows strong positive phases (enhanced SACZ/suppressed SALLJ) between 2900-2700, 2580-2412, 2240-2000 B.P and from LIA to CWP (400-0 B.P) (Fig. 4.5b). Negative phases dominate between 4000–3000 BP and 2000–1100 BP, with strong negative phases between 2000-1600, 1400-1200 B.P and the most pronounced during the transition period (680-400 B.P) (Fig. 4.5b). Neutral phases (between 1 to -1) are observed mainly during the onset of Late Holocene (4000-3000 B.P), with predominantly negative values, and during the MCA (1100 – 680 B.P), indicating a relative in-phase pattern between the records (Fig. 4.5b). Most of the strong phases (positive and negative) were led by a dipolar pattern between the two PCP-indices. There are two exceptions to this pattern, one the period between 2900 to 2700 B.P, correspondent to Bond 2 event (Stríkis et al., 2011) that was led mainly by a pronounced strength in SACZ activity over SEBRA, and another during the strong negative phase between 1400-1200 B.P that mainly reflect a pronounced increase in PCP in CR-1 (Fig. 4.5a). The pronounced dipolar pattern during the Last Millennium (Fig. 4.5b) evidences the climate anomalies impact on the rainfall distribution over SEBRA and Southern Brazil, which highlight the deviations from the mean state of the monsoon systems during this period (Orrison et al., 2022).

4.5.4. Rainfall Seesaw Mechanism and Forcings

Under current climate setting, the SEBRA-SESA (Southeastern South America) rainfall dipole is well documented at intraseasonal timescales (Aguirre-Correa et al., 2025; Boers et al., 2014; Gelbrecht et al., 2018; S-Paegle and Mo, 1997; Tseng et al., 2023), where Rossby wave trains and their modulation of the SALLJ and the SACZ drive the dipole pattern (Aguirre-Correa et al., 2025; Boers et al., 2014; Gelbrecht et al., 2018). This dipole is mainly related to shifts in the low-level jet direction and intensity favoring SACZ or SALLJ and consequently causing a rainfall seesaw between the regions (Aguirre-Correa et al., 2025; Boers et al., 2014; Tseng et al., 2023). The influence of Southern Hemisphere variability on Rossby wave train propagation has been little-studied, which precludes the understanding of the dipole pattern through longer time scales during the Late Holocene. In this section we explore the forcings behind the multi-centennial dipole observed between SEBRA and SB, with mechanisms related to the modulation of Rossby wave trains impacts over south America, accounting for both Southern and Northern Hemisphere impact on the rainfall dipole.

Antarctic seasonal temperatures reconstructions from Western Antarctic ice cores (T. R. Jones et al., 2023) allow us to investigate the role of the southern hemisphere on the hydroclimate of South America, specially over regions highly influenced by extratropical forcing such as SB. We observe a striking agreement between SB rainfall (PCPBTV-index) and Antarctic summer temperatures (AST – δD , T. R. Jones et al., 2023) at annual to multi-

centennial time-scales ($r = 0.5$, $p < 0.01$) between 4000-1000 B.P ($r = 0.5$, $p < 0.01$) (Fig. 4.6c). Warmer ASTs indicated by higher ice core δD values are in agreement with drier conditions in Botuverá Cave and with positive phases of the dipole, with again, the exception to the strong positive phase related to Bond 2 event around 2700-2900 B.P (Strikis et al., 2011). In contrast, colder ASTs are associated with wet conditions in BTV and with negative phases of the dipole, with the strong negative phase of the dipole around 2000-1600 B.P synchronous to the strongest cooling event between 4000-1000 B.P. The striking agreement between the records evidences the influence of AST on rainfall over SB, with colder ASTs associated with enhanced rainfall over SB, and warmer AST showing the opposite effect.

These findings are in agreement with modern observations showing that Antarctic-tropical teleconnections driven by temperature gradients between SB and western Antarctic are linked to changes in atmospheric circulation associated with rainfall over SB, such as SALLJ, mesoscale convective systems, atmospheric blockings and SACZ (Carpenedo et al., 2023). Moreover, modern climatology studies show that temperature variability across Antarctica and South America can significantly impact large-scale atmospheric circulation patterns over South America (Carpenedo et al., 2023). These changes are mainly associated with the Rossby wave train pattern, one of the most important components associated with intraseasonal with the SALLJ-SACZ dipole (Aguirre-Correa et al., 2025).

In contrast, the last millennium presents a decoupling between ASTs and PCPBTV-index, during a strong shift towards colder ASTs similar to Early-to-Middle Holocene ASTs (7000-8000 B.P, (T. R. Jones et al., 2023). The last millennium is characterized by significant deviations from the mean state of SASM/SACZ with multi-centennial deviations from the mean state during LIA and MCA (Della Libera et al., 2022; Orrison et al., 2022). South-westward shifts in mean location of SACZ axis during the LIA resulting in enhanced moisture influx and convergence over the monsoon region with increased SACZ (Orrison et al., 2022) and suppressed SALLJ favouring a strong positive phase of the dipole. The decoupling between ASTs and rainfall over SB is accompanied by a strong coupling between ITCZ displacement (Utida et al., 2023) and the dipole index, with the southward position of the ITCZ reflecting increased rainfall over SEBRA (e.g LIA to CWP) and opposite conditions in SB, and northward displacement of ITCZ during the transition period showing drier conditions in SEBRA and wet anomalies in SB. Despite of the decoupling of the striking agreement between BTV and AST, cross wavelet analyses show a persistent covariation in the periodicity around 128yrs for the last millennium, and around 128-256 yrs for the rest of the period (supp. Fig. 4.10).

Moreover, the $\delta^{18}O$ records of MFZ-N-1 and CR-1 show a persistent interannual periodicity on ENSO timescales during the last millennium. Trace element ratios of CR-1 and BTV also

show significant interannual periodicities along Late Holocene. Together, these observations indicate a strong modulation of atmospheric circulation and hydroclimate variability probably related to Pacific forcing (ENSO) with enhanced activity during the last millennium. Moreover, multi-decadal variability also shows significance over the Late Holocene on $\delta^{18}\text{O}$ records of SEBRA, indicating a potential modulation of atmospheric circulation related to the Atlantic Multidecadal Oscillation (AMO). Solar cycles are present in both $\delta^{18}\text{O}$ (~11) and in the trace elements ratios (~250-500yr), with the multi-centennial persistent periodicity present in the trace element ratios and PCP-index in agreement with Novello et al (2017) that attributes multi-centennial modulation of the SASM through solar cycles.

Overall, our findings indicate that the multi-centennial SEBRA–SB rainfall dipole reflects a non-stationary interplay between tropical and extratropical forcings throughout the Late Holocene. Between 4000 and 1000 B.P., Antarctic–tropical teleconnections seem to have exerted a dominant control on rainfall variability over SB, with AST anomalies modulating Rossby wave propagation and influencing low-level jet dynamics and cold front activity over South America. In contrast, during major climatic anomalies such as the Bond 2 event and the LIA, the dipole was primarily driven by tropical mechanisms, particularly shifts in the ITCZ (Utida et al., 2023) and variations in the SASM/SACZ mean state (Orrison et al., 2022; Della Libera et al., 2022), which enhanced the positive phase of the dipole. The apparent decoupling between AST and rainfall over SB during the last millennium suggests a transition toward a regime dominated by tropical forcing, with enhanced ENSO and SACZ variability as key drivers of SEBRA hydroclimate. The $\delta^{18}\text{O}$ and trace element records further indicate that this shift was accompanied by strong modulation from both Pacific (ENSO) and Atlantic (AMO) variability, as well as multi-centennial solar forcing, consistent with the centennial-scale solar modulation of the SASM documented by Novello et al. (2016). Together, these results suggest a non-stationary interplay between tropical and extratropical drivers that modulated atmospheric circulation and rainfall distribution across South America, evidencing the combined influence of internal ocean–atmosphere variability (ENSO; AMO) and external (solar) forcing on long-term SEBRA–SB hydroclimate dynamics.

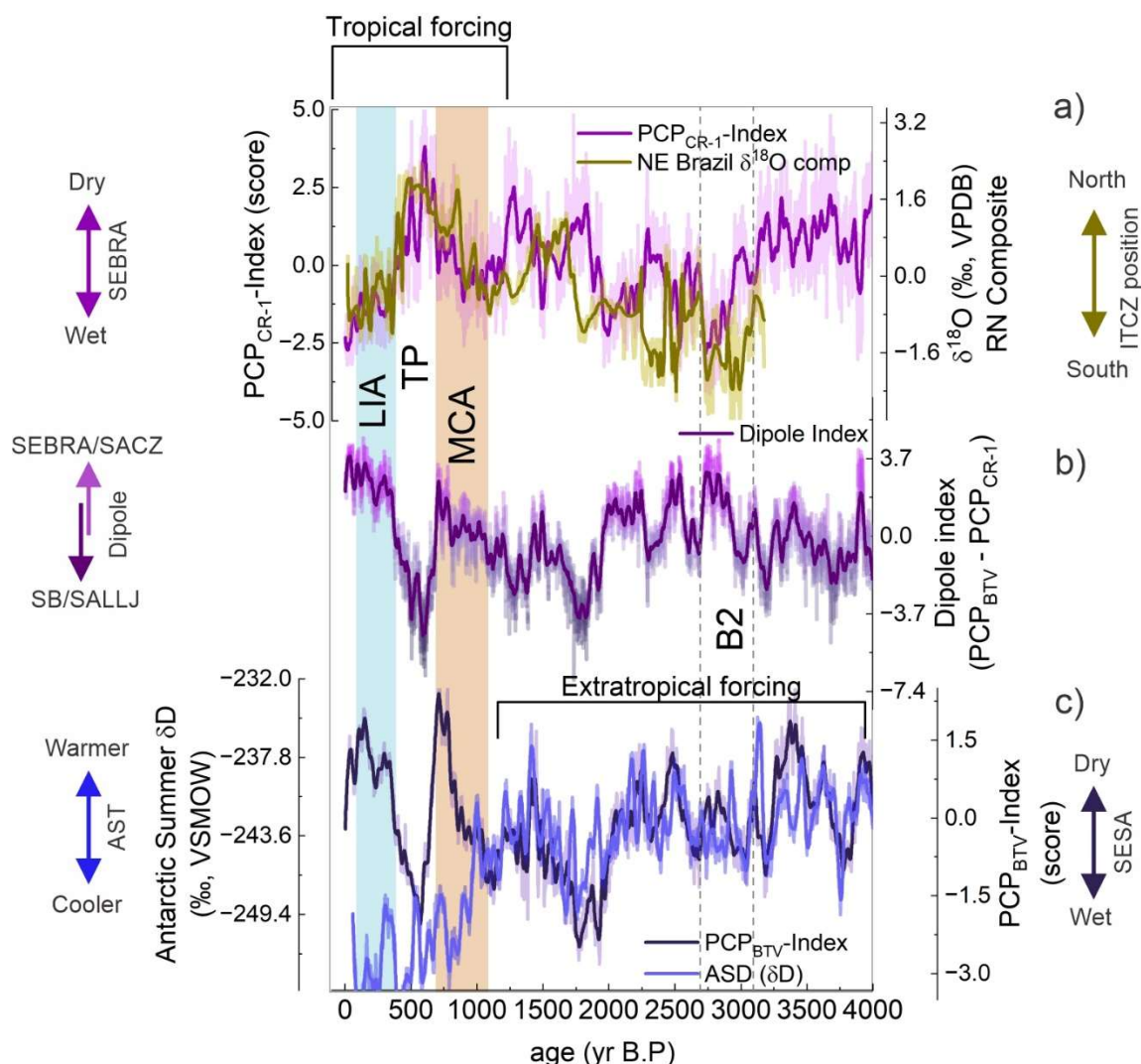


Figure 4.6- a) PCPCR-1-Index compared with ITCZ displacement (Utida et al., 2023); b) dipole-index; c) PCPBTV-Index compared with AST (Jones et al., 2023). Intervals indicated periods of dominance Extratropical or Tropical forcing.

4.5.5. SEBRA-SESA dipole and Extreme Events

The rainfall dipole and its expression on multi-centennial scales provide a more comprehensive understanding of the long-term hydroclimate variability across SEBRA and SB, as well as their impacts on extreme events such as prolonged droughts and flood activity. In this context, a recently published extreme rainfall reconstruction based on stalagmites from Malfazido Cave (MFZ; Cauhy et al., under review) offers a valuable opportunity to assess how hydroclimate variability over SEBRA has influenced the occurrence of extreme rainfall events (EREs) and to explore the dipole–ERE relationship through time.

Overall, the MFZ ERE record indicates an increase in ERE frequency during the onset of the Late Holocene, coinciding with dry conditions over SEBRA and a predominance of the negative phase of the rainfall dipole (Fig. 4.7b, d). This is followed by a pronounced suppressed period in ERE activity between 3000 and 2000 B.P., when positive dipole phases dominate, including

the strong positive phase during the Bond 2 event (2700–3100 B.P.), synchronous with the lowest ERE occurrence in the MFZ record (Fig. 4.7b, d). After this suppressed period, ERE frequency increases again after 2000 B.P., with a brief decline during the transitional phase (680–400 B.P.), and enhanced activity during both the LIA and the CWP (Fig. 4.7b, c).

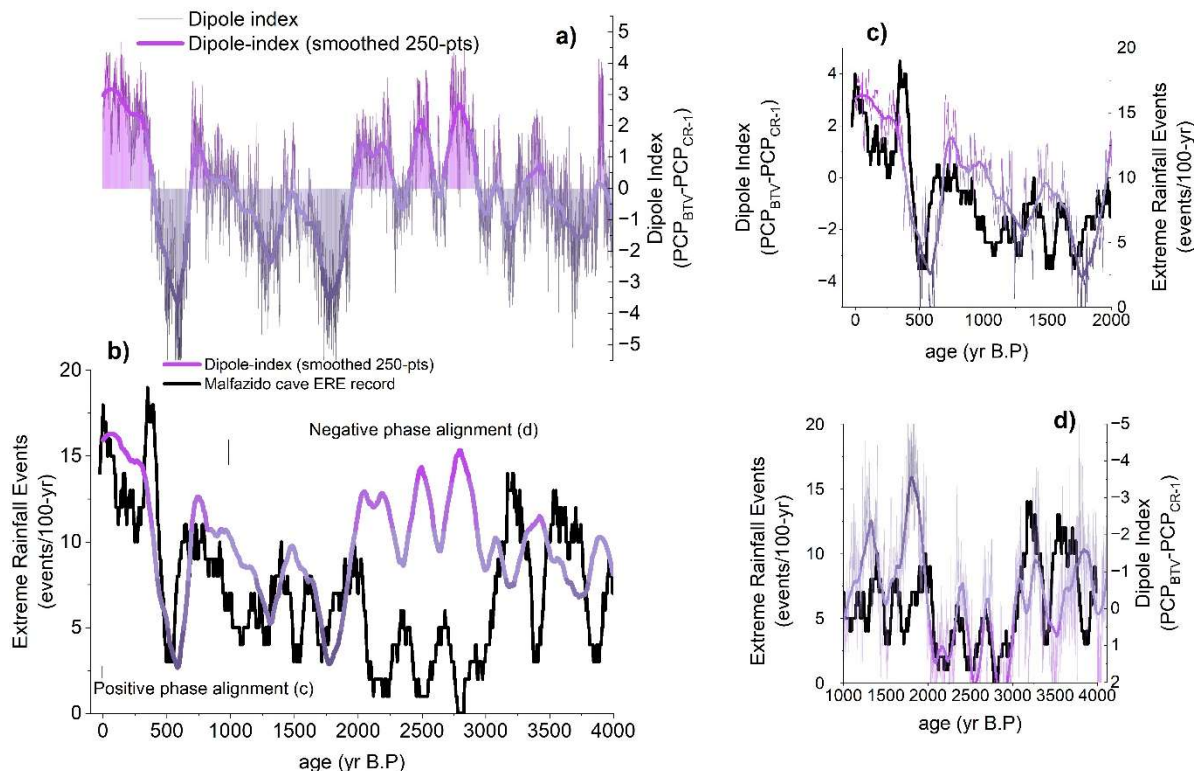


Figure 4.7 – Dipole-index and ERE occurrence (Cauhy et al., under review). a) Dipole-index with positive phases (SEBRA/SACZ) in pink and negative phases (SB/SALLJ) in purple; b) comparison with ERE record of Malfazido Cave (Cauhy et al 2025, under review) with c and d showing in detail the last millennium and the first part of Late Holocene, respectively.

During the last millennium, SEBRA hydroclimate aligns with the dipole-index and with ERE occurrence, where positive phases are associated with wetter conditions and enhanced ERE activity, while negative phases correspond to drier periods and reduced ERE occurrence (Fig. 4.7b, c). The EREs in Malfazido Cave are primarily triggered by circulation anomalies that enhance the transport of warm moist air from the Amazon Basin via low-level jets (Cauhy et al., under review; Cai et al., 2020; Reboita et al., 2021). When this moisture interacts with advancing cold fronts from the south, it creates favorable conditions for intense convection and extreme rainfall over the region (Cai et al., 2020; Boers et al., 2014). These circulation anomalies are linked to Rossby wave train propagation and are modulated by large-scale teleconnection patterns—particularly those associated with tropical Pacific variability during El Niño events and Antarctic–tropical interactions (Cai et al., 2020; Carpenedo et al., 2023; Reis et al., 2020).

The alignment of increased ERE activity with the negative dipole phase during the first part of the Late Holocene, when Antarctic summer temperature exerted a strong influence over SB

hydroclimate, suggests a greater role of extratropical forcing during this interval. Notably, during this time, regional hydroclimate conditions appear partially decoupled from ERE occurrence, as indicated by positive dipole phases coinciding with ERE suppression. In contrast, during the last millennium, SB hydroclimate became increasingly decoupled from Antarctic variability, with the dipole more strongly responding to tropical forcing. This shift coincides with the alignment of the dipole with ITCZ and SACZ displacement (Orrison et al., 2022; Utida et al., 2023), leading to close coupling between SEBRA hydroclimate variability, dipole phases, and ERE frequency. Cauhy et al. (under review) attribute the recent increase in ERE to a higher frequency of El Niño events. Our findings here suggest that hydroclimate conditions over SEBRA also play a key role, as indicated by the concurrent positive dipole phases, wetter conditions in CR-1, and enhanced SACZ activity associated with higher ERE rates.

Overall, the observed shifts in the dipole–ERE relationship evidences a non-stationary interplay between tropical and extratropical forcings influencing ERE occurrence across SEBRA and SB. Prior to the last millennium, extratropical influences—mediated by Antarctic–tropical teleconnections—dominated under weaker monsoon conditions, such as during the first part of Late Holocene. Conversely, during the last millennium, tropical mechanisms—particularly SACZ variability—seem to modulate ERE variability. Moreover, CWT and REDFIT analysis evidenced persistent interannual periodicities over the trace elements of CR-1, indicating ENSO modulation, and $\delta^{18}\text{O}$ of CR-1 and MFZ-N-1, indicating a persistent influence of ENSO over the atmospheric circulation of SEBRA, with enhanced activity over the last millennium.

The persistence of multi-centennial periodicities (~210–420 years) in both ERE (Cauhy et al., under review) and PCPCR-1-index suggests that solar forcing may have acted as an external pacing mechanism over hydroclimate of SEBRA through the Late Holocene, in accordance with Novello et al. (2016). Together, these findings emphasize that the rainfall dipole not only represents a key expression of regional hydroclimate variability but also plays a fundamental role in modulating EREs over long timescales, through non-stationary interactions between tropical and extratropical climate systems.

4.6. References

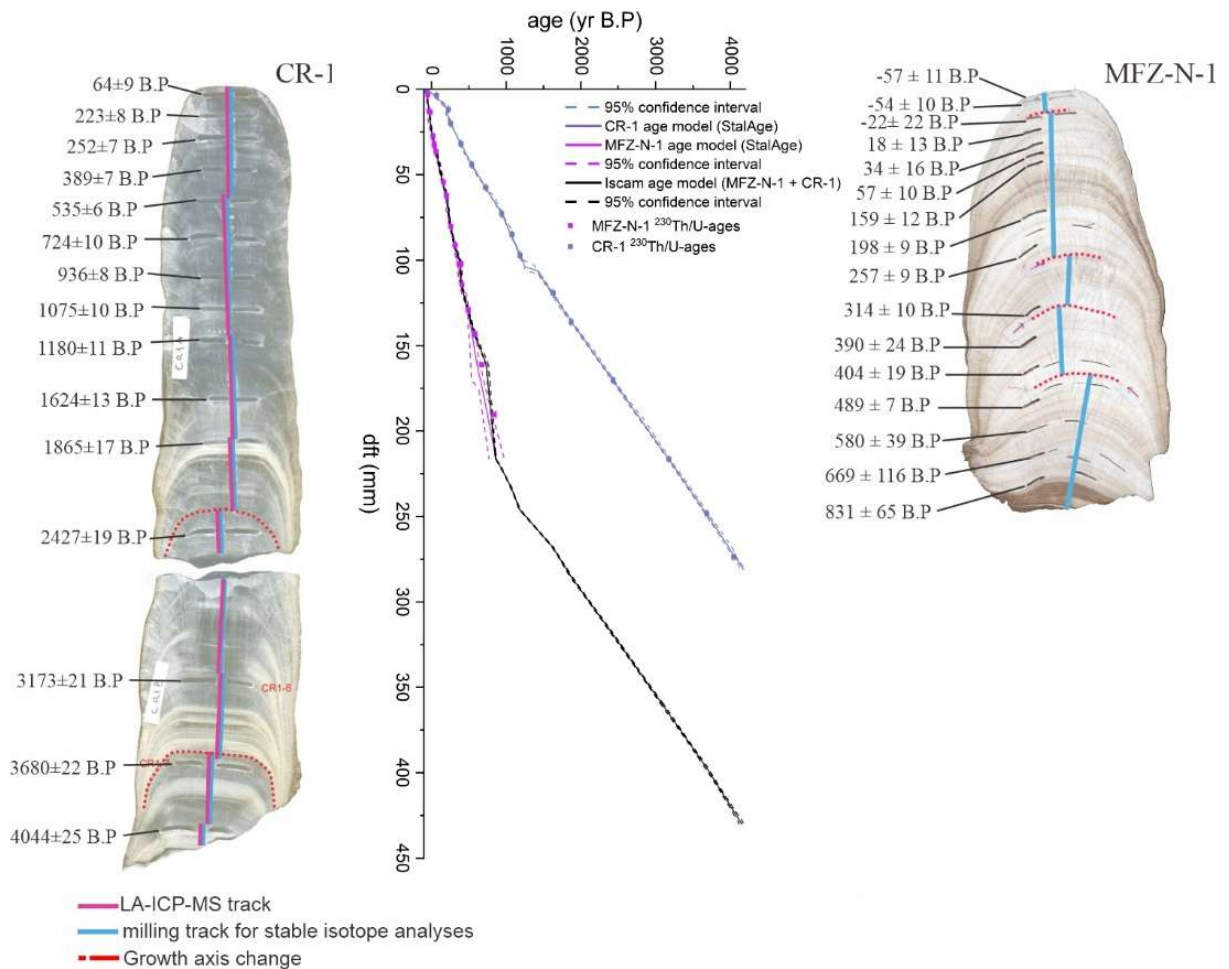
- Aguirre-Correa, F., Bollasina, M., Garreaud, R., Suárez, F., 2025. Rossby waves as key drivers of the South American Monsoon high-frequency variability. *Atmospheric Research* 326. <https://doi.org/10.1016/j.atmosres.2025.108206>
- Ampuero, A., Stríkis, N.M., Apaéstegui, J., Vuille, M., Novello, V.F., Espinoza, J.C., Cruz, F.W., Vonhof, H., Mayta, V.C., Martins, V.T.S., Cordeiro, R.C., Azevedo, V., Sifeddine, A., 2020. The Forest Effects on the Isotopic Composition of Rainfall in the Northwestern

- Amazon Basin. *JGR Atmospheres* 125, e2019JD031445. <https://doi.org/10.1029/2019JD031445>
- Apaéstegui, J., Cruz, F.W., Vuille, M., Fohlmeister, J., Espinoza, J.C., Sifeddine, A., Strikis, N., Guyot, J.L., Ventura, R., Cheng, H., Edwards, R.L., 2018. Precipitation changes over the eastern Bolivian Andes inferred from speleothem ($\delta^{18}\text{O}$) records for the last 1400 years. *Earth and Planetary Science Letters* 494, 124–134. <https://doi.org/10.1016/j.epsl.2018.04.048>
- Bahr, A., Kaboth-Bahr, S., Jaeschke, A., Chiessi, C., Cruz, F., Carvalho, L., Rethemeyer, J., Schefuß, E., Geppert, P., Albuquerque, A.L., Pross, J., Friedrich, O., 2021. Late Holocene Precipitation Fluctuations in South America Triggered by Variability of the North Atlantic Overturning Circulation. *Paleoceanography and Paleoclimatology* 36. <https://doi.org/10.1029/2021PA004223>
- Bernal, J.P., Cruz, F.W., Stríkis, N.M., Wang, X., Deininger, M., Catunda, M.C.A., Ortega-Obregón, C., Cheng, H., Edwards, R.L., Auler, A.S., 2016. High-resolution Holocene South American monsoon history recorded by a speleothem from Botuverá Cave, Brazil. *Earth and Planetary Science Letters* 450, 186–196. <https://doi.org/10.1016/j.epsl.2016.06.008>
- Boers, N., Rheinwalt, A., Bookhagen, B., Barbosa, H.M.J., Marwan, N., Marengo, J., Kurths, J., 2014. The South American rainfall dipole: A complex network analysis of extreme events. *Geophysical Research Letters* 41, 7397–7405. <https://doi.org/10.1002/2014GL061829>
- Bond, G., Kromer, B., Beer, J., Muscheler, R., Evans, M.N., Showers, W., Hoffmann, S., Lotti-Bond, R., Hajdas, I., Bonani, G., 2001. Persistent Solar Influence on North Atlantic Climate During the Holocene. *Science* 294, 2130–2136. <https://doi.org/10.1126/science.1065680>
- Cai, W., McPhaden, M.J., Grimm, A.M., Rodrigues, R.R., Taschetto, A.S., Garreaud, R.D., Dewitte, B., Poveda, G., Ham, Y.G., Santoso, A., Ng, B., Anderson, W., Wang, G., Geng, T., Jo, H.S., Marengo, J.A., Alves, L.M., Osman, M., Li, S., Wu, L., Karamperidou, C., Takahashi, K., Vera, C., 2020. Climate impacts of the El Niño–Southern Oscillation on South America. *Nature Reviews Earth and Environment*. <https://doi.org/10.1038/s43017-020-0040-3>
- Carpenedo, C.B., Viana, D.R., Parise, C.K., Aquino, F.E., Braga, R.B., 2023. Atmospheric circulation patterns associated with surface air temperature variability trends between the Antarctic Peninsula and South America. *Anais da Academia Brasileira de Ciências* 95. <https://doi.org/10.1590/0001-3765202320220591>
- Carvalho, L.M.V., Jones, C., Liebmann, B., 2004. The South Atlantic convergence zone: Intensity, form, persistence, and relationships with intraseasonal to interannual activity and extreme rainfall. *Journal of Climate* 17, 88–108. [https://doi.org/10.1175/1520-0442\(2004\)017%253C0088:TSACZI%253E2.0.CO;2](https://doi.org/10.1175/1520-0442(2004)017%253C0088:TSACZI%253E2.0.CO;2)
- Cheng, H., Edwards, R.L., Shen, C.C., Polyak, V.J., Asmerom, Y., Woodhead, J., Hellstrom, J., Wang, Y., Kong, X., Spötl, C., Wang, X., Alexander, E.C., 2013. Improvements in ^{230}Th dating, ^{230}Th and ^{234}U half-life values, and U-Th isotopic measurements by multi-collector inductively coupled plasma mass spectrometry. *Earth and Planetary Science Letters* 371–372, 82–91. <https://doi.org/10.1016/j.epsl.2013.04.006>
- Cruz, F.W., Karmann, I., Viana, O., Burns, S.J., Ferrari, J.A., Vuille, M., Sial, A.N., Moreira, M.Z., 2005. Stable isotope study of cave percolation waters in subtropical Brazil: Implications for paleoclimate inferences from speleothems. *Chemical Geology* 220, 245–262. <https://doi.org/10.1016/j.chemgeo.2005.04.001>
- Ferreira, G.W.S., Reboita, M.S., 2022. A New Look into the South America Precipitation Regimes: Observation and Forecast. *Atmosphere* 13. <https://doi.org/10.3390/atmos13060873>
- Fohlmeister, J., 2012. A statistical approach to construct composite climate records of dated archives. *Quaternary Geochronology* 14, 48–56. <https://doi.org/10.1016/j.quageo.2012.06.007>

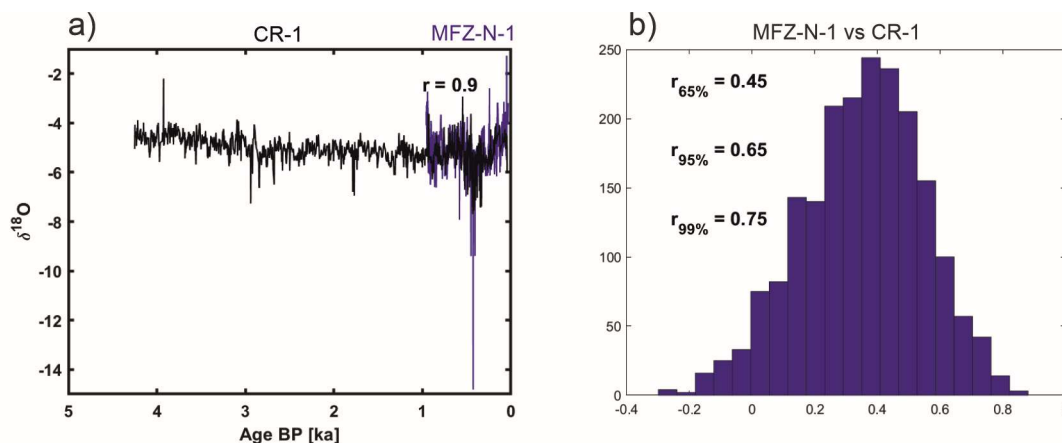
- Gelbrecht, M., Boers, N., Kurths, J., 2018. Phase coherence between precipitation in South America and Rossby waves.
- Jamieson, R.A., Baldini, J.U.L., Brett, M.J., Taylor, J., Ridley, H.E., Ottley, C.J., Pruffer, K.M., Wassenburg, J.A., Scholz, D., Breitenbach, S.F.M., 2016. Intra- and inter-annual uranium concentration variability in a Belizean stalagmite controlled by prior aragonite precipitation: A new tool for reconstructing hydro-climate using aragonitic speleothems. *Geochimica et Cosmochimica Acta* 190, 332–346. <https://doi.org/10.1016/j.gca.2016.06.037>
- Jones, C., Mu, Y., Carvalho, L.M.V., Ding, Q., 2023. The South America Low-Level Jet: form, variability and large-scale forcings. *npj Climate and Atmospheric Science* 6. <https://doi.org/10.1038/s41612-023-00501-4>
- Jones, T.R., Cuffey, K.M., Roberts, W.H.G., Markle, B.R., Steig, E.J., Stevens, C.M., Valdes, P.J., Fudge, T.J., Sigl, M., Hughes, A.G., Morris, V., Vaughn, B.H., Garland, J., Vinther, B.M., Rozmiarek, K.S., Brashear, C.A., White, J.W.C., 2023. Seasonal temperatures in West Antarctica during the Holocene. *Nature* 613, 292–297. <https://doi.org/10.1038/s41586-022-05411-8>
- Kanner, L.C., Burns, S.J., Cheng, H., Edwards, R.L., Vuille, M., 2013. High-resolution variability of the South American summer monsoon over the last seven millennia: Insights from a speleothem record from the central Peruvian Andes. *Quaternary Science Reviews* 75, 1–10. <https://doi.org/10.1016/j.quascirev.2013.05.008>
- Libera, M.E.D., Novello, V.F., Cruz, F.W., Orrison, R., Vuille, M., Maezumi, S.Y., Souza, J. de, Cauhy, J., Campos, J.L.P.S., Ampuero, A., Utida, G., Strikis, N.M., Stumpf, C.F., Azevedo, V., Zhang, H., Edwards, R.L., Cheng, H., 2022. Paleoclimatic and paleoenvironmental changes in Amazonian lowlands over the last three millennia. *Quaternary Science Reviews* 279. <https://doi.org/10.1016/j.quascirev.2022.107383>
- Meier, K.J.F., Jaeschke, A., Rethemeyer, J., Chiessi, C.M., Albuquerque, A.L.S., Wall, V., Friedrich, O., Bahr, A., 2022. Coupled Oceanic and Atmospheric Controls of Deglacial Southeastern South America Precipitation and Western South Atlantic Productivity. *Frontiers in Marine Science* 9. <https://doi.org/10.3389/fmars.2022.878116>
- Novello, V.F., Cruz, F.W., Moquet, J.S., Vuille, M., Paula, M.S. de, Nunes, D., Edwards, R.L., Cheng, H., Karmann, I., Utida, G., Strikis, N.M., Campos, J.L.P.S., 2018. Two Millennia of South Atlantic Convergence Zone Variability Reconstructed From Isotopic Proxies. *Geophysical Research Letters* 45, 5045–5051. <https://doi.org/10.1029/2017GL076838>
- Novello, V.F., Vuille, M., Cruz, F.W., Strikis, N.M., Paula, M.S.D., Edwards, R.L., Cheng, H., Karmann, I., Jaqueto, P.F., Trindade, R.I.F., Hartmann, G.A., Moquet, J.S., 2016. Centennial-scale solar forcing of the South American Monsoon System recorded in stalagmites. *Scientific Reports* 6. <https://doi.org/10.1038/srep24762>
- Orrison, R., Vuille, M., Smerdon, J.E., Apaéstegui, J., Campos, J.L.P.S., Cruz, F.W., Libera, M.E.D., 2022. South American Monsoon variability over the last millennium in paleoclimate records and isotope-enabled climate models. <https://doi.org/10.5194/cp-2022-6>
- Paula-Santos, G.M., Campanha, G.A.D.C., Faleiros, F.M., Hollanda, M.H.B.M., Rodrigues, S.W.D.O., 2021. Carbon isotope variations of high magnitude recorded in carbonate rocks from the Stenian-Tonian Lajeado Group, Southeast Brazil. *Journal of South American Earth Sciences* 109, 103268. <https://doi.org/10.1016/j.jsames.2021.103268>
- Reboita, M.S., Ambrizzi, T., Crespo, N.M., Dutra, L.M.M., Ferreira, G.W. de S., Rehbein, A., Drumond, A., Rocha, R.P. da, Souza, C.A. de, 2021. Impacts of teleconnection patterns on South America climate. *Annals of the New York Academy of Sciences* 1504, 116–153. <https://doi.org/10.1111/nyas.14592>
- Reis, P.A., Aquino, F.E., Schossler, V., Bernardo, R.T., Simões, J.C., 2020. Tropical–antarctic connections of an explosive cyclone in southern Brazil: Rainfall stable isotope ratios and atmospheric analysis. *Advances in Polar Science* 31, 103–111. <https://doi.org/10.13679/j.advps.2019.0039>

- Scholz, D., Hoffmann, D.L., 2011. StalAge - An algorithm designed for construction of speleothem age models. *Quaternary Geochronology* 6, 369–382. <https://doi.org/10.1016/j.quageo.2011.02.002>
- Sinclair, D.J., 2011. Two mathematical models of Mg and Sr partitioning into solution during incongruent calcite dissolution. *Chemical Geology* 283, 119–133. <https://doi.org/10.1016/j.chemgeo.2010.05.022>
- S-Paegle, J.N., Mo, K.C., 1997. Alternating Wet and Dry Conditions over South America during Summer.
- Strikis, N.M., Cruz, F.W., Cheng, H., Karmann, I., Edwards, R.L., Vuille, M., Wang, X., De Paula, M.S., Novello, V.F., Auler, A.S., 2011. Abrupt variations in South American monsoon rainfall during the Holocene based on a speleothem record from central-eastern Brazil. *Geology* 39, 1075–1078. <https://doi.org/10.1130/G32098.1>
- Tseng, W.L., Lee, Y.C., Wang, Y.C., Hsu, H.H., Keenlyside, N., 2023. Characterizing Atlantic interhemispheric teleconnection established by South American monsoon in austral summer. *Environmental Research Letters* 18. <https://doi.org/10.1088/1748-9326/acdbdf>
- Utida, G., Cruz, F.W., Vuille, M., Ampuero, A., Novello, V.F., Maksic, J., Sampaio, G., Cheng, H., Zhang, H., Andrade, F.R.D.D., Edwards, R.L., 2023. Spatiotemporal Intertropical Convergence Zone dynamics during the last 3 millennia in northeastern Brazil and related impacts in modern human history. *Climate of the Past* 19, 1975–1992. <https://doi.org/10.5194/cp-19-1975-2023>
- Vasconcelos, L.C., Cruz, F.W., Bernal, J.P., Campos, M.C., Piacsek, P., Campos, J.L., Zhang, H., Strikis, N., Vuille, M., Utida, G., Mollo, C., Edward, R.L., Cheng, H., 2025. The coupling between monsoon rainfall and Sea Surface Temperature in the subtropical South Atlantic during the Last Glacial Period. *Global and Planetary Change* 255, 105121. <https://doi.org/10.1016/j.gloplacha.2025.105121>
- Vuille, M., Burns, S.J., Taylor, B.L., Cruz, F.W., Bird, B.W., Abbott, M.B., Kanner, L.C., Cheng, H., Novello, V.F., 2012. A review of the South American monsoon history as recorded in stable isotopic proxies over the past two millennia. *Clim. Past* 8, 1309–1321. <https://doi.org/10.5194/cp-8-1309-2012>
- Vuille, M., Werner, M., 2005. Stable isotopes in precipitation recording South American summer monsoon and ENSO variability: Observations and model results. *Climate Dynamics* 25, 401–413. <https://doi.org/10.1007/s00382-005-0049-9>
- Wassenburg, J.A., Riechelmann, S., Schröder-Ritzrau, A., Riechelmann, D.F.C., Richter, D.K., Immenhauser, A., Terente, M., Constantin, S., Hachenberg, A., Hansen, M., Scholz, D., 2020. Calcite Mg and Sr partition coefficients in cave environments: Implications for interpreting prior calcite precipitation in speleothems. *Geochimica et Cosmochimica Acta* 269, 581–596. <https://doi.org/10.1016/j.gca.2019.11.011>

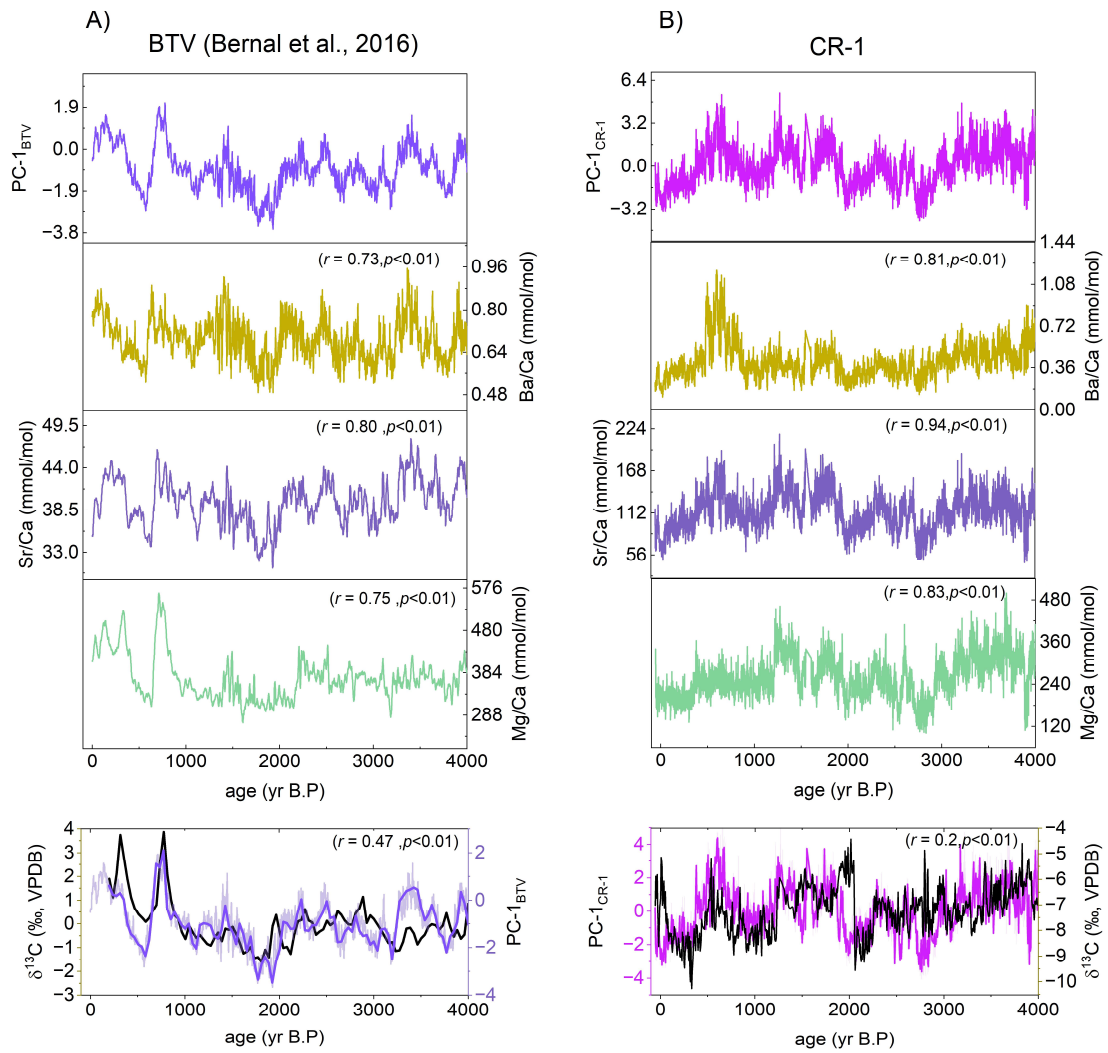
4.7. Supplementary material – Manuscript II



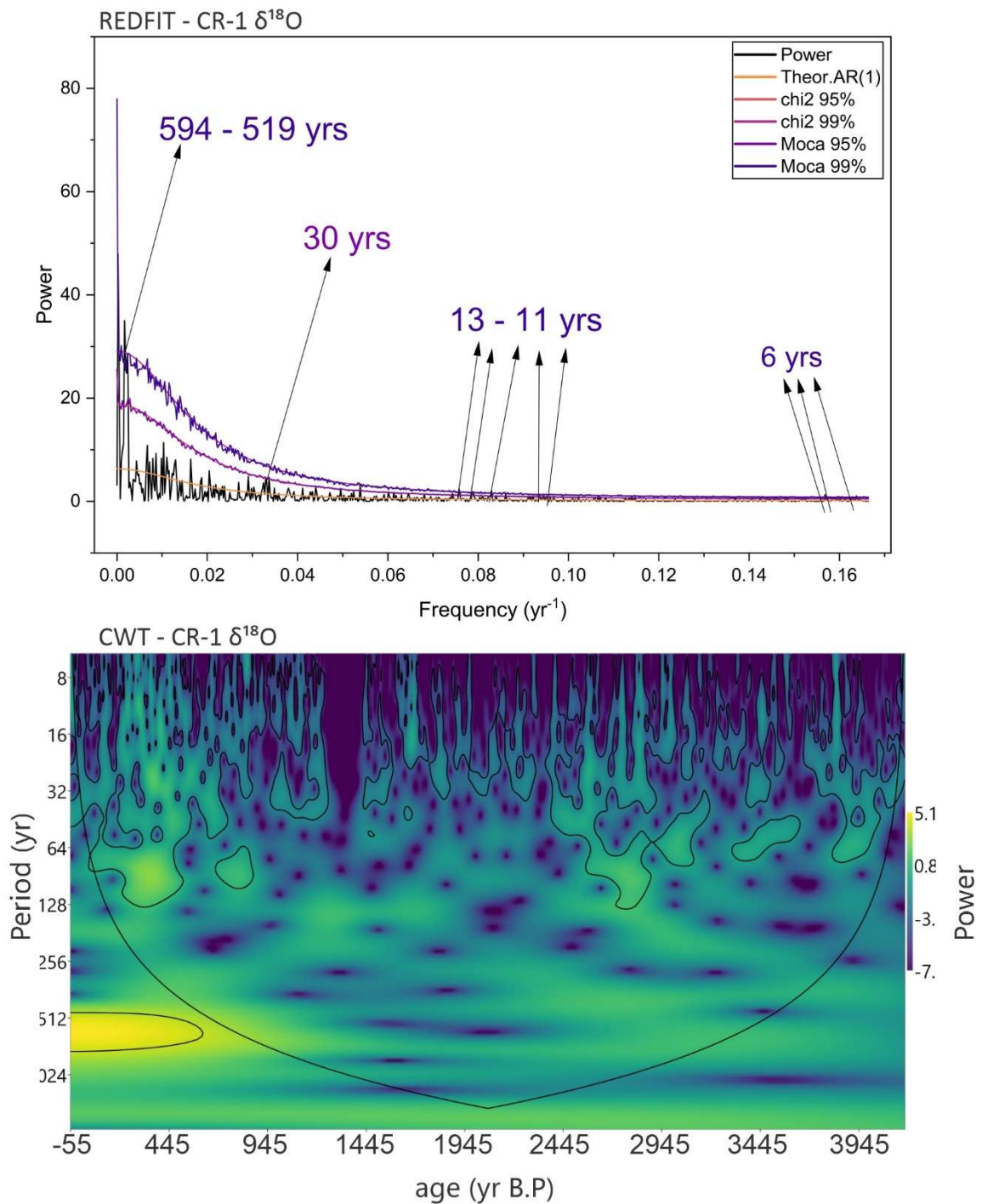
Supplementary Figure 4.1 – Stalagmite samples (CR-1 and MFZ-N-1) with $^{230}\text{Th}/\text{U}$ -ages and analyses profile indicated. Stalagmite age-depth model for CR-1 and MFZ-N-1 reconstructed with StalAge (Scholz and Hoffman 2011) and composite (MFZ-N-1 + CR-1) $\delta^{18}\text{O}$ age-depth model reconstructed with Iscam software (Fohlmeister 2012).



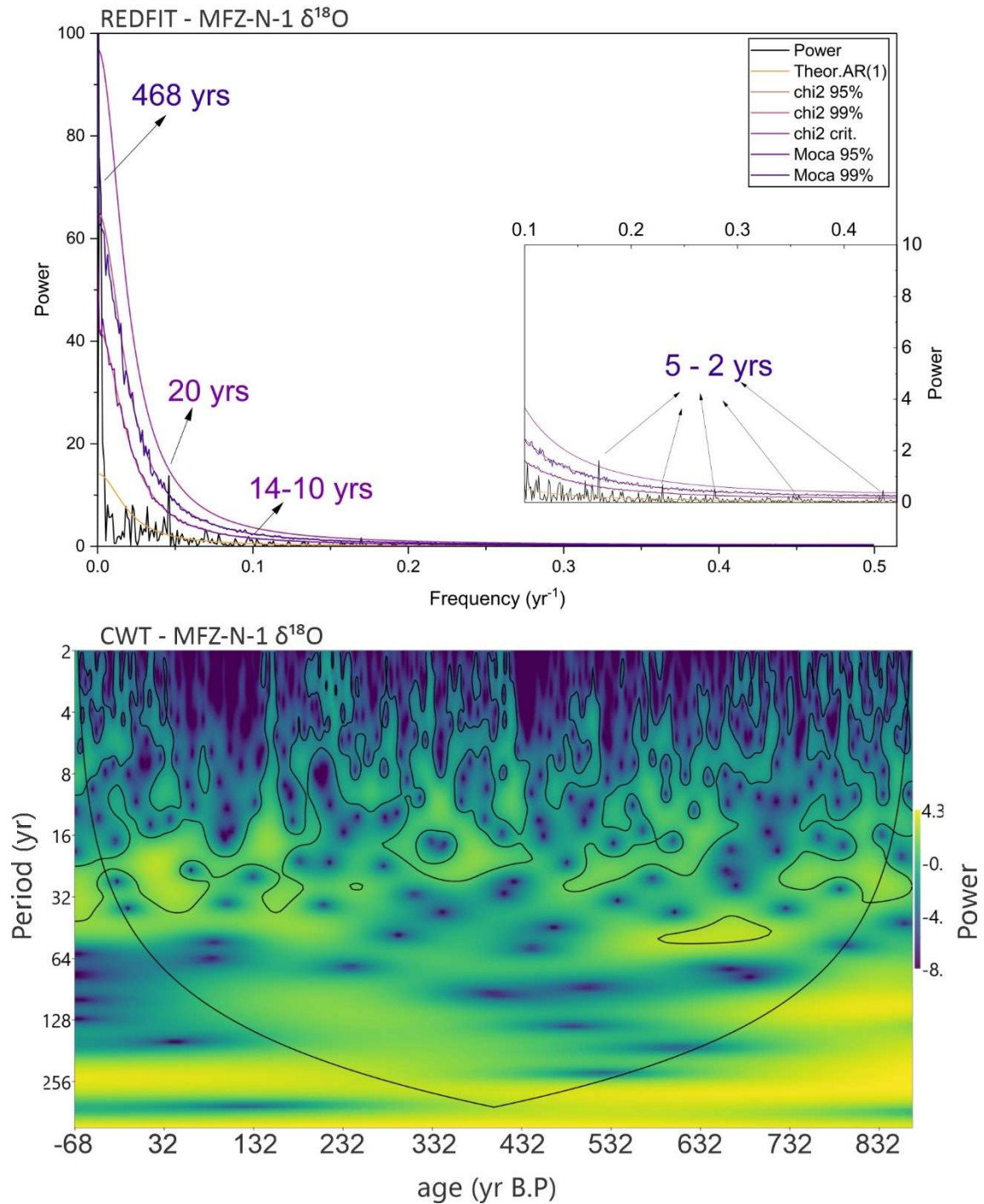
Supplementary Figure 4.2 – Distribution of maximum correlation coefficients for 2000 pairs of AR1 time series with the same characteristics as the measured $\delta^{18}\text{O}$ stalagmite time series. a) best time series results for the individual steps iscam performs for the composite time series construction with highest correlation coefficient indicated. The established time series is significant at the 95% confidence limit; b) distribution for MFZ-N-1 and CR-1.



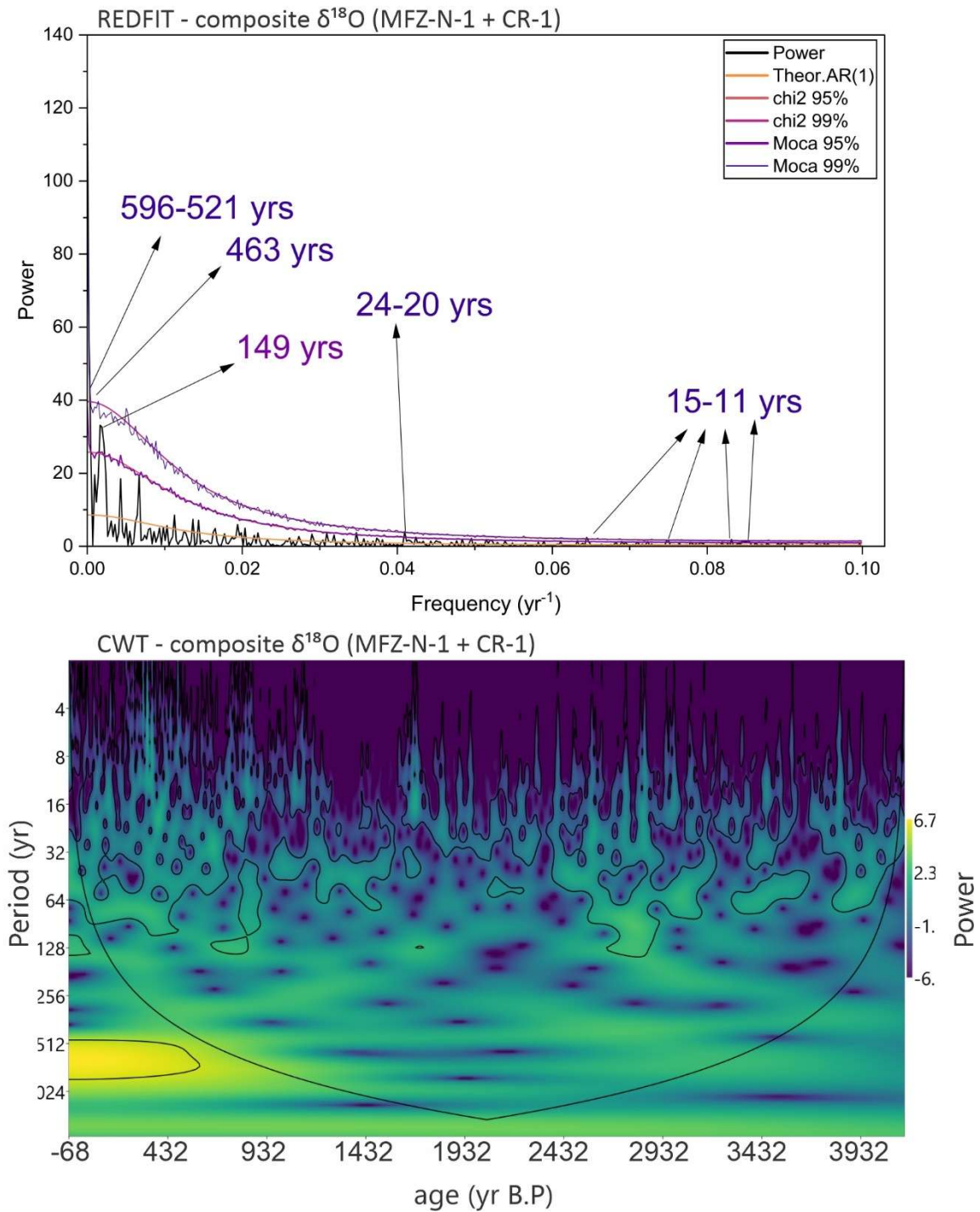
Supplementary Figure 4.3 – Trace element ratios and PCs and comparison with $\delta^{13}\text{C}$ record. A and B show BTV and CR-1 record respectively. From top to bottom; PC-1, Ba/Ca, Sr/Ca and Mg/Ca; and the bottomless plot shows the comparison between PC-1 and $\delta^{13}\text{C}$.



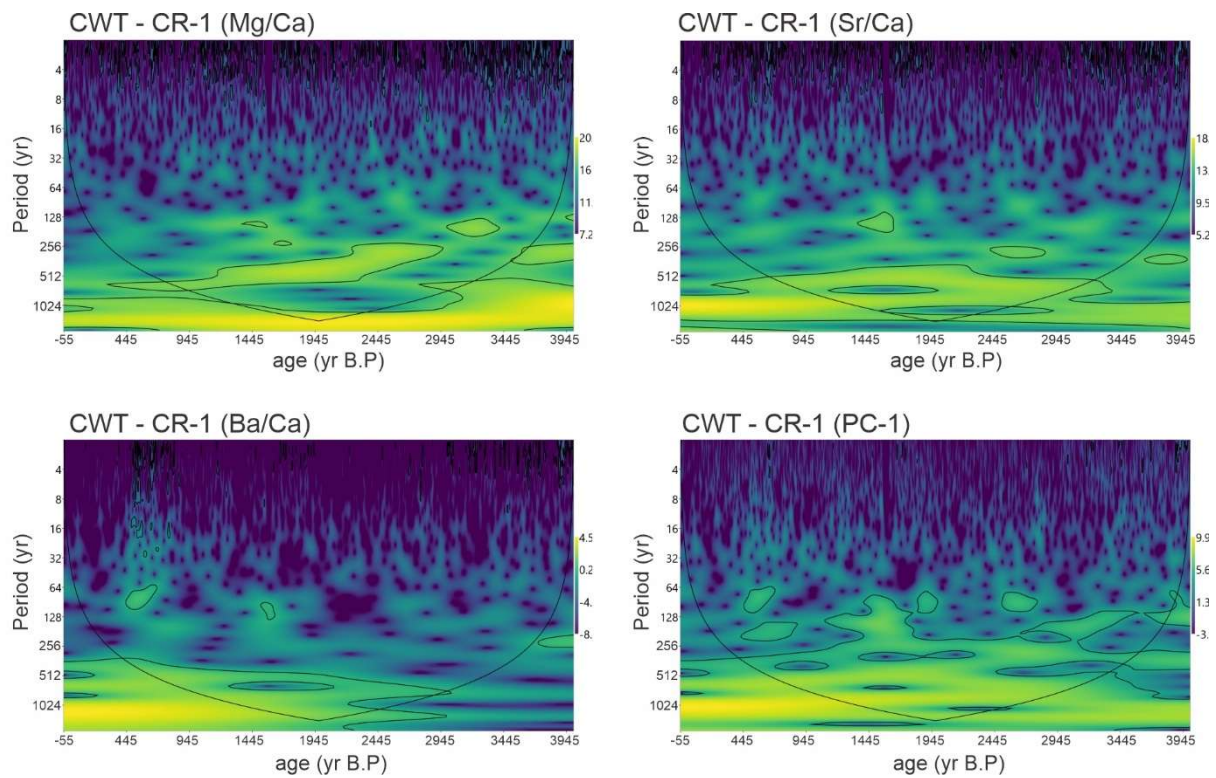
Supplementary Figure 4.4 – REDFIT and Continuous Wavelet Transform (CWT) of CR-1 $\delta^{18}\text{O}$ for periods from -55 to 4175 B.P. Top graph shows REDFIT analysis with periodicities above 95 and 99% test (chi and Monte Carlo) indicated in the graph; bottom graph shows CWT with cone of influence (black line) and significance levels contour for 95% (Hammer 2001).



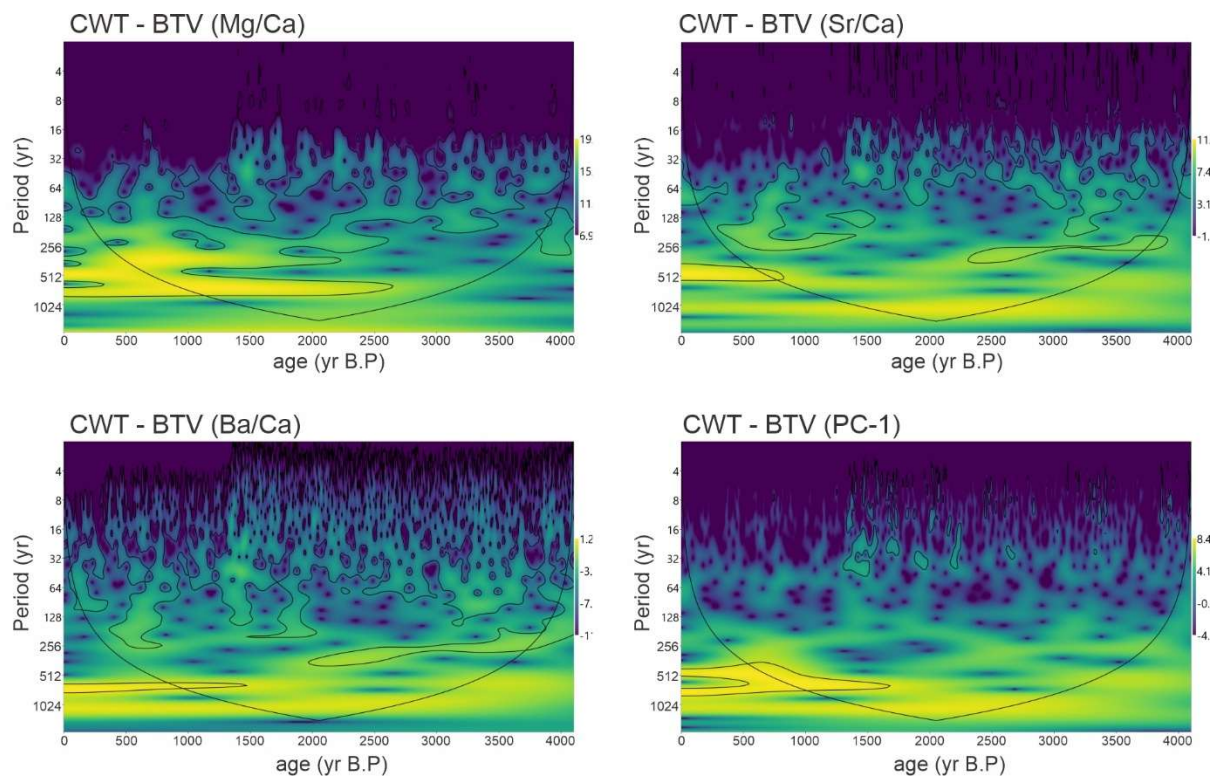
Supplementary Figure 4.5 – REDFIT and Continuous Wavelet Transform (CWT) of MFZ-N-1 $\delta^{18}\text{O}$ for periods from -68 to 868 B.P. Top graph shows REDFIT analysis with periodicities above 95 and 99% test (chi and Monte Carlo) indicated in the graph; bottom graph shows CWT with cone of influence (black line) and significance levels contour for 95% (Hammer 2001).



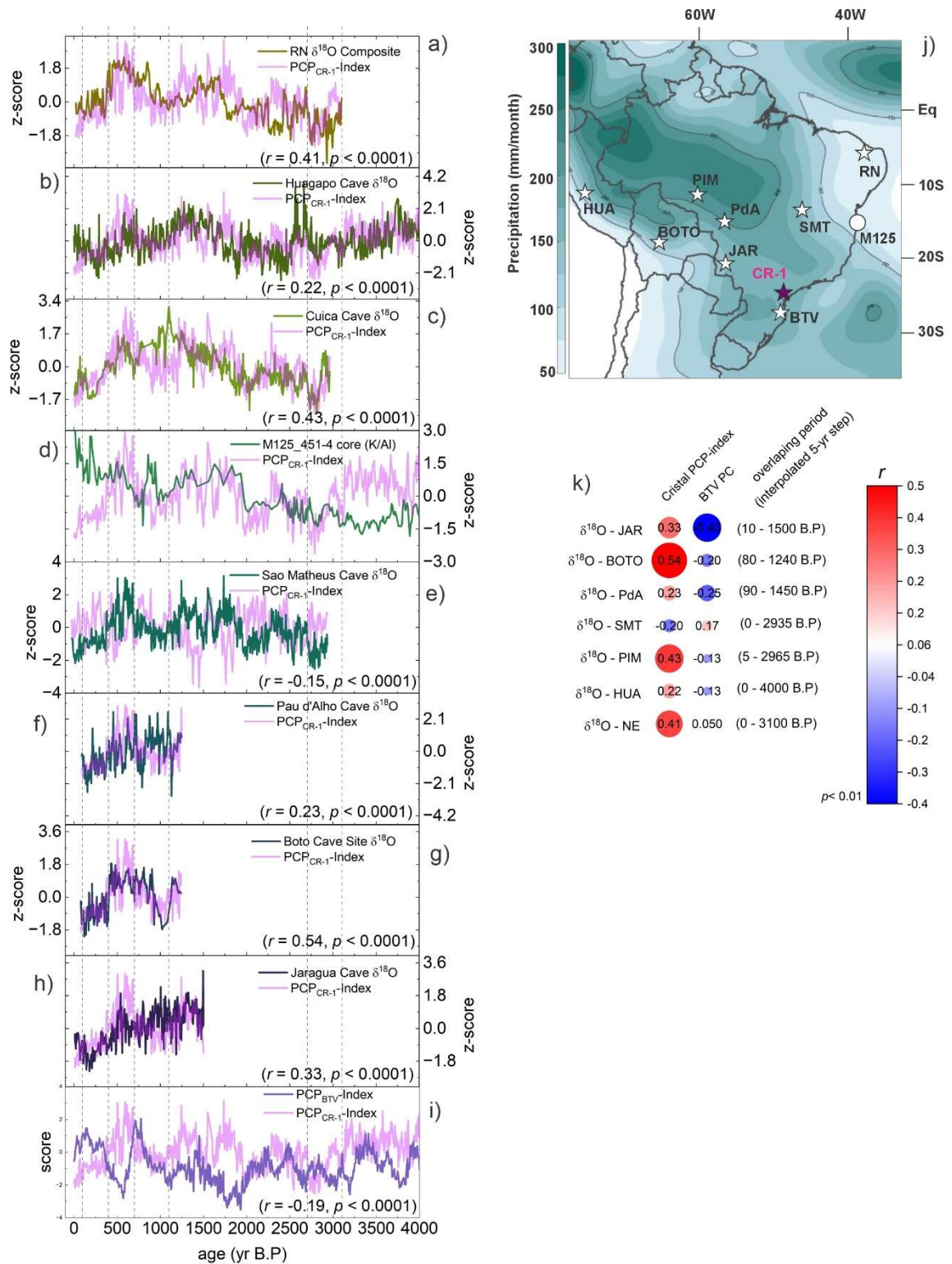
Supplementary Figure 4.6 – REDFIT and Continuous Wavelet Transform (CWT) of $\delta^{18}\text{O}$ composite (MFZ-N-1 + CR-1) for periods from -68 to 4146 B.P. Top graph shows REDFIT analysis with periodicities above 95 and 99% test (chi and Monte Carlo) indicated in the graph; bottom graph shows CWT with cone of influence (black line) and significance levels contour for 95% (Hammer 2001).



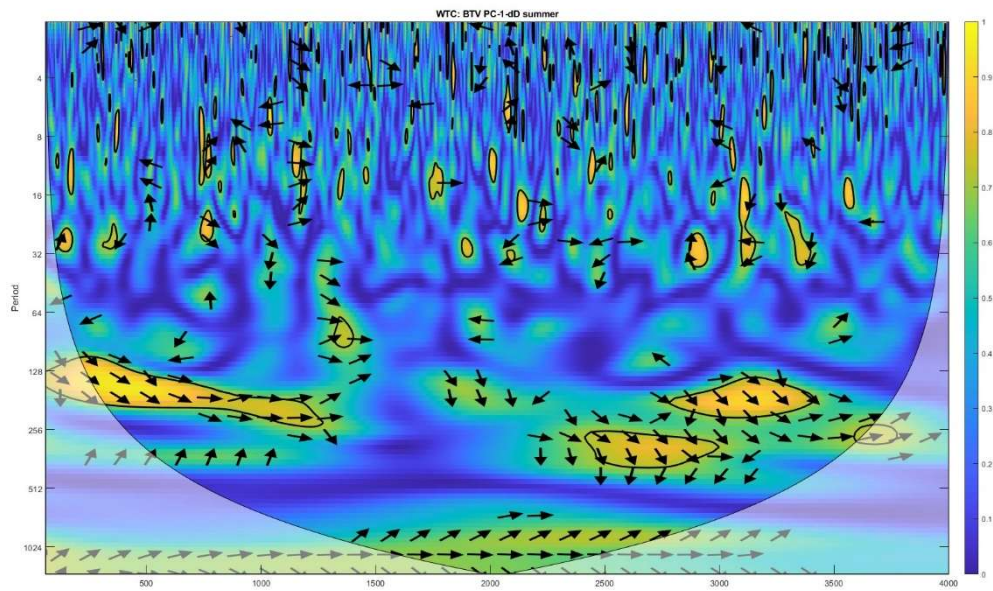
Supplementary Figure 4.7 –Continuous Wavelet Transform (CWT) of CR-1 trace element ratios (Mg/Ca, Sr/Ca and Ba/Ca) and PC-1, with cone of influence (black line) and significance levels contour for 95% (Hammer 2001).



Supplementary Figure 4.8 –Continuous Wavelet Transform (CWT) of BTV trace element ratios (Mg/Ca, Sr/Ca and Ba/Ca) and PC-1, with cone of influence (black line) and significance levels contour for 95% (Hammer 2001).



Supplementary Figure 4.9 – Stalagmites and marine sediment cores from South America. a) Rio Grande do Norte $\delta^{18}\text{O}$ composite (RN - Utida et al 2023); b) Huagapo cave $\delta^{18}\text{O}$ record (HUA - Kanner et al 2013); c) Cuica Cave $\delta^{18}\text{O}$ composite (PIM – Della Libera et al 2022); d) marine sediment core M125_451-4 ln(k/Al) record (M125 – Bahr et al., 2021); e) Sao Mateus $\delta^{18}\text{O}$ record (SMT – Della Libera et al 2025); f) Pau d'Alho $\delta^{18}\text{O}$ record (PdA - Novello et al 2018); g) Boto $\delta^{18}\text{O}$ record (BOTO – Apaestegui et al 2018); h) Jaragua $\delta^{18}\text{O}$ record (JAR – Novello et al 2018); i) PCP_{BTV} -index; j) record site location; k) correlation between PCP-indices from CR-1 and BTV with $\delta^{18}\text{O}$ records. The correlations are calculated for the overlapping period between each record with a 5-yr step interpolation. All correlations show $p < 0.001$.



Supplementary Figure 10 – Cross wavelet analyses between Antarctic Summer δD (Jones et al., 2023) and BTV-PC-1.

Chapter 5 – Manuscript III

Multi-centennial hydroclimate shifts of Southeastern Brazil Hydroclimate in response to North Atlantic Cooling events over the Past 7,500 Years

Julio Cauhy^{1,2*}; Marcela Eduarda Della Libera^{1,2}; Nicolás M. Stríkis^{3,4}; Mathias Vuille⁵; Francisco W. Cruz Junior³; Valdir F. Novello⁶; Hubert Vonhof²; Denis Scholz¹

¹Institut für Geowissenschaften, Johannes-Gutenberg Universität Mainz, Germany

²Max-Planck-Institut für Chemie, Mainz, Germany

³Instituto de Geociências, Universidade de São Paulo, São Paulo-SP, Brazil

⁴Dept. Geoquímica, Universidade Federal Fluminense

⁵Department of Atmospheric and Environmental Sciences, University at Albany, State University of New York, Albany, New York, USA

⁶Institute of Geosciences, University of Brasília, Brasília – DF, Brazil

Corresponding author: Julio Cauhy (cauhy.r@gmail.com)

Paper in preparation - b

5.1. Abstract

New high-resolution trace element record combining two stalagmites from Southeastern Brazil (SEBRA) evidences persistent multi-centennial shifts in hydroclimate conditions over the past 7,500 years, with wet anomalies associated with North Atlantic cooling events, including Bond events and the Little Ice Age (LIA). Our analysis reveals a coupling between Bond events and increased South Atlantic Convergence Zone (SACZ) rainfall over SEBRA, with a persistent pattern over the Middle and Late Holocene. The most pronounced wet anomalies in SEBRA are synchronous with these events, and present a coherent structure with other records from South American Summer Monsoon (SASM) and SACZ, and an antiphase with Southern Brazil (SB) resembling the multi-centennial dipole between SEBRA and SB. This pattern indicates that North Atlantic cooling induced large-scale reorganizations of the Intertropical Convergence Zone (ITCZ) and strengthened SASM/SACZ convection through changes in cross-equatorial heat transport related to waken of AMOC. Furthermore, interhemispheric anti-phase relationship between SEBRA wet anomalies and drying across Asian monsoon evidences the global expression of AMOC–ITCZ modulation under North Atlantic cooling events. These findings demonstrate the pronounced response of SEBRA hydroclimate to even modest perturbations in the interhemispheric energy balance, evidencing the sensitivity of the region towards potential impacts under future AMOC weakening scenarios.

5.2. Introduction

The Holocene period was marked by a long-term increase in South American Summer Monsoon (SASM) activity following the increase in austral summer insolation, superimposed by abrupt climate fluctuations on millennial to centennial time scales (Bernal et al., 2016; Deininger et al., 2019; Strikis et al., 2011). These abrupt climate fluctuations are concomitant with cooling events in the North Atlantic, indicated by the correlation between petrologic tracers of Ice-raft debris (IRD) recorded in sediment cores from the North Atlantic (Bond et al., 1997) and wet anomalies over SASM records (Baker et al., 2009, 2005; Cheng et al., 2009; Strikis et al., 2011). These events are named Bond events and are defined by IRD events (based on quartz and haematite-stained grains) recorded in sediment cores from subpolar North Atlantic marine sediment cores (Bond et al., 1997).

Eight major Bond events have been identified over the past 12 kyr, presenting a cyclicity of $\sim 1470 \pm 500$ years (Bond et al., 2001). Correlations between these events and cosmogenic radionuclide production (carbon-14 and beryllium-10) suggest a solar influence (Bond et al., 2001). However, spectral analyses of marine, continental and ice core records of North Atlantic indicate that the ~ 1500 -year cycle likely reflects an ocean-driven climate oscillation, rather than a purely solar one (Debret et al., 2007). Therefore, these cycles are generally interpreted as expressions of internal ocean–atmosphere dynamics rather than direct solar forcing, evidencing the continued role of ocean circulation in modulating Holocene climate (Debret et al., 2007).

These cold events in Northern Hemisphere are associated with increased convective activity over SASM (Deininger et al., 2019; Strikis et al., 2011). For example, Baker et al. (2009) identified centennial scale wet periods in Lago Umayo (Peruvian altiplano) correlating with Bond events, while Strikis et al. (2011) identified episodic increase in South Atlantic Convergence Zone (SACZ) precipitation on $\delta^{18}\text{O}$ record from Lapa Grande cave (LG) that coincide with Bond events. Strikis et al. (2011) suggest that during these events, the increased SACZ activity over central-eastern Brazil follows the southward displacement of the Intertropical Convergence Zone (ITCZ), resulting in increased moisture transport to SASM and SACZ, analogue to the mechanism that occurred during Heinrichs Stadials, but with smaller amplitude (Deininger et al., 2019; Strikis et al., 2011; Strikis et al., 2015). In fact, Strikis et al. (2011) proposed that the impact of Bond events in SASM precipitation was driven by a slowdown of the Atlantic Meridional Overturning Circulation (AMOC) associated with the freshwater pulses in the North Atlantic.

When the AMOC weakens, cross-equatorial heat transport is diminished, reducing northward heat flux and leads to Northern Hemisphere cooling and a compensating warming in the Southern Hemisphere, a mechanism known as bipolar seesaw (Chiessi et al., 2015; Evangelista et al., 2014; Vasconcelos et al., 2025). This interhemispheric contrast is also supported by anti-phase relationship between SSTs reconstructions from the Brazilian Southwestern Tropical Atlantic sediment core, which indicates warming, and the ITCZ record from Cariaco Basin, which indicates cooling for the same intervals (Evangelista et al., 2014). Such an interhemispheric imbalance causes the ITCZ to migrate southward, increasing convective activity of the SAMS domain (Deininger et al., 2019), as observed in multiple records across South America (Baker et al., 2009, 2005; Libera et al., 2022; Strikis et al., 2011; Strikis et al., 2015; Utida et al., 2023, Cauhy et al., in prep).

Even though the influence of the AMOC–ITCZ mechanism on South American precipitation is well established, its manifestation during the Holocene Bond events remains comparatively underexplored. These events occurred under boundary conditions distinct from glacial periods, characterized by higher insolation and less pronounced AMOC fluctuations, yet they still produced coherent hemispheric-scale hydroclimatic responses (Strikis et al., 2011). Understanding how Bond events impacted South America under these relatively stable conditions provides a valuable analogue for assessing the sensitivity of tropical precipitation to moderate AMOC variability, conditions increasingly relevant in the context of projected AMOC weakening in the coming centuries (Meccia and Blázquez, 2025). In this context, paleoclimate reconstructions are essential for constraining the expected response of key precipitation systems, such as the SASM and SACZ, which are highly sensitive to ITCZ migrations and cross-equatorial energy balance shifts.

Furthermore, previous studies examining Bond event expressions in the SACZ, such as Strikis et al. (2011), relied primarily on $\delta^{18}\text{O}$ variability in stalagmites. However, $\delta^{18}\text{O}$ signals can reflect multiple processes beyond local rainfall amount, including moisture source changes (Cruz et al., 2005; Della Libera et al., accepted) and rainout along transport pathways (Ampuero et al., 2020), potentially biasing interpretations of Bond-event impacts on precipitation. Complementary approaches combining $\delta^{18}\text{O}$ with trace element ratios have shown that Bond events, such as Bond Event 2 (~2.7 kyr BP), significantly influenced regional rainfall, with wet anomalies mainly observed in the trace element records (Cauhy et al., in prep.). Here, we present high-resolution $\delta^{18}\text{O}$ and trace element records from multiple speleothems in southeastern Brazil (SEBRA) spanning the past ~7,500 years. These records allow the reconstruction of SACZ activity over SEBRA at annual to millennial time-scales, providing new insights into the regional hydroclimatic expression of Bond events.

5.3. Cave settings and samples

The stalagmite samples for this study were collected from Laje Branca Cave ($24^{\circ}54'82.75''\text{S}$; $48^{\circ}72'12.58''\text{W}$; 523 m a.s.l.) (Fig. 5.1; Supp. Fig. 5.2), located on the border of Parque Estadual Turístico do Alto Ribeira (PETAR) in Iporanga County, southern São Paulo State, approximately 97 km from the Atlantic coast (Fig. 5.1). Laje Branca Cave is part of the Pérolas–Santana system, with a total passage development of about 900 m, characterized by large, rectilinear galleries with low sinuosity (Supp. Fig. 5.3) (Karmann, 1994). The cave formed along the contact between metapelites of the Betari Formation and metalimestones of the Bairro da Serra Formation, with a vertical difference of ~ 70 m between the entrance and the sinkhole at the lowest gallery (Karmann, 1994).

Two stalagmites were analysed from Laje Branca Cave: LB-1 (Supp. Fig. 5.1c), a 210 mm-long calcitic stalagmite collected in the Mud Gallery (Supp. Fig. 5.3), and LB-3 (Supp. Fig. 5.1d), a 144 mm-long calcite stalagmite collected in the Collapsed Gallery (Supp. Fig. 5.3). We combine Laje Branca with records from other caves from the region including Cristais cave (CR-1 - $24^{\circ}26'32.55''\text{S}$, $48^{\circ}36'9.57''\text{W}$; 600 m a.s.l.) (Supp. Fig. 5.1b) (Cauhy et al (in prep), along PETAR border, approximately ~ 15 km from Laje Branca (Supp. Fig. 5.2), and Malfazido cave (MFZ-N-1 - $24^{\circ}39'\text{S}$, $49^{\circ}32'\text{W}$; 885 m a.s.l.) (Supp. Fig. 5.1a) (Cauhy et al., under review; Cauhy et al., in prep), located in Dr. Ulysses, approximately ~ 70 km west of Laje Branca Cave, in Paraná State, southern Brazil (Supp. Fig. 5.2).

The study area is characterized by subtropical umidy climate without dry season and with mild temperatures during summer, where the mean temperature of the coldest month is below 18°C and the mean temperature of the warmest month is above 22°C . The average year accumulation of 1430 mm (1981 – 2025, CHIRPs) with 60% of the total related to spring and summer precipitation (SONDJF) related to SACZ and cold fronts, and 40% during autumn and winter to cold fronts (Ferreira and Reboita, 2022).

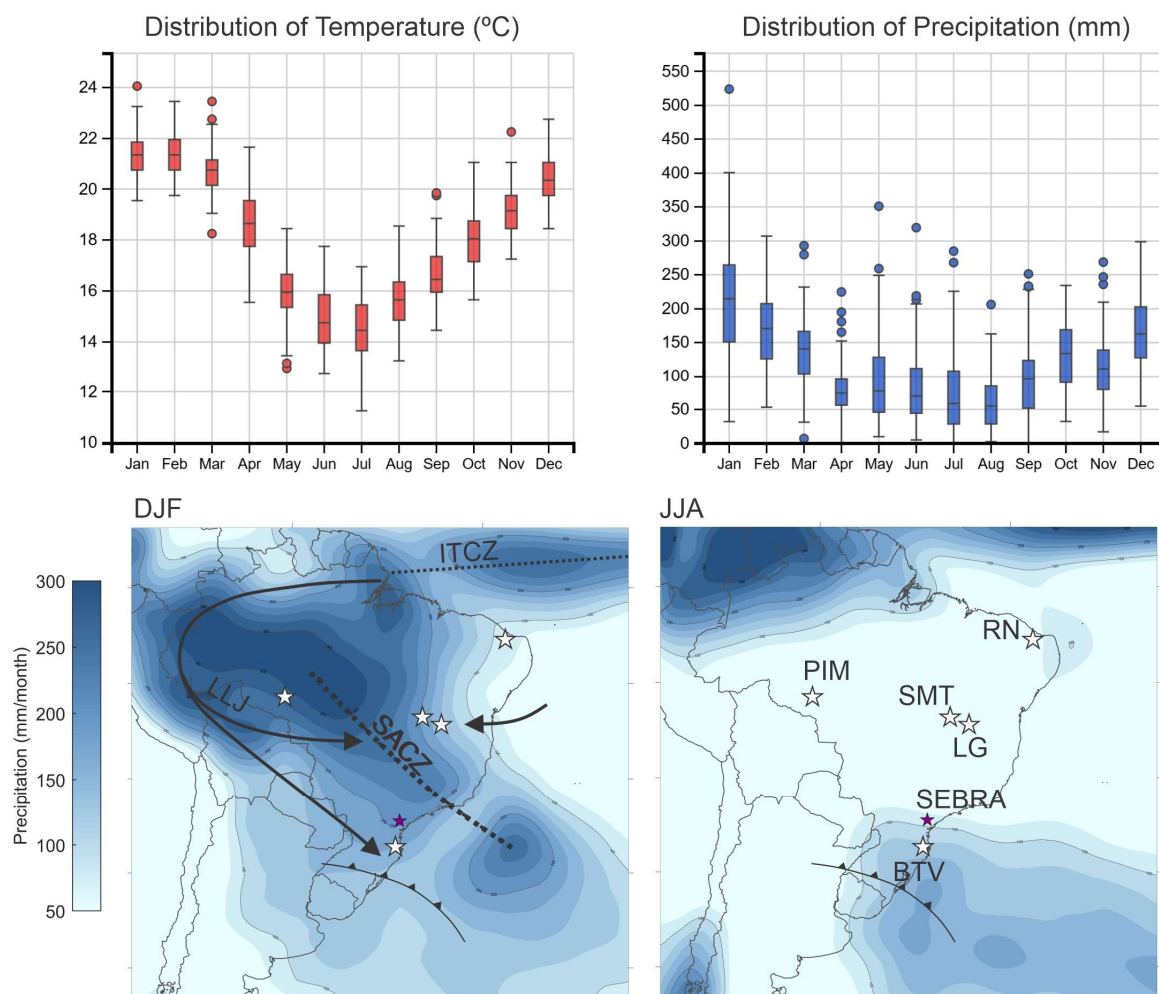


Figure 5.1 – Cave site locations and climatic settings. (a–b) Mean temperature and precipitation distribution for the study area (1993–2022; (Zepner et al., 2021)). (c–d) Mean monthly precipitation during austral summer (DJF) and austral winter (JJA), based on Global Precipitation Measurement Mission data (2001–2020; Huffman et al., 2023). In panel (c), continuous arrows indicate moisture transport pathways associated with the low-level jet (LLJ) and easterly flow; the line with triangles marks the advancing cold fronts, and the dotted line denotes the mean summer position of the Intertropical Convergence Zone (ITCZ); South Atlantic Convergence Zone (SACZ) axis marked by dotted line. Panel (d) shows paleoclimate records used for comparison in this study: RN (Rio Grande do Norte $\delta^{18}\text{O}$ composite; (Utida et al., 2023), SMT (São Mateus $\delta^{18}\text{O}$ record; Della Libera et al., accepted), LG (Lapa Grande $\delta^{18}\text{O}$ record; (Strikis et al., 2011), PIM (Cuica Cave $\delta^{18}\text{O}$ record; (Della Libera et al., 2022), BTV (Botuverá $\delta^{18}\text{O}$ record; (Bernal et al., 2016), and SEBRA (this study).

5.4. Materials and Methods

5.4.1. ^{230}Th -U dating

Stalagmite chronologies were established by ^{230}Th /U dating, using multi-collector inductively coupled plasma mass spectrometry (MC-ICP-MS). LB-3 and LB-1 were analysed at the Geochronology Laboratory at the University of Minnesota (USA) following (Cheng et al., 2013), with 14 ^{230}Th -U ages for each stalagmite. Age models were constructed using StalAge (Scholz and Hoffmann, 2011).

5.4.2. Stable Isotope Analyses

For LB-1 and LB-3, 497 and 340 samples of powdered carbonate were extracted at Institute of Geoscience (University of Sao Paulo, Brazil), using a manual Sherline Mill with a 0.1 diameter drill bit, with a constant spacing of 0.4 mm along the central growth axis of the speleothem. The $\delta^{18}\text{O}$ and $\delta^{13}\text{C}$ analyses were performed at the Stable Isotope Laboratory at the Institute of Geoscience of the University of Sao Paulo, Brazil (LES-CPGeo), using a Thermo-Finnigan Delta Plus Advantage mass spectrometer. Detailed information about the analytical protocols is described at (Medina et al., 2023). The stable isotopes from CR-1 and MFZ-N-1 are detailed described at Cauhy et al (in prep-a).

5.4.3. Trace element analysis and principal component analysis

The stalagmite LB-3 was analysed for trace elements ratios with sub-annual resolution at Johannes Gutenberg University Mainz, Germany, using a ArF Excimer 193 nm laser system (ESI NWR193), coupled to an Agilent 7500ce ICP-MS (Jochum et al., 2007). We apply a similar approach than Cauhy et al (in prep-a), using Principal Component Analyses (PCA) on trace-element ratios dataset to reduce dimensionality and identify dominant modes of variability (Jamieson et al., 2016). Prior to PCA, trace-element ratios were normalized to z-scores to remove sensitivity to variable scaling. Analyses were conducted in PAST v4.13 (Hammer, 2001), which provided principal component coefficients, scores, and explained variance. Statistical significance was assessed using a bootstrapping procedure (20,000 resamples, 95% confidence interval) and the broken stick model (Hammer, 2001).

The stalagmite MFZ-N-1 was analysed for trace elements ratios with sub-annual resolution at Centro de Geociencias, Universidad Nacional Autónoma de México (UNAM) using Laser-ablation ICP-MS with a Resonetics L-50 excimer laser-ablation workstation (ArF, $\lambda = 193\text{ns}$, 23ns FWHM, fluence of $\sim 6\text{J}/\text{cm}^2$). Details on the analytical protocols used here are described in Bernal et al (2016).

5.4.4. $\delta^{18}\text{O}$ composite

The intra-site correlation model (iscam; Fohlmeister, 2012)) was used to construct a composite record for the stalagmites (MFZ-N-1, CR-1, LB-1, and LB-3). The method correlates dated proxy records from contemporaneous stalagmites to derive a unified age–depth model and a single composite proxy series (Fohlmeister, 2012). The software assumes a common climatic signal among the input records and minimizes age uncertainties within overlapping intervals (Fohlmeister, 2012). For the composite, the age–depth modeling routine was set to point-wise linear interpolation, performing 10,000 Monte Carlo simulations on the absolute age determinations. To estimate the uncertainty of the composite age–depth model, 2,000 first-

order autoregressive (AR1) processes were generated, with 1,000 Monte Carlo simulations for each AR1 process. Age data were treated as Gaussian distributed and calculated pointwise. The individual stalagmite records were arranged from the youngest to the oldest before compositing to maximize the correlation between overlapping intervals (Fohlmeister, 2012).

5.5. Results

5.5.1. ^{230}Th -U dating

Results of the ^{230}Th /U-dating for stalagmites LB-1 and LB-3 are presented in Supplementary Table 1. Both samples show high ^{238}U concentrations, with average values of 4.8 ppm for LB-1 and 6.5 ppm for LB-3. Stalagmite LB-3 exhibits a pronounced shift in its growth axis after 2242 ± 42 yr BP associated with a detrital layer, whereas LB-1 contains a thick detrital layer with increased detrital content after 2047 ± 26 yr BP. These features are associated with major floods within Laje Branca cave. The ($^{230}\text{Th}/^{232}\text{Th}$) activity ratio, an indicator for the degree of detrital contamination, also present significant lower values after this period changing from an average value around 376,000 for LB-1 and 11,140 for LB-3, to a value of 39 and 193 for LB-1 and LB-3 respectively. Therefore, we do not account the period after ~ 2000 B.P for Laje Branca Stalagmites. The presence of detrital layers within Laje Branca stalagmites does not pose a major issue for Th contamination, as the detrital material is easily recognized visually and avoided during sampling. High U concentrations and careful sampling away from detrital horizons allow for accurate ^{230}Th /U ages, as evidenced by the high ($^{230}\text{Th}/^{232}\text{Th}$) activity ratios.

Both samples cover a similar time period with the top-most ages around ~ 2000 B.P (LB-1 top age 2047 ± 26 , LB-3 top age 2039 ± 15) and bottom most ages around ~ 7300 (LB-1 top age 7289 ± 79 , LB-3 top age 7304 ± 23 yr B.P). The U/Th-ages present 2σ errors of 0.5% or ± 16 yrs for LB-1 ages and 2σ U/Th age uncertainty of 0.3% or 17 yrs for LB-3. LB-1 shows median growth rates calculated based on U/Th age of 0.03 mm/yr and LB-3 median growth rate of 0.02 mm/yr, with both samples showing a trend towards slow growth rate throughout the Holocene, with an abrupt shift in growth rate in both records after 2000 yrs, corroborating with an hiatus related to increased flood activity in Laje Branca cave.

5.5.2. Stalagmite stable isotopes and $\delta^{18}\text{O}$ composite record

We combined the two new $\delta^{18}\text{O}$ records from Laje Branca cave (LB-1 and LB-3) with the records of Cristais and Malfazido cave (CR-1 and MFZ-N-1, respectively), presented in a manuscript in preparation (Cauhy et al, in prep-a) to construct a composite $\delta^{18}\text{O}$ covering the past 8,000 years (Fig. 5.2). The isotope record of LB-1 and LB-3 span from 2047 to 7464 B.P., and from 2242 to 7492 B.P., respectively, with decadal to multidecadal resolution (averages of

12 and 20 yrs, respectively). The aragonitic stalagmite MFZ-N-1 spans the period from 868 B.P. to -68 B.P. (2018 C.E.), with sub-annual to annual resolution (mean: 0.8 yr) and CR-1 covers the period from 4237 B.P. to 4 B.P. (1946 C.E.), with an annual to interannual resolution (mean: 2.77 yrs) (Cauhy et al, manuscript in prep. a). All records show positive correlations between $\delta^{13}\text{C}$ and $\delta^{18}\text{O}$ values, with all the calcitic stalagmites showing correlation around ~ 0.5 and the aragonitic stalagmite MFZ-N-1 showing 0.36 (Supp. Fig. 5.4). The $\delta^{18}\text{O}$ values of LB-1 and LB-3 range from -2.7‰ to -6.7‰ , with mean values of -3.8‰ and -3.7‰ , respectively. In comparison, CR-1 and MFZ-N-1 display $\delta^{18}\text{O}$ values between -2.2‰ and -7.7‰ , with an overall mean of -5.0‰ (Supp. Fig. 5.4) (Cauhy et al, in prep. a).

The composite record of four stalagmites $\delta^{18}\text{O}$ records, entitle here as SEBRA composite (MFZ-N-1 + CR-1 + LB-1 + LB-3), result in a continuous record covering the past ~ 7450 years (Fig. 5.2, 3). The correlation coefficient (r) between each measure $\delta^{18}\text{O}$ stalagmite time series is >0.67 , significant at the 95% level (Fig. 5.2). The composite is composed by 3465 $\delta^{18}\text{O}$ measurements, with an average temporal resolution of ~ 2 years, with the Middle Holocene (prior to ~ 4000) showing an average of ~ 5 years.

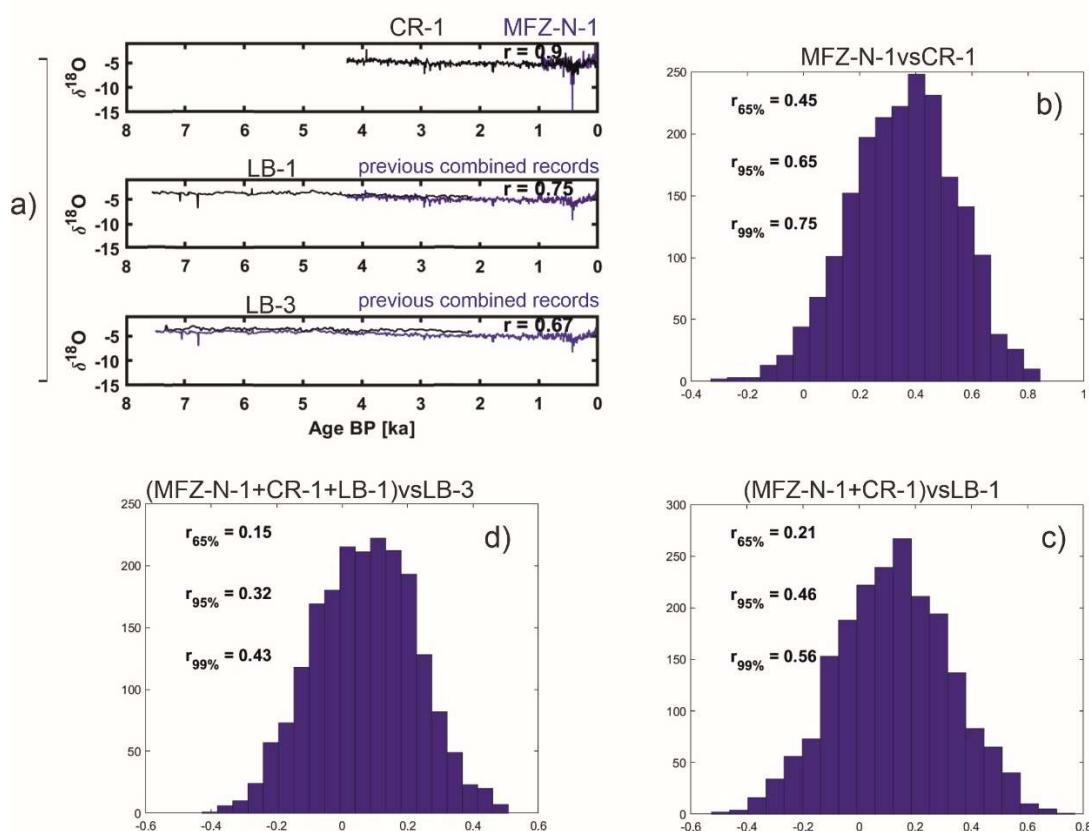


Figure 5.2 – Distribution of maximum correlation coefficients for 2000 pairs of AR1 time series with the same characteristics as the measured $\delta^{18}\text{O}$ stalagmite time series. a) Best time series results for the individual steps iscam performs for the composite time series construction. Highest correlation coefficient is indicated for each correlation step. All established time series are significant at the 95% confidence limit; b) distribution for MFZ-N-1 and CR-1; c) distribution for MFZ-N-1+CR-1 and LB-1; d) distribution for MFZ-N-1+CR-1+LB-1 and LB-3.

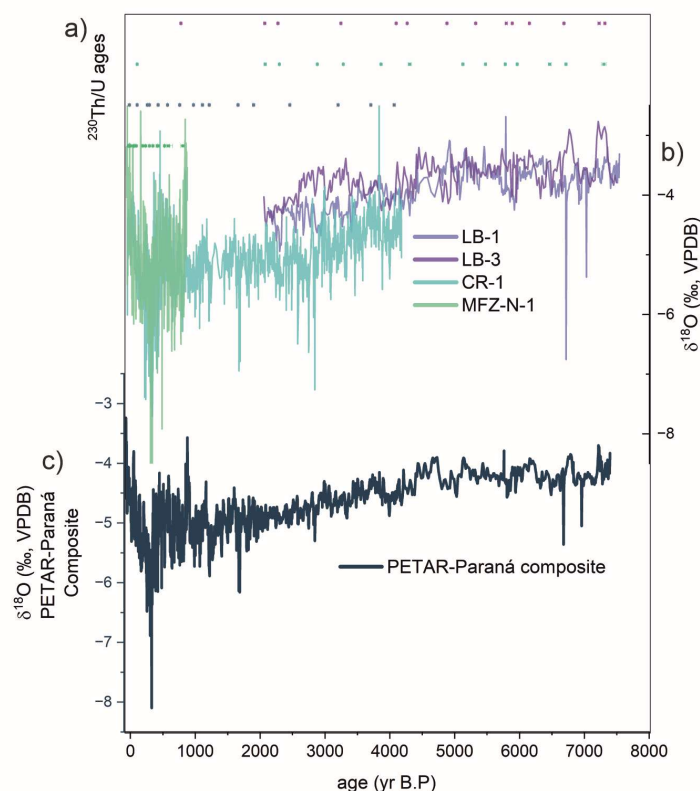


Figure 5.3 – Petar and Paraná sites stalagmites $\delta^{18}\text{O}$ records and SEBRA $\delta^{18}\text{O}$ composite. (a) $^{230}\text{Th}/\text{U}$ ages of stalagmites following the same color pattern of the records. (b) $\delta^{18}\text{O}$ records from Laje Branca (LB-1 and LB-3), Cristais cave (CR-1) and Malfazido cave (MFZ-N-1) with age model calculated using StalAge (Scholz and Hoffmann, 2011). (c) SEBRA $\delta^{18}\text{O}$ Composite constructed using iscam (Fohlmeister, 2012).

The trace elementary ratios with calcium (TE/Ca – Mg/Ca, Sr/Ca and Ba/Ca) time series of LB-3 present a sub-annual resolution with average resolution of ~ 0.2 years. Mg/Ca ratios range from 38 to 90 mmol/mol (with average of 60 mmol/mol) (Fig. 4c). The Sr/Ca time series range between 3 and 9 mmol/mol (with average values of ~ 6 mmol/mol), while Ba/Ca range from 0.17 to 0.07 mmol/mol (average of 0.11 mmol/mol) (Fig. 4b). The TE/Ca ratios present positive correlation between each other, with strong positive correlation between Sr/Ca and Ba/Ca ($r = 0.82$, $p < 0.001$) and weak to moderate correlation between Mg/Ca and the others (Mg/Ca vs Sr/Ca, $r = 0.34$, $p < 0.01$; Mg/Ca vs Ba/Ca, $r = 0.21$, $p < 0.01$) (Fig. 4b, c).

Cross-plot on ln-space were used to test for Prior Calcite Precipitation control over the trace elementary ratios following Sinclair et al (2011) and Wassenburg et al (2020) (Fig. 5.4b, c). LB-3 $\ln(\text{Mg}/\text{Ca})$ vs $\ln(\text{Sr}/\text{Ca})$ covary linearly despite the shallower slope of 0.389 ± 0.09 , while Sr/Ca present linear covariation with slope of 0.859 ± 0.004 (Fig. 5.4b, c), within the range expected for PCP as the main dominant processes over the TE/Ca ratios. These results suggest that while PCP is the dominant process affecting te/Ca variability, additional processes may modulate Mg/Ca ratios in LB-3.

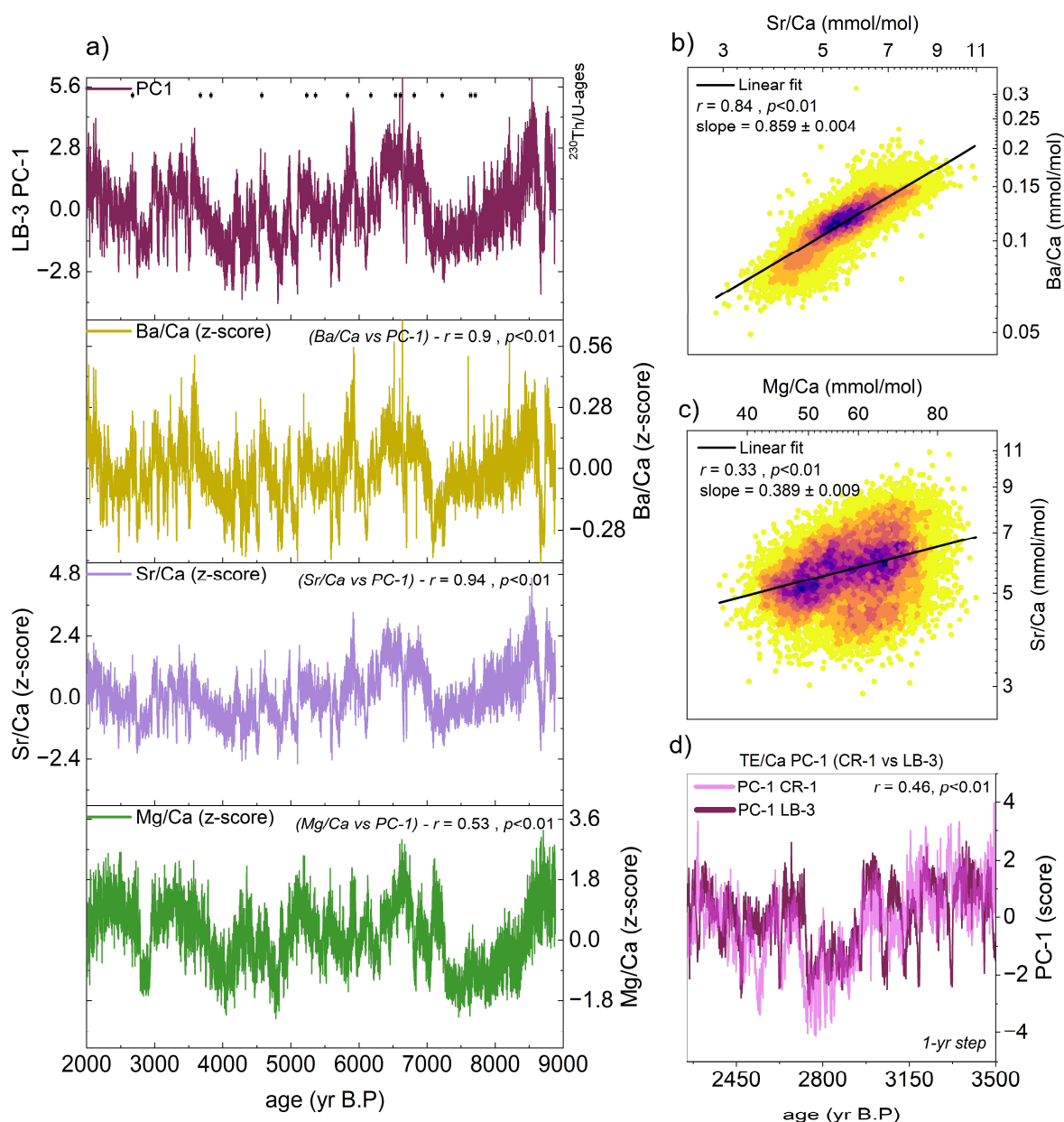


Figure 5.4 – Trace element ratios crossplot (Sinclair test) and PC-1. a) Normalized trace element time series and corresponding PC-1 scores; b–c) Cross-plots in ln-space of (b) Sr/Ca vs. Ba/Ca and (c) Mg/Ca vs. Sr/Ca. The black line represents the linear fit, and the color scale indicates point density, with blue showing higher densities. (d) Overlapping period between PC-1 from LB-3 and PC-1 from CR-1 (Cauhy et al., in prep).

Following Cauhy et al. (in prep-a) and Jamieson et al. (2016), principal component analyses (PCA) was performed in the TE/Ca in order to extract a common signal between the time series. A principal component 1 (PC-1_{LB-3}) shows eigenvalue of 1.96, explaining 65.4% of the variance, with similarly strong correlations (Mg/Ca: $r = 0.54$; Sr/Ca: $r = 0.94$; Ba/Ca: $r = 0.90$) (Fig. 5.4a). We further compare our PC-1_{LB-3} with the PCP_{CR-1}-Index (Cauhy et al., in prep-a) for the overlapping period to test our PCP hypotheses (Fig. 5.4d). A common variability is observed between the overlapping period specially between 2000-3800 B.P, with striking agreement between the overlapping period 2300-3500 B.P with positive correlation of 0.46 ($p < 0.01$) for annually interpolated time series (Fig. 5.4d), corroborating with the PCP hypothesis. The oldest part of CR-1 shows discrepancies with LB-3 record, with CR-1 also presenting a decoupling

with CR-1 $\delta^{13}\text{C}$ record. Despite these differences, the strong correspondence between the principal components derived from TE/Ca ratios in LB-3 and CR-1 indicates that the PCP index based on TE/Ca PCs effectively captures regional hydroclimate variability beyond cave-specific processes.

Since the PCs range within the same value intervals and are correlated between each other during the overlapping period, we calculate a composite time series for the annually interpolated PCP indices as the mean of both records, equally weighted (Fig. 5.5). The composite covers the period between -55 to 8800 B.P. Despite of the age-depth model cover the period until 8800 B.P the older $^{230}\text{Th}/\text{U}$ -age of LB-3 is 7304 B.P \pm 23 and therefore paleoclimatic interpretations are restricted until this period. The composite reflects CR-1 only variability prior to 2000 B.P and only LB-3 after 4000 B.P. For the overlapping period the composite present high correlation with both records (0.8 and 0.7 for CR-1 and LB-3 respectively) (Fig. 5.5). We use mainly the composite in further discussions to access the variability of hydroclimate over the Holocene.

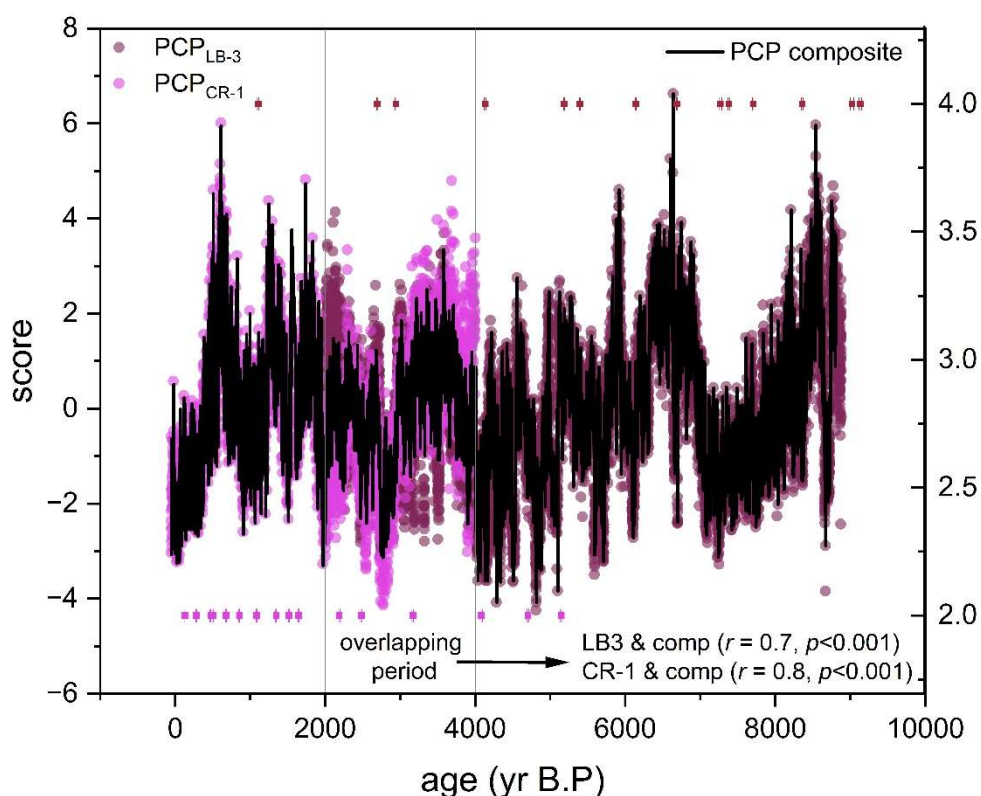


Figure 5.5 – PCP-indices and composite record. PCPCR-1 index in dotted pink (Cauhy et al, in prep) and PCPLB-3 in dotted dark red (wine). The composite time series is represented by black line. The overlapping period is marked by continuous vertical grey lines. ^{230}Th -ages are shown using the same color scheme as the respective PCs.

5.6. Discussion

5.6.1. Proxy interpretations

Trace element ratios were previously interpreted as a proxy to recharge conditions over the cave in SEBRA region (Cauhy et al, in prep-a). LB-3 present covariation between the trace

element ratios (Mg/Ca, Sr/Ca, Ba/Ca) with Sinclair test showing slopes within the expected for prior-calcite precipitation (PCP) as the dominant control over trace element variability (Sinclair, 2011; Sinclair et al., 2012; Wassenburg et al., 2020). Moreover, LB-3 principal component analysis shows striking agreement with CR-1 PC-1 for the coeval period, indicating a common variability between the records. The significant positive correlation and the common variability further support the interpretation of PCP as the main control, and the replicability between the records evidences a response to regional hydroclimate controls (such as effective rainfall over the cave sites) rather than site specific processes. We therefore use the trace element PCs as PCP indices (following Cauhy et al, in prep) and combine the records to create a composite PCP record of SEBRA. We interpret SEBRA PCP record as a suitable indicator of recharge conditions over SEBRA, with positive values indicating lower recharge (drier) over the cave site, and negative values indicating increased recharge (wet).

The $\delta^{18}\text{O}$ variability in speleothems from SEBRA region is mainly interpreted as reflecting changes in moisture contributions (source effect), driven by shifts in large-scale atmospheric circulation with changes in the relative contributions of tropical (monsoonal) versus extratropical (subtropical south Atlantic) moisture (Cruz et al., 2006, 2005b, 2005a). The main rainfall regime over the area during austral late-spring and summer is related to the SACZ, bringing isotopically depleted moisture from tropical Atlantic along Amazon basin, with SEBRA located at the exit of SACZ. Therefore, tropical Atlantic source reflects mainly the degree of rainout upstream along the moisture trajectory rather than rainfall amount on the study area, while the extratropical proximal source presents a less negative $\delta^{18}\text{O}$ values (Ampuero et al., 2020; Vasconcelos et al., 2025; Vuille and Werner, 2005). Therefore, stalagmite $\delta^{18}\text{O}$ do not only reflect changes in atmospheric circulation with different contribution from the tropical and extratropical source, but is also modulated by the rainfall upstream the tropical moisture trajectory. We combining $\delta^{18}\text{O}$ with complementary analysis (such as trace elements) in order to reconstruct a more comprehensive paleohydroclimate history of SEBRA region.

5.6.2. Hydroclimate variability over the past 7500 years

Cauhy et al. (in prep-a) identified a persistent multi-centennial pattern in the Cristais Cave trace element record (PCPCR-1) throughout the Late Holocene, characterized by alternating periods of prolonged wet and dry conditions across the SEBRA. In this study, we integrate the previously published Cristais Cave record (PCPCR-1; Cauhy et al., in prep-a) with a new high-resolution trace element record from Laje Branca Cave (PCPLB-3). The overlapping interval between both records reveals a coherent regional hydroclimatic signal, with striking agreement in trace element ratio variability between records (Fig. 5.5). Based on the consistency between the PCP indices, we constructed a composite trace element record (PCPCR-1 + PCPLB-3) that

reflects changes in effective moisture and recharge conditions above the study area. This new composite provides a robust reconstruction of hydroclimate variability over SEBRA for the past 7500 years.

Furthermore, $\delta^{18}\text{O}$ variability in SEBRA predominantly reflects large-scale atmospheric circulation shifts, specifically variations in the relative influence of monsoonal versus extratropical moisture sources (Cruz et al 2005a, b; 2006a). To explore the link between atmospheric circulation changes and local hydroclimate, we construct a $\delta^{18}\text{O}$ composite record combining four stalagmite records from SEBRA region: two records from Cauhy et al (in prep-a) with two novel $\delta^{18}\text{O}$ records from Laje Branca Cave (LB-1 and LB-3). Together, these complementary records allow us to assess whether hydroclimate variability over southeastern Brazil was associated with shifts in atmospheric circulation.

The SEBRA composite PCP record reveals a persistent multi-centennial to millennial shifts between wetter and dry conditions throughout Middle and Late Holocene (Fig. 5.6c). The recorded multi-centennial events of increased wetter conditions over SEBRA are centered at 7300, 6100, 5680, 4800, 4500, 4200, 4100, 2750, 1900, 1100 and 400-70 B.P. (Fig. 5.6c), with a duration of wet events ranging from 160 to ~500 years. The Middle Holocene shows longer wetter events (average duration of ~365 years) with the period between 4000 to 4600 B.P presenting persistent wet conditions throughout almost ~600 years. The Late Holocene presents shorter events (~250 years), with the exception to the period between Little Ice Age (LIA 400-100) and the present, with a wet anomaly persistent for almost ~500 years. The expression of multi-centennial wet events in the SEBRA $\delta^{18}\text{O}$ composite record is weak compared to the PCP record (Fig. 5.6d). Shifts from the long-term trend centered at 7300, 4800, 4300, 4100, 2750, 1100 B.P present an amplitude of around ~ 0.5‰ (Fig. 5.6d). In contrast, the last millennium presents a remarkable increase on variability attributed to significant deviations from the mean state of SAMS and SACZ displacement (Della Libera et al., 2022; Orrison et al., 2022). The most pronounced events in SAMS are attributed to the LIA, with negative excursion reaching down to -7‰, and the Medieval Climate Anomalies (MCA) (Bernal et al., 2016; Deininger et al., 2019; Della Libera et al., 2022; Orrison et al., 2022). Overall, the trace element variability presents a stronger response to the multi-centennial wet events than the $\delta^{18}\text{O}$ record.

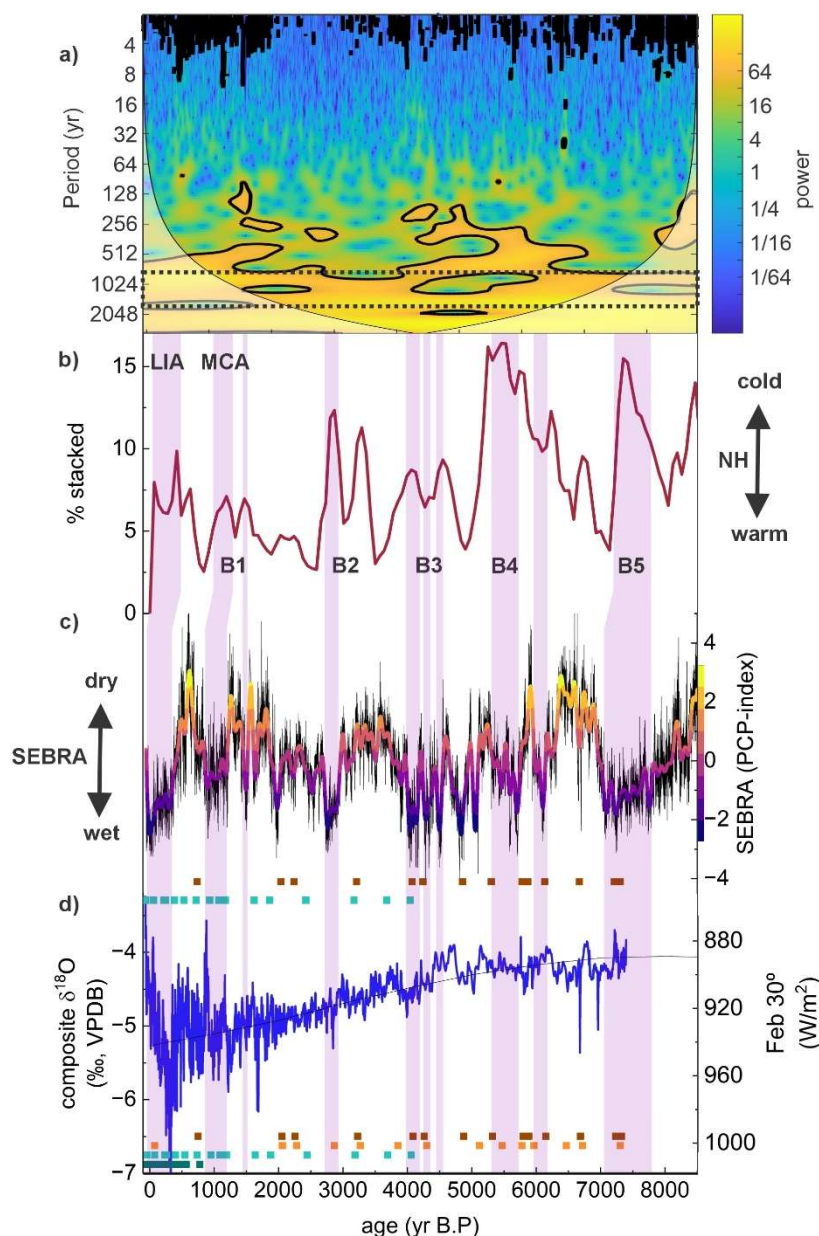


Figure 5.6 – SEBRA composite $\delta^{18}\text{O}$ and PCP index. a) Coherence Wavelet Analysis of SEBRA PCP composite, with black contour showing the significant periodicities (Grinsted et al., 2004). The dashed line marks the interval with periodicities related to Bond events (Bond et al., 2001); b) Stacked percentages of combining petrologic tracers of lithic grains in ice-raft debris (IRD) (Bond et al., 2001); c) SEBRA PCP-index (composite of $\text{PCP}_{\text{CR-1}}$ -index and $\text{PCP}_{\text{LB-3}}$ -index) with color scale showing drier (yellow) and wet (purple) conditions; d) SEBRA $\delta^{18}\text{O}$ composite and February insolation curve (30°) (Berger and Loutre, 1991). ^{230}Th -U ages are shown by square dots with error bars from top to bottom (LB-3, LB-1, CR-1 and MFZ-N-1). The pink bars show negative anomalies (wet) in SEBRA PCP-index and its potential correspondence with Bond events represented by the stacked percentages of IRD tracers.

The SEBRA $\delta^{18}\text{O}$ composite exhibits a negative trend throughout the Holocene, consistent with other SASM records driven by austral summer insolation and a progressive strengthening of monsoon activity (Bernal et al., 2016; Bustamante et al., 2016; Cruz et al., 2006, 2005a; Deininger et al., 2019; Kanner et al., 2013) (Fig. 5.6d). A similar long-term trend is observed in the trace element ratio record from Botuverá Cave (BTV; Bernal et al., 2016), indicating a coupling between $\delta^{18}\text{O}$ and trace elements in millennial scales, with enhanced precipitation over southern Brazil associated with the increase monsoon contribution over the region (Bernal et al., 2016).

In contrast, the SEBRA PCP record does not display a marked long-term trend, but instead resembles records within the SACZ region, such as Lapa Grande and Angelica Cave record, with the absence of trend over the Holocene (Strikis et al., 2011; Wong et al., 2021). The absence of a long-term trend in Lapa Grande has been interpreted as a consequence of its location within the SACZ throughout the Holocene, reflecting changes in SACZ intensity rather than latitudinal shifts in its position (Strikis et al., 2011; Wong et al., 2021). Similarly, the lack of a long-term signal in the SEBRA PCP record suggests that effective precipitation over southeastern Brazil is not primarily driven by the gradual increase in monsoon activity, as showed by the $\delta^{18}\text{O}$. Instead, the SEBRA $\delta^{18}\text{O}$ long-term trend likely reflects enhanced upstream convection and a greater degree of rainout within the monsoon core region, rather than an increased monsoon contribution to SEBRA (Ampuero et al., 2020; Vuille and Werner, 2005).

The contrasting behaviour between the Botuverá $\delta^{18}\text{O}$ and PCP records and those from SEBRA evidences a geographic complexity associated with the precipitation regime of Southern Brazil and SEBRA with distinct response to long-term variations in SASM domain precipitation, and evidences again the need for complementary analysis along $\delta^{18}\text{O}$ records to account for changes in effective precipitation.

5.6.3. Bond event expression over SEBRA region

The SEBRA PCP record presents significant responses to all Bond event observed for the middle and late Holocene. There is a striking correspondence of SEBRA record strongest wet anomalies, within age-model uncertainty, with the IRD peaks (B0-B5) in the North Atlantic (Bond et al., 2001; Fig. 5.6b). Furthermore, the wavelet coherence analysis of the SEBRA PCP record (Fig. 5.6a) reveals significant multi-centennial to millennial periodicities (~500–1500 years). This is consistent with the ~800-year pacing of wet anomalies detected in the LG $\delta^{18}\text{O}$ record (Strikis et al., 2011), also within the SACZ domain, lasting ~100–300 years, broadly consistent with the periodicity observed in SEBRA PCP record. This periodicity is consistent with the characteristic Bond-cycle frequency in Northern Hemisphere records (Bond et al., 2001; Debret et al., 2007), indicating a link between North Atlantic cold events and effective rainfall over SEBRA region, highlighting its sensitivity towards this kind of event. The relationship between North Atlantic SSTs and tropical rainfall over South America was extensively discussed for the glacial and deglacial period in several studies (Baker et al., 2009, 2005; Bustamante et al., 2016; Deininger et al., 2019; Strikis et al., 2011; Strikis et al., 2018, 2015; Vasconcelos et al., 2025).

The wet anomalies identified in SEBRA present a strong regional correspondence with other records influenced by the SASM and SACZ (Fig 5.7, 5.8). The São Mateus $\delta^{18}\text{O}$ record (Della Libera et al., 2025, accepted), located in central-eastern Brazil (Fig. 5.2d), exhibits increased $\delta^{18}\text{O}$ values synchronous with SEBRA wet phases (Fig. 5.7c, 5.8d). Variations in $\delta^{18}\text{O}$ at São Mateus are primarily driven by changes in the relative contribution of easterly (higher $\delta^{18}\text{O}$) versus SACZ (lower $\delta^{18}\text{O}$) moisture sources (Della Libera et al 2025, accepted). Thus, higher $\delta^{18}\text{O}$ values at this location indicate enhanced easterly moisture transport, consistent with intensified SACZ convection over SEBRA during Bond event intervals. This configuration suggests a southward migration of the ITCZ, which enhances trade winds flow over SMT (easterlies) and convective activity over SEBRA (Broccoli et al., 2006).

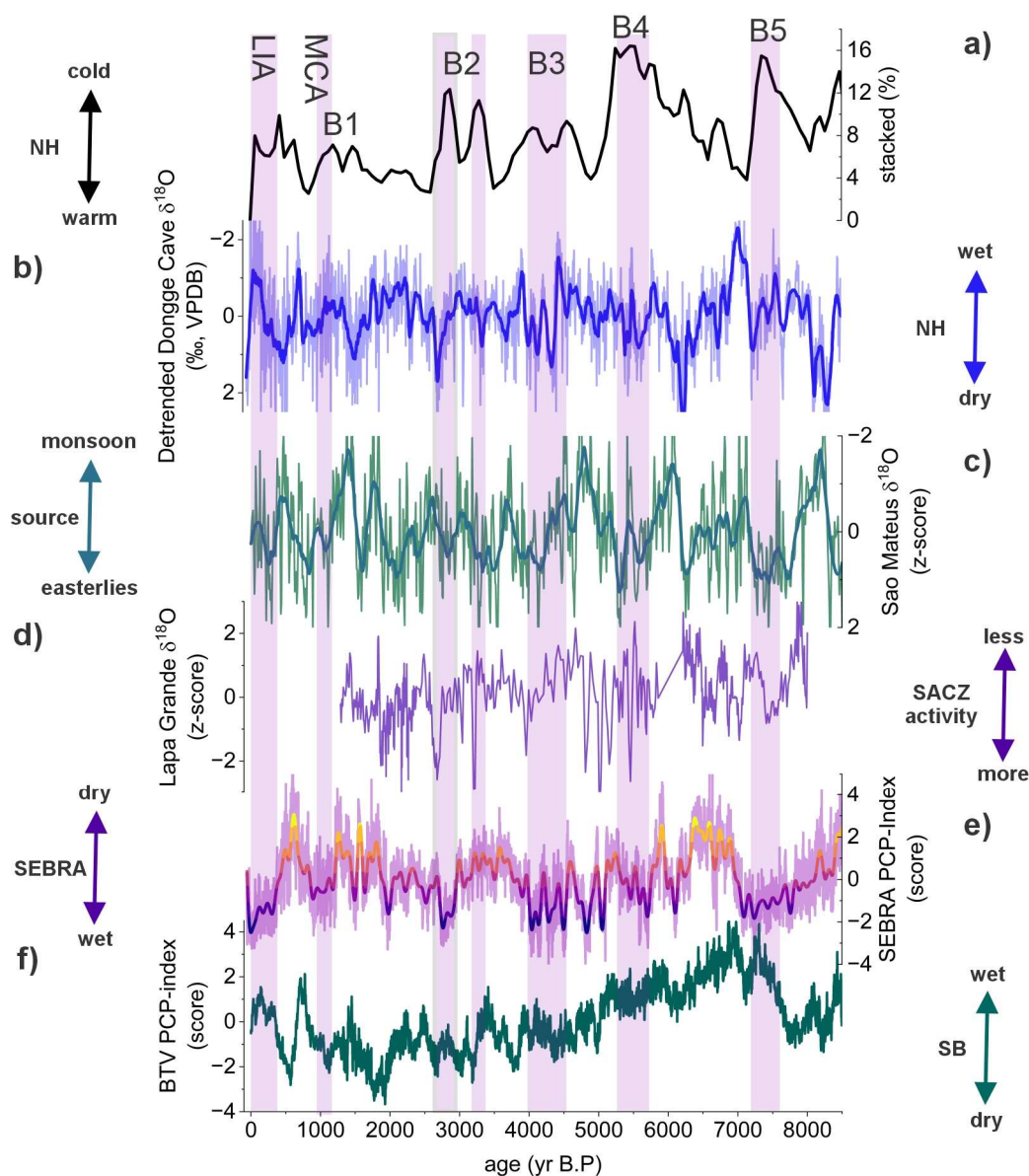


Figure 5.7 – Regional and interhemispheric comparisons; a) Stacked percentages of combining petrologic tracers of lithic grains in ice-raft debris (IRD) (Bond et al., 2001); b) Detrended Dongge $\delta^{18}\text{O}$ record from China (Dykoski et al., 2005); c) Sao Mateus $\delta^{18}\text{O}$ cave record (Della Libera et al., accepted); d) Lapa Grande $\delta^{18}\text{O}$ record (Strikis et al., 2011); SEBRA PCP-index (composite of $\text{PCP}_{\text{CR-1}}$ -index and $\text{PCP}_{\text{LB-3}}$ -index); Botuverá PCP-index record (Bernal et al., 2016). The pink bars represent intervals of peaked IRD occurrence in North Atlantic.

Moreover, an interhemispheric coupling is also evident between SEBRA and the Dongge Cave $\delta^{18}\text{O}$ record from China (Fig. 5.7b, 5.8a, g). Multi-centennial wet anomalies in SEBRA coincide with dry conditions in Dongge Cave, indicating an anti-phasing between tropical South America and Asia monsoon (Stríkis et al., 2011). The anti-phase relationship between these two monsoons systems was also observed for Bond event 5 (8.2 kyr event) (Zhang et al., 2025). Our comparisons evidences how this relationship is consistent in multi-centennial scales (attributed to Bond events), reflecting the interhemispheric signature of Bond events and global reorganizations of the ITCZ and monsoon systems.

The Botuverá Cave record in southern Brazil (Bernal et al., 2016) exhibits both wet (Fig. 5.8i) and dry (Fig. 5.8f) anomalies during Bond events, with marked antiphase with SEBRA during Bond 2 (Fig. 5.8f). This antiphase between SEBRA and Southern Brazil is attributed to variations in low-level moisture trajectories associated with the SACZ and the South American Low-Level Jet (SALLJ) over multi-centennial time-scales (Cauhy et al, in prep). The rainfall dipole between these regions, evident at intraseasonal (Boers et al., 2014) and multi-centennial scales (Cauhy et al, in prep), also persists at millennial timescales (Vasconcelos et al., 2025), evidences a non-stationary pattern with alternating periods of phase and anti-phase between the regions (Vasconcelos et al., 2025). Consequently, the hydroclimatic response to Bond events in southern Brazil exhibits a more complex and variable expression over multi-centennial timescales.

The connection between North Atlantic SST variability and tropical South American hydroclimate has been well established in regions influenced by the SASM (Baker et al., 2009; Stríkis et al., 2011; Novello et al., 2012; Bustamante et al., 2016). Collectively, these studies suggest that Bond-type events in South America manifest primarily as multi-centennial wet episodes across the Andes and central-eastern Brazil, coincident with drying north of the Equator (Deiniger et al., 2019). This antiphase pattern reflects large-scale teleconnections via changes in the mean ITCZ position due to Northern Hemisphere climate variability, which leads to changes in SACZ intensity and/or its position over South America (Stríkis et al., 2011).

5.6.4. Internal structures of Bond Events in South America

The Bond Events 2 and 3 show the most coherent and consistent intra-event patterns across SEBRA, SASM (Della Libera et al., 2022), ITCZ (Utida et al., 2023), SACZ (Stríkis et al., 2011; Della Libera et al., accepted), and Northern Hemisphere records (Bond et al., 2001; Dykoski et al., 2005) (Figs. 5.7, 5.8), evidencing an agreement between different rainfall domains and hemispheres on multi-centennial time scales. This synchronicity between different rainfall domains (Ferreira and Reboita, 2022) and hemispheres support the idea of the coupled mechanism related to the waken of AMOC with decreased cross equatorial interhemispheric

heat transport, with southward ITCZ displacement modulating tropical rainfall over SASM and SACZ (Strikis et al., 2011, 2018, 2015).

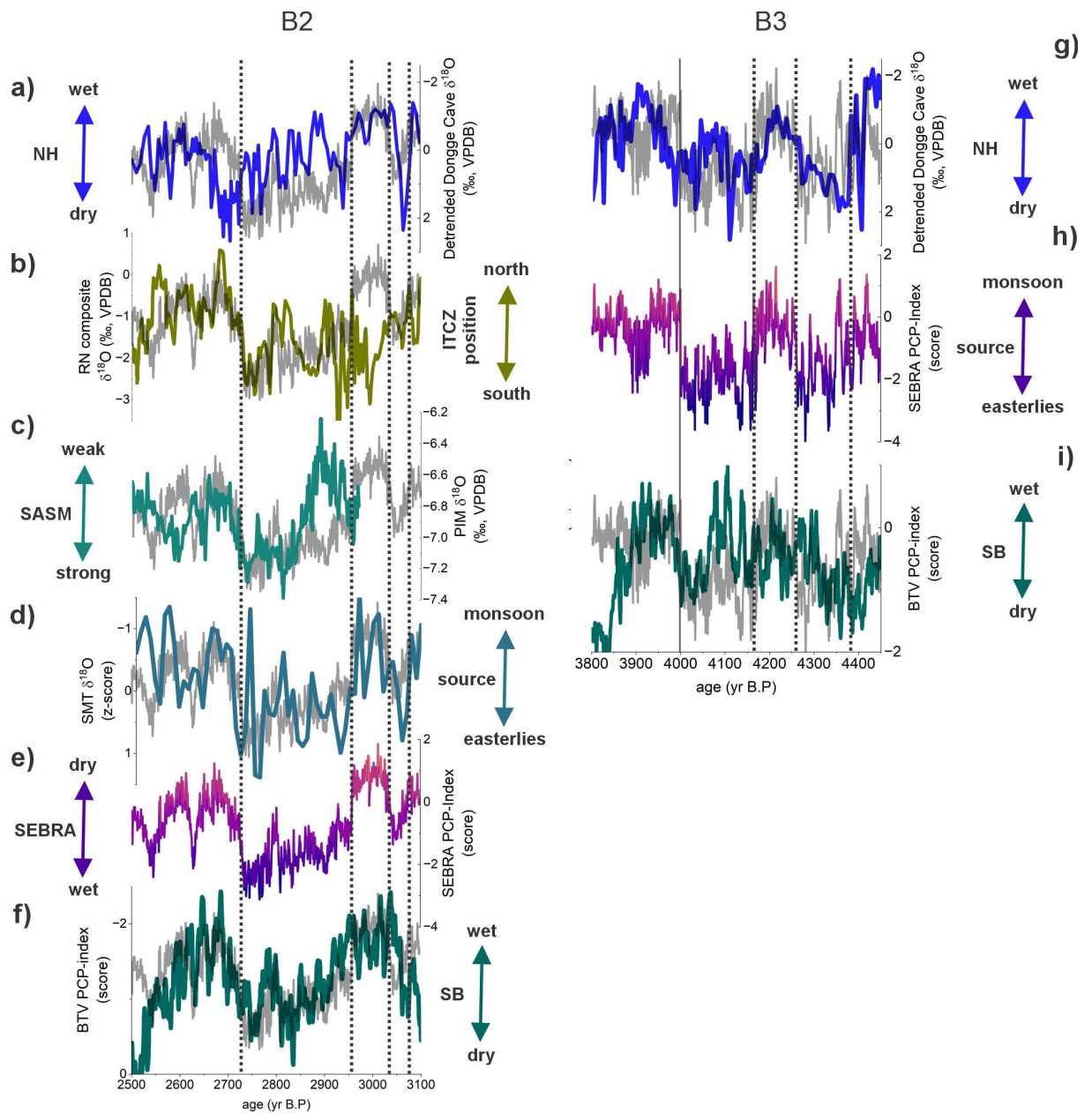


Figure 5.8 – a-f) Period related to Bond event 2; g-i) period related to Bond event 3 (4.2 kyr event); major deviations from SEBRA PCP record marked by dashed lines. a and g) Detrended Dongge $\delta^{18}\text{O}$ record from China (Dykoski et al., 2005); b) Rio Grande do Norte $\delta^{18}\text{O}$ composite (Utida et al., 2023); c) Cuica $\delta^{18}\text{O}$ cave record (Della Libera et al., 2022); d) Sao Mateus $\delta^{18}\text{O}$ cave record (Della Libera et al., accepted); e and h) SEBRA PCP-index (composite of $\text{PCP}_{\text{CR-1}}$ -index and $\text{PCP}_{\text{LB-3}}$ -index); f and i) Botuverá PCP-index record (Bernal et al., 2016).

The wet anomaly associated with Bond Event 2 in SEBRA is marked by a pronounced deviation from the local mean (Fig. 5.8e), with onset around 2960 yr BP and termination approximately at 2730 yr BP. The internal structure of the event is marked by a progressive negative trend in PCP values toward wetter conditions throughout this interval. A comparable but antiphase structure is observed in the Botuverá Cave record, where a positive PCP index excursion indicates drier conditions in southern Brazil (Fig. 5.8f) (Bernal et al., 2016). This opposite-phase behaviour evidences the multi-centennial hydroclimatic dipole between

SEBRA and southern Brazil (Cauhy et al., in prep-a), modulated by shifts in low-level jet, specifically, the interplay between the SACZ and the South American Low-Level Jet (SALLJ) (Cauhy et al., in prep-a).

On the other hand, other regional sites from SASM (Fig. 5.8c), ITCZ (Fig. 5.8b) and SACZ (Fig. 5.8d) resembles the structure and timing of SEBRA PCP record for the Bond event 2 with general enhanced convective activity over the different rainfall domains near 2.7 ka. For instance, the São Mateus cave $\delta^{18}\text{O}$ record (Della Libera et al., accepted) shows a synchronous rise in the $\delta^{18}\text{O}$ consistent with an increased contribution of easterly moisture sources during the Bond event. Also, the Cuíca Cave $\delta^{18}\text{O}$ record in lowland southwestern Amazon basin (PIM, Della Libera et al., 2022) presents the same wet event, but its onset appears roughly 100 years later. At the northern margin of the system, the Rio Grande do Norte record, reflecting ITCZ-related moisture variability (RN - Utida et al., 2023), shows a synchronous shift toward lower $\delta^{18}\text{O}$ values, consistent with a southward displacement of the ITCZ (Utida et al., 2023). Finally, this structure is observed even at the inter-hemisphere spatial-scale (Fig. 5.8a). The Dongge Cave $\delta^{18}\text{O}$ record reveals concomitantly dry conditions, with an onset synchronous with SEBRA and a termination lag of ~40 years, accompanied by a gradual drying trend within the event (Fig. 5.8a).

Moreover, the climate anomaly associated with Bond Event 3 also presents a strong expression in our SEBRA PCP record (Fig. 5.8h). It presents a distinctive double-plunge structure, characterized by two pronounced wet intervals between ~4350–4260 yr BP and ~4160–4000 yr BP. The Botuverá Cave record displays a comparable double-plunge morphology in antiphase, with a short-wet phase between ~4100 and 4060 yr BP. Similarly, the Dongge Cave $\delta^{18}\text{O}$ record exhibits an analogous double-plunge structure, with synchronous onsets and similar pacing, highlighting the globally coherent, interhemispheric expression of this event.

Together, these records indicate a regionally coherent intensification of convection across the SASM domain during these Northern Hemisphere cooling episode, with only Southern Brazil showing a drier response due to the dipole dynamics between SEBRA and southern Brazil (Cauhy et al., in prep-a).

5.7. Summary and implications

Our findings reveal that multi-centennial hydroclimatic variability in southeastern Brazil confirms a persistent and sensitive interhemispheric teleconnection to North Atlantic Climate on multiple time-scales (Baker et al., 2005; Strikis et al., 2018, 2015, 2011; Vasconcelos et al., 2025).

The coherence between regional records along SASM, SACZ and ITCZ, and the antiphase with Asian monsoon during Bond events indicates that the multi-centennial shifts observed in SEBRA hydroclimate is mainly reflecting large-scale reorganizations of the ITCZ–SACZ system related to changes in the cross-equatorial heat transport related to waken of AMOC (Cheng et al., 2009; Strikis et al., 2011).

The spectral coherence with Bond periodicities further contributes to this interpretation with interhemispheric ocean–atmosphere coupling modulating SEBRA rainfall (Debret et al., 2007; Strikis et al., 2011). These results demonstrate that even during periods of relatively stable AMOC and insolation, such as Bond Events 2 and 3, Northern Hemisphere cooling and southward ITCZ displacement exerted a significant influence on SEBRA hydroclimate. This sensitivity to modest perturbations in the interhemispheric energy balance indicates the vulnerability of SEBRA rainfall regime to future changes in Atlantic circulation. Given projections of AMOC weakening and hemispheric asymmetries under anthropogenic warming, the SEBRA record provides a valuable analogy for assessing future hydroclimatic responses. More broadly, the integration of stalagmite PCP and $\delta^{18}\text{O}$ proxies offers a comprehensive reconstruction of spatial patterns (Cauhy et al., in prep-a), mechanisms, and climate impacts of Bond-like variability, providing critical constraints for testing and refining climate models aimed at predicting future monsoon and SACZ behaviour under ongoing climate change (Kageyama et al., 2024).

5.8. References

- Ampuero, A., Stríkis, N.M., Apaéstegui, J., Vuille, M., Novello, V.F., Espinoza, J.C., Cruz, F.W., Vonhof, H., Mayta, V.C., Martins, V.T.S., Cordeiro, R.C., Azevedo, V., Sifeddine, A., 2020. The Forest Effects on the Isotopic Composition of Rainfall in the Northwestern Amazon Basin. *JGR Atmospheres* 125, e2019JD031445. <https://doi.org/10.1029/2019JD031445>
- Baker, P.A., Fritz, S.C., Burns, S.J., Ekdahl, E., Rigsby, C.A., 2009. The Nature and Origin of Decadal to Millennial Scale Climate Variability in the Southern Tropics of South America: The Holocene Record of Lago Umayo, Peru, in: Vimeux, F., Sylvestre, F., Khodri, M. (Eds.), *Past Climate Variability in South America and Surrounding Regions, Developments in Paleoenvironmental Research*. Springer Netherlands, Dordrecht, pp. 301–322. https://doi.org/10.1007/978-90-481-2672-9_13
- Baker, P.A., Fritz, S.C., Garland, J., Ekdahl, E., 2005. Holocene hydrologic variation at Lake Titicaca, Bolivia/Peru, and its relationship to North Atlantic climate variation. *J Quaternary Science* 20, 655–662. <https://doi.org/10.1002/jqs.987>
- Berger, A., Loutre, M.F., 1991. Insolation values for the climate of the last 10 million years. *Quaternary Science Reviews* 10, 297–317. [https://doi.org/10.1016/0277-3791\(91\)90033-Q](https://doi.org/10.1016/0277-3791(91)90033-Q)
- Bernal, J.P., Cruz, F.W., Stríkis, N.M., Wang, X., Deininger, M., Catunda, M.C.A., Ortega-Obregón, C., Cheng, H., Edwards, R.L., Auler, A.S., 2016. High-resolution Holocene South American monsoon history recorded by a speleothem from Botuverá Cave, Brazil. *Earth and Planetary Science Letters* 450, 186–196. <https://doi.org/10.1016/j.epsl.2016.06.008>
- Boers, N., Rheinwalt, A., Bookhagen, B., Barbosa, H.M.J., Marwan, N., Marengo, J., Kurths, J., 2014. The South American rainfall dipole: A complex network analysis of extreme events. *Geophysical Research Letters* 41, 7397–7405. <https://doi.org/10.1002/2014GL061829>
- Bond, G., Kromer, B., Beer, J., Muscheler, R., Evans, M.N., Showers, W., Hoffmann, S., Lotti-Bond, R., Hajdas, I., Bonani, G., 2001. Persistent Solar Influence on North Atlantic Climate During the Holocene. *Science* 294, 2130–2136. <https://doi.org/10.1126/science.1065680>
- Bond, G., Showers, W., Cheseby, M., Lotti, R., Almasi, P., deMenocal, P., Priore, P., Cullen, H., Hajdas, I., Bonani, G., 1997. A Pervasive Millennial-Scale Cycle in North Atlantic Holocene and Glacial Climates. *Science* 278, 1257–1266. <https://doi.org/10.1126/science.278.5341.1257>
- Broccoli, A.J., Dahl, K.A., Stouffer, R.J., 2006. Response of the ITCZ to Northern Hemisphere cooling. *Geophysical Research Letters* 33, 2005GL024546. <https://doi.org/10.1029/2005GL024546>
- Bustamante, M.G., Cruz, F.W., Vuille, M., Apaéstegui, J., Stríkis, N., Panizo, G., Novello, F.V., Deininger, M., Sifeddine, A., Cheng, H., Moquet, J.S., Guyot, J.L., Santos, R.V., Segura, H., Edwards, R.L., 2016. Holocene changes in monsoon precipitation in the Andes of NE Peru based on $\delta^{18}\text{O}$ speleothem records. *Quaternary Science Reviews* 146, 274–287. <https://doi.org/10.1016/j.quascirev.2016.05.023>
- Cheng, H., Fleitmann, D., Edwards, R.L., Wang, X., Cruz, F.W., Auler, A.S., Mangini, A., Wang, Y., Kong, X., Burns, S.J., Matter, A., 2009. Timing and structure of the 8.2 kyr B.P. event inferred from $\delta^{18}\text{O}$ records of stalagmites from China, Oman, and Brazil. *Geology* 37, 1007–1010. <https://doi.org/10.1130/G30126A.1>

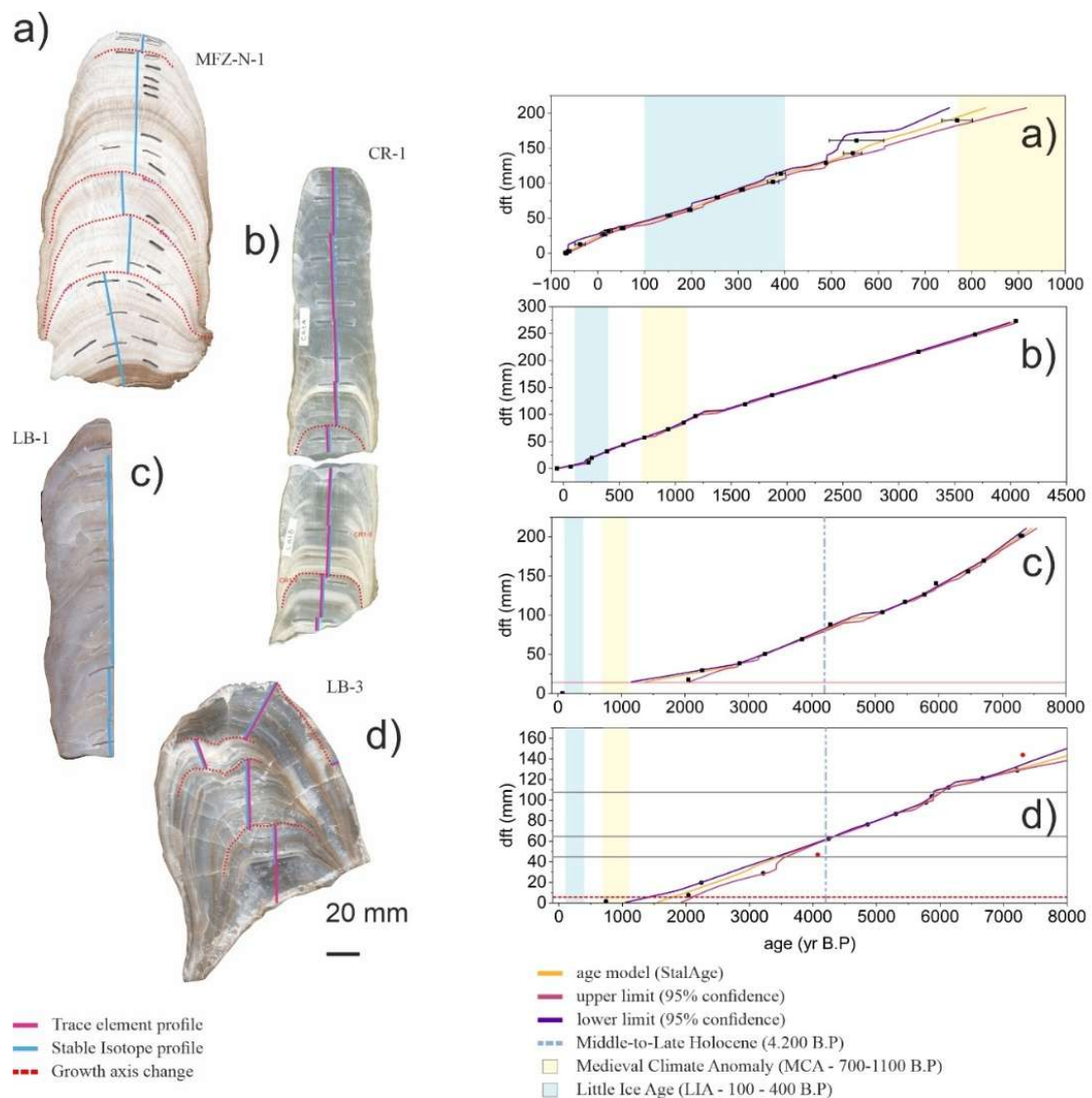
- Cheng, H., Lawrence Edwards, R., Shen, C.-C., Polyak, V.J., Asmerom, Y., Woodhead, J., Hellstrom, J., Wang, Y., Kong, X., Spötl, C., Wang, X., Calvin Alexander, E., 2013. Improvements in ^{230}Th dating, ^{230}Th and ^{234}U half-life values, and U–Th isotopic measurements by multi-collector inductively coupled plasma mass spectrometry. *Earth and Planetary Science Letters* 371–372, 82–91. <https://doi.org/10.1016/j.epsl.2013.04.006>
- Chiessi, C.M., Mulitza, S., Mollenhauer, G., Silva, J.B., Groeneveld, J., Prange, M., 2015. Thermal evolution of the western South Atlantic and the adjacent continent during Termination 1. *Clim. Past* 11, 915–929. <https://doi.org/10.5194/cp-11-915-2015>
- Cruz, F.W., Burns, S.J., Karmann, I., Sharp, W.D., Vuille, M., 2006. Reconstruction of regional atmospheric circulation features during the late Pleistocene in subtropical Brazil from oxygen isotope composition of speleothems. *Earth and Planetary Science Letters* 248, 495–507. <https://doi.org/10.1016/j.epsl.2006.06.019>
- Cruz, F.W., Burns, S.J., Karmann, I., Sharp, W.D., Vuille, M., Cardoso, A.O., Ferrari, J.A., Silva Dias, P.L., Viana, O., 2005a. Insolation-driven changes in atmospheric circulation over the past 116,000 years in subtropical Brazil. *Nature* 434, 63–66. <https://doi.org/10.1038/nature03365>
- Cruz, F.W., Karmann, I., Viana, O., Burns, S.J., Ferrari, J.A., Vuille, M., Sial, A.N., Moreira, M.Z., 2005b. Stable isotope study of cave percolation waters in subtropical Brazil: Implications for paleoclimate inferences from speleothems. *Chemical Geology* 220, 245–262. <https://doi.org/10.1016/j.chemgeo.2005.04.001>
- Debret, M., Bout-Roumazielles, V., Grousset, F., Desmet, M., McManus, J.F., Massei, N., Sebag, D., Copard, Y., Trentesaux, A., 2007. The origin of the 1500-year climate cycles in Holocene North-Atlantic records. *Clim. Past*.
- Deininger, M., Ward, B.M., Novello, V.F., Cruz, F.W., 2019. Late Quaternary Variations in the South American Monsoon System as Inferred by Speleothems—New Perspectives Using the SISAL Database. *Quaternary* 2, 6. <https://doi.org/10.3390/quat2010006>
- Dykoski, C., Edwards, R., Cheng, H., Yuan, D., Cai, Y., Zhang, M., Lin, Y., Qing, J., An, Z., Revenaugh, J., 2005. A high-resolution, absolute-dated Holocene and deglacial Asian monsoon record from Dongge Cave, China. *Earth and Planetary Science Letters* 233, 71–86. <https://doi.org/10.1016/j.epsl.2005.01.036>
- Evangelista, H., Gurgel, M., Sifeddine, A., Rigozo, N.R., Boussafir, M., 2014. South Tropical Atlantic anti-phase response to Holocene Bond Events. *Palaeogeography, Palaeoclimatology, Palaeoecology* 415, 21–27. <https://doi.org/10.1016/j.palaeo.2014.07.019>
- Ferreira, G.W.S., Reboita, M.S., 2022. A New Look into the South America Precipitation Regimes: Observation and Forecast. *Atmosphere* 13, 873. <https://doi.org/10.3390/atmos13060873>
- Fohlmeister, J., 2012. A statistical approach to construct composite climate records of dated archives. *Quaternary Geochronology* 14, 48–56. <https://doi.org/10.1016/j.quageo.2012.06.007>
- Grinsted, A., Moore, J.C., Jevrejeva, S., 2004. Application of the cross wavelet transform and wavelet coherence to geophysical time series. *Nonlin. Processes Geophys.* 11, 561–566. <https://doi.org/10.5194/npg-11-561-2004>
- Jamieson, R.A., Baldini, J.U.L., Brett, M.J., Taylor, J., Ridley, H.E., Ottley, C.J., Pruffer, K.M., Wassenburg, J.A., Scholz, D., Breitenbach, S.F.M., 2016. Intra- and inter-annual uranium concentration variability in a Belizean stalagmite controlled by prior aragonite precipitation: A new tool for reconstructing hydro-climate using aragonitic

- speleothems. *Geochimica et Cosmochimica Acta* 190, 332–346. <https://doi.org/10.1016/j.gca.2016.06.037>
- Jochum, K.P., Stoll, B., Herwig, K., Willbold, M., 2007. Validation of LA-ICP-MS trace element analysis of geological glasses using a new solid-state 193 nm Nd:YAG laser and matrix-matched calibration. *J. Anal. At. Spectrom.* 22, 112–121. <https://doi.org/10.1039/B609547J>
- Kageyama, M., Braconnot, P., Chiessi, C.M., Rehfeld, K., Ait Brahim, Y., Dütsch, M., Gwinneth, B., Hou, A., Loutre, M.-F., Hendrizan, M., Meissner, K., Mongwe, P., Otto-Bliesner, B., Pezzi, L.P., Rovere, A., Seltzer, A., Sime, L., Zhu, J., 2024. Lessons from paleoclimates for recent and future climate change: opportunities and insights. *Front. Clim.* 6, 1511997. <https://doi.org/10.3389/fclim.2024.1511997>
- Kanner, L.C., Burns, S.J., Cheng, H., Edwards, R.L., Vuille, M., 2013. High-resolution variability of the South American summer monsoon over the last seven millennia: Insights from a speleothem record from the central Peruvian Andes. *Quaternary Science Reviews* 75, 1–10. <https://doi.org/10.1016/j.quascirev.2013.05.008>
- Libera, M.E.D., Novello, V.F., Cruz, F.W., Orrison, R., Vuille, M., Maezumi, S.Y., Souza, J. de, Cauhy, J., Campos, J.L.P.S., Ampuero, A., Utida, G., Stríkis, N.M., Stumpf, C.F., Azevedo, V., Zhang, H., Edwards, R.L., Cheng, H., 2022. Paleoclimatic and paleoenvironmental changes in Amazonian lowlands over the last three millennia. *Quaternary Science Reviews* 279. <https://doi.org/10.1016/j.quascirev.2022.107383>
- Meccia, V.L., Blázquez, J., 2025. Impacts of a Reduced AMOC on the South America Mean Climate and Extremes. *JGR Atmospheres* 130, e2025JD044103. <https://doi.org/10.1029/2025JD044103>
- Medina, N.M.M., Cruz, F.W., Winter, A., Zhang, H., Ampuero, A., Vuille, M., Mayta, V.C., Campos, M.C., Rámirez, V.M., Utida, G., Zúñiga, A.C., Cheng, H., 2023. Atlantic ITCZ variability during the Holocene based on high-resolution speleothem isotope records from northern Venezuela. *Quaternary Science Reviews* 307, 108056. <https://doi.org/10.1016/j.quascirev.2023.108056>
- Orrison, R., Vuille, M., Smerdon, J.E., Apaéstegui, J., Campos, J.L.P.S., Cruz, F.W., Libera, M.E.D., 2022. South American Monsoon variability over the last millennium in paleoclimate records and isotope-enabled climate models. <https://doi.org/10.5194/cp-2022-6>
- Scholz, D., Hoffmann, D.L., 2011. StalAge – An algorithm designed for construction of speleothem age models. *Quaternary Geochronology* 6, 369–382. <https://doi.org/10.1016/j.quageo.2011.02.002>
- Sinclair, D.J., 2011. Two mathematical models of Mg and Sr partitioning into solution during incongruent calcite dissolution. *Chemical Geology* 283, 119–133. <https://doi.org/10.1016/j.chemgeo.2010.05.022>
- Sinclair, D.J., Banner, J.L., Taylor, F.W., Partin, J., Jenson, J., Mylroie, J., Goddard, E., Quinn, T., Jocson, J., Miklavič, B., 2012. Magnesium and strontium systematics in tropical speleothems from the Western Pacific. *Chemical Geology* 294–295, 1–17. <https://doi.org/10.1016/j.chemgeo.2011.10.008>
- Stríkis, N.M., Chiessi, C.M., Cruz, F.W., Vuille, M., Cheng, H., De Souza Barreto, E.A., Mollenhauer, G., Kasten, S., Karmann, I., Edwards, R.L., Bernal, J.P., Sales, H.D.R., 2015. Timing and structure of Mega-SACZ events during Heinrich Stadial 1. *Geophysical Research Letters* 42, 5477. <https://doi.org/10.1002/2015GL064048>
- Stríkis, N.M., Cruz, F.W., Barreto, E.A.S., Naughton, F., Vuille, M., Cheng, H., Voelker, A.H.L., Zhang, H., Karmann, I., Edwards, R.L., Auler, A.S., Santos, R.V., Sales, H.R., 2018. South

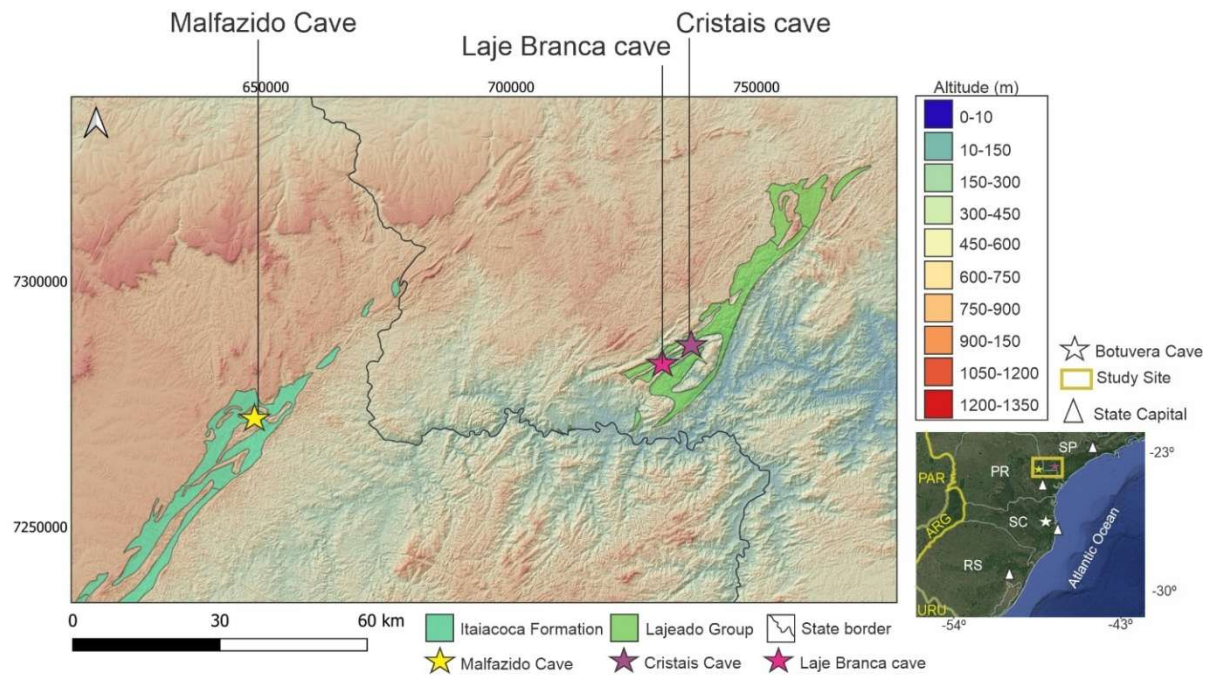
- American monsoon response to iceberg discharge in the North Atlantic. *Proc. Natl. Acad. Sci. U.S.A.* 115, 3788–3793. <https://doi.org/10.1073/pnas.1717784115>
- Strikis, N.M., Cruz, F.W., Cheng, H., Karmann, I., Edwards, R.L., Vuille, M., Wang, X., De Paula, M.S., Novello, V.F., Auler, A.S., 2011. Abrupt variations in South American monsoon rainfall during the Holocene based on a speleothem record from central-eastern Brazil. *Geology* 39, 1075–1078. <https://doi.org/10.1130/G32098.1>
- Strikis, N.M., Cruz, F.W., Cheng, H., Karmann, I., Edwards, R.L., Vuille, M., Wang, X., Paula, M.S. de, Novello, V.F., Auler, A.S., 2011. Abrupt variations in South American monsoon rainfall during the Holocene based on a speleothem record from central-eastern Brazil. *Geology* 39, 1075–1078. <https://doi.org/10.1130/G32098.1>
- Utida, G., Cruz, F.W., Vuille, M., Ampuero, A., Novello, V.F., Maksic, J., Sampaio, G., Cheng, H., Zhang, H., Andrade, F.R.D.D., Edwards, R.L., 2023. Spatiotemporal Intertropical Convergence Zone dynamics during the last 3 millennia in northeastern Brazil and related impacts in modern human history. *Climate of the Past* 19, 1975–1992. <https://doi.org/10.5194/cp-19-1975-2023>
- Vasconcelos, L.C., Cruz, F.W., Bernal, J.P., Campos, M.C., Piacsek, P., Campos, J.L., Zhang, H., Strikis, N., Vuille, M., Utida, G., Millo, C., Edward, R.L., Cheng, H., 2025. The coupling between monsoon rainfall and Sea Surface Temperature in the subtropical South Atlantic during the Last Glacial Period. *Global and Planetary Change* 255, 105121. <https://doi.org/10.1016/j.gloplacha.2025.105121>
- Vuille, M., Werner, M., 2005. Stable isotopes in precipitation recording South American summer monsoon and ENSO variability: observations and model results. *Climate Dynamics* 25, 401–413. <https://doi.org/10.1007/s00382-005-0049-9>
- Wassenburg, J.A., Riechelmann, S., Schröder-Ritzrau, A., Riechelmann, D.F.C., Richter, D.K., Immenhauser, A., Terente, M., Constantin, S., Hachenberg, A., Hansen, M., Scholz, D., 2020. Calcite Mg and Sr partition coefficients in cave environments: Implications for interpreting prior calcite precipitation in speleothems. *Geochimica et Cosmochimica Acta* 269, 581–596. <https://doi.org/10.1016/j.gca.2019.11.011>
- Wong, M.L., Wang, X., Latrubesse, E.M., He, S., Bayer, M., 2021. Variations in the South Atlantic Convergence Zone over the mid-to-late Holocene inferred from speleothem $\delta^{18}\text{O}$ in central Brazil. *Quaternary Science Reviews* 270, 107178. <https://doi.org/10.1016/j.quascirev.2021.107178>
- Zepner, L., Karrasch, P., Wiemann, F., Bernard, L., 2021. ClimateCharts.net – an interactive climate analysis web platform. *International Journal of Digital Earth* 14, 338–356. <https://doi.org/10.1080/17538947.2020.1829112>
- Zhang, X., Zhang, H., Zhang, R., Wang, J., Wang, M., Liang, Z., He, M., Wei, R., Cheng, H., 2025. Spatiotemporal pattern of the East Asian monsoon hydroclimate during the 8.2 ka event inferred from a new speleothem multi-proxy record from SE China. *Quaternary Science Reviews* 349, 109141. <https://doi.org/10.1016/j.quascirev.2024.109141>

5.9. Supplementary material – Manuscript III

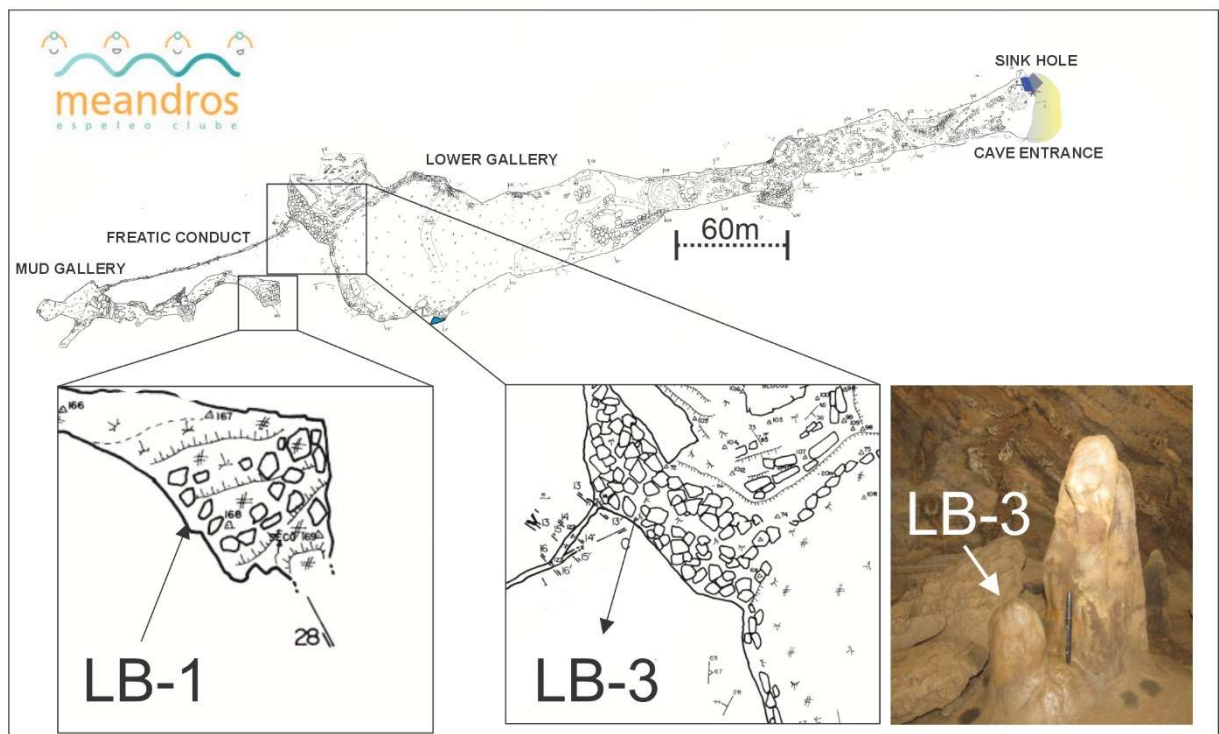
5.9.1. Supplementary Figures



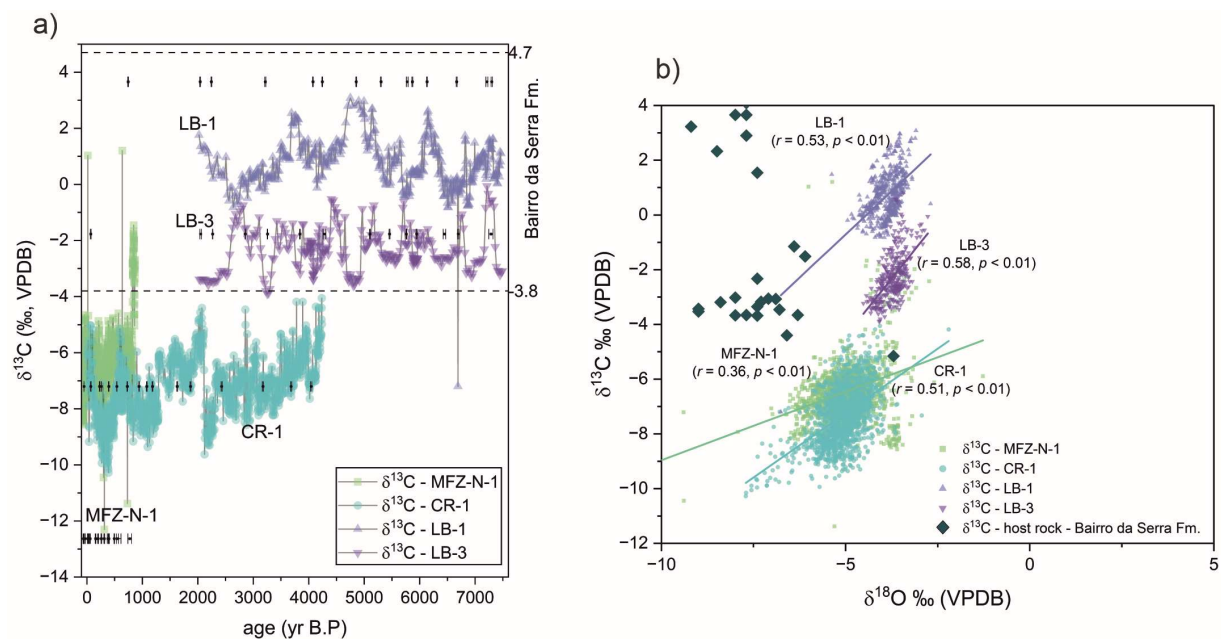
Supplementary Figure 5.1 – Stalagmite samples and analyses profile (trace elements and stable isotopes) indicated and $^{230}\text{Th}/\text{U}$ -ages and age models. a) MFZ-N-1 (Malfazido cave); b) CR-1 (Cristais cave); c-d) LB-1 and LB-3 respectively (Laje Branca cave). The age models showed here were reconstructed using StalAge (Scholz and Hoffman 2011).



Supplementary Figure 5.2 - Hypsometric map of the study area showing elevation (a.s.l.), carbonate units, and cave sites. Purple, Pink and yellow stars mark the locations of Cristais, Laje Branca and Malfazido caves, respectively. The black line indicates the state border between Paraná (west) and São Paulo (east). Carbonate units corresponding to the Itaiococa Formation and Lajeado Group are highlighted (Caltabellotta et al. (2017)). The map in the bottom-right shows the regional context in southeastern/southern Brazil, with the white star marking the location of Botuverá Cave in Santa Catarina State.



Supplementary Figure 5.3 – Laje Branca cave topography map provided by Meandros espeleo group. Details on the sample collection sites, and picture of LB-3 in-situ. LB-1 was collected in the 1990s and therefore we do not have a picture of its exactly location within the cave.



Supplementary Figure 5.4 – a) $\delta^{13}\text{C}$ records from SEBRA. The dashed lines indicate the isotopic composition range for the host rock of Laje Branca cave according to Paula-Santos et al. (2021). $^{230}\text{Th}/\text{U}$ ages are represented by dots with error bars; b) Cross plot between stable isotopes ($\delta^{13}\text{C}$ vs $\delta^{18}\text{O}$) from SEBRA and Laje Branca host rock stable isotopes values from Paula-Santos et al. (2021). The correlation between isotopes and the statistical significance is indicated in the figure. Straight lines show linear fit with the cross plots.

Reference

Caltabellotta, F.P., Pavan, M., Lopes, A.P., Brumatti, M., Almeida, V.V., Rodrigues da Silva, A.D., Lima, R.A.P., Severino, R.R., Andrade, J.J.C., Almeida, L.C.M., Mapa, F.B., Marques, I.P., Turra, B.B., Costa, V.S., Campos, F.F., Ferrari, V.C., Mendes, D. 2017. Departamento de Geologia - DEGEO. Mapa Geológico de Integração do ARIM Vale do Ribeira (SP e PR). Carta Geológica. São Paulo: CP R M, 2017, 1 mapa colorido, 256 x 88 cm. Escala 1:250.000.

5.9.2. Supplementary Tables

Supplementary Table 4.1 – LB-1 and LB-3 ^{230}Th -U ages.

Sample	^{238}U [$\mu\text{g/g}$]	\pm	$(^{230}\text{Th}/^{232}\text{Th})$	\pm	$(^{234}\text{U}/^{238}\text{U})$	\pm	$(^{230}\text{Th}/^{238}\text{U})$	\pm	age corr.[a]	error [a]	age uncorr. [a]	error [a]	dft [cm]	analyse date
LB-1	4.6434	0.0296	4993	104	1023.6	5.5	0.00260	0.00003	122	11	138	1	3.0	2008
LB-1	5.0565	0.0446	155	3	994.8	7.3	0.03820	0.00044	2105	26	2105	26	19.0	2008
LB-1	5.3969	0.0058	249	6	1007.6	2.1	0.04260	0.00010	2335	6	2336	6	30.0	2020
LB-1	4.5379	0.0045	85	4	1007.9	2.0	0.05320	0.00010	2922	7	2922	7	40.0	2020
LB-1	4.9465	0.0049	88	5	1015.6	1.9	0.06070	0.00013	3324	8	3324	8	51.0	2020
LB-1	4.2506	0.0040	129	5	1007.6	1.9	0.07090	0.00020	3909	10	3910	10	70.0	2020
LB-1	4.9972	0.0373	196	4	1007.9	6.3	0.07860	0.00080	4342	47	4343	47	89.0	2008
LB-1	3.8800	0.0059	487	11	1004.7	2.5	0.09330	0.00020	5175	13	5176	13	105.0	2020
LB-1	5.0821	0.0081	362	9	1000.4	2.5	0.09930	0.00025	5527	16	5528	16	118.0	2020
LB-1	5.9413	0.0075	188	6	994.5	2.3	0.10430	0.00020	5833	13	5833	13	126.0	2020
LB-1	4.2943	0.0051	135	5	995.4	2.1	0.10760	0.00022	6018	14	6018	14	139.0	2020
LB-1	5.2581	0.0271	340	7	996.3	4.9	0.11623	0.00081	6509	49	6510	49	156.0	2008
LB-1	5.2414	0.0087	247	6	1010.6	5.0	0.12164	0.00024	6771	22	6772	22	170.0	2020
LB-1	4.7102	0.0345	168	4	997.6	6.1	0.13084	0.00130	7347	79	7348	79	203.0	2008
LB-3	2.6570	0.0024	3368	68	967.8	1.9	0.01491	0.00012	810	15	829	7	1.7	2020
LB-3	5.3541	0.0058	7366	148	1043.5	2.0	0.03956	0.00010	2109	15	2129	6	7.7	2020
LB-3	3.5644	0.0071	3304	66	1022.2	2.3	0.04270	0.00010	2311	12	2324	7	19.6	2020
LB-3	3.9436	0.0147	803	16	1003.3	3.3	0.05960	0.00030	3285	17	3288	17	28.8	2020
LB-3	6.6692	0.0096	2318	47	993.5	2.4	0.07470	0.00010	4145	10	4150	9	46.9	2020
LB-3	7.4840	0.0119	472	10	1005.8	2.5	0.07810	0.00020	4315	10	4316	10	62.3	2020
LB-3	8.1826	0.0141	1670	34	988.6	2.5	0.08820	0.00020	4928	12	4931	12	76.3	2020
LB-3	6.2672	0.0091	1299	27	989.8	2.4	0.09610	0.00020	5373	13	5376	12	86.5	2020
LB-3	5.4988	0.0236	1530	31	994.0	3.6	0.10460	0.00050	5847	31	5851	31	97.6	2020
LB-3	10.6103	0.0184	4627	93	987.7	2.3	0.10590	0.00020	5941	15	5948	15	103.7	2020
LB-3	8.8533	0.0139	1443	29	992.3	2.3	0.11070	0.00020	6205	14	6207	14	112.1	2020
LB-3	9.0764	0.0146	564	12	980.5	2.4	0.11930	0.00020	6741	16	6742	16	121.2	2020
LB-3	5.6397	0.0234	419	9	988.3	3.4	0.12920	0.00060	7284	37	7285	37	129.1	2020
LB-3	6.7168	0.0170	778	16	960.9	2.5	0.12890	0.00040	7373	23	7374	23	143.9	2020

Conclusions

The goal of this thesis is to reconstruct a record of extreme rainfall events across Southeastern and Southern Brazil throughout the Holocene, providing the first insights into their natural variability. For that, we developed a multi-year cave monitoring program to characterize how caves in the region respond to extreme rainfall events. Between the caves studied, Malfazido Cave stands out. Our five-year hydrological monitoring recorded Malfazido cave response to ERE, including the deposition of sediment over stalagmites. Moreover, this cave present fast-growing stalagmites with potential for preserving interannual flood events, with natural barriers that create slack-water conditions, promoting sediment deposition during flood recession. These characteristics evidences its exceptional potential for reconstructing past ERE. Detailed petrographic analyses of detrital layers within stalagmites from Malfazido Cave allowed us to reconstruct the frequency of ERE over the past 7,500 years using three samples collected from the cave flood zone.

The novel ERE record presented in this study reveals persistent centennial to multi-centennial periodicities over the past 7,500 years, superimposed on a long-term sinusoidal trend. A strong agreement is observed between our reconstruction and Antarctic summer temperature variability, with higher ERE frequencies occurring during colder Antarctic summers. This relationship indicates large-scale teleconnection patterns that increase the likelihood of circulation anomalies related to extreme rainfall events in southern Brazil. During the last millennium, the ERE record exhibits a strong correspondence with El Niño frequency, indicating the increased influence of Pacific–South American teleconnections on the modulation of ERE. Notably, the record shows an anomalously high frequency of ERE during the 20th century, potentially associated with anthropogenic climate change.

Our multi-proxy reconstructions further reveal persistent multi-centennial cycles in trace-element ratios, indicating alternating wet and dry phases throughout the Middle and Late Holocene. The wet periods coincide with Northern Hemisphere cooling events, such as the Little Ice Age and Bond Events, suggesting strong interhemispheric teleconnections. This relationship is further supported by coherent regional patterns across records from the South American Summer Monsoon (SASM) and the South Atlantic Convergence Zone (SACZ), both showing wet anomalies synchronous with North Atlantic cooling. Moreover, an interhemispheric antiphase between these South American records and the Asian monsoon evidences a global-scale response to North Atlantic cooling events, potentially linked to the weakening of the Atlantic Meridional Overturning Circulation (AMOC). The resulting reduction in cross-equatorial heat transport and increase in the interhemispheric temperature gradient

induced a southward displacement of the Intertropical Convergence Zone (ITCZ), enhancing SASM and SACZ activity.

A persistent antiphase relationship between southeastern and southern Brazil further reveals a remarkable dipole pattern at multi-centennial timescales. This dipole resembles the modern South American Dipole observed between southeastern Brazil (SEBRA) and southeastern South America (SESA), mainly driven by Rossby wave train propagation. The dipole seems to be modulated both by Antarctic teleconnections, enhancing rainfall in southern Brazil, associated with the Rossby wave train propagation, and by North Atlantic sea surface temperature (SSTs) variability, with cooling events associated with an intensified SACZ phase. Importantly, our results demonstrate a non-stationary relationship between the dipole pattern and ERE occurrence. While the last millennium corresponds predominantly to the positive (SEBRA) phase of the dipole, earlier intervals of the Late Holocene align more closely with the SESA phase. These changes indicate non-stationary teleconnection, with ERE variability during the last millennium being more strongly modulated by north Atlantic SSTs changes and SEBRA hydroclimate, and during the rest of Late Holocene under higher influence of southern circulation patterns. Together, these findings highlight the complex and evolving interplay between tropical and extratropical teleconnections in modulating extreme rainfall over southern and southeastern Brazil throughout the Holocene.

Overall, the findings of this thesis evidence the sensitivity of Southeastern and Southern Brazil to large-scale atmospheric and oceanic reorganizations and the role of both tropical and extratropical forcings in modulating the long-term variability of hydroclimate and ERE.

Acknowledgements

Julio Cauhy Rodrigues

Date of birth: 07.11.1992

Education

- 2022 – 2025 PhD student at Johannes-Gutenberg Universität – Institute for Geosciences
- 2020 - Research internship at the geochronology laboratory of the University of Minnesota (USA).
- 2018 – 2020 University of São Paulo (USP) - Institute of Geosciences - MSc in Geochemistry of Exogenous Processes
- 2012 – 2016 University of São Paulo (USP) – Institute of Geosciences - BSc Geosciences
- 2019 Summer School on Speleothem Science (S4) – Babes-Bolyai University (Romania) - Poster presentation.
- 2019 PIRE - CREATE Summer School - Climate Research Education in the Americas using tree-ring and cave sediment examples. Organized and attended the event.

Conferences and events:

2024-2025

- 03.2025 – Karst Record conference X - Cape Town, South Africa.
- 03.2025 - Award received: Karst Record conference X – Outstanding Poster Presentation Award
- 04.2024 - European Geosciences Union General Assembly – Vienna, Austria.

2022-2023

- 01.2022-08-2023 - Part of the organizing committee of the 2023 Summer School on Speleothem Science (S4) - São Paulo, Brazil. S4 is a student-led event that brings together PhD, Masters, and Early Career Researchers in speleothem science for lectures, workshops, and discussion on the fundamentals and latest advances in speleothem science.
- 12.2022 – AGU Fall Meeting – Chicago, US – poster presentation
- 07.2022 - Karst Record IX - Innsbruck, Austria– oral presentation
- Mini Summer School on Speleothem Science (S4) – Innsbruck, Austria – attended

Publication

- 01.2022, Quaternary Science Reviews – published paper entitled "Paleoclimatic and paleoenvironmental changes in Amazonian lowlands over the last three millennia".
- 08.2024, JGR Atmospheres – published paper entitled "Pacific Interannual and Multidecadal Variability Recorded in $\delta^{18}O$ of South American Summer Monsoon Precipitation"
- 09.2024, Sciences Advances – published paper entitled "South American monsoon intensification during the last millennium driven by joint Pacific and Atlantic forcing"
- 10.2025, Quaternary Science Reviews – published paper entitled "Reliable identification of flood-borne deposits in speleothems using magnetic microscopy"